ENCAPSULATION OF PROTEINS AND CELLS IN SILICA NANOPOROUS MATERIALS

A DISSERTATION
SUBMITTED TO THE FACULTY OF THE GRADUATE SCHOOL
OF THE UNIVERSITY OF MINNESOTA
BY

Eduardo Reátegui

IN PARTIAL FULFILLMENT OF THE REQUIREMENTS
FOR THE DEGREE OF
DOCTOR OF PHILOSOPHY

Adviser: Alptekin Aksan

November 2011

ACKNOWLEDGEMENTS

I would like to thank my adviser, Professor Alptekin Aksan, for his meaningful guidance and support at all stages on this research. He has been instrumental in helping me become a better scientist. I really appreciate his patience and dedication to this research.

I would like to acknowledge all the present and past members of the Biostabilization laboratory for their support and collaboration during the development of this research: Lisa Kasinkas, Katrina Kniesz, Baris Mutlu, Jason Malsam, and Vishard Ragoonanan. All have helped me through their valuable ideas, discussions, and criticisms. Thanks to members from other research groups: Erik Reynolds, Amit Aggarwall, Jeung-Hwan Choi, Neha Shah, Zengpeng Qin, and Ramji Venkatasubramanian for useful discussions and collaborative work.

I would like to thank all faculty members I have interacted on various research topics. Thanks to Professor Lawrence Wackett and Professor Michael Sadoswky for their collaboration in the preparation of Chapter 4 of this thesis. I am grateful to my doctoral committee, Professor Allison Hubel, Professor Chris Hogan, and Professor Aaron Massari.

I would also like to thank my parents, Mr. German Reátegui and Mrs. Silvia M. Pizarro, and my sister Eliana Herrera. Without their support and help, I would never have been able to achieve what I have. I also like to thank my cousin, Magaly Bailon, for her help, generosity, and hospitality.

Last but not least, I would like to thank Adeli Samame, my beloved wife and best friend, for her support and encouragement during the completion of my doctoral research.

DEDICATION

This dissertation is dedicated to my parents, my sister, my wife, and my aunt Nila (you will always remain present in our hearts and memories).

ABSTRACT

My dissertation presents fundamental and practical scientific contributions. I demonstrated the versatility of the sol-gel processing technology for the study of the basic science behind water and protein structure under confinement, and for the development of novel biotechnology and biomedical engineering applications based on cell encapsulation in nanoporous silica gels.

For the basic science studies of my dissertation, silica nanoporous gels were used to investigate the kinetic and thermodynamic transitions of water under confinement. I demonstrated a direct correlation between the structure of confined water and the secondary structure of proteins in a wide range of temperatures (- 196°C to 95°C). I showed qualitatively that the incorporation of a highly hydrogen bonding osmolyte contributed to improve the thermal stability of encapsulated proteins by a mechanism based on prevention of adsorption at the surface of the nanoporous silica material.

For the practical contributions of my dissertation, I developed two novel applications relevant to the biotechnology and biomedical engineering fields. These applications were based on the encapsulation of prokaryotic and eukaryotic cells in silica nanoporous gels. First, I developed a highly selective and efficient biodegradation platform for the removal of an herbicide, atrazine, from contaminated water. In the second application, I invented a cell capture and isolation methodology that was successfully tested as a cancer cell isolation tool from mixed populations of eukaryotic

cells (normal and cancer cells). Miscellaneous applications were also investigated such as encapsulation as a means of cryopreservation of mammalian and algae cells, and were incorporated in the Appendices of this thesis.

TABLE OF CONTENTS

LIST OF TABLES

LIST OF FIGURES

Chapter 1: Introduction

1.1) Motivation

Encapsulation of macromolecules and cells in biocompatible matrices with retention of activity, viability and metabolic functionality has extensive applications in biotechnology (e.g. biosensing, biocatalysis, photobioreactors) and medicine (e.g. tissue engineering, recombinant protein production, and drug delivery) [1, 2]. Successful encapsulation depends on developing a highly biocompatible encapsulation biomaterial of sufficient mechanical robustness and permeability to permit transport of molecules such as oxygen, nutrients, electrolytes, and also toxic metabolites, hormones, and other bioactive compounds [1].

Silica gels have been studied in the last decade with significant success for encapsulating a large variety of proteins and enzymes [3]. Briefly, when the proteins or enzymes are confined in the silica gel matrix they retain their structure and activity even at harsh conditions of pH or temperature [4]. Moreover, silica gel confinement has been extended to prokaryotic and eukaryotic cells with promising results [5-8]. The tunability of the properties of the silica materials have enable versatile applications in important areas such as bioremediation, regenerative medicine, and new hybrid materials with improved functional and structural properties [9]. The development of these materials represents an emerging multidisciplinary topic at the intersection of life sciences, material sciences, and nanotechnology.

1.2) Sol-gel process

The sol-gel processing of inorganic and glass ceramics is a versatile process that involves the manufacturing of a variety of materials at ambient temperature and pressure. The sol-gel process typically involves the formation of a colloidal dispersion 'sol' that contains a suitable precursor (e.g., colloidal silica nanoparticles) and a solvent, and the subsequent gelation of the sol. Depending on the processing technique powders, films, monoliths or fibers can be prepared under mild synthesis conditions [10]. Even though two main reactions govern the process of gel formation (i.e., hydrolysis and condensation), there are different reaction parameters that allow engineering the material structure and characteristics over different length scales [11].

1.2.1) Types of precursors used for the sol-gel process

The selection of the precursors for the sol-gel processing depends largely on the requirements of the application. The most widely used precursors are TEOS (tetraethyl orthosilicate), and TMOS (tetramethyl orthosilicate). Table 1.1 has a list of the typical precursors that can be used for the preparation of silica matrices following the hydrolysis and condensation reactions, the alkali metal silicate, and the silica nanoparticle routes. In general, any alkoxide precursor that has hydrolysable groups or any metal silicate can be used to form silica gels. However, base or acid catalysis is required in order to hydrolyze the alkoxides. More recently, diol- or polyol-modified precursors such as tetrakis (2-hydroxyethyl) orthosilicate (THEOS) or poly(glyceryl silicate) PGS, an ethylene glycol-modified silane, and a sugar-modified silane appeared as alternatives for

bioencapsulation sol-gel processes. What makes these precursors unique is that the by-products of gelation are biocompatible.

Table 1.1 Silica network precursors.

Chemical Name	Acronym	Molecular Formula	Reactive Groups	Type of reactive group
Tetramethylorthosilicate	TMOS	$Si(OCH_3)_4$	-OH	Inorganic
Tetraethylorthosilicate	TEOS	$Si(OC_2H_5)_4$	-OH	Inorganic
Tetrakis(2-hydroxyethyl)orthosilicate	THEOS	$Si(OCH_2CH_2OH)_4$	-OH	Inorganic
Methyldiethoxysilane	MDES	$C_5H_{14}O_2Si$	-OH	Inorganic
3-(Glycidoxypropyl)triethoxysilane	GPTES	$C_{12}H_{26}O_5Si$	-OH, epoxy ring	Inorganic, organic
3-(Glycidoxypropyl)trimethoxysilane	GPTMS	$C_9H_{20}O_5Si$	-OH, epoxy ring	Inorganic, organic
3-(Trimethoxysilyl)propylacrylate	TMSPA	$H_2C=CHCO_2(CH_2)_3Si(OCH_3)_3$	-OH, acrylate group	Inorganic, organic
N-(3-Triethoxysilylpropyl)pyrrole	TESPP		-OH, pyrrole group	Inorganic, organic
Vinyltriethoxysilane	VTES	$H_2C=CHSi(OC_2H_5)_3$	-OH, vinyl group	Inorganic, organic
Vinyltrimethoxysilane	VTMS	$H_2C=CHSi(OCH_3)_3$	-OH, vinyl group	Inorganic, organic
Methacryloxypropyltriethoxysilane	TESPM		-OH, methacryloxy group	Inorganic, organic
Silica Nanoparticles (e.g. Ludox, Nyacol, cab-o-sil)		SiO_2	-OH	Inorganic
Sodium Silicate (e.g., 27% Silicic Acid 10% NaOH)	Water glass		-OH	Inorganic
Diglycerylsilane	DGS		-OH	Inorganic
Structure Modifiers				
Methyltriethoxysilane	MTMOS	$CH_3Si(OCH_3)_3$	-OH	Inorganic
Trimethylmethoxysilane	TMMS	$CH_3OSi(CH_3)_3$	-OH	Inorganic
Ethyltriethoxysilane	TEES	$C_2H_5Si(OC_2H_5)_3$	-OH	Inorganic
n-propyltriethoxysilane	TEPS	$C_2H_5O)_3SiCH_2CH_2CH_3$	-OH	Inorganic
n-butyltriethoxysilane	TEBS	$C_{10}H_{24}O_3Si$	-OH	Inorganic
3-aminopropyltriethoxysilane	APTS	$H_2N(CH_2)_3Si(OC_2H_5)_3$	-OH, NH2	Inorganic, organic
3-(2,4-Dinitrophenylamino)propyltriethoxysilane			-OH, Dinitropropylamino	Inorganic, organic
Mercaptopropyltriethoxysilane	TEPMS	$HS(CH_2)_3Si(OCH_2CH_3)_3$	-OH, Thiol	Inorganic, organic
3-(2-Aminoethylamino)propyltriethoxysilane		$(CH_3O)_3Si(CH_2)_3NHCH_2CH_2NH_2$	-OH, NH2	Inorganic, organic
Isocyanatopropyltriethoxysilane		$C_{10}H_{21}NO_4Si$	-OH, Isocyanato	Inorganic, organic
Hydroxyl-terminated polydimethylsiloxane	PDMS		-OH	Inorganic
triethoxysilyl-termonated polydimethylsiloxane	PDMS		-OH	Inorganic
Methyltriethoxysilane	MTES	$CH_3Si(OC_2H_5)_3$	-OH	Inorganic
Triethoxysilyl-terminated poly(oxypropylene)			-OH	Inorganic

1.2.2) Reaction mechanisms of the sol-gel processes

1.2.2.1) Hydrolysis and condensation of alkoxides

This route is based on the hydrolysis of alkoxide precursors under acidic or basic conditions in the presence of water. The water/alkoxide molar ratios may vary from 2 to 50. Hydrolysis of the alkoxide leads to the formation of silanol moieties (Si-OH) that are very reactive. Through condensation, these silanol moieties react further and form siloxanes (-Si-O-Si-). At the final step, through polycondensation of silanol and

siloxanes, an interconnected rigid network with pores of submicrometer dimensions and polymeric chains of SiO_2 are formed (gelation) [12]. There is no heat adsorption or release during gelation; only gradual increase in viscosity. The gel formed initially has a high viscosity but low elasticity. Following gelation, further crosslinking and chemical inclusion of isolated sol particles into the spanning cluster continues (aging), leading to an increase in the stiffness of the sample [13]. At the functional group level, three reactions are generally used to describe the sol-gel process by this route:

Hydrolysis reaction

$$\text{-Si-OR} + H_2O \leftrightarrow \text{-Si-OH} + \text{R-OH} \quad (1)$$

Alcohol condensation

$$\text{-Si-OR} + \text{OH-Si-} \leftrightarrow \text{-Si-O-Si-} + \text{R-OH} \quad (2)$$

Water condensation

$$\text{-Si-OH} + \text{OH-Si-} \leftrightarrow \text{-Si-O-Si-} + H_2O \quad (3)$$

1.2.2.2) Hydrolysis and condensation in alkali metal silicate route

This route is based on acid neutralization of silicate solutions. Typically, sodium silicate solutions with SiO_2 content between 27 to 30% (w/w) are used. A dilution in water of the metal silicate is prepared first in order to reduce the amount of acid that needs to be added to the solution [10]. Additionally, silica nanoparticles of different sizes (e.g., Ludox or Nyacol) can also be added to the sodium silicate solution to increase the stiffness of the silica matrix. The principal advantage of this route is that there is no liberation of alcohols as by-products. The silica network is formed by acidifying a solution of sodium silicate (Fig. 1.1). One disadvantage of this method is that an excess

of sodium ions may be released and can cause osmotic stress in the encapsulated biomolecules and cells [14].

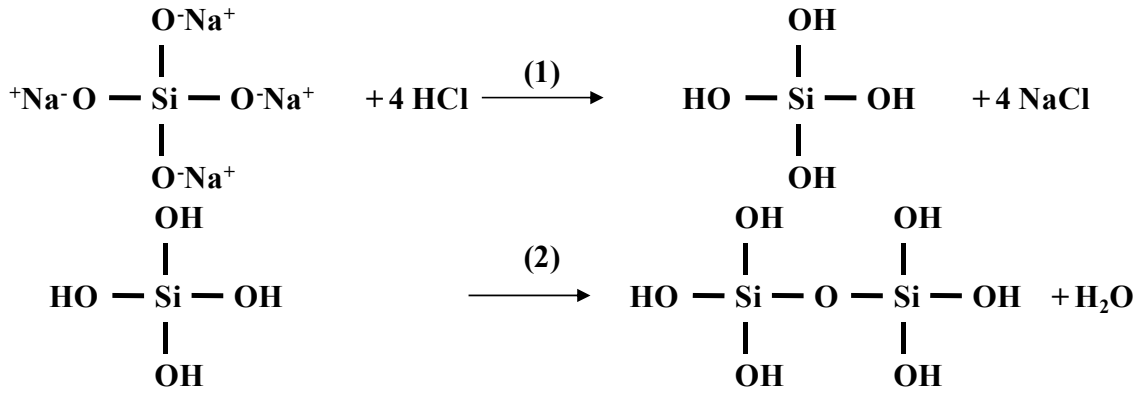

Figure 1.1 Aqueous pathway to silica gel formation: (1) neutralization, (2) polycondensation.

1.2.2.3) Condensation of silica nanoparticles (colloidal gels)

A common method for preparing monodisperse silica spheres, developed by Stöber [15], is to hydrolyze TEOS in a basic solution of water and alcohol. The overall hydrolysis and condensation reactions are given by [10]:

$$Si(OC_2H_5)_4 + 4H_2O \rightarrow Si(OH)_4 + 4C_2H_5OH \quad (4)$$

$$Si(OH)_4 \rightarrow SiO_2 + 2H_2O \quad (5)$$

Hydrolysis and condensation reactions proceed concurrently, as described in the previous section. The stoichiometric amount of water for hydrolysis is 4 moles for every mole of silicon alkoxide, or 2 moles if condensation goes to completion. However, in the preparation of particles, the ratio of water to TEOS is kept typically more than 20:1 and the pH is kept very high. This is done to promote condensation. This encourages the formation of compact structures, rather than extended polymeric networks of the kind generally found in alkoxide-derived gels. Very recently, Yokoi et al [16] demonstrated the fabrication of SNPs using amino acids as a catalyst agent instead of ammonia. The

particles produced in this study had a very high degree of monodispersity and were very stable at acidic pH values (4 to 5).

In aqueous colloidal silica suspensions, the particles at high pH are negatively charged [17]. The colloidal suspension is stabilized against flocculation by the electrostatic repulsion between particles that is controlled with the ionic strength and pH of the solution. Moreover, the addition of a counter ion such as sodium or potassium (e.g., Na^+, K^-) contributes to stabilize the dispersion. When the pH is neutralized with an acid or sometimes with a salt, there is a reduction of the electrostatic repulsion by reducing the Debye screening length and the zeta-potential, which destabilizes the colloidal system and produced aggregation and gelation of the silica nanoparticles [17]. Fig. 1.2A shows the process of destabilization of a colloidal suspension when an acid is added to the solution to neutralize the silica nanoparticles. The change in the pH produces changes in the surface of the silica nanoparticles that are stabilized with a counter ion (e.g., Na^+), as a result the system forms a gel. Fig. 1.2B shows the image of a porous gel formed by the aggregation of silica nanoparticles.

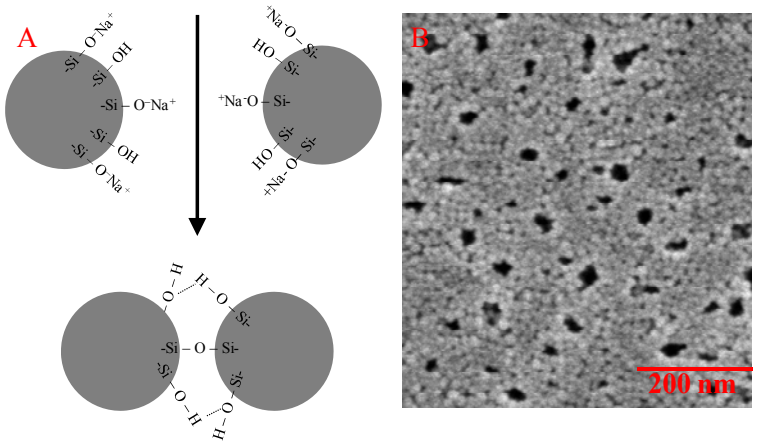

Figure 1.2 Gelation of a colloidal suspension by pH neutralization.

1.2.2.4) Gelation

Gelation happens when the silica particles produced during hydrolysis and condensation start to link together to form a three-dimensional network. The physical characteristics of the gel network depend greatly upon the size of the particles and extend of crosslinking [13, 18]. The gelation kinetics can be described by analyzing at the complex viscosity change of a sol-gel [9]: Three regions can be identified (Fig. 1.3). The first region, where the complex viscosity does not experience a significant change, corresponds to the precursor hydrolysis and sol formation. The gelation transition is represented in region II as an abrupt increase in the complex viscosity. At region III, the complex viscosity also increases, but not as sharply as in the previous region. The change in rheological characteristics in region III show that after gelation, hydrolysis and condensation reactions continue for a long period of time. This is called maturation of the gel or aging [9, 10].

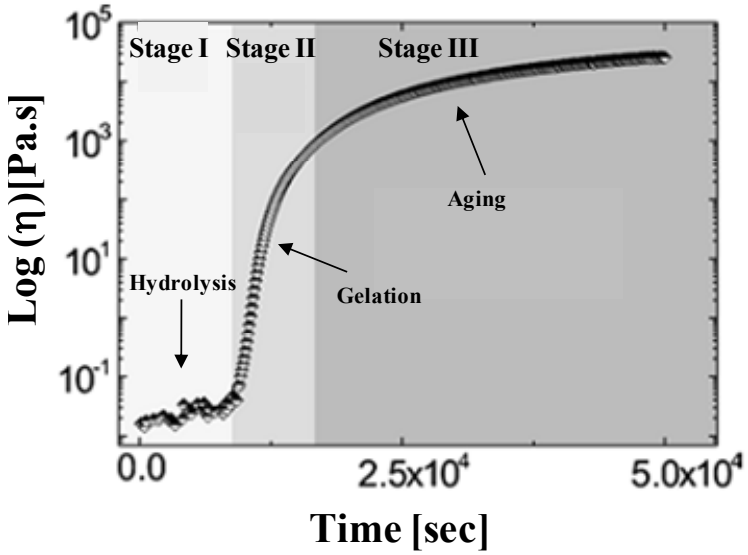

Figure 1.3 Time dependence of the complex viscosity of a sol-gel measured at frequency of 1 Hz (adapted from [9]).

1.2.2.5) Aging process

It has been shown that after gelation, hydrolysis and condensation reactions continue. Nuclear Magnetic Resonance (NMR) studies of the gelled samples show a continuing gradual increase in the number of Q3 and Q4 Si species (i.e. Q shows the tetrafunctionality of the silicon atom through oxygen atoms: Q3 population corresponds to hydroxyl groups (-OH); and Q4 population increases in the absence of hydroxyl groups [19]) due to crosslinking via trans-pore condensation reactions of pore surface hydroxyl groups [20]. This process can continue for months for samples kept at room temperature. The rate of aging depends on pH, temperature and gel composition. The net effect of these processes is stiffening and shrinkage of the sample. Shrinkage occurs because new bonds are formed in place of the weak interactions between surface hydroxyl and alkyl groups. Shrinkage leads to expulsion of liquid from the pores of the gel. This process is known as syneresis [13]. Moreover, at neutral pH, the gel syneresis rate is maximized; continued siloxane condensation reactions cause gel contraction and expulsion of pore fluid. It is plausible that during this time, compressive stresses are formed on the confined cells. These mechanical stresses combined with the presence of alcohol by-products have a negative effect on the encapsulated biomolecules and cells [21].

The silica gel process for bio-encapsulation is modified to avoid the detrimental effects on the encapsulated biomolecules and cells. Rotoevaporation may be used to remove the alcohol during the hydrolysis step before the addition of the biomolecules or cells [22]. Aqueous silica condensation routes have also been developed to avoid alcohols

by-products [23]. Aging and syneresis is reduced by maintaining the silica gel hydrated at all times and also by incorporating osmolytes such as sugars and glycerol into the solution [4].

1.2.3) Chemistry of the sol-gel process

Numerous investigations have shown that the synthesis conditions (e.g., type of the precursor, catalyst, ratio of water to precursor, the concentration of precursor, the medium pH, and the solvent) determine the structure and properties of the final gel [10]. Therefore, the gel may be tailored to meet the requirements of a particular application. [13].

1.2.3.1) The effect of pH

The rates of the hydrolysis and condensation reactions can be influenced by pH [10]. The lowest reaction rate for hydrolysis is obtained at pH = 7 and for condensation around 2. Under acidic condition (pH < 5), the hydrolysis reaction is favored and the condensation reaction is the rate limiting step [24]. The acid-catalyzed gelation is characterized by a cluster-cluster growth model, where the kinetics of aggregation may be limited by the rate of condensation or the rate of diffusion [10, 25, 26]. Under basic conditions (pH > 7), the hydrolysis and particle nucleation processes are dominated by the condensation reaction [10]. Therefore, the precursor molecules aggregate into larger, and denser particles (fewer in number) than at low pH [24]. The larger particles result in smaller surface area and larger pores. More branched networks are formed under basic conditions while chain-like networks are formed under acidic conditions [24].

1.2.3.2) The effect of catalyst

Hydrolysis of alkoxides is promoted with the addition of a catalyst. The activity of the catalyst is determined by pH, since the catalyst for the sol-gel methods is typically and acid or base. Acid catalysts are usually: HCl, H_2SO_4, HNO_3, HF, and acetic acid. Base catalysts are: NH_3, and NaOH. It is well known that the catalyst influences the physical properties of the silica. An acid catalyst produces a dense gel with small pores; on the other hand, a basic catalyst produces highly cross-linked particles which eventually link to form a network with large pores between the interconnected particles. [10, 27]. The concentration of the catalyst is important since turbid colloidal suspensions are obtained when insufficient amounts of catalyst is used (e.g., incomplete hydrolysis of TEOS [28]). A complete hydrolysis of the alkoxide using a catalyst is characterized by a clear and transparent solution.

1.2.3.3) The effect of water content

When silicon alkoxides are reacted at low concentrations of water (moles of H_2O / moles of Si < 2) partially hydrolyzed monomers are formed. These condense to form almost completely esterified linear or branched polymeric species [10, 13]. The molar ratio of $H_2O/Si(OR)_4$ in the gelation solution should be at least 2:1 to approach the minimal hydrolysis level of alkoxide required for gelation [24]. At higher molar ratios, hydrolysis reaction proceeds faster, and the condensation proceeds slower. Molar ratios of H_2O / alkoxide > 4 induce a very loose gel network with high porosity and smaller particle size. The excess water reduces the polymerization rate with respect to the

condensation rate. This produces cyclization and enhances siloxane bond formation within the particles [28].

1.2.3.4) The effect of precursor concentration

The bulk density of the silica gels are gradually enhanced with increasing precursor concentrations in the initial and aging stages of sol-gel processing [24]. At higher precursor concentrations, condensation rates are enhanced since the larger amount of solvent separates the reacting species from each other. On the other hand, at low precursor concentrations, hydrolysis reactions are favored instead of the condensation reactions. The precursor concentration has the most dominant effect on the density and the pore size of the final sol-gel material [29].

Table 1.2 Biohybrid Materials (do not include proteins or cells).

Product	Material		Application	Stage
	Organic Part	Inorganic Part		
Anti Acne Kits (Cool Pearls™)	Benzoyl peroxidase	Silica macrocapsules	Acne treatment	Development & certification
UV-Pearls (Eusolex®)	Organic UV filters	Silica macrocapsules	Sun screen	Commercial development
Scott Dental Glass®	Methacrylic resin	Silane ceramic	Dental fillers	Commercial development
Filtek™, Ketac™, Vitrebond™, Z100™, Vitremer™, RelyX™, Vanish™, Clinpro™	Methacrylic resin / epoxy silane derivatives	Silane treated ceramics	Dental direc restorative cement, sealant, varnish	Commercial development
Nexterion® Microarray	Organosilanes	Organosilanes	DNA and protein microarray	Commercial development
Intra-Cylane™	Organosilanes	Organosilanes	Cosmetic-hair care	Commercial development
Gastromark®	Poly[N-(2-amino ethl)-3-aminopropyl] silane	Non-stoichiometric magnetite	Oral gastrointestinal imaging agent	Commercial development
Nanotherm®	Aminosilane derivatives	Superparamagnetic iron oxide nanoparticles	Liver imaging agent / cancer treatment	Commercial development
Auroshell®	Thiol-derived PEG	Core-shell nanoparticles	Cancer therapy under laser excitation	Development & certification

1.3) Hybrid Sol-Gel Chemistry

It is known that hybrid organic-inorganic materials represent not only a new field of basic research but also, due to their remarkable properties, hybrid materials play a vital

role for the development of diverse technologies [30]. For a complete overview of hybrid sol-gel technology the readers are referred to [9, 30, 31].

Hybrid sol-gel chemistry consists on the incorporation of organic components during or after the sol-gel processing in order to change the physical and chemical properties of the resultant material. This includes the incorporation of macromolecules, enzymes or cells in order to create bioactive materials such as cleaning systems, biosensors, and artificial organs [32]. Nowadays, most of the hybrid materials that have already entered to the market are synthesized and processed by using conventional soft chemistry based on routes developed in the eighties [30]. A distinct characteristic of hybrid materials is that their properties are related not only to the chemical nature of the organic or inorganic components, but also rely on their synergy. In the past decade, a vast number of hybrid materials have been developed for dental applications and cosmetic products [30]. Table 1.2 shows some bio-hybrid products that are in development or commercially available. Moreover, new materials following the sol-gel process have been synthesized for the development of therapeutic vectors and drug delivery platforms [30, 33]. Hybrid materials that include the incorporation of biomolecules and cells will be described in the following sections with more detail.

1.3.1) Silica encapsulation of biomolecules and cells

Even though sol-gel processing has been used for more than a century [18, 34], it was not until the mid 1980s that incorporation of biomolecules such as enzymes, and antibodies within ceramic materials has started to be explored [35]. Since these pioneering studies, biomolecules, prokaryotic and eukaryotic cells have been

encapsulated in inorganic and inorganic-organic hybrid-sol gel polymers [35]. The purpose of bioencapsulation is to retain the structural integrity of the encapsulated biomolecules and their functionality, catalysis, and signal transduction, and to maintain cell metabolism [35, 36]. Encapsulation of cells and proteins in porous silica matrices is achieved when the silica matrix is formed by hydrolysis and condensation reactions of alkoxide or aqueous precursors to yield a polymeric oxygen bridged (O-Si-O) network [4].

When alkoxide precursors such as TMOS or TEOS are used, alcohol by-products (e.g., methanol, ethanol) are formed after the hydrolysis process. The alcohol should be removed prior to incorporation of the biomolecules or cells into the matrix in order to prevent damage [6, 23]. On the other hand, when an aqueous precursor (such as sodium silicate) is used, the hydrolysis reaction releases ions (e.g., Na^+), which need to be removed through ion exchange before encapsulation, in order to avoid osmotic stress (and even toxicity) to the cells [14, 37].

In order to avoid the detrimental effects of these by-products (e.g., alcohols, Na^+), water soluble alkoxides can be used. THEOS is one of the precursors that does not require a catalyst agent and releases ethylene glycol as a by-product, which at moderate concentrations, does not have detrimental effects on biomolecules and cells [38, 39].Moreover, poly(glyceryl silicate) (PGS), which is a silicate derived from glycerol, has been shown to be effective for bioencapsulation since a biocompatible by-product is released during the hydrolysis step [40].

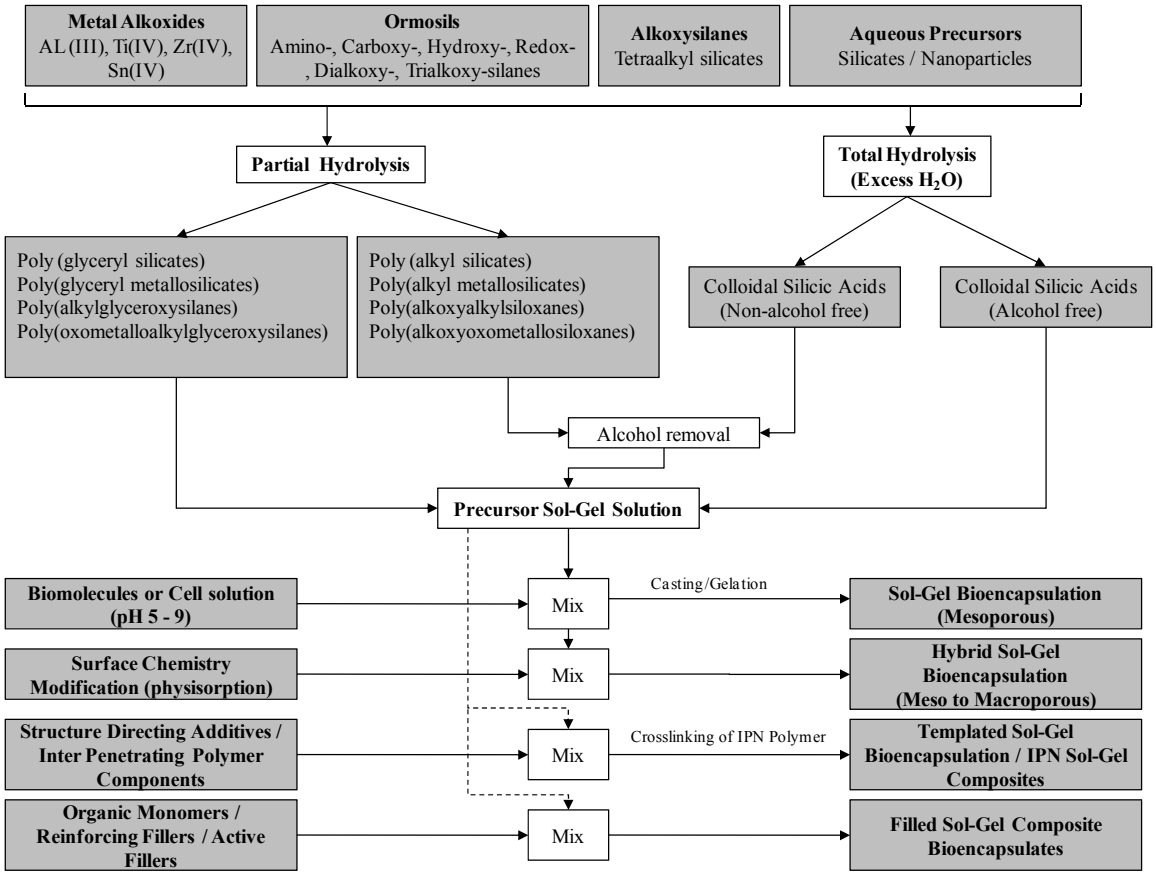

Figure 1.4 General protocols for silica bioencapsulation (adapted from [35]).

Fig. 1.4 shows the different precursor routes that can be used for bioencapsulation. Note that it is also possible to incorporate stabilizing additives such as sugars (sorbitol, trehalose), and organic polymers to modify the surface of the silica gel in order to stabilize enzymes or cells [4].

1.3.2) Encapsulation of macromolecules and proteins

Encapsulation of macromolecules and proteins in a sol-gel matrix preserves protein structure and functionality and protects the proteins against physicochemical perturbations [12]. The route of protein encapsulation is shown in Fig. 1.4 and is

performed in two steps in order to avoid protein denaturation. Post-encapsulation, control of porosity is one of the major challenges in silica encapsulation of proteins. The pores have to be small enough to avoid leaching of the proteins out of the matrix but large enough to allow diffusion of the analytes. The porosity can be tailored by controlling the water content during the hydrolysis process when an alkoxide is used [41].

To date, many proteins and enzymes have been encapsulated in silica gels for catalytic and biosensor applications making use of the inherent features of silica materials such as optical transparency, high specific surface area, and photochemical inertness. Table 1.3 shows a list of enzymes encapsulated in sol-gels to be used as electrochemical and optical biosensors.

Table 1.3 List of enzymes encapsulated in silica gel matrices in biosensor applications (Adapted from [12]).

Biomolecule	Analyte	Sol-gel Precursor	Detection Mode	Reference
GOD	Glucose	TEOS/ Cellulose	Fluorescence	[42]
GOD	Glucose	Ormosil/MTMOS	Amperometric	[43]
GOD/HRP	Glucose	TEOS	Fiber optic	[44]
GOD/Catalase	Glucose	TEOS	Thermometry	[45]
HPR	H_2O_2	TEOS/luminol	Chemiluminiscence	[46]
Tyrosinase	Phenolics	TMOS/Nafion	Amperometric	[47]
Urease	Urea	TMOS/IDA/gold electrode	Conductimetry	[48]
LDH	L-lactate	TMOS	Fluorescence	[49]
Alkaline phosphatase	Pesticides	TMOS	Fluorescence	[50]
Cholesterol oxidase	Cholesterol	TEOS	Amperometric	[51]
Hemoglobin	H_2O_2	TEOS/luminol	Chemiluminescence	[52]

GOD: Glucose oxidase, HPR: horseradish peroxidase, LHD: lactate dehydrogenase

Structure of encapsulated proteins and enzymes depends on the interplay of different forces developed at the silica surface. These forces can be classified as

geometric confinement effects, surface interactions, and changes in the structure of the confined solutions (e.g., water) [53-55]. Theoretical studies of confined proteins show that geometric confinement reduces the entropy of the protein unfolded state by limiting the conformational space available to the protein in the unfolded state [56]. Surface interactions between the silica matrix and the confined proteins appear due to the heterogeneous surface domains of the proteins [57]. These interactions include electrostatic forces, hydrogen bonding and van der Waals forces, and even covalent interactions. The surface interactions between the silica gel and the protein are protein type specific since different proteins have different surface charge distribution, hydration shell water structures, secondary and tertiary structures, and surface reactivity. Moreover, silica surface affects the structure of the confined water and also the hydration water of the confined proteins. This is because, the physical, chemical and thermodynamic properties of water change in close proximity to surfaces or when it is associated with biomolecules and membranes [58-63]. Confined water affects the structural stability of the confined proteins since the dynamics of the hydration layer and the protein are intimately related [64, 65]. The effect of confined water on confined proteins is confirmed when confined globular proteins changed their secondary structures in sync with the structure of the confined water [54].

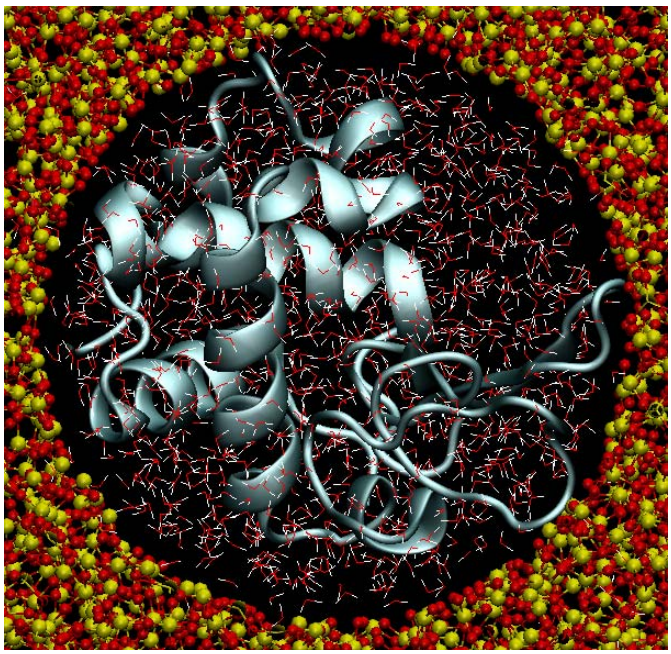

Figure 1.5 Representation of a confined protein (hen egg white lysozyme) in a silica nanopore. The protein appears at the center of the pore embedded in water, image was generated using Visual Molecular Dynamics.

1.3.4) Encapsulation of prokaryotic and eukaryotic cells in nanoporous silica materials

Yeast spores, bacteria and mammalian cells have been encapsulated within silica gels where they have been shown to retain their metabolic activity [5, 8]. For example, prokaryotic cells such as *E. coli* and cyanobacteria retain their metabolic activity for up to 4 weeks when encapsulated in silica gels. Whereas eukaryotic cells such as endothelial cells and fibroblasts, can only stay metabolically active for 1 to 2 days [5-8]. Table 1.4 is a list of different cell types encapsulated in silica gels of different compositions. The main cause of decreased viability and metabolic activity in confined cells is not completely established. However, reports show that mechanical, osmotic, and oxidative stresses together with specific surface interactions play important roles in affecting the

viability and membrane structure of the encapsulated cells [7, 8, 66-71].

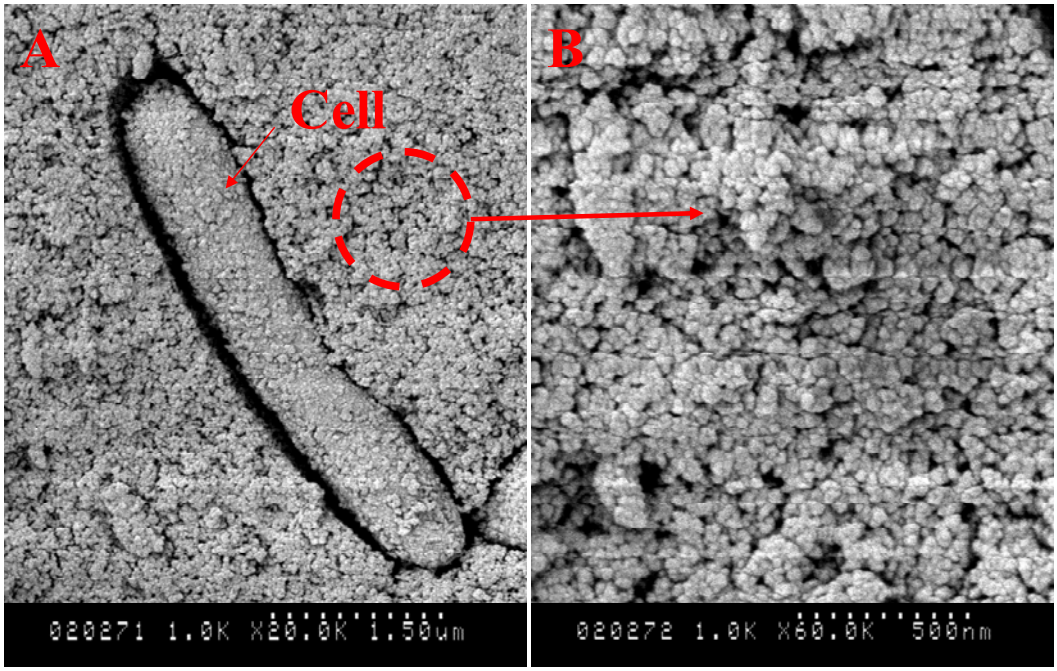

Figure 1.6 (A) Electron microscope (EM) image of an encapsulated E. coli in a nanoporous silica matrix formed using a biocompatible alkoxide route, (B) EM image of the formed nanoporous matrix.

Compressible mechanical stresses on confined cells increase when the silica matrix is aging. These stresses may reach a critical level eventually causing cell lysis [23]. Also, the structural changes in the silica matrix during aging can damage the cellular membrane irreversibly (see Chapters 4 and 5). Additionally, the tensile stresses generated by the encapsulated cells by the pressure of cellular division may cause elevated compressive stresses at the boundary. Note that in the silica gels, the cells are physically constrained from dividing. Therefore, we hypothesized that reducing the effects of aging and eliminating cellular division would reduce the effect of the mechanical stress buildup on confined cells. Aging of the gel could be greatly reduced

when the silica gel maintain its hydration level [7], or by using osmolytes (e.g. glycerol [8], sugars [4]) or biopolymers (e.g., gelatin [67], polyethylene glycol (PEG) [72]). Irradiation or nutrient starvation could be used to minimize the mechanical stresses generated by eukaryotic and prokaryotic cellular division, while maintained viability and functionality.

Table 1.4 Encapsulated cells in silica and silica hybrid materials

Cell Type	Sol-Gel Precursors	Matrix Porosity	Matrix Surface Chemistry	Reference
Saccharomyces cerevisiae	TEOS, TEOS/lipid, PGS, TMOS, TMOS/alginate, sodium silicate/silica nanoparticles, TEOS/GPTMS	Mesoporous	-OH, epoxy ring, -COOH	[69, 73-76]
Pseudomonas fluorescences HK44	TMOS, TMOS/alginate	Mesoporous	-OH, -COOH	[76]
Sulfate-reducing bacteria (SRB)	Silica nanoparticles	Mesoporous	-OH	[77]
Moraxella spp.	Sodium silicate, TMOS	Mesoporous	-OH	[78]
Serratia marcescens	Sodium silicate	Mesoporous	-OH	[68]
Chlorella vulgaris (CCAP 211/12)	Sodium silicate/silica nanoparticles/glycerol	Mesoporous	-OH	[79]
Methylomonas sp. strain GYJ3	Sodium silicate, MTMOS/TEOS	Mesoporous	-OH, $-CH_3$	[80]
E. coli	Sodium silicate/silica nanoparticles/glycerol, TMOS, TEOS, TMOS/GPTMS/PEG	Mesoporous, macroporous	-OH, -COOH	[8, 22, 81-86]
Staphyloccus aureous	TEOS/lipid	Mesoporous	-OH	[87]
Haematococcus	TEOS/GPTES	Mesoporous	-OH, epoxy ring	[88]
Cylindrotheca fusiformis	Sodium silicate	Mesoporous	-OH	[89]
Thylakoids	DGS, Sodium silicate/silica nanoparticles	Mesoporous	-OH	[90]
Synechocystis sp. PCC 6803	TEOS/TMOS/MTEOS	Mesoporous	-OH, $-CH_3$	[91]
Synechococcus sp. PCC6301, PCC	Sodium silicate/silica nanoparticles	Mesoporous	-OH	[14, 37]

7002				
Chorella vulgaris (SAG 211/11b), *Botryococcus braunii* (SAG 30.80)	Sodium silicate/silica nanoparticles	Mesoporous	-OH	[92]
Cyanidium caldarium (SAG 16.91)	Sodium silicate/silica nanoparticles/glycerol	Mesoporous	-OH	[93]
Pancreatic islets	TEOS, TMOS, TEOS/DEMS, Silica nanoparticles	Mesoporous, macroporous	-OH, $-NH_2$	[94-96]
Hepatocytes	TEOS/DEMS/collagen	Mesoporous, macroporous	-OH, $-CH_3$	[97]
HepG2, Jurkat Cells, β-cell (MIN6)	TEOS/DEMS/alginate, APTMS/alginate, TEOS/PDMS	Mesoporous, macroporous	-OH, $-CH_3$	[98-101]
Human dermal fibroblasts	Silicic acid/collagen	Macroporous	-OH	[102]
3T3 mouse fibroblasts	TEOS	Mesoporous	-OH	[6]
HUVEC	Silica nanoparticles	Mesoporous	-OH, $-NH_2$	[5]
Mesenchymal stem cells (MSCs), MC3t3-El	GPTMS/gelatin	Macroporous	-OH, epoxy ring	[103, 104]
Human mesenchymal stem cells (HMSCs), MCF-7, HSC-T6, MC3T3	TEOS/PEG	Macroporous	-OH	[105]
Hybridomas	THEOS	Macroporous	-OH	[39]

Osmotic stress on confined cells builds up in the presence of ions or small molecules that are released during the synthesis of the silica matrices. Oxidative stresses also affected confined cells at the silica-lipid membrane interface, and in the cytoplasm of confined cells since silica motifs (e.g. –Si-O-Si-) may be able to reach the cytoplasm by endocytosis during the silica gel condensation step. Oxidative stress is the result of an imbalance in the pro-oxidant/antioxidant homeostasis of various reactive oxygen species [106]. The reactive oxygen species may appear due to the extended exposure of the cell membrane to the silanol groups (Si-OH) of the silica surface producing lipid peroxidation

[106]. The osmotic and oxidative stresses can be reduced by the incorporation of osmolytes during the synthesis of the silica matrix. One common osmolyte is glycerol, which is usually added to counteract ion concentrations (e.g. Na+) present during silica matrix synthesis and reduce the activity of water [8].

Surface interactions of cellular membranes with silica surfaces are influenced by the chemistry and topography of the silica surface [107]. The cellular membrane is composed of transmembrane proteins, glycolipids, and ion channels that are heterogeneously distributed; therefore, it is expected that interactions of the membrane components with the silica surface are very specific. This has a considerable impact on biological performance at the micrometer scale, influencing cell behavior such as adhesion, intracellular cell signaling pathways, morphology, and proliferation [108, 109]. Moreover, smaller surface features (< 50 nm) influence cytoskeletal assembly by promoting F-actin alignment [110]. Transmembrane proteins such as integrins are the key cell surface receptors that function as the primary bridge between the cell and the external matrix and play a critical role in modulating adhesive cell-silica interactions [111]. It has been shown that cells cultured in silica substrates exhibit a rounded morphology, poor adhesion, and low rates of division [109]. Moreover, the cells return to normal growth and division, when they were removed and placed under normal culture conditions. Structural changes in the adsorbed serum proteins that condition the signal transduction of integrin receptors are one of the explanations for the cellular behavior [109]. The lipid domains of cellular membranes also interact with silica surfaces, lipid membranes of cells consist predominantly of molecules of phosphatidic acids, phospatidycholines,

phosphatidylserine, phosphatidylethanolamide, and cholesterol [112]. There is always a negative charge at the cell surface caused by dissociation of phosphatidic acids. This charge is largely off-set by positively charged groups $[-N(CH_3)_3]^+$ of phosphatidylcholine. Despite the mosaic structure of the external surface of a cell membrane (alternating of positive and negative charged sites), the surface is negatively charged (e.g. erythrocytes). Silica surfaces are known to bear a negative charge due to dissociation of surface silanol groups [113]. However, experimental data shows a strong interaction between the silica surface and the lipid membrane. A simple model has been proposed to ascertain some chemical aspects the interaction of silica surfaces has with lipid membrane components. A membrane has been represented by a cluster of phosphatidic acid and phosphatidylcholine molecules [113]. It is surmised that at distances of 5 to 7°A, the interaction is mediated with charged electrolyte particles, whereas a net with hydrogen bonds is formed close to the surface where the orbital overlap of edge atoms is essential [113].

1.4) Overview of dissertation

The main goals of this thesis are:

- Investigate the effects of silica encapsulation in the secondary structure of proteins and in the structure of lipid membranes.
- Design a rationale approach for the encapsulation of proteins and cells such that the adverse effects of the encapsulating silica matrix can be minimized.
- Develop novel applications for the encapsulation of cells in silica gels.

The first chapter presents an overview of the silica sol-gel process. Common encapsulation protocols for protein and cell encapsulation are described. Moreover, the effects that encapsulation in silica matrices produces in the structure of water, proteins and cellular membranes are discussed.

The second chapter describes the structural changes between bulk water and confined water in silica gel nanoporous matrices. IR spectroscopy revealed that confined water did not freeze at temperatures as low as -180^{o}C, but had liquid-liquid, and liquid-glass transitions during cooling. Moreover, during warming from cryogenic temperatures, the formations of cubic and hexagonal ice in confine water were detected.

The third chapter investigates the effects of confined water on the secondary structure of encapsulated proteins. Different model proteins were encapsulated in silica nanoporous matrices and their structure were analyzed using IR and fluorescence spectroscopy. Direct evidence that the changes in the hydrogen bonding of water induced changes in the structure of encapsulated proteins was obtained. At high temperatures, a reduction of hydrogen bonding of water facilitated protein-silica interactions and the encapsulated proteins underwent denaturation. However, the incorporation of the osmolyte, trehalose, reduced protein-silica interactions, and altered the hydrogen bonding of water. As a result, the high temperature thermal stability of the encapsulated proteins was greatly improved.

The forth chapter describes the sol-gel silica encapsulation of recombinant *E. coli* cells for the development of a biotechnology application. A combination of silica nanoparticles (Ludox TM40), alkoxides, and an organic polymer were used for the

synthesis of the sol-gel silica matrix. After encapsulation, cells maintained their enzymatic activity even though they were not viable. Moreover, the enzymatic activity of encapsulated cells was close to the values of cells that were not encapsulated. Surprisingly, the encapsulated cells maintained enzymatic activity for over four months while free cells only last for 21 days. We also investigated the conformational changes of lipid membranes of encapsulated cells. Our results showed that after encapsulation a significant increase in the packing of the lipid membranes occurred which was attributed to the increase in viscosity of the silica sol-gel during and after the gelation process.

The fifth chapter investigates the viability and metabolic activity of mammalian cells encapsulated in silica matrices. The encapsulation was performed using a water soluble alkoxide in order to reduce the cytotoxicity of the by-product produced during the hydrolysis process. Silica encapsulation conferred conformational change in lipid organization of the encapsulated cells, which was reflected in a drop in the viability and metabolic activity. Moreover, a biocompatible polymer (PEG) was incorporated during the gel synthesis in order to reduce surface interactions between the silica surface and the cell membranes. These new gels (called SPEG gels) allowed the encapsulated cells to maintain their metabolic activity for longer periods of time. The integrity of the cell membranes in SPEG gels was corroborated indirectly by measuring the leakage of the cytoplasmic enzyme lactate dehydrogenase (LDH). Moreover, arresting cellular division of cells by irradiation further extended the metabolic activity of encapsulated cells.

The sixth chapter describes the development of a thixotropic “reversible” biomaterial gel. A thixotropic gel transitions into a liquid when a shear stress is applied to

the gel. The produced gels were used for the reversible encapsulation of mammalian cells. Moreover, when mixtures of cancer and normal cell lines were encapsulated in the gel, most of the extracted cells were cancer cells, which showed the potential of the reversible gels as a screening tool for cancer cells from tumors.

The seventh chapter contains the conclusions of this thesis and includes suggestions for future work.

Chapter 2: Effects of the Low Temperature Transitions of Confined Water on the Structures of Isolated and Cytoplasmic Proteins[1]

2.1) Introduction

Macromolecules such as enzymes and antibodies can be encapsulated in nanoporous matrices, stabilized, and stored for extended periods of time without loss of activity (for recent reviews see Flickinger et al. [114], and Avnir et al. [4]). Interestingly, certain enzymes also have significantly higher reactivity, and stability when confined in nanoscale pores [115-117]. This allows the development of novel technologies that incorporate macromolecules into "reactive" coatings to be used as bioreactors, biosensors, and even biological batteries [114]. Similarly, a handful of studies conducted with bacterial, plant, and mammalian cells show that these more complex entities also have increased stability, and can function when they are encapsulated [94, 118, 119]. In these studies, microorganisms are encapsulated in rigid mesopores (which prevent their proliferation) surrounded by a high permeability nanoporous matrix, which enables diffusion of nutrients and by-products. Encapsulated, non-growing bacteria are shown to be biologically reactive for 60 days to 5 years when used in a variety of applications ranging from hydrogen production, measurement of nitrate levels, and detection of heavy metals, and toxins [120].

---

[1] Reprinted from *Journal of Physical Chemistry B*, E. Reátegui, A. Aksan Effects of Low Temperature Transitions of Confined Water on the Structures of Isolated and Cytoplasmic Proteins 2009, 113, 13048 – 13060, copyright (2009), with permission from American Chemical Society.

It is still not known what mechanism(s) enable the encapsulated biological macromolecules to be stable and functional, and the microorganisms to be reactive for long periods (even exceeding their biological life expectancy). However, there is accumulating evidence for the role of water in confinement affecting the molecular motions of the macromolecules, and the cellular membranes [58-61, 121]. The physical, chemical and thermodynamic properties of water change when it is in close proximity to surfaces or is associated with biomolecules and membranes [58-63]. Also, it is known that there is a strong correlation between the solvent motions and the motions of macromolecules [122-124]. Therefore, to determine the mechanism(s) of stabilization offered by confinement it becomes important to understand the interactions of the confined water with the biological macromolecules.

Similarities between confined water (water in close proximity to solid surfaces) and hydration water (associated with macromolecules and membranes) are profound [125-129]. Much of the intracellular water exhibits physical properties unlike those in the bulk [130, 131]. This is attributed to the presence of high concentrations of proteins (200 to 300 g/l) [132], inorganic ions, and a variety of other small solutes in the cytoplasm enmeshed in a network of cytoskeletal proteins (actin filaments, microtubules, and intermediate filaments). In individual organelles such as mitochondria protein concentration may be even higher [133]. It is speculated that the crowding in the cytoplasm is a major mechanism enabling unusually high reactivity of biomolecules resulting in faster reaction rates (similar to what is observed in confinement) [130, 134, 135].

The present study is focused on understanding the effects of confinement on the kinetic and thermodynamic transitions of water at low temperatures, and also identifying the effects of those transitions on the structures of confined isolated proteins, and the cytoplasmic proteins of encapsulated, intact bacterial and mammalian cells.

2.2) Materials and methods

All of the chemicals and the model protein (hen egg white lysozyme) were purchased from Sigma (Sigma-Aldrich Corp., St. Louis, MO). All of the solutions were prepared gravimetrically on a microbalance using ultrapure water (UPW). For the stock solution, lysozyme was dissolved in UPW at a concentration of 20 mg/ml, and kept refrigerated at -4°C until used.

2.2.1) Cell culture

LNCaP cells were grown following established protocols. Briefly, DMEM/F-12 (Invitrogen Co., Carlsbad, CA) medium was supplemented with 5% fetal bovine serum (Invitrogen), 1% penicillin/streptomycin (Mediatech Inc., Herndon, VA), and 0.01% of 10^{-5} M Dihydrotestosterone. Cells were cultured in 250 ml flasks in growth media and incubated in 5% CO_2 atmosphere at 37ºC until they reached confluence. Before the experiments, cell monolayers were suspended by treatment with 1 ml Trypsin-EDTA (Invitrogen) solution for 5 min at 37ºC. Trypsin was then neutralized by adding 10 ml of DMEM/F-12 to the solution. Cell suspensions were transferred to 50 ml tubes and centrifuged at 800 RPM for 5 min. The supernatant was removed and the cells were re-suspended in 0.5 ml isotonic phosphate buffer (1XPBS: Cambrex Co. East Rutherford,

NJ). The suspended cell solution was then kept in the incubator until encapsulation. Encapsulated cells were analyzed by fluorescence microscopy using an Olympus BX50 microscope (Olympus Inc., Center Valley, PA). The fluorescent dyes used in the viability analysis were Hoescht and Propidium Iodide (Sigma).

Geobacter sulfurreducens was obtained from ATCC (Manassas, VA). Bacteria were grown in media containing (per liter basis): 0.1 g of KCl, 0.2 g of NH_4Cl, 0.6 g of NaH_2PO_4, 10 ml of vitamin mix, and 10 ml of trace mineral mix. The pH of the medium was adjusted to 6.8. Prior to incubation at 30ºC, the medium was flushed with N_2/CO_2 (80%/20%). After the bacteria were inoculated, they were transferred to 10 ml conical tubes and centrifuged at 2500 RPM for 5 min. The supernatant was removed and 0.5 ml of 1XPBS was added. The bacteria were gently agitated and then stored in the incubator until encapsulation.

2.2.2) Encapsulation and characterization

To prepare the nanoporous gels, 1 ml of colloidal silica Ludox 30SM (Sigma-Aldrich Corp., St. Louis, MO) was mixed with 60 µl of 3M HCl. The final pH was 7.2. Later, 1 ml of sol was mixed with 0.5 ml of protein solution (20 mg/ml of lysozyme in UPW). 0.1 ml of the sol was mixed with 0.1 ml of PBS cell solution in all experiments involving mammalian cells, and bacteria. pH was checked and, if needed, re-adjusted by adding small quantities of 3M HCl. Later, 0.5-2µl of the solution was deposited on a CaF_2 window, placed on a modified spin coating device and spun at high speeds to form a thin film over the surface of the CaF_2 window. In all cases gelation was achieved immediately. Some of the samples were equilibrated for 24 h in a controlled humidity

chamber (e.g. 30 and 50% RH) at room temperature. Additionally, UPW samples were prepared by sandwiching 5 µl of UPW between two CaF_2 windows and sealing with vacuum grease.

A nitrogen sorption method was used to measure the pore size distribution in the silica gels. These studies utilized a TriStar 3000 Surface Area and Pore Size Analyzer (Micromeritics Corp., Norcross, GA). Prior to analysis, the sample was degassed for 1 h at 1 mmHg pressure. Pore sizes were calculated from the absorption/desorption isotherms against the vapor pressure at 77.3 K. Fig. 2.1 shows the pore size distribution in the silica gels. The pores had an average diameter of 5.11 nm (absorption) and 4.53 nm (desorption) and a distribution of pore diameters that ranged from 1.8 to 80 nm.

Scanning Electron Microscopy was performed with a Hitachi S-900 FESEM (Hitachi Co., Lawrenceville, GA) Scanning Electron Microscope. Samples of nanoporous gels were sputtered with tungsten at rate of 1A°/min for 10 minutes, and were directly mounted on the microscope.

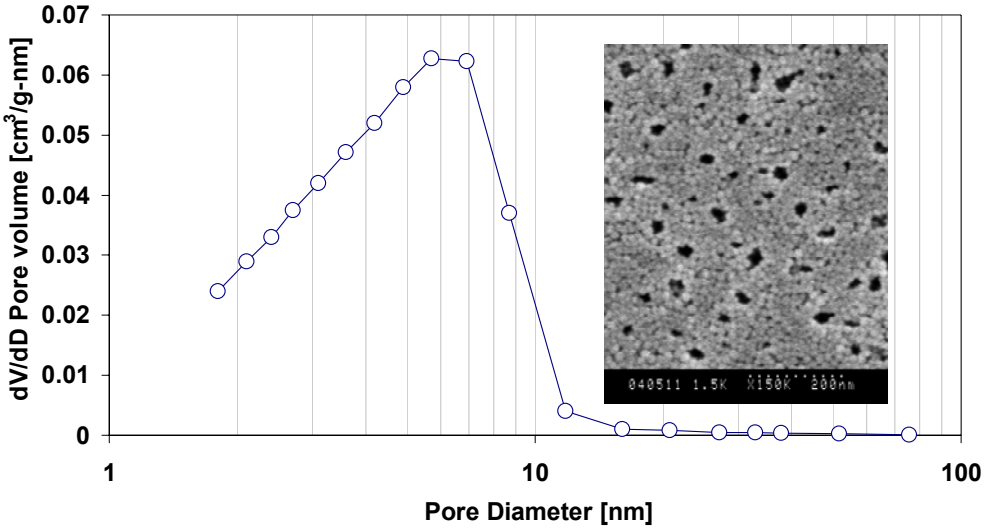

Figure 2.1 Pore size distribution in the silica gel (adsorption). The insert is an SEM image of the silica matrix surface.

2.2.3) FTIR microscopy and spectral analysis

Fourier Transform Infrared Spectroscopy (FTIR) measurements were performed using a Nicolet Continuμm FTIR microscope (equipped with a MCT micron detector, Thermo Electron Corporation LLC, Waltham, MA). IR spectra in the range of 930-4000 cm^{-1} were recorded using an aperture size corresponding to an area of 100 x 100 μm on the sample. The resolution was 4 cm^{-1}, and 128 co-added interferograms were averaged at each data point. A freeze-drying cryostage (FDCS 196, Linkam Scientific Instruments Ltd., UK) was mounted on the FTIR microscope for cooling and heating of the samples at a controlled rate. Spectral analysis was performed using Omnic (Thermo-Nicolet) and Peakfit4 software (Systat Software, Inc., San Jose, CA).

Quantification of the protein secondary structure change was based on the second derivative analysis of the Amide II band (1500 – 1570 cm^{-1}). Note that as opposed to the Amide I band, the Amide II band does not include spectral contributions from water [136], and therefore is more suitable for structural analysis. Second derivative analysis is a standard procedure for quantify the secondary structure of proteins [136-142]. In this method the second derivative of the IR spectra is taken (e.g. second derivative of the Amide II region) and then the intensity of the appeared bands are proportional to the protein secondary structure [136, 138, 140, 141, 143-146]. In the case of the Amide II band, two peaks appeared after the second derivative was taken: (1) β-sheet band (1526-1504 cm^{-1}) [147-149]; (2) α-helix + β-sheet band (1540-1560 cm^{-1}) [148, 150]. The intensities of these bands were measured respect to a common baseline for all the spectra.

2.3) Results

Experiments were conducted with liquid (i.e., bulk water) and nanoporous silica matrix-confined water to identify its kinetic, and thermodynamic transitions in the temperature range of $-180 < T < 45^{o}C$. Similar experiments were conducted to determine the corresponding changes in the secondary structures of a model protein (lysozyme) as well as in the endogenous proteins of silica-encapsulated bacterial and mammalian cells.

2.3.1) Identification of the water families

The ν-OH (OH stretch) band of liquid water was fitted using a Gaussian free-fitting routine. Three water populations with distinct hydrogen bonding (H-bonding) characteristics were identified (Fig. 2.2A). The lowest frequency Gaussian band (ω = 3295 cm^{-1}) corresponded to the water molecules with a H-bonding coordination number of 4, and originated from a population of water molecules organized in a tetrahedral geometry, similar to what is seen in ice. This population was identified as the "Network Water (NW)" [151, 152]. The highest frequency Gaussian band (ω = 3598 cm^{-1}) was assigned to non-H-bonded or weakly H-bonded OH groups.

This band was identified as the "Multimer Water (MW)" [151, 152] and corresponded to water molecules with the H-bonding coordination numbers of 1 and 2. The Gaussian band at the intermediate frequency (ω =3456 cm^{-1}) belonged to the water molecules participating in irregular, energetically unfavorable H-bonded networks. This band was identified as the "Intermediate Water (IW)" [151, 152]. The relative area of each one of these fitting bands have been related to the NW, MW and IW populations

[152]. However, it is important to mention that the ν-OH band absorbs IR energy depending on the degree of hydrogen bonding [153] therefore, there must be a difference between the relative areas and the populations. However, the changes on the relative areas are significant and still can be related to the populations [154, 155]. The scope of this work follows this consideration and the term population will be used. When the temperature is decreased the NW population increases, IW population decreases, and MW population also decreases [151, 152].

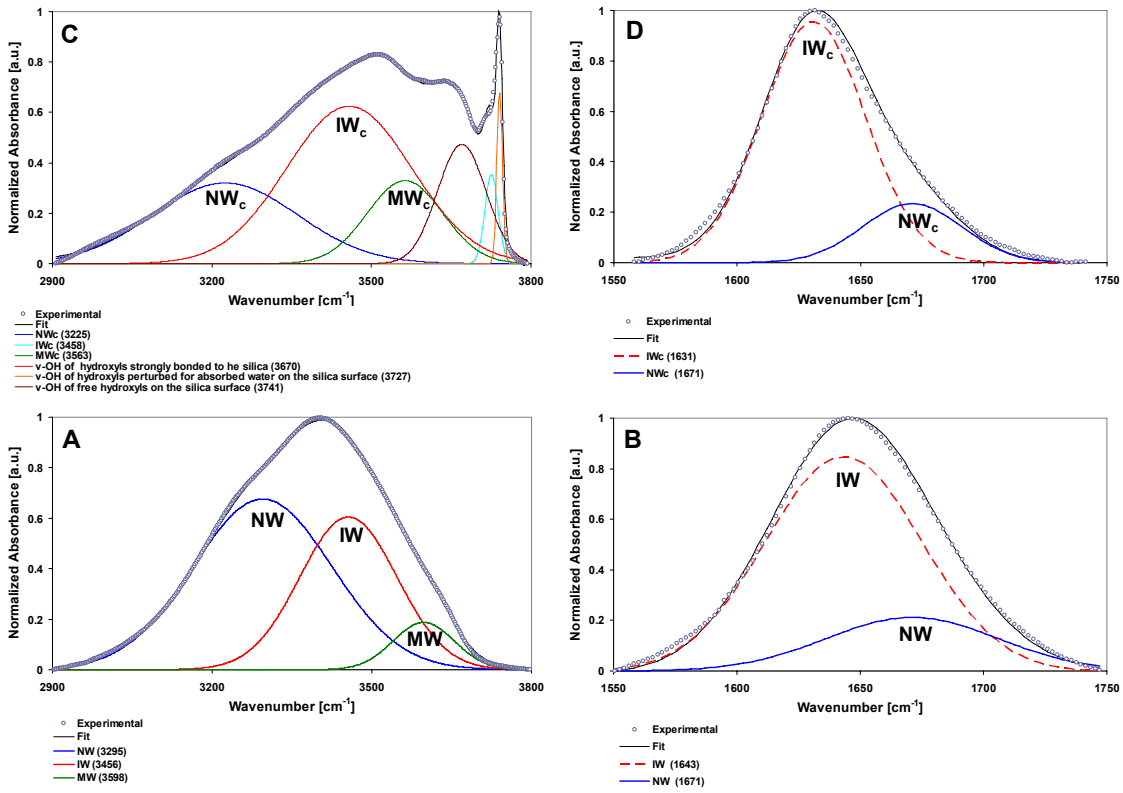

Figure 2.2 (A) ν-OH band of liquid water, (B) δ-OH band of liquid water, (C) ν-OH band of silica confined water, (D) δ-OH band of silica confined water. All IR spectra were collected at T = 23°C.

Due to its asymmetric shape, the δ-OH (OH bend) band was fitted using two Gaussian bands, which centered at 1671, and 1643 cm^{-1} (Fig. 2.2B). The higher frequency band was assigned to water molecules involved in a tetrahedrally arranged H-bond network (NW), whereas the lower frequency band was attributed to water trapped in irregularly H-bonded networks (IW) [152]. The populations of NW and IW water molecules are also represented by the area of each one of these fitting bands [152]. When the temperature is decreased the NW and IW populations increase and decrease, respectively [151, 152].

When the ν-OH band of the water confined in the silica matrix was fitted, in addition to the water families, several high frequency peaks appeared (Fig. 2.2C). These peaks corresponded to the vibrations of the OH groups that were very strongly associated with the silica surface [156]. The Gaussian peaks contributing to the ν-OH band of the confined water were assigned as follows: 3741 cm^{-1}, ν-OH of the free hydroxyl groups on the surface of the silica gel; 3727 cm^{-1}, ν-OH of the hydroxyls weakly bonded to the silica surface and perturbed for near absorbed liquid water on the silica surface [157]; 3670 cm^{-1}, ν-OH of the hydroxyls strongly bonded to the silica [156]; and 3563 cm^{-1}, ν-OH of water monomers, and dimmers, and water molecules absorbed to the silica surface (MW_c) [156]. The bands located near 3225 cm^{-1} and 3458 cm^{-1} corresponded to the stretching vibrations of completely self-associated "ice-like" water (NW_c) and water molecules in irregular H-bonded networks (IW_c) [156, 158]. Considering that there are no silica bands near the δ-OH region of confined water [156], this band was fitted with two Gaussian components [159], at 1631 cm^{-1}, and 1671 cm^{-1}. The assignment of these components were in agreement with the studies of confined water in zeolites [128]. When

the temperature is decreased, the bands at 1631 cm^{-1} and 1671 cm^{-1} follow the same trends as the IW and NW of liquid water, respectively [128]. Therefore, the band at 1631 cm^{-1} was assigned to IW_c and the band at 1671 cm^{-1} was assigned to NW_c (Fig. 2.2D). The additional water families located at high frequencies bands identified in the ν-OH band did not contribute to the δ-OH band due to the nature of the bonds they formed. Note that the water families of confined water have been marked with the subscript "c" because it is indeed possible to have small differences in the composition of the families in liquid and in confined water.

2.3.2) Low temperature transitions of the confined water

Changes in the IR spectra of silica-confined water during constant cooling rate experiments (2^oC/min) were analyzed to reveal the kinetic and thermodynamic transitions of water at low temperatures. Fig. 2.3 shows the changes in different spectral regions of the liquid (i.e., bulk) and confined water during cooling. With decreasing temperature H-bonding among water molecules increased, increasing the NW_c population and thus pushing the δ-OH peak maximum to higher frequencies. The opposite was observed in the ν-OH band, where the peak maximum shifted to lower frequencies.

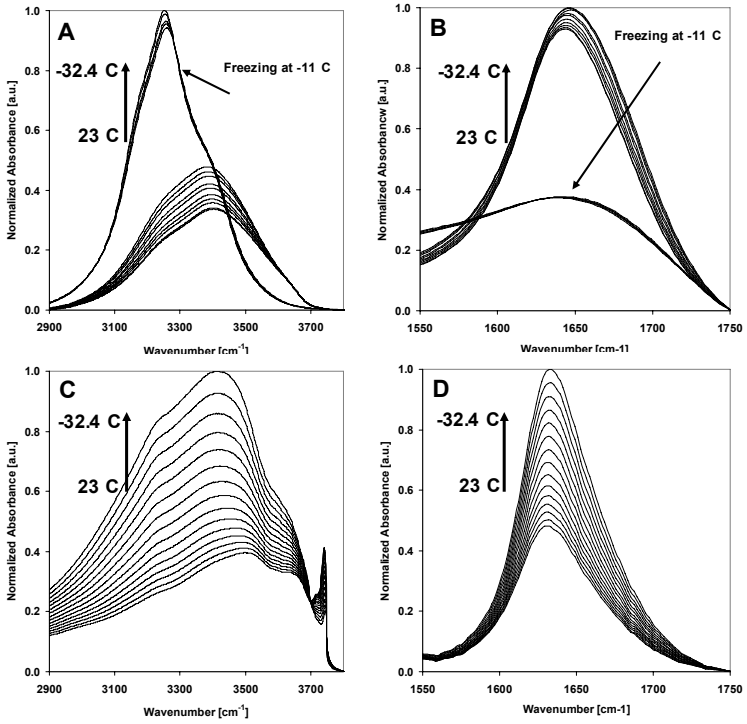

Figure 2.3 Change in the IR spectra during cooling: (A) ν-OH band of liquid water, (B) δ-OH band of liquid water, (C) ν-OH band of silica confined water, (d) δ-OH band of silica confined water.

The δ-OH band of confined water was used to investigate the changes in the NW_c and IW_c populations during cooling. The software PeakFit 4 was used for this task with the appropriate baseline correction. The populations of NWc and IWc were obtained as the area of each fitting band at the different temperatures. Fig. 2.4A shows the change in the NW_c population with temperature. Region I ($0 < T < 20^oC$) corresponds to the stable liquid phase. Region II ($-38 < T < 0^oC$) corresponds to supercooled water, covering the

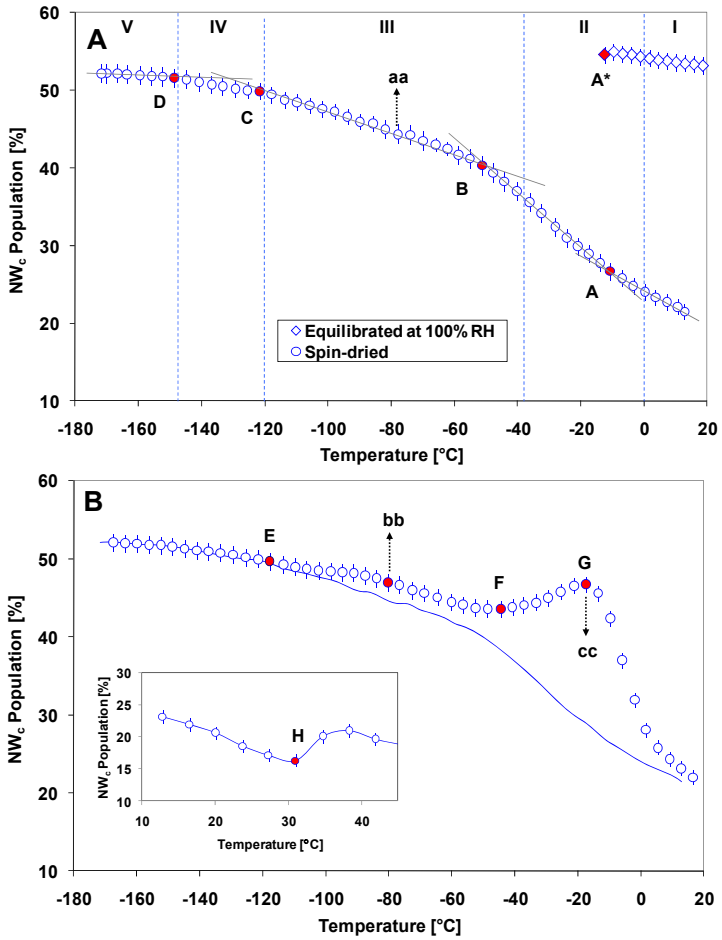

Figure 2.4 Change in the NWc population of confined water during (A) cooling and (B) heating at dT/dt = 2°C/min. The solid line in (B) shows the path during cooling. The insert in (B) is a zoom view in the range 10°C ≤ T < 45°C. The NWc population was calculated using the δ-OH band.

range of subzero temperatures down to the homogeneous nucleation temperature of the liquid water at -38°C. The water in the silica gels equilibrated at 100% RH froze in this temperature range (Point A*). This was observed in their IR spectra by a shift in the δ-OH band maximum to higher frequencies accompanied by a significant reduction in the absorbance of the δ-OH peak at freezing (Point A*). At the same temperature, the water combination peak (~ 2120 cm^{-1}) also shifted to higher frequencies, showing

characteristics of freezing [151, 160]. For the spin-dried gels a slight slope change in the NW_c population curve was observed at approximately -10^oC (Point A). This was attributed to the freezing of water in some of the larger pores (few in number) in the matrix (see Fig. 2.1). However, as evidenced by the lack of the spectral features that accompany freezing (described above), it was concluded that water in the majority of the nanopores did not freeze.

Region III (-120 < T < -38^oC) starts at the homogeneous nucleation temperature and covers the range down to the crystallization temperature (T_x = -120°C) [161]. This region is called the "no Man's land", since it is not possible for the bulk water to remain liquid in this temperature range either during cooling or heating [161]. However, spectroscopic analysis revealed that even in Region III confined water in the spin-dried gels did not freeze but remained liquid. It is known that the freezing temperature of confined water is depressed as a function of the pore size [162-164]. In Region III, a slope change in the NW_c population increase was observed at approximately -51^oC (Points B and B*). This temperature corresponds to the Fragile-to-Strong Transition (FST) of water [165]. It is also is in the neighborhood of the specific heat maximum of supercooled liquid water (-45^oC) [166].

Regions IV and V correspond to the metastable states of water, where the water is ultraviscous and glassy, respectively [167]. Point C (-120^oC) in Fig. 2.4A, another small inflection point, corresponded to the onset of Region IV. Point D (-145^oC), on the other hand, marked the transition of the confined water to a glass, where the temperature dependence of the NW_c population disappeared in all gels. The exact glass transition

temperature of liquid water is widely debated. However, the proposed values generally fall within the range of -134 < T < -149°C [161, 168, 169]. Given that encapsulation also changes the glass transition temperatures of solutions [170], the measured value of -145^{o}C for the glass transition of confined water was considered to be a reasonable value.

During warming from -180^{o}C, the NW_c population followed the same course recorded during cooling up to -118°C (point E), which correlated to T_x. Beyond this point, the NW_c population started to increase with increasing temperature, indicating the formation of cubic ice (I_c). This is in agreement with the published data, which show that when glassy water is slowly heated to a temperature above its T_g at ambient pressure, it crystallizes into I_c [171]. Formation of I_c during warming was attributed to the slow heating rate (2°C/min) utilized, which was not sufficient to eliminate recrystallization [172]. With further heating, I_c transitioned into hexagonal ice (I_h) at -45°C (Point F) [171, 173]. It is known that I_c crystals irreversibly convert to I_h upon heating [174]. NW_c has a structure closely resembling I_h (both have tetrahedral H-bonds). Therefore, transition of I_c to I_h created a significant increase in the NW_c population (much more than that measured during the I_c transition). Point G (-17^{o}C), a local maximum in the NW_c population, corresponded to the onset of the melting of I_h phase. It is known that confinement also depresses the melting point temperature of water [175, 176]. Point H (Fig. 2.4B insert) corresponds to another transition of the confined water (at ~31^{o}C) observed during warming: The specific heat minimum of water [177]. To our knowledge, this was a first time observation of this phenomenon in confined water using FTIR spectroscopy.

In parallel experiments, the cooling/warming rates were altered (1°C/min and 4°C/min) and no significant changes in the locations of the previously described transitions were detected. Moreover, stabilities of the supercooled liquid and the ice phase were probed by holding the temperature of the samples constant at predetermined temperatures. The arrow shown by "aa" in Fig. 2.4A corresponds to a "hold" point (T= -80^{o}C) below FST. With time, the NW_c population gradually increased and eventually reached equilibrium (data not shown). The NW_c population at equilibrium condition for point "aa" was 3.35% more than the NW_c population value obtained during cooling at 2°C/min. Similarly, the arrows marked "bb" and "cc" in Fig. 2.4B show the locations of the "hold" points for the I_c phase, and the I_h melting point, respectively. When the sample was kept at constant temperature at "bb", the size of the I_c phase increased and eventually reached equilibrium (data not shown) indicated by no further change on the NW_c population. The NW_c population at equilibrium condition for point "bb" was 3.80% more than the NW_c population value obtained during warming at 2°C/min. On the other hand, when the sample was kept at "cc", the NW_c population decreased continuously, eventually reaching the values recorded during cooling. The experiments presented here helped identify the different phases, and the kinetic and thermodynamic transitions of confined water during cooling to and from cryogenic temperatures.

2.3.3) Transitions of the encapsulated macromolecules

In the second part of the study, experiments were performed with a model isolated protein (lysozyme), a model bacterium (*Geobacter sulfurreducens*), and model

mammalian cells (LNCaP) that were encapsulated in silica gel matrices. Fig. 2.5 shows the Amide II region of the spectra collected from the encapsulated organisms and lysozyme. The silica gels that contained lysozyme were spin-dried or equilibrated at different RH environments (0%, 30% and 50%). The gels that contained the mammalian or the bacterial cells were spin dried. Fluorescence microscopy-based live/dead analysis (results not shown) indicated that all of the cells survived the silica gel encapsulation process and were intact.

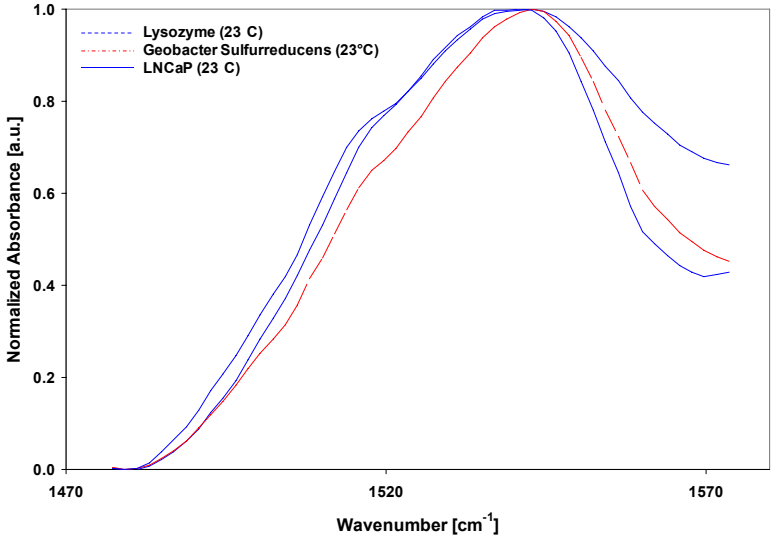

Figure 2.5 Amide II region of lysozyme, Geobacter sulfurreducens, and LNCaP.

Significant changes were observed in the Amide I and Amide II bands of the encapsulated lysozyme when temperature and hydration levels were changed. The Amide I and II bands of the 0% RH equilibrated encapsulated lysozyme were broadened and shifted towards lower frequencies (compared to those for the fully-hydrated lysozyme in solution). These changes were similar to what is observed during decreased hydration

[178, 179]. The spin-dried, the 30% and 50% RH equilibrated samples had spectral features similar to the fully-hydrated lysozyme in solution. During cooling experiments, in all of the gels Amide II peak frequency increased with decreasing temperature. Note that Amide II peak arises from the secondary structures of the proteins and is not affected by water. Fig. 2.6A shows the change in the Amide II peak position as a function of temperature during cooling of the encapsulated and spin-dried lysozyme, LNCaP cells and *Geobacter sulfurreducens*. Note that the inflection (Point B) located at -51^{o}C is at the same temperature as FST observed in confined water (Fig. 2.4A). This temperature also corresponds to the "Protein Glass Transition (PGT) temperature" [180, 181]. PGT is thought to be coupled to the FST of the water molecules that are bound to the amino groups of the proteins [178]. The synchrony between the temperature-dependent structural transitions of the proteins and confined water was also observed during warming (Fig. 2.6B), mainly at point F, which is the I_c to I_h phase change of the confined water; at point G, the I_h melting temperature; and Point H, which is the specific heat minimum of water. Other transitions observed in confined water such as the glass transition (Point D in Fig. 2.4A) and crystallization into I_c (Point E in Fig. 2.6A) were difficult to detect in the Amide II band due to lower signal to noise ratio. These experiments demonstrated the strong coupling between the transitions of the confined water and the secondary structures of the encapsulated lysozyme, and the cytoplasmic proteins of encapsulated organisms.

In order to further quantify the encapsulation-induced changes in the protein secondary structure, second derivative spectral analysis of the fully hydrated and

encapsulated lysozyme were performed. Additionally, FTIR and DSC experiments were conducted with air-dried, fully-hydrated, and thermally denatured lysozyme to quantify the corresponding structural changes of the protein, and to form the basis of the spectral analysis presented below.

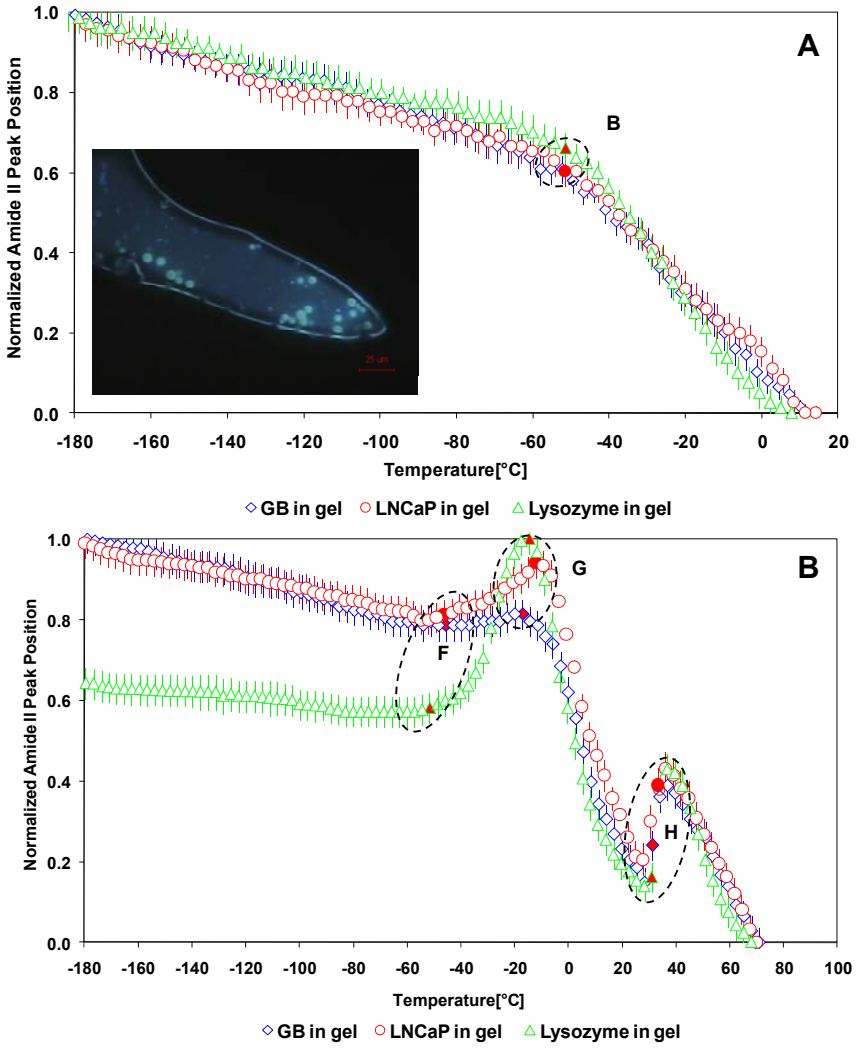

Figure 2.6 Change in the location of the amide II band peak for isolated and cellular proteins during (A) cooling and (B) heating at dT/dt = 2°C. The insert in A is a fluorescence photomicrograph of silica-encapsulated LNCaP cells

Fig. 2.7 shows the β-sheet and α-helix+β-sheet band intensities of fully hydrated and encapsulated lysozyme at different hydration levels as a function of temperature. Structural ordering of the fully-hydrated lysozyme increased with decreasing temperature in the stable and supercooled liquid phases. However, freezing at T ~ -15^{o}C induced a sudden decrease in the α-helix+β-sheet intensity (Fig. 2.7B) and also altered the β-sheet formation kinetics (note the slope change at T~ -15^{o}C in Fig. 2.7A). After freezing, the structural changes of proteins depend on additional factors such as cold temperature, freeze-concentration, ice formation [182], and ice-induced denaturation [183]. The exact contribution of each of these factors to the structural changes of the proteins is not fully understood and presents an active area of research [182-185]. Therefore, the structural changes of proteins does not necessarily correlate directly with changes in the water structure due to the other factors that are inherently present.

In the encapsulated lysozyme (spin-dried, equilibrated at 30% and 50% RH), the β-sheet intensity decreased linearly with decreasing temperature with a slope change at -51°C (2.7C, E, and G). However, the α-helix+β-sheet intensity (Fig. 2.7D, F, and H) increased linearly with decreasing temperature with a slope change at -51°C (corresponding to the FST of the confined water and the PGT temperature of the proteins). The results below PGT temperature must be interpretated carefully. Below PGT energy restrictions render conformational changes of the protein nearly impossible, although small-amplitude vibrational and torsional motions may still be present [57]. Therefore, the existing non-zero slope observed after FST in the α-helix+β-sheet intensities were attributed to backbone intrinsic vibrations, or backbone vibrations induce

by temperature [186]. The existing non-zero slope below FST therefore should not be interpretated as protein structural change [57].

The α-helix + β-sheet intensities (i.e., the structural ordering) of the encapsulated lysozyme, and the cytoplasmic proteins of the bacteria and mammalian cells were linearly correlated to the NW_c content of the surrounding water (Fig. 2.8). This is in accord with the results presented in Fig. 2.6A and 2.6B, supporting the argument that the organization of the surrounding water define the structural changes of proteins in confinement.

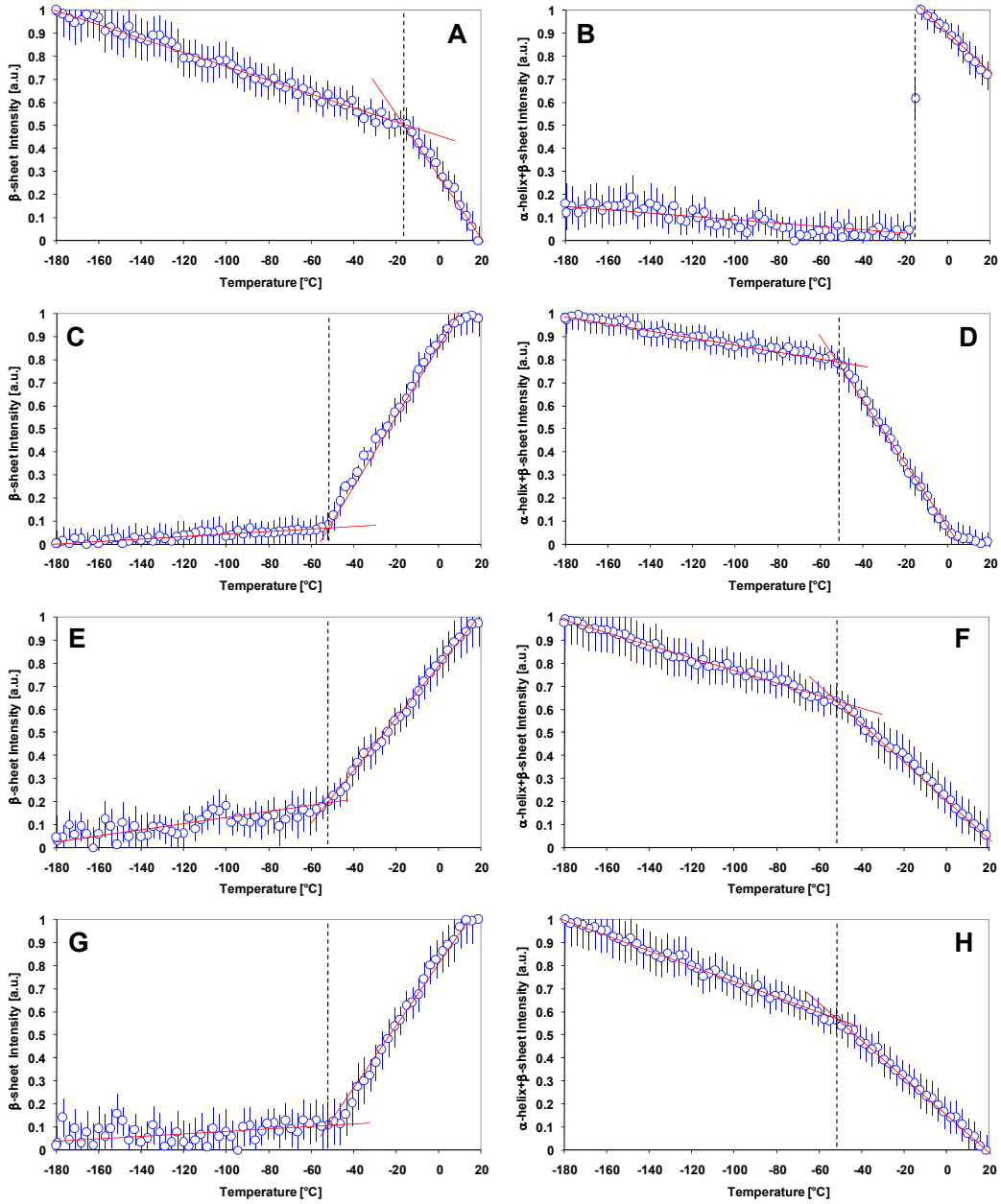

Figure 2.7 Temperature induced secondary structural changes in (A) , (B) fully hydrated lysozyme; (C), (D) silica-encapsulated lysozyme ()spin-dried); (E), (F) silica-encapsulated lysozyme (equilibrated at 30 % RH); (G), (H) silica encapsulated lysozyme (equilibrated at 50 % RH).

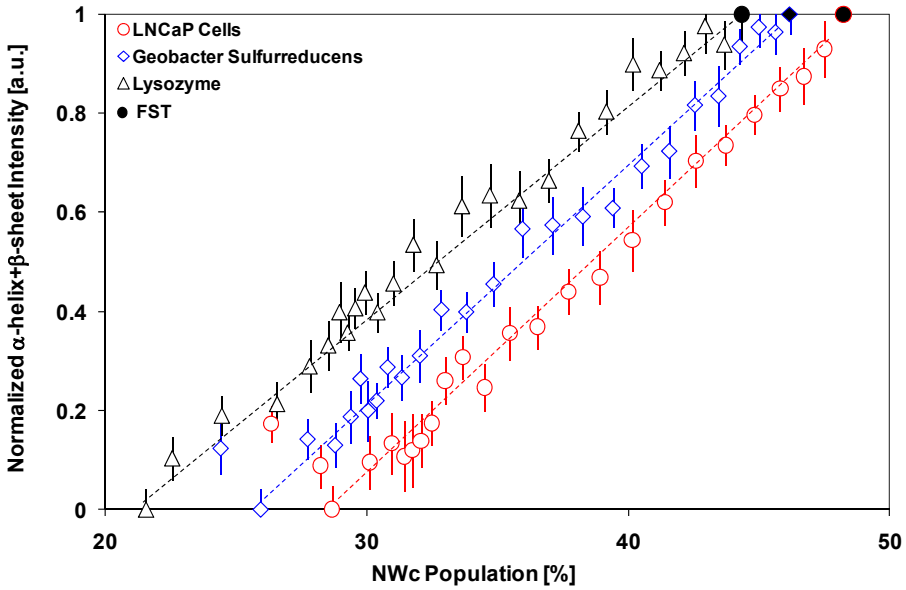

Figure 2.8 Change in the α-helix+β-sheet intensities of the spin-dried encapsulated lysozyme and the cytoplasmic proteins of encapsulated bacteria and encapsulated mammalian cells with NWc population.

2.4) Discussion

Encapsulation alters protein motions and structure at different timescales [187], depending on the hydration level, temperature and the surface charge of the matrix [188-190]. Altered protein motions can be purely vibrational and slaved to the hydration layer or can be conformational and coupled to the viscosity of the solution [191]. For example, CO rebinding kinetics, and the population distribution of different affinity conformations of the sol-gel encapsulated human hemoglobin can be altered by aging the matrix, changing the ratio of water to silica or the pH of the solution [58, 61].

The ability to stabilize different conformations of the same molecule enables the development of new methods to quantify the ligand binding affinity and kinetics of proteins [192] at normally unstable configurations [191]. Encapsulation also enables stabilization of proteins and organisms in functional forms [114]. Therefore, it is

important to quantify the interactions between the protein, its hydration layer and the encapsulating matrix [94, 118-120].

2.4.1) Behavior of confined water

The silica matrix is highly hydrophilic [84, 158] thanks to the hydroxyl and silanol groups that form during gelation. These functional groups can be identified by the unique vibrational bands they generate in the ν-OH region of the IR spectra. They also contribute to a MW_c population increase specifically at close proximity to the surface of the nanopores. Rest of the water in the pores form NW_c and IW_c families and populate the center of the nanopores [193, 194].

In our studies conducted at cryogenic temperatures while the δ-OH band of the liquid water shifted to higher frequencies accompanied by a significant decrease in magnitude (a well-established sign of freezing caused by a very significant change in the bending modes upon solidification [151, 160]). However, confined water preserved its liquid-like characteristics down to -180^{o}C [195]. It is known that the freezing temperature of the water in hydrophilic confinement is depressed significantly as a function of pore size [196]. Freezing point depression may be attributed to the "size effects" (that the water molecules cannot form a large enough nucleation embryo), or to the "surface effects" that change H-bond characteristics and organization. The observed shift in the peak location of the ν-OH bands in the confined water showed differences in H-bond characteristics that were attributed to the surface contributions to the free energy of the fluid in confinement (i.e., the "surface effect") [194]. However, there was also

evidence of the "size effects" playing a role (the presence of NW_c and IW_c families throughout the temperature range) in the observed freezing point depression. This is supported by the published reports correlating the depression of the melting point of confined liquids to pore radius [175, 176, 193, 194, 197].

In the "no Man's land" (Region III), we identified a temperature (-51^oC), at which the temperature dependence of NW_c population growth suddenly changed. This point is at the same temperature as the FST of liquid water (located at $T_c \approx -53°C$, $P_c \approx 1$ kbar) predicted by the Liquid-Liquid Critical Point (LLC) Theory [198]. LLC theory proposes the existence of a first order phase transition between the two phases of liquid water: a High-Density Liquid (HDL) and a Low-Density Liquid (LDL) [198]. LLC theory gives rise to the Widom line, which extends into the one phase region [199]. The FST temperature is pressure dependent and decreases with increasing pressure, until it intersects the crystallization temperature line for bulk water at $P \sim 1.6$ kbar [200]. HDL has tetrahedral H-bonded structure that is not fully developed, whereas LDL has an ice-like, completely developed H-bond structure [201, 202]. Activation energy for HDL is lower than the activation energy for the LDL [198]. This indicates that the NW_c family dominates the LDL, while the IW_c family dominates the HDL, and the FST is a critical transition in the composition of the mixture made up of the NW_c and IW_c families [203]. This is also supported by the fact that near its glass transition temperature water is a very strong liquid, whereas in the supercooled region it is fragile [165]. Therefore, confined water must undergo a structural change (HDL → LDL) before reaching the glassy state.

Experiments performed with liquid water using Nuclear Magnetic Resonance (NMR) [200, 204] and Quasielastic Neutron Scattering (QENS) [198] show that there is a transition in the self diffusion coefficient (D) and the average translational relaxation time (τ_T) of water when the Widom line is crossed. These properties initially show a super-Arrhenius dependence on 1/T at room temperature and at moderately low temperatures (in the fragile liquid regime), but an Arrhenius dependence on 1/T below -51°C (in the strong liquid regime) [198, 199]. FTIR measurements reported here also identified the FST of water. A comparison of the reported NMR data [200] and FTIR data from our research is shown in Fig. 2.9. Change in the temperature dependence of both translational and vibrational motions of water at FST point to possible coupling of these modes.

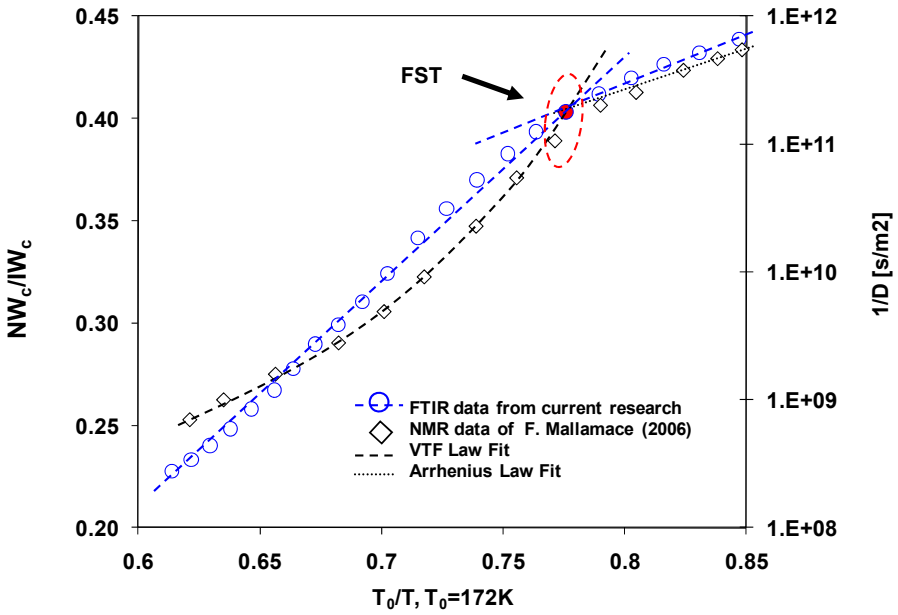

Figure 2.9 Comparison of the FTIR data (this study) with NMR data [200].

During warming of confined water a deviation from the cooling behavior was observed near -120°C, which was caused by re-crystallization. This was also observed

during warming of mesoporous Vycor and sol-gel glasses from cryogenic temperatures [193]. Non-freezing layers cause an apparent decrease in the transition enthalpy, mainly due to the difference in the heat capacities of the liquid and the crystalline phases [205, 206]. Upon heating, the non-freezing layers favor the nucleation of the confined liquid and cause hysteresis between heating and cooling [207].

In confined water, I_h melting point was depressed to -17°C. Depression of the melting point in confined water as a function of pore radius was previously reported in the literature [175, 176, 193, 194, 197]. The Gibbs-Thomson equation can be used to predict the melting point depression of water confined in pores at a radius, *R*,: [197, 207]

$$\frac{T_m^R}{T_m^{free}} = \exp\left[-\left(\frac{2\gamma_{s,l}V_s}{\Delta H_m^R}\right)\frac{1}{R}\right], \quad (1)$$

where T_m^R is the equilibrium melting temperature of the confined solid, T_m^{free} is the melting point of the free solid (0°C), $\gamma_{s,l}$ is the interfacial tension between the solid and its melt, V_s is the molar volume of the solid, and ΔH_m^R is the molar enthalpy of melting at T_m^R. Using Eq. 1 and the values obtained from the literature (ΔH_m^R = 334 J/g, $\gamma_{s,l}$ = 25.5 mJ/m^2, and V_s = 18 cm^3/mol) [193] it was confirmed that the melting point was depressed to -17°C for an average pore diameter of 5.11 nm (Fig. 2.1).

2.4.2) Behavior of confined proteins

Proteins have heterogeneous surfaces and are structurally flexible [187, 208], Confinement in a nanoporous matrix alters the vibrational and conformational motions of

proteins through, *a)* geometrical restrictions imposed by the rigid surfaces known as the "wall effect", *b)* specific interactions between the protein surface and the matrix wall and *c)* the change in the relative populations of the surrounding water [155, 209].

Geometric restrictions imposed by confinement limits the conformational space and hence destabilizes the unfolded state of the protein by reducing its entropy [56]. This increases the stability of the native state in encapsulation [60, 116]. In a recent study [188], it is reported that the global rotational motion of lysozyme is restricted in silica gels at neutral pH, and low ionic strength environment. The origin of the restriction is shown to be due to electrostatic interactions between the encapsulated lysozyme and the silica matrix. However, the segmental vibrational rotations and the conformation of the protein are unaffected [188]. This is in agreement with our results. FTIR spectra in the Amide I and II regions of encapsulated and lysozyme in solution did not show differences, which indicated that the overall secondary structure was preserved.

Protein absorption onto silica surfaces changes its secondary structure, in the literature there are reports that observe changes in the secondary structure of lysozyme due to absorption onto silica nanoparticles [210, 211]. However, in our study the experimental conditions were different, we encapsulated the protein in silica sol-gel, which means that the silica nanoparticles formed a gel through a condensation reaction encapsulating the protein, and the absorption area of the silica particles were reduced due to coalescing of the particles. A very recent study on protein absorption [212] also found that the secondary structures of proteins (cytochrome C and apomyoglobin) differ considerably when they are absorbed onto the silica surfaces (where they lose their

helicity) as opposed to when they are encapsulated in silica (where they maintain their helicity). Additionally, reports in the literature show that interactions of the silica matrix with globular protein can be detected by comparison the IR regions near 3750 to 3650 cm^{-1}. According to these studies, those bands should disappear from the spectrum as a result of strong interactions of the protein with the silica surface [213]. In our experiments, we did not find any difference in the ν-OH band near 3750 to 3650 cm^{-1} between confined water and confined lysozyme (data not shown). There is a possibility that the secondary structure of lysozyme changed locally (probably at the sites that the protein is closer to the silica surface). Another experimental technique such as intrinsic fluorescence could be used to investigate this possibility, but the fact that FTIR analysis failed to detect any structural changes in the overall secondary structure of lysozyme implies that protein-surface matrix interactions must have a local effect. Therefore, even though that there may be specific interactions between the lysozyme and the silica surface (which cannot be detected by FTIR), during cooling the structure of the encapsulated lysozyme was altered mainly due to changes in the solvation properties of the surrounding water [64].

Recent studies on encapsulated proteins suggest that confined water plays an important role in the structural changes of proteins, it is showed that changing the activity of confined water with ions (e.g. phosphates) enhance the α-helix content of proteins. It is hypothesized that an interchange in the order of water molecules between the silica surface and the ions are determinant for the protein stability [65, 121]. At low temperatures the structuring effect that water has seem to be the responsible for ordering

the protein. The observed difference in the temperature dependence of the β-sheet and the α-helix+β-sheet intensities of the fully-hydrated (Fig. 2.7A,B) and encapsulated (Fig. 2.7C-H) lysozyme can be attributed to the difference in the surrounding water populations [209]. Freezing results in an abrupt change in the H-bonding organization of water causing a net reduction in the conformational flexibility, the hydration level, and the structure of the protein [182]. This was confirmed by the evolution of the β-sheet and α-helix+β-sheet intensities, which showed a drastic change at the freezing point (Fig. 2.7A, B).

In all the cases, the β-sheet intensity of the encapsulated lysozyme decreased very significantly down to -51°C. On the other hand, in all of the encapsulated samples the α-helix+β-sheet intensity increased linearly until FST was reached. The FST temperature is also very close to the reported PGT temperature of the lysozyme at -48°C [179, 214]. At FST, confined water changes from an HDL-dominant to an LDL-dominant organization [203]. When surrounded by the HDL-dominant water (which has weaker, energetically unfavorable H-bonds) the α-helix content of the encapsulated lysozyme increased with decreasing temperature (as shown by a higher slope in Fig. 2.7D, F, and H in the range $-51 < T < 0^{o}C$). It is known that a greater change in the conformation of the lysozyme occurs in the protein regions with α-helical and RC domains where there are many weak or bifurcated H-bonds (high IW and MW content) [215]. We propose that with increasing population of NW_c more water molecules are stripped from the RC domains [216]. Scarcity of water forced the RC domains to transition into an α-helical configuration where the remaining structural water could be tightly locked in the α-helix core. A very

similar behavior is also observed in apomyoglobin in the presence of increased amounts of neutral salts[65]. Note that the "structuring behavior" seen here at low temperatures is opposite of what is observed during high temperature denaturation where the amount of protein-associated water increases by an increase in the α-helix to RC conversion [217].

It is important to indicate that at temperatures below PGT the protein does not exhibit conformational flexibility and shows no biological function [125, 218]. Therefore, RC to α-helix conversion is probably prohibited due to energetic reasons [57]. Interestingly, we were still able to measure the signal corresponding to α-helix+β-sheet and β-sheet intensities at temperatures below -51°C. We attributed this phenomenon to the vibrations of the backbone atoms of the protein that are still present at these temperatures [57]. Neutron scattering, X-Ray scattering, and computational studies explore the dynamic transition of proteins by the analysis of the mean square thermal fluctuations of the atoms of the hydration water and the atoms of the protein [124, 186] [179, 219, 220]. It is claimed by these techniques that harmonic protein vibrations are present at temperatures below the dynamic transitions and large unharmonic vibrations are present above the transition [219]. The harmonic vibrations of the protein (below the dynamic transition) are interpretated as protein backbone intrinsic vibrations, or backbone vibrations induce by temperature which can not cause protein structural changes [186].

The increase in the structuring of the encapsulated lysozyme (until FST) with the change in the surrounding water H-bonding characteristics becomes more obvious when the α-helix+β-sheet intensity of confined Lysozyme, and the cytoplasmic proteins of

confined bacteria (Geobacter Sulfurreducens), and the mammalian cells (LNCaP) are plotted with respect to the NW_c population (Fig. 2.8), where a strong, linear correlation is observed. Note that these transitions were reversible and the protein reverted back to its initial conformation with it was heated back to room temperature. We postulate that the NW_c population increases with decreasing temperature, reducing the H-bond interactions of water with the protein, causing re-structuring. This behavior is not seen when the protein is trapped in a frozen solution. More detailed studies are required to understand whether this is the main distinction between the "cold denaturation" observed in proteins in frozen solutions and the stabilization of proteins by encapsulation.

Temperature-induced kinetic and thermodynamic transitions of the confined supercooled liquid water had a strong influence not only on the structures and dynamics of isolated proteins but also on the endogenous proteins of intact mammalian cells and bacteria encapsulated in the silica matrix. We propose that due to the high permeability of the cell membrane to water there is an equilibrium between the extracellular and intracellular water H-bonding structure and activity. Therefore, confinement-induced changes in the extracellular water was also reflected in the intracellular water. This shows the equivalency of the hydration water and confined water, and may create a platform to devise new methods to explain the crowding-induced high reaction rates in cells [60]. This observation requires further analysis and experiments are being conducted in our lab to further analyze the mechanisms.

2.5) Conclusions

Physical and chemical properties of water define life. Exploring these -mostly anomalous- properties, its phases, thermodynamic, and kinetic transitions reveals the fundamentals of most biological processes. From biopreservation/biostabilization perspective, behavior of water at cryogenic temperatures, and at lower chemical activity is of utmost interest [221, 222]. The principal obstacle to studying water at low temperatures is that bulk water cannot remain liquid below its homogeneous nucleation temperature (T_H = -38°C) [161, 165, 200]. However, when confined in nanoporous matrices, crystallization can be inhibited enabling exploration of its behavior even at cryogenic temperatures [198, 200].

Silica matrix confinement provided an excellent opportunity for exploring the thermodynamic transitions of the supercooled water, and its direct interactions with proteins. Using FTIR spectroscopy, we have identified the kinetic and thermodynamic transitions of confined water at cryogenic temperatures. We have also shown that the structural transitions of isolated and cytoplasmic proteins are dictated by the thermodynamic and kinetic transitions of their hydration water.

Chapter 3: Effects of Water on the Structure and Low/High Temperature Stability of Confined Proteins[2]

3.1) Introduction

Encapsulation of proteins and enzymes in nanoporous silica matrices has received considerable attention in recent years [4]. Certain enzymes retain high levels of activity and functionality in confinement [59], and develop resistance against pH or temperature-induced unfolding [4]. Even though the exact mechanisms by which these enzymes acquire these characteristics in confinement are yet not known, it has been proposed that: 1) specific interactions of the enzymes with the nanopore surfaces; 2) the altered properties of the interfacial water (that is in very close proximity to the enzyme and the nanopore surface) [4, 60, 223]; and 3) geometric confinement play significant roles.

The unique characteristics proteins and enzymes acquire in confinement enabled development of new materials and technologies such as reactive coatings for optical and electrochemical biosensors [224], affinity chromatography [225], immunoadsorbent and solid-phase extraction materials [115], porous matrices for controlled release [226], and solid-phase biosynthesis systems [227]. Additionally, confinement in nanoporous silica matrices mimics the conditions in the crowded cytoplasms of living cells [134]. Therefore, confinement offers a new platform to be used in biophysical/biochemical studies[223] for exploring the mechanisms and kinetics of folding and unfolding of proteins in crowding [4, 65, 228].

[2] Reprinted from *Physical Chemistry and Chemical Physics,* E. Reátegui, A. Aksan, Effects of water on the structure and low/high temperature stability of confined proteins 2010, 12, 10161 – 10172, copyright (2010), with permission from Royal Chemistry Society.

Surfaces alter the molecular motions (and the physical, chemical and thermodynamic properties) [58-63] of water in their close proximity. Therefore, when confined, the freezing temperature of water is suppressed and thus it may remain as a supercooled liquid even at cryogenic temperatures [229]. Since, water is known to govern the motions of the macromolecules it is in contact with [58-61, 122-124] it is plausible that at cryogenic temperatures (in the absence of freezing) unique structural configurations for macromolecules can be achieved. Therefore, confinement at cryogenic temperatures also offers a platform to probe the previously unexplored configurations of proteins.

In this study, structural changes in model proteins encapsulated in silica nanoporous matrices were examined. This was done to understand the role of water hydrogen Bonding (HB) on the structural changes and the thermal stability of the confined proteins at low (cryogenic) and high temperatures. Tryptophan (W) Intrinsic Fluorescence (IF), Fourier Transform Infrared (FTIR) Spectroscopy, and Differential Scanning Calorimetry (DSC) analyses were utilized. In order to further explore the roles of protein-silica interactions and water HB, a cryo-/lyoprotectant agent, trehalose (Tre) was also incorporated into the matrix. Tre was chosen based on its common use in protein formulations as a stabilizer, its high solubility and compatibility with the proteins and the silica matrix.

3.2) Materials and methods

Three model proteins were used in this study: Bovine serum albumin (BSA, 99% pure), hen egg white lysozyme (LYS, 98% pure), and porcine pancreatic trypsin (PPT,

98% pure). 30% (w/w) colloidal silica (Ludox 30SM) was used as the primary precursor for the silica matrix. The proteins and the colloidal silica were purchased from Sigma (Sigma-Aldrich Corp. St. Louis, MO). α,α-Trehalose Dihydrate (99% pure) was purchased from Ferro-Pfanstiehl (Ferro-Pfanstiehl Laboratories, Waukegan, IL).

3.2.1) Protein encapsulation and nanoporous gel characterization

Experimental solutions were prepared gravimetrically on a microbalance using ultrapure water (UPW). For the stock solutions, BSA, LYS, and PPT were dissolved in UPW at a concentration of 20 mg/ml (BSA, 315.3 μM; LYS, 1397 μM; PPT, 840.3 μM). Stock solutions were kept refrigerated at 4°C until used. To prepare the nanoporous silica sol-gels, 100 μl of the colloidal silica was mixed with 6 μl of 3M HCl to form the sol at a pH of 7.2. Later, 10 μl of sol was mixed with 5 μl of the protein solution (LYS, BSA, or PPT). When needed, Tre was added to the sol at a concentration of 0.25 M or 0.5 M. The solution was then vortexed for 5 min. 0.5 - 2μl of the experimental solution was deposited on a CaF_2 window forming a thin film layer. In all experiments, gelation was achieved immediately. The gels were equilibrated for 24 h in a controlled humidity chamber at 40% relative humidity (RH) and room temperature. At the end of the equilibration period the gels were sandwiched between two CaF_2 windows and sealed with vacuum grease.

A nitrogen sorption method was used to measure the pore size distribution in the silica gels. Porosity of the prepared gels (in the absence of any encapsulated protein) was measured using a TriStar 3000 Surface Area and Pore Size Analyzer (Micromeritics Corp., Norcross, GA). Details of the experimental procedure are given in the previous

chapter [55]. The sol-gel method and the conditioning procedures described above produced gels with average pore diameters of 5.11 nm and 8.35 nm for silica and silica-Tre, respectively. The incorporation of the osmolyte Tre produced a shift on the pore size distribution on the silica-Tre gels (Fig. 3.1).

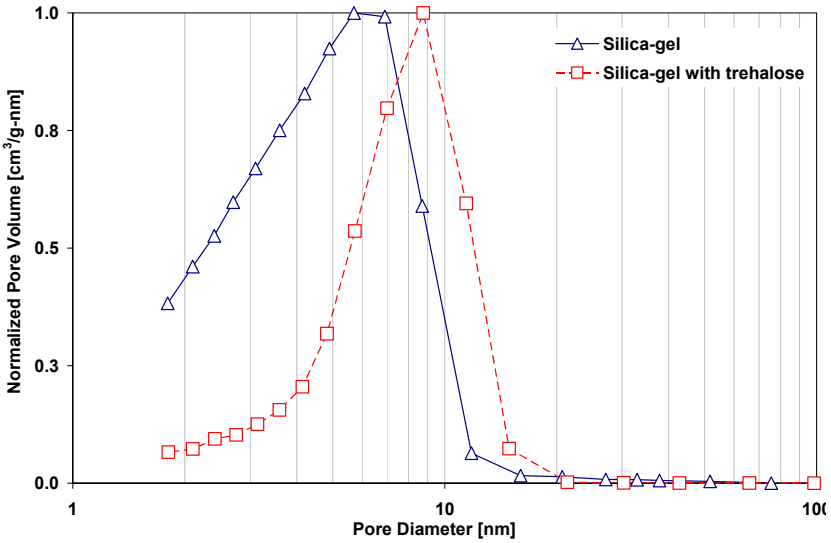

Figure 3.1 Pore size distribution of silica-gel and silica-gel with trehalose.

3.2.2) Intrinsic fluorescence experimentation

Intrinsic Fluorescence (IF) measurements were conducted using a Fargoland/Eclipse spectrophotometer (Varian Inc., Palo Alto, CA), which uses second or third harmonic of the passive Q-switched YAG microchip laser as the excitation source and a DS252 8Gs/s digitizer. The emission spectra were recorded in the 300 to 500 nm range at a resolution of 0.5 nm at 1s response time. The scan speed was 600 nm/min. The excitation wavelength (λ_{exc} = 295 nm) was chosen to excite the Tryptophan (W) residues of the model proteins [230]. Note that LYS, BSA, and PPT have 6, 2, and 4 W residues per protein, respectively [231]. The photomultiplier tube voltage was automatically set to

500 V. A Peltier cuvette holder was used to keep the temperature of the sample constant at 23°C during the measurement.

3.2.3) IR spectroscopy and spectral analysis

Fourier Transform Infrared (FTIR) Spectroscopy measurements were conducted using a Nicolet Continuμm FTIR microscope (equipped with a MCT micron detector, Thermo Electron Corporation LLC, Waltham, MA). Details of FTIR data acquisition are described elsewhere [55]. A cryostage (FDCS 196, Linkam Scientific Instruments Ltd., UK) was mounted on the FTIR microscope for cooling and heating of the encapsulated proteins at controlled rates. Spectral analysis was performed using the software provided by the manufacturer (Omnic by Thermo-Electron).

Changes in the confined protein secondary structure were quantified by the second derivative analysis of the amide II region (1500 – 1570 cm^{-1}). Note that the intensities of the spectral bands in the second derivative spectra are known to be proportional to the protein secondary structure content [136, 138, 140, 141, 143-146]. In the amide II region, two peaks appeared in the second derivative spectra: The β-sheet band located at 1504 - 1526 cm^{-1} [147-149], and the α-helix + β-sheet band located at 1540 -1560 cm^{-1} [148, 150]. The intensities of these bands were measured with respect to a common baseline. In the presence of Tre, it was not possible to analyze the changes in the secondary structures of the encapsulated proteins using the second derivative analysis described above since Tre spectrum partially overlaps with the amide II peak. Therefore, in the presence of Tre an alternative method was used to analyze the protein structure. The alternative method is based on measuring the change in the peak position of the

amide II band (which is shown to correlate well with the second derivative analysis (Fig. 3.2) [232], however it does not provide the detailed information obtained from the second derivative analysis.

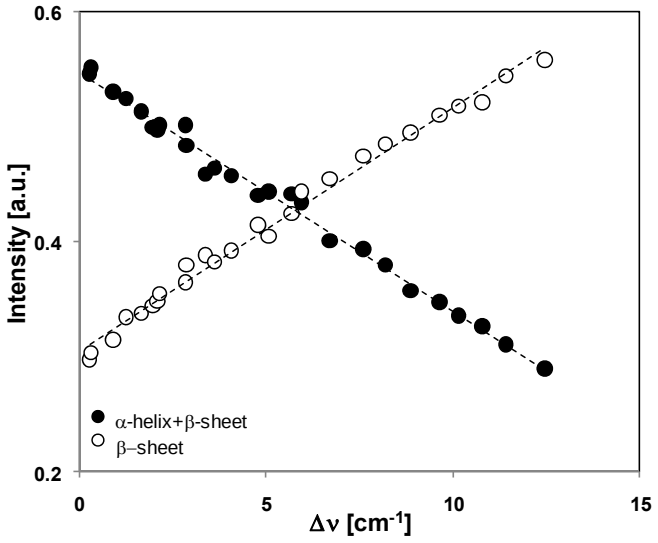

Figure 3.2 Correlation of Δν (change in wavenumber position) with α-helix + β-sheet and β-sheet intensity.

HB (i.e., the structure) of the confined water was quantified by the analysis of the asymmetric near-infrared (NIR) combination peak of water ($NIR_{\nu 2+\nu 3}$) located at 4600 - 5300 cm^{-1}. This was done since the stretching (ν-OH) and the bending (δ-OH) bands of the confined water overlap with the amide A and amide I bands of the proteins [233]. Note that the spectral contribution from the proteins to the NIR combination band of the confined water is negligible (insert in Fig. 3.3). The $NIR_{\nu 2+\nu 3}$ peak was fitted with three Gaussian peaks representing different water populations using the Peakfit4 software (Systat Software, Inc., San Jose, CA) as follows: The lowest-frequency band ($S2_c$: 5093 cm^{-1}) was assigned to the water molecules with both hydrogens bonded to other water

molecules; the $S1_c$ band (5185 cm^{-1}) was assigned to the water molecules with one bonded hydrogen; and the highest-frequency band ($S0_c$: 5261 cm^{-1}) was attributed to water molecules that were not hydrogen bonded [234, 235]. The water populations in the bulk and confined water were measured using the integrated areas of the $S2_c$, $S1_c$ and $S0_c$ fitting bands (Fig. 3.3) [234-236].

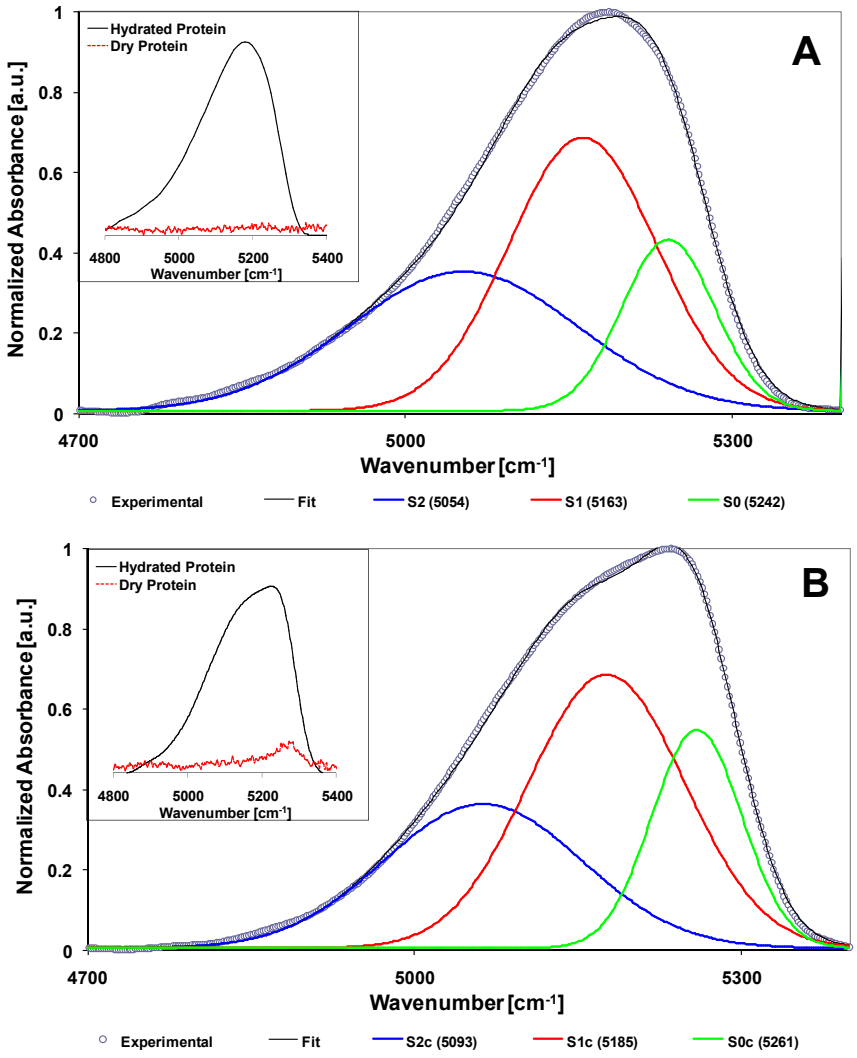

Figure 3.3 Decomposition analysis of the $NIR_{\nu 2+\nu 3}$ band: (A) for bulk water, (B) for confined water.

In a previous study [55] our group examined the temperature-induced changes in hydrogen bond networking of confined water using the ν-OH and δ-OH bands. In that study, ν-OH and δ-OH were used to determine the water populations as: the Networking Water "NW_c", the Intermediate Water "IW_c", and the Multimer Water "MW_c". NW_c population was assigned to water molecules with a coordination number of four (4 hydrogen bonds), IW_c was assigned to water molecules that had energetically unfavorable hydrogen bonds, and MW_c was assigned to water molecules that had 1-2 hydrogen bonds [151, 152]. We found that the $S2_c$ and NW_c populations showed identical temperature dependence (see Fig. 3.4) in confined as well as bulk water (see the insert in Fig. 3.4). In the presence of Tre the $NIR_{\nu 2+\nu 3}$ region had an additional peak, which was fitted with one Gaussian band ($S2_c^*$: 4800 cm^{-1}). This peak originated from the water molecules strongly bonded to Tre molecules [237], as indicated in Fig. 3.5.

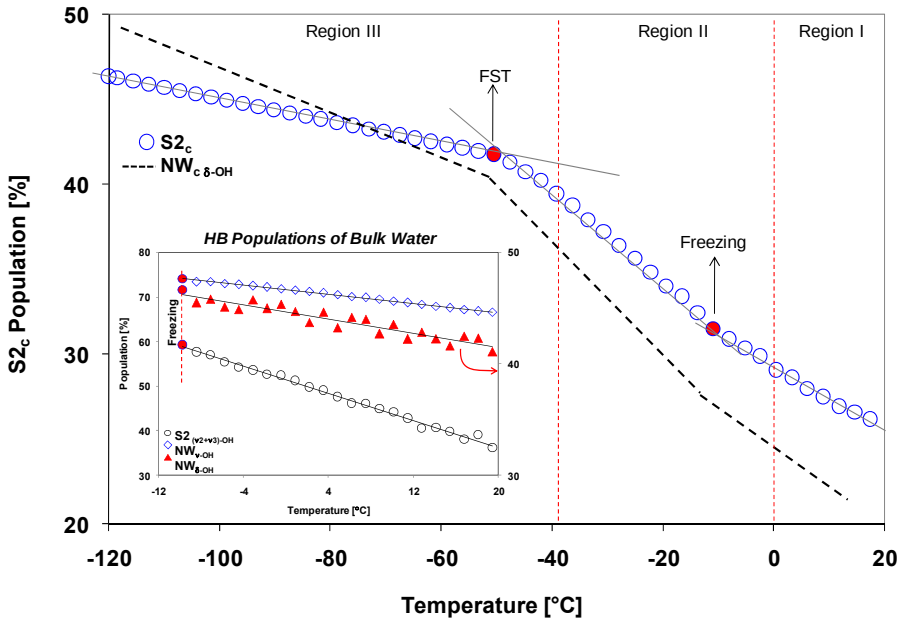

Figure 3.4 Temperature-induced changes in the S2c water population. The insert shows the temperature-induced in S2, $NW_{\delta\text{-}OH}$ and $NW_{\nu\text{-}OH}$ for bulk water.

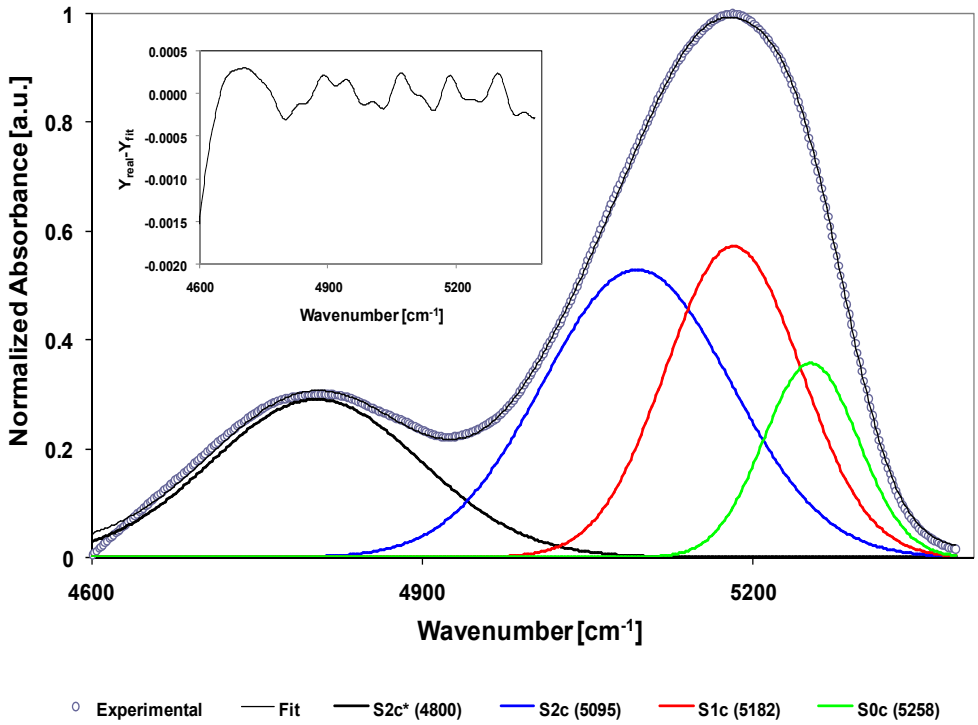

Figure 3.5 Decomposition analysis of the $NIR_{\nu 2+\nu 3}$ band for silica-Tre gel (0.25 M). The insert correspond to the residual values of the fitting process.

3.2.4) Differential Scanning Calorimetry Analysis

The glass transition (T_g) and denaturation temperatures (T_D) of the samples were measured using FTIR spectroscopy and also by Differential Scanning Calorimetry (DSC) using a Pyris 1 DSC (Perkin-Elmer Inc., Shelton, CT). Temperature measurements were calibrated using the phase transition temperatures of Cyclopentane (-151.16°C), Cyclohexane (-85.8°C and 6.4°C), and Hexatriacontane (72.14°C). Heat flow measurements were calibrated against the latent heat of melting of the pure cyclohexane crystals (79.6 J/g). In DSC experiments, approximately 10 mg of the sample was loaded in an aluminum pan (Perkin-Elmer) and crimp-sealed. All the experiments were

conducted at a fixed heating/cooling rate of 2°C/min. The data was analyzed using the software provided by the manufacturer (Perkin-Elmer).

3.3) Results

The purpose of this study was to determine the influence of the water HB organization on the structures of the model proteins confined in nanoporous silica gels during low (cryogenic) and high temperature incursions. The model proteins used in this study had different secondary structures: LYS has a combination of α-helix and β-sheet structures (α-helix: 30%, β-sheet: 13%, and β-turn: 27%) [238]; BSA structure is dominated by α-helices (67%) [239], while PPT structure is mainly composed of β-sheets (α-helix: 10%, β-sheet: 25%, and β-turn: 14%) [240]. The Define Secondary Structure of Proteins (DSSP) database and the Accessible Surface Area (ASA-View) algorithm [241, 242] were used to determine solvent accessibility to the amino acid residues of LYS, BSA, and PPT.

3.3.1) Change in protein structure with confinement in silica nanopores

The emission spectrum of the W residues is highly sensitive to the changes in solvent polarity and therefore can be used to monitor the structural changes in proteins [243]. IF analysis of the encapsulated model proteins were conducted after the samples were equilibrated under identical conditions as described in the methods section. When encapsulated, the IF spectra of the model proteins were red-shifted by 0.8, 0.5, and 1.1 nm for LYS, BSA, and PPT, respectively (Fig. 3.6A, B, C). BSA was the least affected

by encapsulation. The red shift was observed even in the presence of Tre such that LYS, BSA, and PPT experienced shifts of 0.6, 0.5, and 0.9 nm, respectively.

The red-shift values measured in confinement (~ 1 nm) reflected the relatively mild local changes in the solution environment of the W residues [55, 60, 64]. These changes were not attributed to complete unfolding (or denaturation) of the proteins: The IF spectra collected from fully thermally-denatured proteins (pre-heated to 95°C before encapsulation) exhibited significantly larger red-shifts in the order of 10 - 20 nm (Fig. 3.6). These observations were in agreement with the previous reports [60] and were also confirmed by FTIR analysis (Fig. 3.6D, E, F). FTIR spectra showed some change in the secondary structures of the proteins due to confinement however, these changes were not as drastic as those seen in fully-denatured proteins.

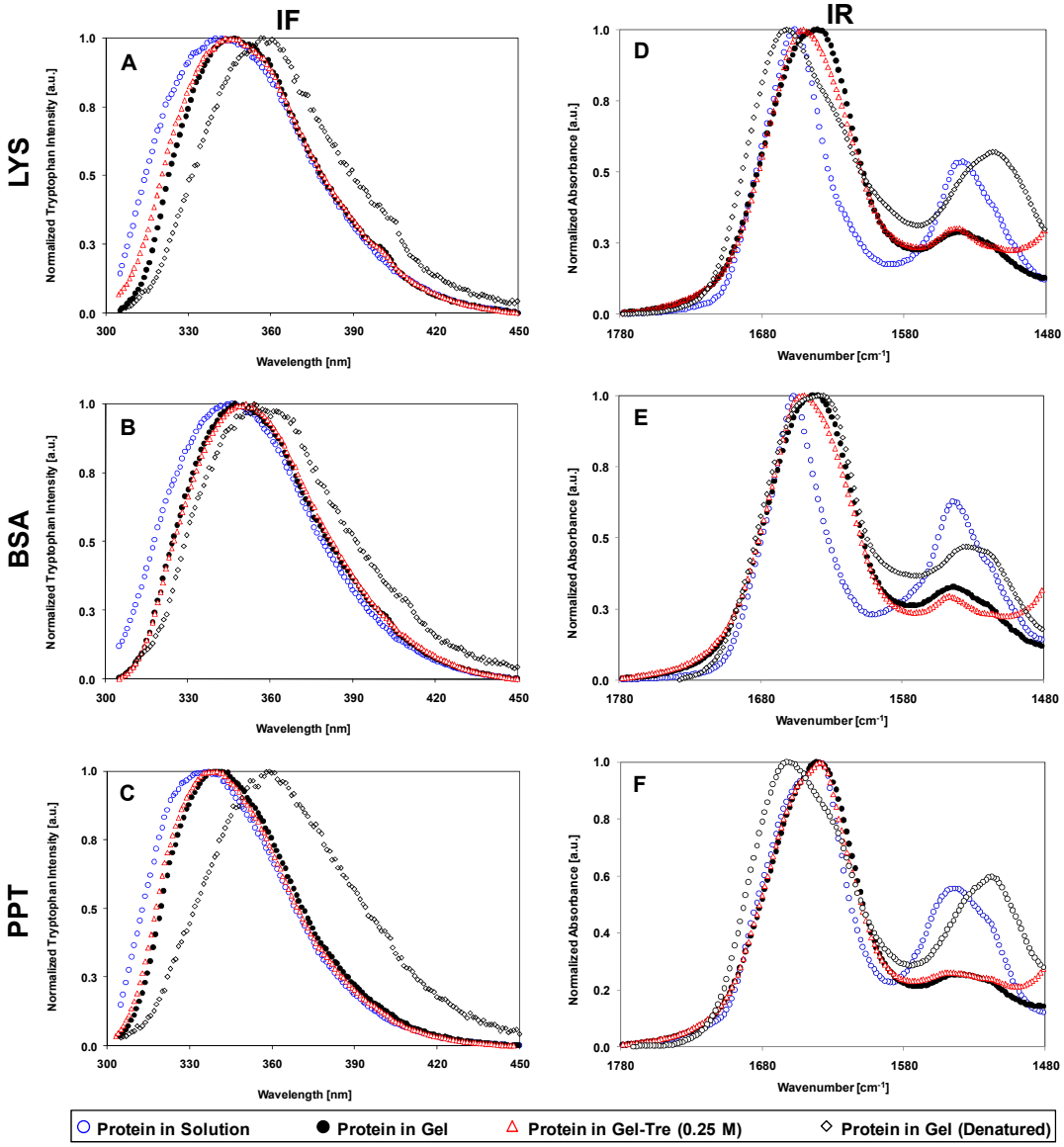

Figure 3.6 Normalized IF spectra of W residues: (A) LYS, (B) BSA, (C) PPT. Normalized IR spectra: (D) LYS, (E) BSA, (C) PPT.

3.3.2) Structural changes in confined proteins at low (cryogenic) temperatures

When water is confined in nanopores, its freezing temperature is significantly depressed [54, 55]. Therefore, encapsulation of the model proteins in nanoporous silica gels enables exploration of protein structural changes at cryogenic temperatures in the absence of freezing (Fig. 3.7). For all model proteins α-helix + β-sheet content increased

(while the β-sheet content decreased) linearly with cooling (at a rate of 2°C/min). This indicated a net increase in the α-helix content, and a corresponding compaction with decreasing temperature. Note that an increase in α-helix + β-sheet content was also observed in proteins in solution during supercooling (dashed line in Fig. 3.7B). However, in solution the β-sheet content also increased (dashed line in Fig. 3.7A) and upon freezing at T = -15^{o}C, majority of the structural changes stopped.

Since freezing temperature of water was suppressed in confinement, structural changes in proteins continued even at cryogenic temperatures (Fig. 3.7). However, a sudden decrease in structural mobility was detected at T = -51°C (full circles in Fig. 3.7). This temperature corresponds to Fragile-to-Strong Transition (FST) of liquid water [154, 165, 200, 244] and also to Protein Glass Transition (PGT) temperature [125, 155]. It has previously been shown that below PGT large conformational changes are prohibited, although vibrational and torsional motions may still be present [57]. Therefore, the non-zero slopes present for T < -51^{o}C in Fig. 3.7 should not imply ongoing conformational changes in the protein structure [57]. When the same experiments were conducted with thermally denatured LYS no significant change in the α-helix+β-sheet or the β-sheet contents was observed (Fig. 3.7). This showed that the measured kinetics were strictly structural. Yet, at -51°C a very small change in slope could still be identified in the thermally denatured LYS. This was thought to be originating from the residual structure remaining in denatured LYS.

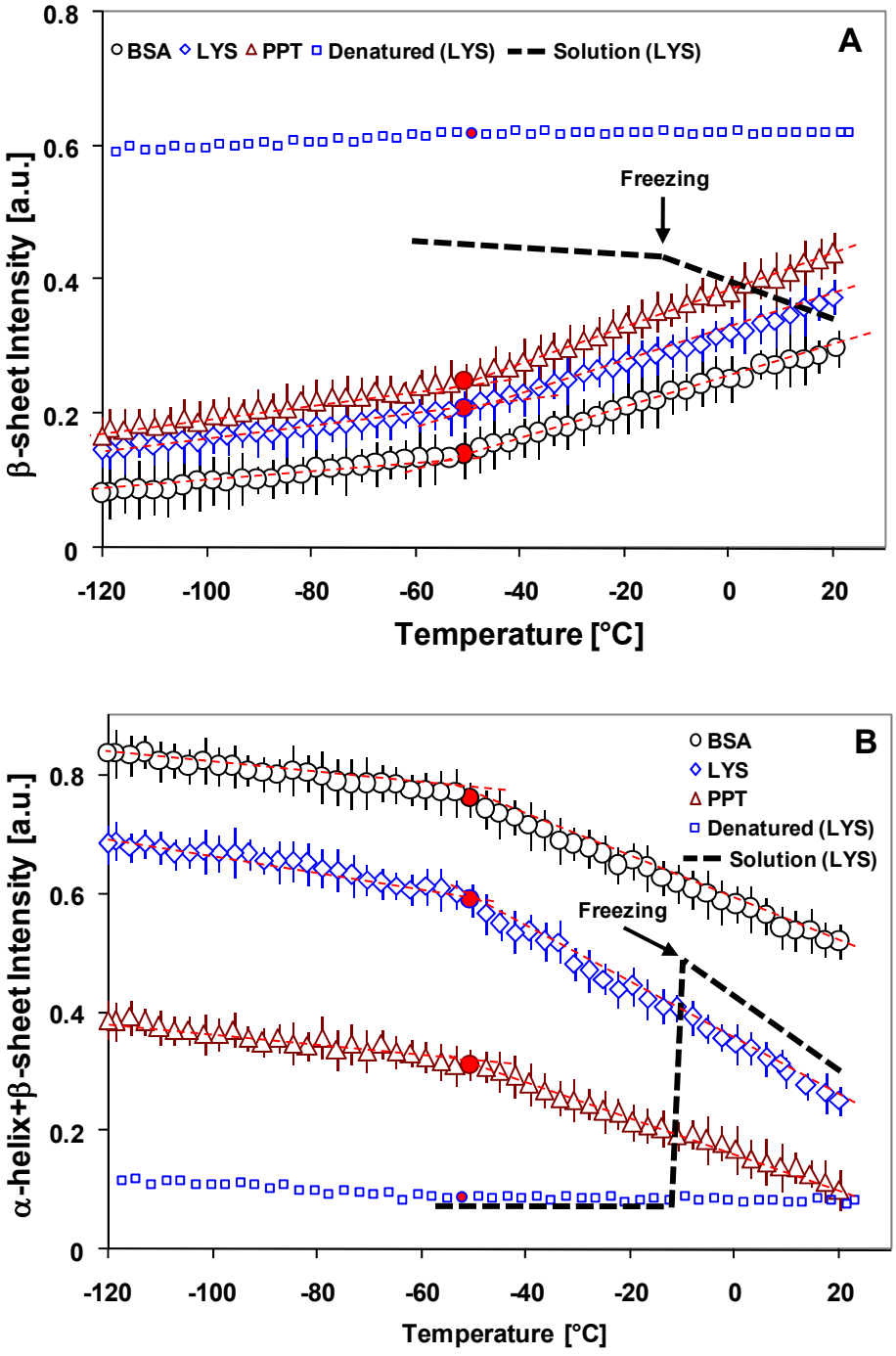

Figure 3.7 Structural changes in encapsulated proteins at low temperatures.

Corresponding changes in HB of the water populations in the immediate vicinity of the encapsulated model proteins were also examined. The $S2_c$ population of water in

the vicinity of the encapsulated proteins followed the same trend as the $S2_c$ population of silica-confined water (in the absence of any protein). When the temperature-induced changes in the protein secondary structure were plotted with respect to the change in water HB, a direct linear correlation was observed (Fig. 3.8). Since the measured behavior of water was independent of the presence of protein in the silica gel, and the encapsulated denatured proteins did not exhibit any significant structural transition, the observed correlation hinted at a causal relationship. It is known that HB of water increases with decreasing temperature giving rise to an increase in NW and S2 populations both in solution [237] and in confinement [55]. Therefore, it is plausible that with reduction in temperature, vicinal water molecules are increasingly stripped from the protein surface (and form extensive hydrogen bonds with the other water molecules) causing the observed structural changes in proteins. Naturally, this behavior would not be observed in the frozen state since the frozen medium would prevent the protein from changing its structure.

Table 3.1 Denaturation temperatures of proteins in different environments (DSC results).

	Water	Water-Tre (1.8 M)	Gel	Gel-Tre (0.25 M)
LYS	72.3°C ± 5°C	83.55°C ± 0.1°C [99]	72.5°C ± 2.6°C	>95°C
BSA	61°C ± 3.9°C	92.7°C ± 0.1°C [100]	59.7°C ± 3.6°C	> 95°C
PPT	73.3°C ± 3.3°C	-	71.6°C ± 2.5°C	> 95°C

3.3.3) Structural changes in confined proteins at high temperatures

Encapsulated proteins were heated at 2°C/min from 20°C to 95°C. In all model proteins, with increasing temperature the β-sheet content increased while the α-helix + β-

sheet content decreased (Fig. 3.9A, B). A change in slope in the α-helix + β-sheet and the β-sheet intensity plots were detected at high temperatures and it was attributed to denaturation. Denaturation temperatures for the confined proteins were T_D = 70.1, 60.0, and 72.6°C for LYS, BSA, and PPT, respectively. The measured T_D values are in agreement with the previously reported values for LYS and BSA [60]. Note that T_D of confined PPT has not previously been reported. T_D values measured by FTIR analysis were confirmed by DSC analysis. These values were also very close to the values measured for proteins in solution (Table 1), supporting the proposition that encapsulation (as detailed in the methods section) caused very small changes in protein structure.

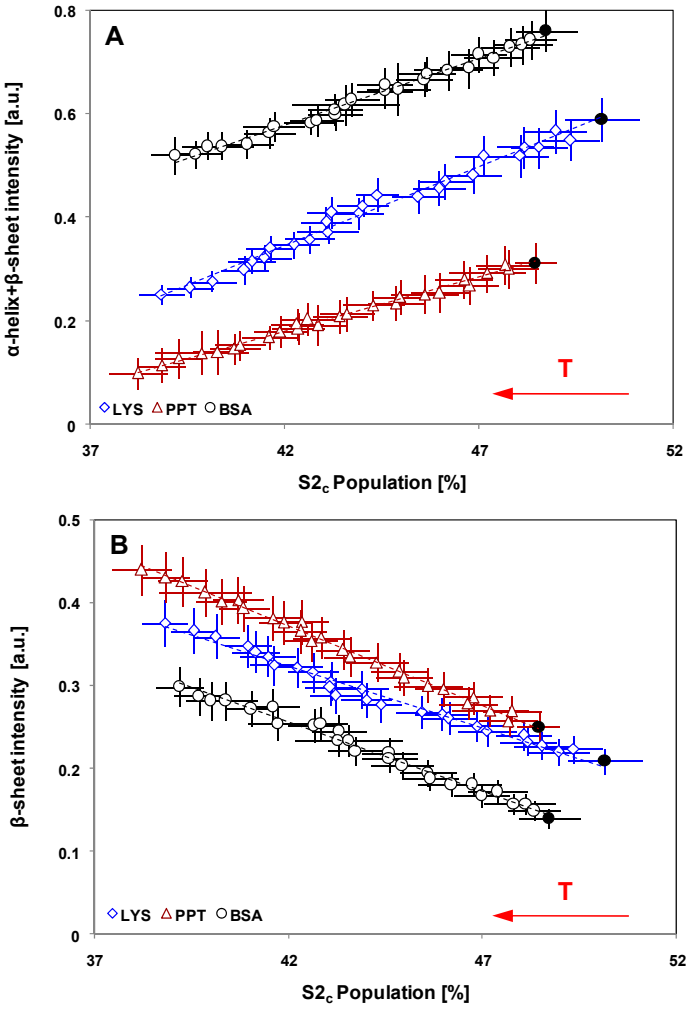

Figure 3.8 Change in protein structure with water structure at low temperatures. The black circles show protein glass transition. T increases in the direction of the arrow.

Above T_D, significant changes in the amide I and II regions of the IR spectra were observed. These changes indicated formation of specific interactions between the silica gel and the confined protein. Fig. 3.9C shows the changes in the secondary structures (due to thermal denaturation and surface adsorption) of confined BSA, LYS, and PPT during heating: In the amide I region (1600 - 1700 cm^{-1}) a net increase in the extended β-sheet and random coil (RC) structures was observed [136, 146]. However, no sign of

intermolecular β-sheet structure (1675-1685 cm^{-1}) [245] formation was present. This indicated that even after denaturation, aggregation was not present (one major difference from what was observed with proteins in solution). Note that when compared to LYS and PPT, the structural changes experienced by confined BSA (Fig. 3.9C) were less drastic, which suggested that confined BSA was not completely denatured during heating.

The structural changes experienced by confined BSA, LYS, and PPT correlated well with the changes in the S2c water population until denaturation (Fig. 3.10). Thermal denaturation causes a significant loss of (secondary and tertiary) structure for the protein due to unfolding, and also results in exposure of the protein's hydrophobic core [246, 247]. These two phenomena result in a significant decrease in protein-water interactions, potentially causing the disappearance of the correlation between water HB and residual protein structure.

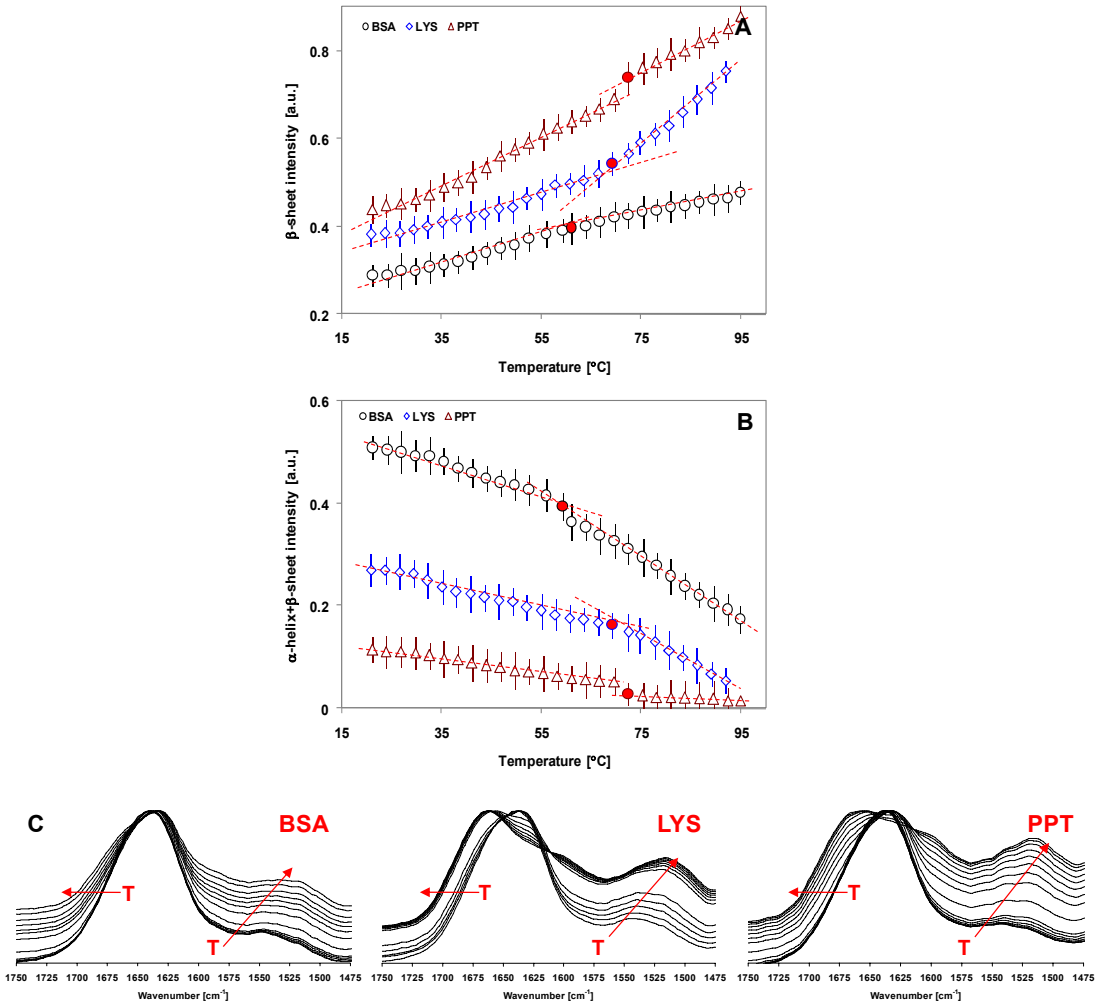

Figure 3.9 Structural changes in encapsulated proteins at high temperatures: (A) β-sheet intensity; (B) α-helix+β-sheet intensity; (C) IR spectra of BSA, LYS, and PPT, respectively. T increases in the direction of the arrow from 20°C to 95°C.

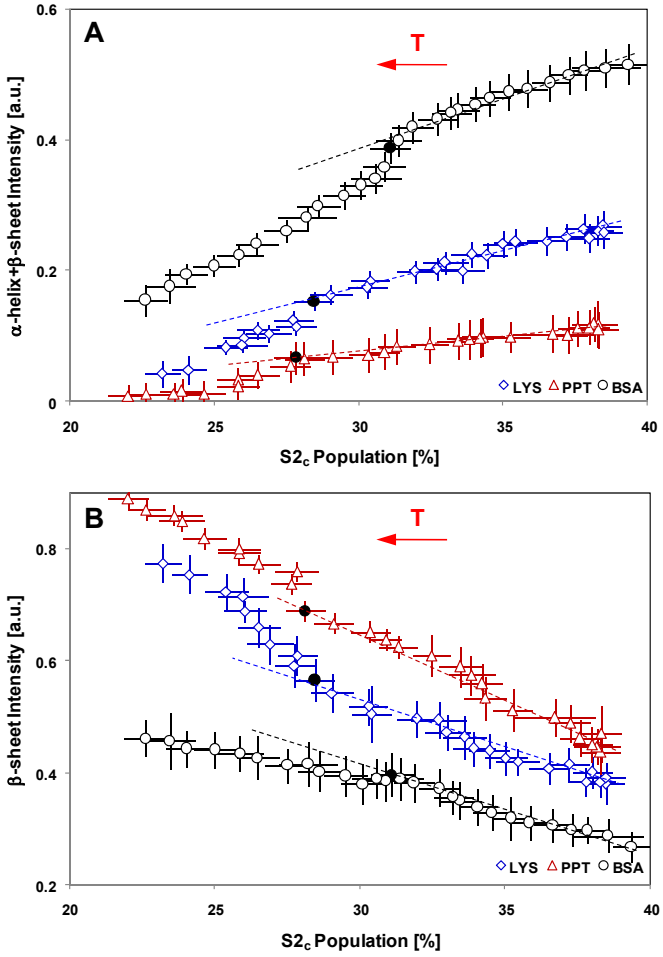

Figure 3.10 Change of protein structure with water structure at high temperatures. The black circles show protein denaturation. T increases in the direction of the arrow from 20°C to 95°C.

3.3.4) Structural changes in confined proteins in the presence of trehalose

Tre is a cryo-/lyoprotectant agent [248-250], which is known to alter HB of water. Alterations in water HB bonding in the presence of Tre can be directly evidenced in the $NIR_{\nu 2+\nu 3}$ band of water where, in addition to the changes observed in the existing water bands, a new water population (the $S2_c^*$ band centered at 4800 cm^{-1}; see Fig. 3.3) appears. $S2_c^*$ band has been shown to be associated with the water molecules strongly bonded to Tre [237].

Tre was incorporated into the silica matrices to investigate its influence on the structural transitions of confined proteins (either through specific interactions with the protein or through altering water HB) and to evaluate its potential to eliminate protein-silica surface interactions (by specific silica-trehalose interactions).

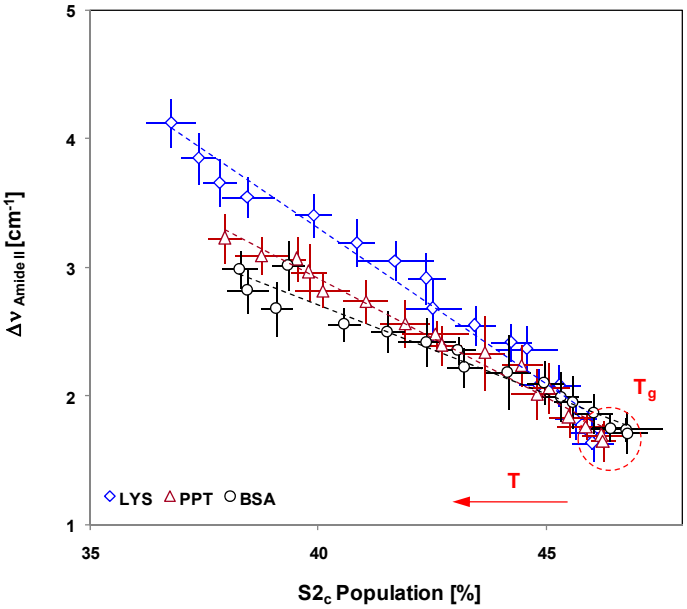

Figure 3.11 Change of protein structure with water structure at low temperatures in the presence of 2.5 M trehalose. T increases in the direction of the arrow.

During cooling of the Tre containing gels at 2°C/min, a linear correlation between the shift in amide II peak position ($\Delta\nu_{amide\text{-}II}$) and the $S2_c$ population was observed (Fig. 3.11). Note that in the presence of Tre, $\Delta\nu_{amide\ II}$ was used (instead of the second derivative analysis of the spectra) to quantify the change in the protein structure since the spectral contributions of Tre made second derivative analysis unreliable (see methods section). The observed correlation between $S2_c$ and $\Delta\nu_{amide\ II}$ indicated that also in the presence of Tre, the increase in the HB population of the confined water induced changes in the structure of confined proteins.

Tre is a glass-forming sugar [251]. Therefore, when a Tre concentration of 0.25 M was reached in the silica gel, upon cooling, glass transition was observed at -23^{o}C. Note that what is described here is glass transition of the confined solution, which should not to be confused with PGT. Glass transition of the solution was detected as a slope change in $\Delta\nu_{amide\text{-}II}$ and was also confirmed with DSC measurements (Fig. 3.12).

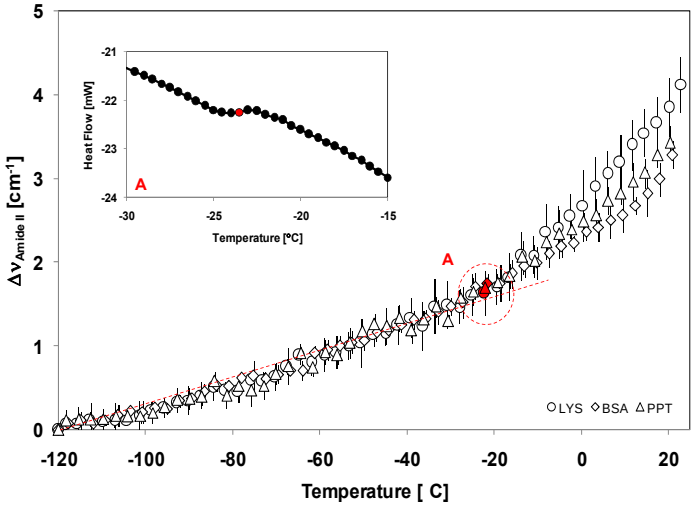

Figure 3.12 Glass Transition Temperature of the Confined Solution.

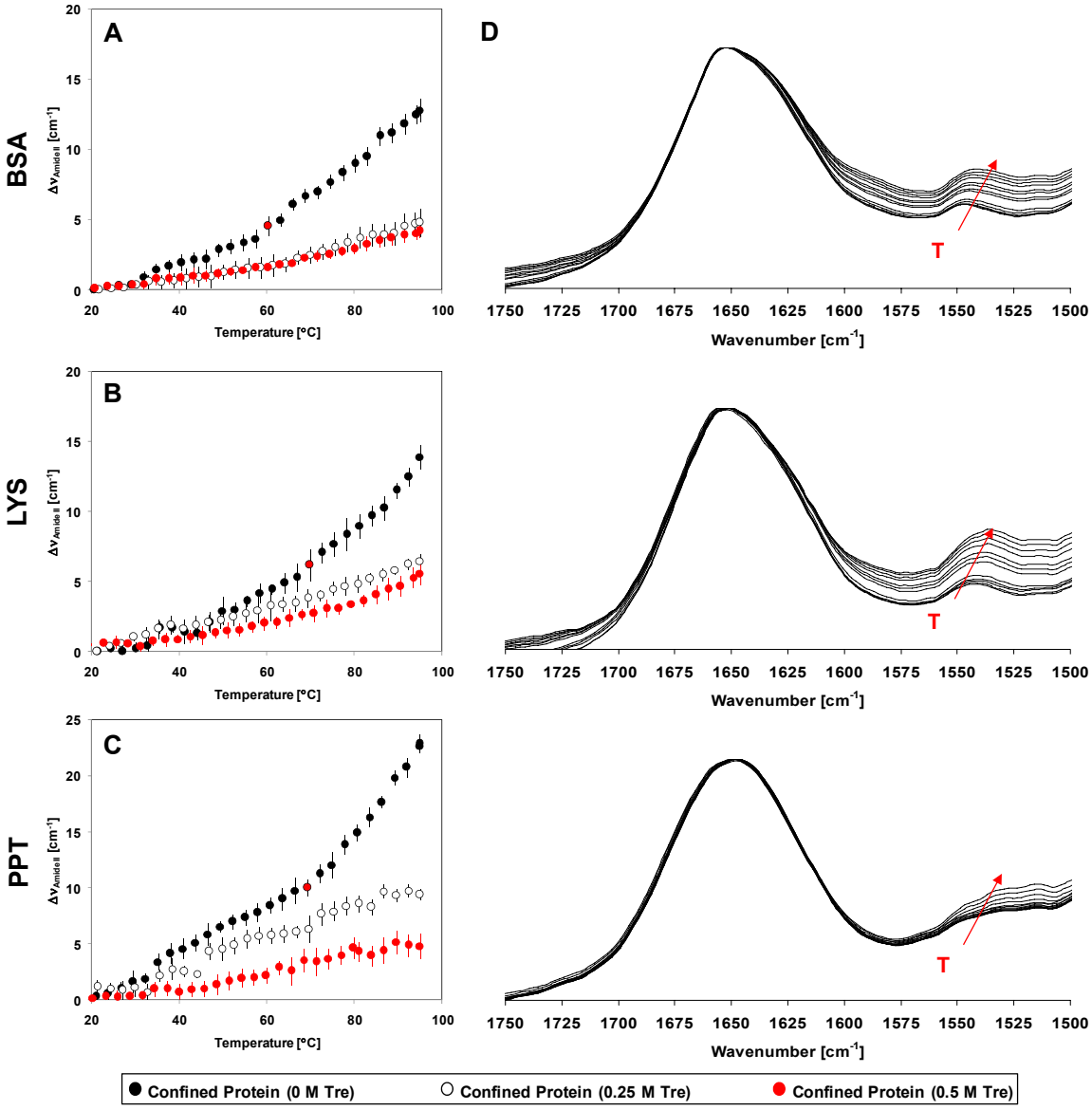

Figure 3.13 Change in protein structure with water structure at high temperature in the presence of trehalose: (A) BSA, (B) LYS, (C) PPT. (D) IR spectra of BSA, LYS, , and PPT during heating. T increases in the direction of the arrow from 20°C to 95°C.

Also, when it reached a concentration of 0.25 M in the silica gel, Tre inhibited high temperature denaturation of the confined proteins (Table 1). Fig. 3.13A-C compare the structural changes in confined proteins to those encapsulated in the presence of Tre

during heating to 95°C. $\Delta\nu_{\text{amide II}}$ values for confined BSA, LYS, and PPT increased rapidly with temperature with BSA exhibiting the least ($\Delta\nu_{\text{amide II}}$ = 12 cm^{-1}) and PPT exhibiting the largest change ($\Delta\nu_{\text{amide II}}$ = 23 cm^{-1}) in structure with 75°C of temperature increase. With increasing concentration of Tre (0.25 vs. 0.5 M) in the gel, temperature dependence of $\Delta\nu_{\text{amide II}}$ decreased. At 0.5 M Tre concentration, $\Delta\nu_{\text{amide II}}$ values measured for all proteins during heating from room temperature to 95°C were identical (~ 5 cm^{-1}). Fig. 3.13D shows the amide I and II regions of the confined BSA, LYS, and PPT in the presence of 0.25 M Tre. It is clear that the changes in the secondary structure of the confined proteins with temperature have decreased significantly in the presence of Tre (compare Fig. 3.13D to Fig. 3.9C).

In the presence of Tre, at high temperatures $\Delta\nu_{\text{amide II}}$ of BSA, LYS, and PPT correlated linearly with $S2_c$ (Fig. 3.14) within the full temperature range. In the absence of Tre, the linear relationship between the structural changes and $S2_c$ held until T_D for each protein was reached.

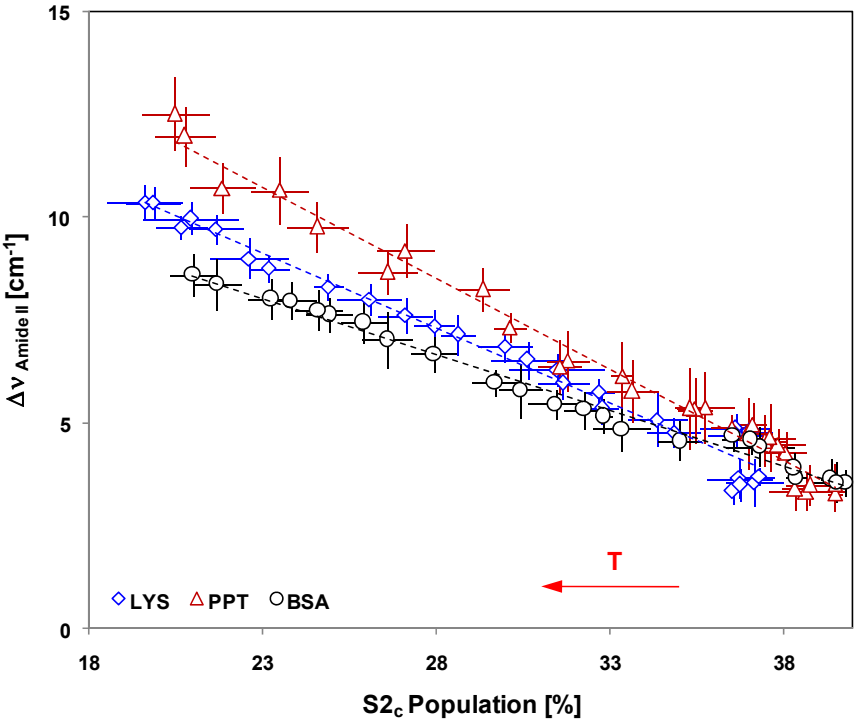

Figure 3.14 Change of protein structure with water structure at high temperatures in the presence of trehalose. T increases in the direction of the arrow.

3.4) Discussion

Conformational motions of a macromolecule are "slaved" to the viscosity of the medium [191, 219, 252], while its vibrational motions are "slaved" to the motions of its hydration layer (the interfacial water) [229]. Our results showed a correlation between the HB of water (which could be called the structure of water) and the change in the conformation of a confined protein. This correlation existed at cryogenic as well as high temperatures, and even in the presence of an osmolyte, trehalose, of known cryo-/lyoprotectant characteristics. The correlation was lost when the protein was denatured at high temperatures.

3.4.1) Protein structure in confinement

When encapsulated, proteins may have specific interactions with the silica surface, and are affected by the geometric confinement and the changes in the kinetic and thermodynamic properties of the water surrounding them. When it is at close proximity to a surface HB kinetics of water are slowed down, which alters its physical and chemical properties [253-255]. The altered properties of the confined water therefore affect the structure of the protein, producing the small shifts in the W emission spectra, which are known to depend on the solvent environment [243]. On the other hand, it is known that globular proteins can easily be adsorbed onto the silica surfaces [210, 211]. Adsorption is a kinetic process that involves surface interactions (e.g. hydrophobic interactions, electrostatic interactions, hydrogen bonding, and Van der Waals forces) [107]. Therefore in encapsulation in silica, electrostatic interactions could also be an issue. This is more likely for LYS and PPT considering that at pH 7.2 they are below their isoelectric points (pI_{LYS} = 11.35, pI_{PPT} = 10.2) [256]. Therefore, in confinement the positively charged amino groups of these proteins can interact with the negatively charged silica surface. BSA on the other hand, at pH 7.2, is above its pI_{BSA} (4.7) [256] and electrostatic interactions with the silica surface are less likely. PPT was the protein most affected by encapsulation. This can be explained by the fact that PPT is the least packed protein examined here. Solvent accessibility analysis performed by ASA-View [242] showed that the neutral polar residues (including W) of PPT have significantly more access to the solvent (>60%) when compared to LYS (~ 50%) and BSA (~ 20%), and therefore would be more susceptible to the changes in their solution environments. Additionally,

adsorption depends on the size of the silica nanoparticles with larger particles (d = 20 - 100 nm) causing larger perturbations to the protein secondary structure [257, 258]. In our study, we believe that adsorption of the proteins on the silica was limited since the silica particles used were d = 7 nm, and the area available for protein adsorption in the gel was reduced when the particles coalesced to form the nanoporous gel. This is supported by the findings of a recent study, which showed significant differences between the structures of proteins adsorbed on silica surfaces and when proteins confined within a silica gel [212]. Additionally, the adsorption of globular proteins onto the silica surface changes the IR spectra significantly in the region 3750 to 3650 cm^{-1} [213]. Our experiments did not find any differences in the ν-OH bands from confined water and confined proteins in the region 3750 to 3650 cm^{-1}. Therefore we believe that in the experiments presented here, an interplay of altered water HB and mild specific interactions with the silica surface caused the observed small red shifts in IF spectra of the proteins upon encapsulation however, majority of the model proteins remained in their native states after encapsulation at room temperature.

3.4.2) Confined protein structure at low temperatures

Since the porosity of the silica matrix is in the nanometer range (Fig. 3.1), the properties of the confined water are significantly different from the properties of bulk water at the same temperature [55]. That is, while freezing of the bulk water occurs at T < 0°C, confined water did not freeze even at cryogenic temperatures (~ -120°C) [55]. This has allowed examination of the structural transitions of water and of proteins in at

cryogenic temperatures[154, 244]. One of the transitions of water that is relevant to this work is the change in the temperature dependence of the density of the confined water at -51°C. This is known as the Fragile-to-Strong transition (FST) of liquid water. FST has also been detected in the hydration layers of proteins [155, 253]. The dynamics of the proteins change in sync with the dynamics of the solvent (e.g., water) at the FST temperature [54, 125, 155, 259], which indicates that the protein dynamics are linked to solvent dynamics [253]. Therefore, in systems containing proteins, the transition at -51°C is also known as the protein glass transition (PGT) temperature [125]. We showed here that this dependence is also present in confinement.

It is known that below PGT, large structural changes are prohibited but only small atomic fluctuations are believed to exist, restricting the flexibility of the macromolecules [186, 219]. DNA and proteins (e.g. myoglobin, ribonuclease, elastase, bacteriorhodopsin) are inactive below the PGT temperature [186]. Above PGT, on the other hand, anharmonic vibrations contribute to the internal motions of the proteins increasing their flexibility and conferring them the ability to achieve functional configurations (e.g. interconversion between secondary structures and change the tertiary structure) [219]. Reduction in the protein structural flexibility at temperatures below PGT/FST is in agreement with our results. PGT is even observed in denatured proteins, albeit at a lesser extent [260]. We also found that when lysozyme was denatured (by heating at high temperatures), confined in a silica matrix and then cooled down to -120°C at 2°C/min, no significant change in the α-helix+β-sheet and β-sheet intensity were detected down to -51°C (Fig. 3.7A-B). However, at -51°C a slightly slope change could be observed.

The difference in the temperature dependence of the β-sheet and the α-helix+β-sheet intensities of the proteins in solution and confinement (Fig. 3.7A-B) are attributed to the difference in the behavior of the HB populations of bulk and confined water at low temperatures [55, 209]. With decreasing temperature there is an increase in the HB of water (freezing stops this evolution while in confinement it continues) [55]. Fully HB population increases (e.g. $S2_c$), while the water dimer and monomer populations decrease ($S1_c$ and $S0_c$, respectively). We hypothesize that the reduction of the $S1_c$ and $S0_c$ populations with temperature reduces the number of protein water interactions, mainly stripping them from the RC domains of the proteins. This forces the RC domains to transition into an α-helical (or α-helix like) configuration. It is known that a greater change in the conformation of proteins occurs in the protein regions with α-helical and RC domains where there are many weak or bifurcated HB (high $S1_c$ and $S0_c$ content) [215].

3.4.3) Confined protein structure at high temperatures

During heating, the geometrical constraints imposed by the nanoporous matrix are expected to restrict (or retard) protein denaturation. On the other hand, we expect denaturation to promote protein-silica surface interactions through HB and electrostatic forces. When proteins in solution thermally denature they tend to form aggregates, which can be detected spectroscopically by the formation of strong intermolecular β-sheet bands (1610-1615 cm^{-1} and 1675-1685 cm^{-1}) in the amide I region resulting from the close alignment of the neighboring peptide chains [245]. In silica gel confined proteins, there

was no sign of the intermolecular β-sheet band formation (1675-1685 cm^{-1}) during heating, which suggested that aggregation was not present (Fig. 3.9C). This was expected since proteins were entrapped in the pores of the silica matrix. However, when denatured in confinement, the proteins showed signs of interaction with the silica surface. The interaction with the silica surface caused irreversibility since when the confined proteins were cooled down to room temperature; the native structure was not completely regained.

Two types of silanols are present on the silica gel surface: Single $(-O)_3Si(OH)$ and geminal $(-O)_2Si(OH)_2$ [261]. These groups reflect their local environments through altered interactions with the neighboring molecules enabling determination of HB and topological surface variations [262]. Therefore, increase in the SiOH peak intensity can be attributed to breaking of the hydrogen bonds between the surface groups and the water molecules (Fig. 3.15A) [261, 263-265] causing the observed T_D of confined proteins (Table 1).

As shown in Fig. 3.10A-B, the linear correlation between the protein structure and the $S2_C$ water population hold until T_D. It has been proved for hydrated LYS that the inverse self-diffusion coefficient, and the average migration distance of the water molecules in the hydration layers of LYS change drastically at temperatures between 57°C to 72°C (near T_D) [266]. Our data for the confined proteins are in agreement with these findings and show that the reduction in HB in the confined water gives enhanced flexibility to the proteins at high temperatures. This idea is further supported by the fact that the correlation breaks up at different $S2_c$ water populations for different proteins.

3.4.4) Confined protein structure in the presence of trehalose

Our results suggest that in confinement, Tre molecules preferentially interact with the silica surface (both silica and Tre molecules are hydrophilic) and as a result, water molecules are excluded from the silica surface. When Tre was absent in the confined protein samples, a very well defined silanol (SiOH) peak (3740 cm^{-1}) was detected in the IR spectra. In the presence of Tre however, the SiOH peak disappeared. SiOH is known to be a hydrogen bond donor for water. Therefore, an increase in the magnitude of the SiOH peak is correlated to breaking of water HB with the silica surface. In the presence of Tre, the SiOH peak did not appear even at high temperatures, which was a clear indication that Tre molecules strongly interacted with the silica surface (Fig. 3.15B).

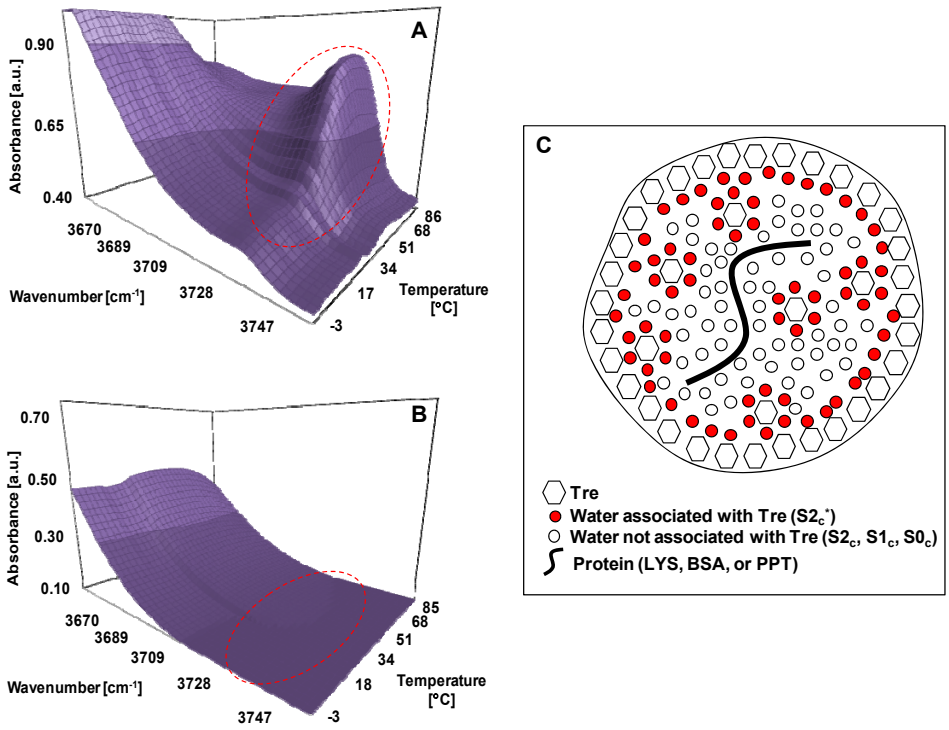

Figure 3.15 Changes in the silanol (SiOH) band absorbance: (A) in the absence of trehalose, (B) in the presence of trehalose; (C) schematic representation of the proposed mechanism of action of trehalose in confinement.

At low temperatures, Tre caused the formation of a glass (T_g ~ -23°C). Fig. 3.11 suggests that during cooling in the presence of Tre the increase in the $S2_c$ water population correlated to the structural changes of confined proteins. This is similar to the changes in confined protein structure in the absence of Tre described before, and it is further supported by the fact that $S2_c^*$ population does not change significant at low temperatures [237]. As T_g is approached, $\Delta\nu_{\text{amide II}}$ values for the proteins converge (Fig. 3.12). We interpret this as an indication that Tre suppressed the anharmonic protein vibrations, which are responsible for protein structural changes [267, 268]. Raman and neutron scattering experiments have also demonstrated that protein dynamics are affected by the presence of solvents (e.g. Tre, or glycerol) over a large temperature range (-173°C to 77°C) [124].

At high temperatures, the presence of Tre (even at concentrations as low as 0.25 M) increased the thermal stability of the confined proteins (to see the enhanced effect of Tre in confinement, compare the T_D values of proteins in 1.8 M Tre solutions and in silica gels with 0.25 M Tre in Table 1). The change in $\Delta\nu_{\text{amide II}}$ with temperature also decreased with increasing Tre (Fig. 7A-C) indicating reduced structural flexibility. This also supported the previous conclusions that Tre interacted preferentially with the silica surface and with the surrounding water molecules (see Fig. 3.15C). In summary; (1) the affinity of the silica surface to Tre prevented protein adsorption to the silica surface even during denaturation; and (2) Tre altered HB of interfacial water and thus decreased the conformational flexibility of the proteins [237, 269].

3.5) Conclusion

FTIR, IF, and DSC analyses presented here revealed aspects about the mechanisms that govern protein structure in confinement. Interplay of solvent HB and surface interactions governed the structural changes of confined proteins with temperature with the latter being less dominant at lower temperatures. IF and FTIR analyses showed that proteins remain in the native state after encapsulation under the experimental conditions tested here. At low temperatures, water HB increased as shown by an increase in the $S2_c$ population. Our results showed a direct correlation between water HB organization and protein secondary structure. FST/PGT of water at -51^{o}C as well as TRE glass transition changed the allowable motions of the confined proteins. In the presence of Tre, these motions were restricted at a low temperature due to glass transition of the solution at -23°C, generating a similar effect on the protein structural motions. At high temperatures, confined proteins underwent denaturation and adsorbed to the silica surfaces even though denaturation occurred without aggregation. Thermal stability of the proteins in confinement was greatly improved by the addition of Tre because of the strong affinity of the silica surface to the hydroxyl groups of the sugar and the structuring of water around the protein due to preferential exclusion.

Chapter 4: Silica Gel Encapsulation of Recombinant *E.coli* Cells Expressing AtzA for the Biodegradation of Atrazine into Hydroxyatrazine[3]

4.1) Introduction

The herbicide atrazine (2-chloro-4-ethylamine-6-isopropylamino-s-triazine) is used for control of broadleaf weeds, principally in corn, sorghum, and sugarcane [270]Atrazine is currently used in 70 countries at an estimated annual rate of 111,000 tonnes [271, 272]. Atrazine is typically applied early in the planting season. Heavy rainfall events shortly after application may lead to detectable atrazine concentrations in waterways and in drinking-water supplies. In some instances, municipal water treatment plants may use chemicals and other treatment processes such as activated carbon to reduce atrazine and to improve drinking water quality.

Naturally-occurring microbes with the ability to degrade atrazine have been isolated from soil. The well-studied atrazine-degrading bacterium *Pseudomonas* sp. strain ADP metabolizes atrazine to carbon dioxide and ammonia via a series of six enzyme-catalyzed hydrolysis reactions [273, 274]. The genes encoding those enzymes have been sequenced and are found on a broad host-range plasmid denoted pADP1 [275]. Enzymatically-catalyzed atrazine degradation is initiated by atrazine chlorohydrolase,

[3] This chapter contains material that has been submitted to the *Journal of Applied Microbiology and Biotechnology* for publication: Gel Encapsulation of Recombinant *E. coli* Cells Expressing AtzA for the Biodegradation of Atrazine into Hydroxyatrazine, E. Reátegui, E. Reynolds, L. Kasinkas, A. Aggarwal, M. Sadowsky, A. Aksan, L. Wackett, 2011.

AtzA, that hydrolytically removes the chlorine substituent from the ring to produce hydroxyatrazine. This reaction has important environmental consequences; hydroxyatrazine is not herbicidally active, is dissimilar toxicologically from atrazine, and is more readily degraded than atrazine [276]. In this context, atrazine treatments that transform atrazine to hydroxyatrazine are considered sufficient for regulatory agency approval [277].

The strategy of transforming atrazine to hydroxyatrazine was previously used to remove 900 pounds of atrazine from a spill contaminated soil [277]. In that application, recombinant *E. coli* cells expressing AtzA were treated with glutaraldehyde to chemically kill the cells and stabilize enzyme activity in soil. Other methods for atrazine transformation have also been tested in the laboratory. For example, atrazine-degrading *Pseudomonas* sp. strain ADP cells have been entrapped in alginate or sol-gel glass [278]. In the latter test, however, significant atrazine-degrading activity was lost following encapsulation. To be useful in a water-treatment application, a microbial-based treatment method should: (i) have stable, long-term atrazine-degradation activity; (ii) be mechanically stable and sturdy; (iii) be conducive to high-water flow; (iv) maintain non-viable but active cells in the matrix without significant release, and (v) be inexpensive.

In this study, we developed a hybrid biomaterial to be used for atrazine biodegradation that should meet the requirements for use in municipal water-treatment facilities. The biomaterial consisted of recombinant *E. coli* cells overexpressing atrazine chlorohydrolase (AtzA) encapsulated in a polymer/silicon oxide matrix prepared by the sol-gel process. The gelation process was conducted through mild chemical reactions,

thus overcoming previously described problems of loss of enzyme activity over time. Moreover, conditions were developed that led to non-viable cells that remained fully active in degrading atrazine over a long time scale. The silica base matrix encapsulating the microorganisms consisted of a combination of silicon oxide precursors (e.g., silica nanoparticles, alkoxides) and a biocompatible organic polymer (e.g., polyethylene glycol, PEG). The porous material enabled diffusion of water and atrazine into the gel, and diffusion of hydroxatrazine out of the gel. The gel also adsorbed atrazine, a property that contributed to removal of atrazine from the solution in the process. In this context, the material we developed has the potential to outperform activated carbon in a water treatment application since it acts to both adsorb and subsequently to degrade atrazine. As shown here, the final material exhibited activity for four months. In total, these studies indicated that the described hybrid biomaterial could potentially be used continuously for the biodegradation of atrazine without the need for regeneration.

4.2) Materials and methods

4.2.1) Silica gel synthesis

Different silica precursors were used for the synthesis of the porous gel matrix. The gel consisted of colloidal silica nanoparticles Ludox TM40 (40 % w/w), tetramethyl orthosilicate (TMOS, 98 %), and methyltrimethoxy silane (MTMOS, 97 %). The organic polymer, polyethylene glycol (PEG, molecular weight (M_w): 600 Da), was incorporated into the porous matrix in order to increase biocompatibility of the matrix. All of the materials were purchased from Sigma (Sigma-Aldrich Corp. St. Louis, MO).

4.2.2) Bacterial strains and growth conditions

E. coli DH5α (pMD4) [274] was grown at 37°C in superbroth medium comprised of 1.2 % tryptone (w/v), 1.4 % yeast extract (w/v), 0.5 % glycerol (v/v), 0.38 % monobasic potassium phosphate, 1.25 % dibasic potassium phosphate, and 30 μg/ml chloramphenicol (at pH 7.4). Starter cultures were made by inoculating 5 ml of superbroth with an isolated colony and incubating overnight at 37°C, with shaking at 250 rpm. Intermediate cultures were grown by inoculation with 3 % (v/v) starter culture. Cultures were grown to an optical density (OD) of 0.5 - 0.75 with shaking at 250 rpm. Cell production flasks were inoculated with 3 % (v/v) of intermediate cultures and grown for 16 h under the same growth conditions. Cells were harvested by centrifugation at 9000 rpm for 20 min at 4°C and re-suspended in water to a final concentration of 0.1 - 0.2 g of cell/ml.

Table 4.1 Composition of silica gels.

Gel Type	Precursor [M]	PEG	Cross-linker		*E. coli* cells		Incubation
		r_{PEG} [v/v]	Type	r_{cl} [v/v]	r_{cs} [v/v]	[g of cell/ml]	[°C]
N1	1.24	-	I	0.5	1	0.1	23
N2	1.13	0.25	I	0.5	1	0.1	23
N3[a]	1.13	0.25	I	0.5	1	0.1	23
N4[b]	1.13	0.25	I	0.5	1	-	23
N5	1.71	0.25	II	0.5	1	0.1 or 0.2	23 or 45

[a] *E. coli* non-expressing AtzA, [b] No cells, I: TMOS:Water:0.01M HCL (1:1:0.1 v/v/v), II: TMOS:MTMOS:Water:0.01M HCL (1:1:1.5:0.15 v/v/v/v), r_{PEG} = volume of PEG / volume of precursor, r_{cl} = volume of cross-linker / volume of precursor, r_{cs} = volume of cell solution / volume of precursor.

4.2.3) Reactive biomaterial production

Bacterial cells were encapsulated using a variation of a sol-gel method previously described [279]. Cells were encapsulated in silica or silica-PEG (SPEG) gels. Porous gels were formed by diluting TM40 silica nanoparticles in ultra pure water (with electrical resistivity > 18.2 MΩ.cm at 25°C). PEG (M_w = 600 Da) was added to the solution at a volume ratio of 1:4 (r_{PEG}), and the mixture was stirred vigorously for 10 min. The resulting TM40-PEG solution was cooled in an ice bath. Separately, TMOS or TMOS/MTMOS were hydrolyzed by sonication in the presence of 0.01 M HCl. A typical volume ratio was 1:1:0.1 for TMOS/water/HCl and 1:1:1.5:0.15 for the TMOS/MTMOS/water/HCl solution. The hydrolyzed solution was mixed with the TM40-PEG solution at a volume ratio of 1:2 (r_{cl}). Finally, a cell suspension (0.1 or 0.2 g of cells /ml) was added to the mixture at a volume ratio of 1:1 (r_{cs}). The samples (Table 4.1) were transferred to glass or metal molds and were cured at different temperatures and times in a convection oven. The final products was formulated into microbeads (1.0 - 1.5 mm diameter) or into a cylinder block (~ 1 ml in volume formed inside a scintillation vial, resulting in a diameter of approximately 25 mm and a thickness 2 mm).

4.2.4) Cell viability assay

The plate-count assay was used to determine cell viability of encapsulated cells. A known mass of wet gel was pulverized by gentle compression between two glass slides to release the encapsulated *E. coli*, as reported before [68]. The resulting material was suspended in 3 ml of sterile phosphate buffered saline (PBS). The solution was serially

diluted at 100-fold increments and spread-plated, in triplicate, onto LB-agar plates. Plates were incubated at 37°C for 24 h.

4.2.5) Lipid membrane analysis of encapsulated cells

Conformation of cellular membrane lipids was characterized using Fourier Transform Infrared (FTIR) spectroscopy. Before gelation, 0.2 μL of the cell sample was sandwiched between two CaF_2 windows that were separated by a thin layer of vacuum grease on the sides and placed on a temperature controlled cryostage (FDCS 196, Linkam Scientific Instruments Ltd., UK). FTIR spectra were collected in the 930 - 7000 cm^{-1} range using a Nicollet Continuμm FTIR microscope, equipped with a DTGS detector (Thermo-Nicollet Corp., Madison, WI). FTIR spectra were collected at 4, 10, 23, and 37°C. Spectral analysis was performed using Omnic software provided by the manufacturer. The lipid conformation change in the cellular membranes was monitored by measuring the peak location of the ν-CH_2 (symmetric stretching) band located near 2850 cm^{-1}. Due to significant contributions of the PEG CH_2 chains in the 2700 - 3000 cm^{-1} region of the IR spectra, only silica gels without PEG were used for the analysis.

4.2.6) Atrazine dechlorination activity assay

Activity measurements of the encapsulated cells, in a cylinder block or in microbead form, were conducted at room temperature and at 4°C in 20 ml glass scintillation vials. The reaction was initiated by exposing the cylinder block on one surface to 5 ml of 0.1 M potassium phosphate buffer (at pH 7.0) containing 150 μM (32.4

ppm) atrazine. In the experiments conducted with microbeads, 100 microbeads were suspended 5 ml of the same solution used for the cylinder blocks. The solution was continuously stirred using an orbital shaker at 200 rpm. The supernatant was sampled at four time points until 10 - 20 % of the substrate was reacted. Each time point was taken in duplicate, and each sample was taken from an individual scintillation vial. The samples were heated to boiling point for 5 min to ensure that any released enzyme was inactivated, and filtered through a 0.2 μm pore size PTFE syringe filter to remove any bead fragments or cells that may have been released. The concentrations of atrazine and its metabolite, hydroxyatrazine, in the sample solution were measured by High-Performance Liquid Chromatography (HPLC) as previously described [274]. For long term activity measurements, the encapsulated and free cells were stored in water at 4°C and assayed as described above.

4.2.7) Characterization of the porous gel

For electron microscopy imaging, silica or SPEG gels that contained encapsulated bacteria were chemically fixed initially using 2 % glutaraldehyde, and then 1 % osmium tetraoxide diluted in 0.1 M sodium cacodylate. After fixation, samples were gradually dehydrated by exposure to 50, 70, 80, 95, and 100 % ethanol. The samples were then transferred to a CO_2 critical point drier (Samdri-780A, Tousimis, Rockville, MD). Dried samples were sputtered with tungsten at a rate of 1 A°/min for 10 min. The gels that did not contain bacteria were sputtered without fixation. Scanning electron microscopy was conducted with a Hitachi S-900 FESEM (Hitachi Co, Lawrenceville, GA) scanning

electron microscope. Samples were imaged at different magnifications using a 1.5 or 2 KV accelerating voltage.

4.3) Results

The purpose of this study was to use encapsulated recombinant *E. coli* cells expressing AtzA to reduce atrazine in water. The gels have two desirable characteristics with respect to the herbicide; they are able to both adsorb atrazine and to transform it into hydroxyatrazine, which is dissimilar toxicologically from atrazine and is more biodegradable [276]. The cells were rendered non-viable to eliminate any risk of a potential release during use.

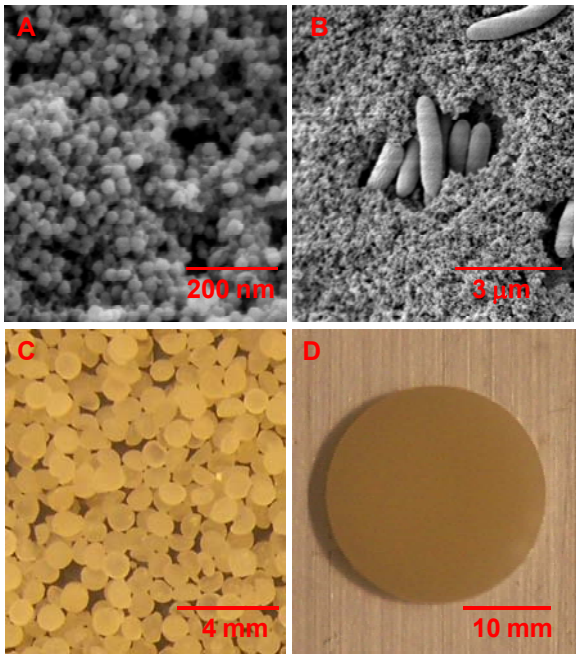

Figure 4.1 (A) Electron microscopy image showing the porous gel formed as aggregation and condensation of silica nanoparticles, (B) *E. coli* encapsulated in N1 expressing AtzA, (C) microbeads containing *E. coli* expressing AtzA, (D) cylinder block containing *E. coli* expressing AtzA.

4.3.1) Viability of encapsulated recombinant *E. coli*

Different silica gel compositions were tested for encapsulation efficiency and enzymatic activity (Table 4.1). The ultrastructure of the gels showed uniform condensation and aggregation of silica nanoparticles (Fig. 4.1A) around the encapsulated cells, generating a hyperporous network. At lower resolutions (Fig. 4.1B) small groups of *E. coli* were observed to be homogeneously distributed across the volume of the gels. Figures 4.1C and 4.1D show the two geometries used in this study; microbeads and a cylinder block containing *E. coli* expressing AtzA, respectively. Cylinder blocks were used in initial experiments for optimization of the silica gel material and maximum bioactivity. In contrast, the microbeads were used for long-term activity assays and were developed for future field studies since they have the highest area/volume ratio and thus are expected to yield the highest activity (among offering other advantages).

Most of the studies conducted to date with encapsulated *E. coli* in silica gels focus on the long-term cell viability after encapsulation [8, 85]. However, the degradation of atrazine by recombinant *E. coli* expressing AtzA does not require viable cells since the atrazine is dechlorinated by a non-metabolic hydrolytic reaction [277]. This is a very important aspect for practical decontamination of drinking water since negligible (if possible, zero) viability of the encapsulated cells is required. This minimizes the environmental risks in case of an accidental release of the recombinant microorganisms. Therefore, we developed a way of minimizing the viability of the encapsulated cells.

Figure 4.2 shows the loss of viability of cells encapsulated in different porous gels as measured by colony forming units (CFU) per a gram of gel material. The cells extracted

from the N1, N2, and N5 (non-thermally treated) gels after 3 weeks of encapsulation had 93.4 %, 49.3 %, and 92.2 % fewer viable cells, respectively, when compared to cells extracted at t = 0 weeks (Fig. 2). This showed that encapsulation of E. coli in the gels non-thermally treated still contained viable cells even after a long encapsulation periods. However, when the N5 gels were incubated at 45°C for 24 h, a reduction in survival/viability of the encapsulated cells close to 100 % was accomplished. In fact, cell CFU counts were so low in the oven-treated N5 gels that they were below the detection limit of our assay; we could not physically plate enough gel material to obtain accurate cell counts.

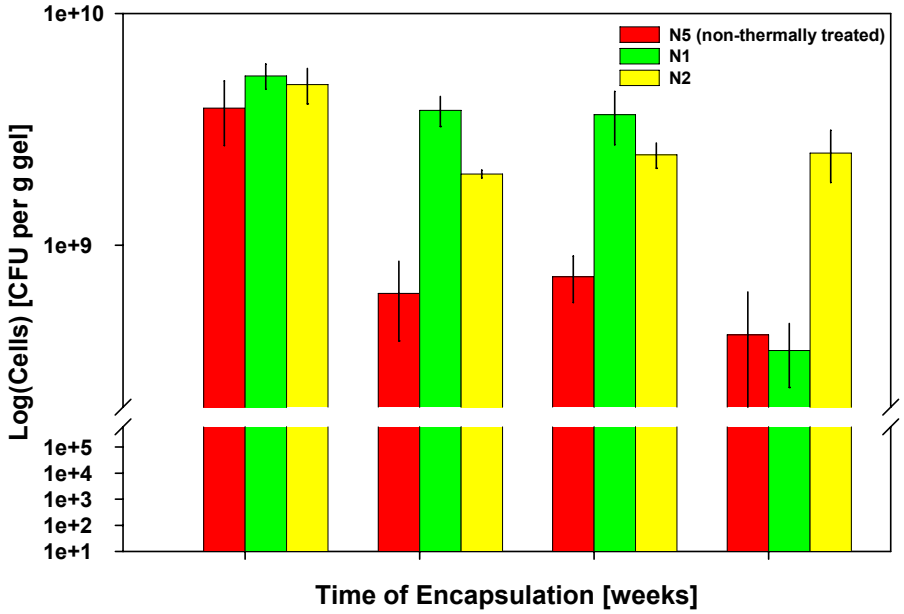

Figure 4.2 CFU of E. coli expressing AtzA extracted from different porous gels (n = 3).

4.3.2) Membrane analysis of encapsulated cells

The reason for the significant decrease in survival of the encapsulated *E coli* with increased gelation temperature was explored using FTIR spectroscopy by monitoring the change in the location of the lipid acyl chain (ν-CH_2) stretching peak (located near 2850 cm^{-1} in solution). Before gelation, the ν-CH_2 peak locations of the cells in the silica solution were similar to the cells in water (Table 4.2) indicating that the microenvironment of the cells in the silica solution were similar to the cells in water. When the measurements were repeated 30 min after the gels were formed, the encapsulated cells had significantly lower ν-CH_2 values than the cells in water (Table 4.2). The decrease in the ν-CH_2 wavenumber reflects an increased packing of the membrane lipids of the cells due to encapsulation. When the encapsulated cells were incubated for 24 h at 45°C, there was a gradual shift in the ν-CH_2 peak location to higher wavenumbers, which indicated disruption of the cellular membranes of the encapsulated cells. In parallel experiments, encapsulated cells were dried over time at room temperature to monitor the changes in the ν-CH_2 peak position. The results showed that the ν-CH_2 peak position shifted towards higher wavenumbers as the sample was dried over time (Fig. 4.3). Additionally, measurements of the ν-CH_2 peak position for free and encapsulated cells at different temperatures revealed that the fluidity of the membrane decreased with encapsulation. For a temperature change from 4°C to 37°C, $\Delta\nu$-CH_2 was 1.13 cm^{-1} for the free cells while it decreased down to $\sim$ 0.47 cm^{-1} for the encapsulated cells.

Table 4.2 Changes in the structural conformation of lipid membranes of E. coli expressing AtzA with temperature and encapsulation conditions.

Temperature [°C]	ν-CH_2 Peak Position [cm^{-1}]		
	Solution	Gel	Gel (Thermally Treated)
4	2851.77 ± 0.1	2844.13 ± 0.2	2847.53 ± 0.6
10	2851.90 ± 0.0	2844.17 ± 0.1	2847.36 ± 0.8
23	2852.33 ± 0.1	2844.40 ± 0.2	2847.66 ± 0.8
37	2852.90 ± 0.0	2844.60 ± 0.1	2847.96 ± 0.1

A comparison of the cells in solution and encapsulated cells did not show any significant difference in the morphology of their external membranes (Fig. 4.4A and Fig 4.4B). Distinctive raffles of the external membrane were observed in both cases. However, cells that were encapsulated and incubated for 24 h at 45°C did not have the same characteristics of the external membrane. Instead, the membrane looked shrunken and dehydrated (Fig. 4.4C). Both the FTIR analysis and SEM imaging showed the significant differences between the cells encapsulated at room temperature and the cells treated at 45°C which resulted in decrease viability (Table 4.2).

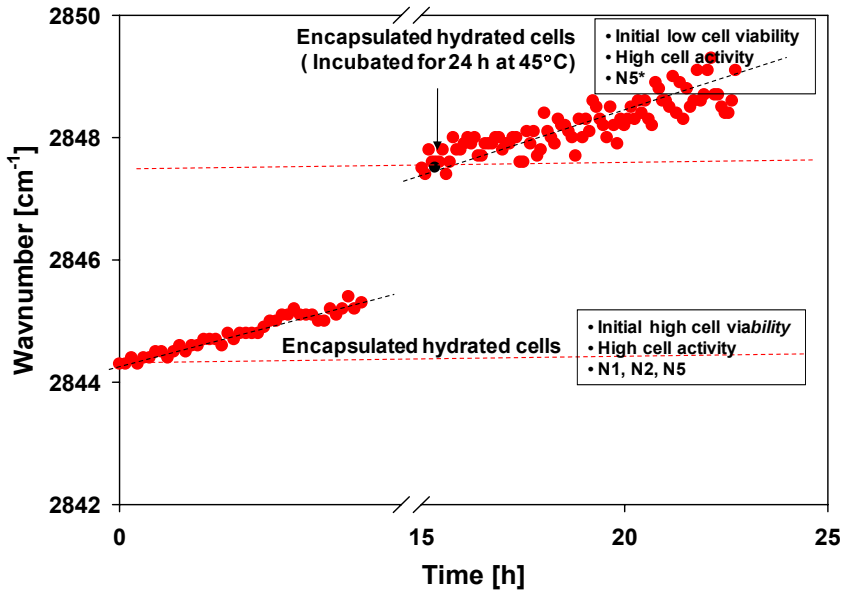

Figure 4.3 Time-dependent ν-CH_2 peak position of encapsulated E. coli expressing AtzA in silica gels.

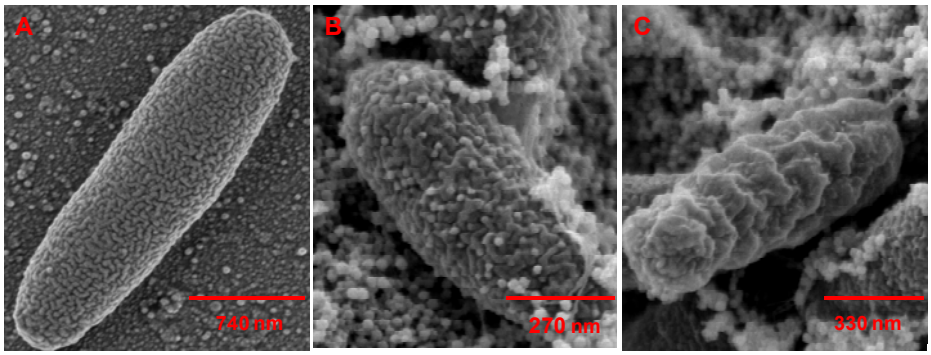

Figure 4.4 Electron microscopy images of E. coli expressing AtzA: (A) free cell in solution, (B) E. coli encapsulated in SPEG gel, N5, (C) E. coli encapsulated in SPEG gel, N5 after thermal treatment at 45°C.

4.3.3) Atrazine biodegradation

Atrazine degradation activity of the encapsulated microorganisms was evaluated using HPLC analysis. Due to the high atrazine adsorption characteristic of the gels, the rate of hydroxyatrazine production was used in all activity calculations. Figure 4.5A illustrates the atrazine adsorption ability of the gels by showing the change in atrazine concentration when exposed to silica beads that do not contain any cells. In the first 10 minutes, there was almost a 30 % decrease in atrazine concentration in the solution followed by equilibration. As expected, hydroxyatrazine was not detected in this solution due to the absence of the enzyme AtzA. Figure 4.5B shows the drop in atrazine concentration via the combined effect of atrazine adsorption by the silica gel and the degradation of the atrazine by the encapsulated cells. The rate of hydroxyatrazine production was linear over time, which indicated that hydroxyatrazine had less affinity to the silica gel and was more readily released into the solution environment. This observation was supported by assays similar to those shown in Fig. 4.5A but with hydroxyatrazine and cell-free beads (Fig. 4.6).

Table 4.3 Comparison of normalized activity of encapsulated and free *E. coli* expressing AtzA in different gels. Note that (*) indicates microbeads. Rest of the gels were tested in cylinder form. N3 gels contained non-expressing cells, N4 gels did not contain cells. Activity was measured at room temperature after 24 h of encapsulation.

Normalized Specific Activity [mmol/min.g]	
Gel Type	**Hydroxyatrazine**
N1	0.159
N2	0.224
N3	0.000
N4	0.000
N5	0.124
N5*	0.953* ± 0.35
Free Cells	1.000

Table 4.3 summarizes the results of the atrazine conversion activities obtained using different gel compositions and geometries (cylinder block vs. microspheres). The activity in cylinder blocks was significantly lower than those encapsulated in microbeads. This result was expected since only one surface of the cylinder was exposed to the solution and therefore only the cells very close to the surface of the product were involved in degradation of the atrazine. Cells encapsulated in N1 and N2 gels in cylinder blocks had only 16 %, and 22 % of the activity of the free cells in solution. As expected, gels that contained cells that did not express AtzA (N3) or gels that did not contain any cells (N4) did not show any hydroxyatrazine production. It was not possible to test the N1 and N2 gels in microbead form since the microbeads did not show any mechanical integrity and easily pulverized. This made them unsuitable for any bioremediation application in the field. On the other hand, the N5 gels could easily be manufactured in the form of cylinder blocks and microbeads. Note the significant increase in specific activity when the cells were encapsulated in the high specific surface area microbeads

(N5*) when compared to the gels encapsulated in a cylinder block of limited specific surface area (N5).

Figure 4.7 shows the activities of the free and microbead encapsulated cells (N5*) over 4 months. When the activity was measured at room temperature, free cells showed an average of 0.61 ± 0.04 μmol/g-min of activity over 21 days. After 21 days, significant cell lysis was observed in the free cells; this was likely due to long-term hypoosmotic stress induced by water. Therefore, the experiments on the free cells were stopped at that time point. On the other hand, cells encapsulated in N5 porous gels (microbeads) showed a stable activity between 0.44 ± 0.06 μmol/g-min to 0.66 ± 0.12 μmol/g-min for up to 4 months. This showed that even though the encapsulated cells were dead and had lost their membrane integrity, AtzA was protected and active in the silica matrix. The activities of the free and encapsulated cells were found to be temperature dependent. At 4°C, activity dropped by 45 % and 30 % for the free and encapsulated cells, respectively. The activity of encapsulated cells was 33.3 % higher than the cells in solution.

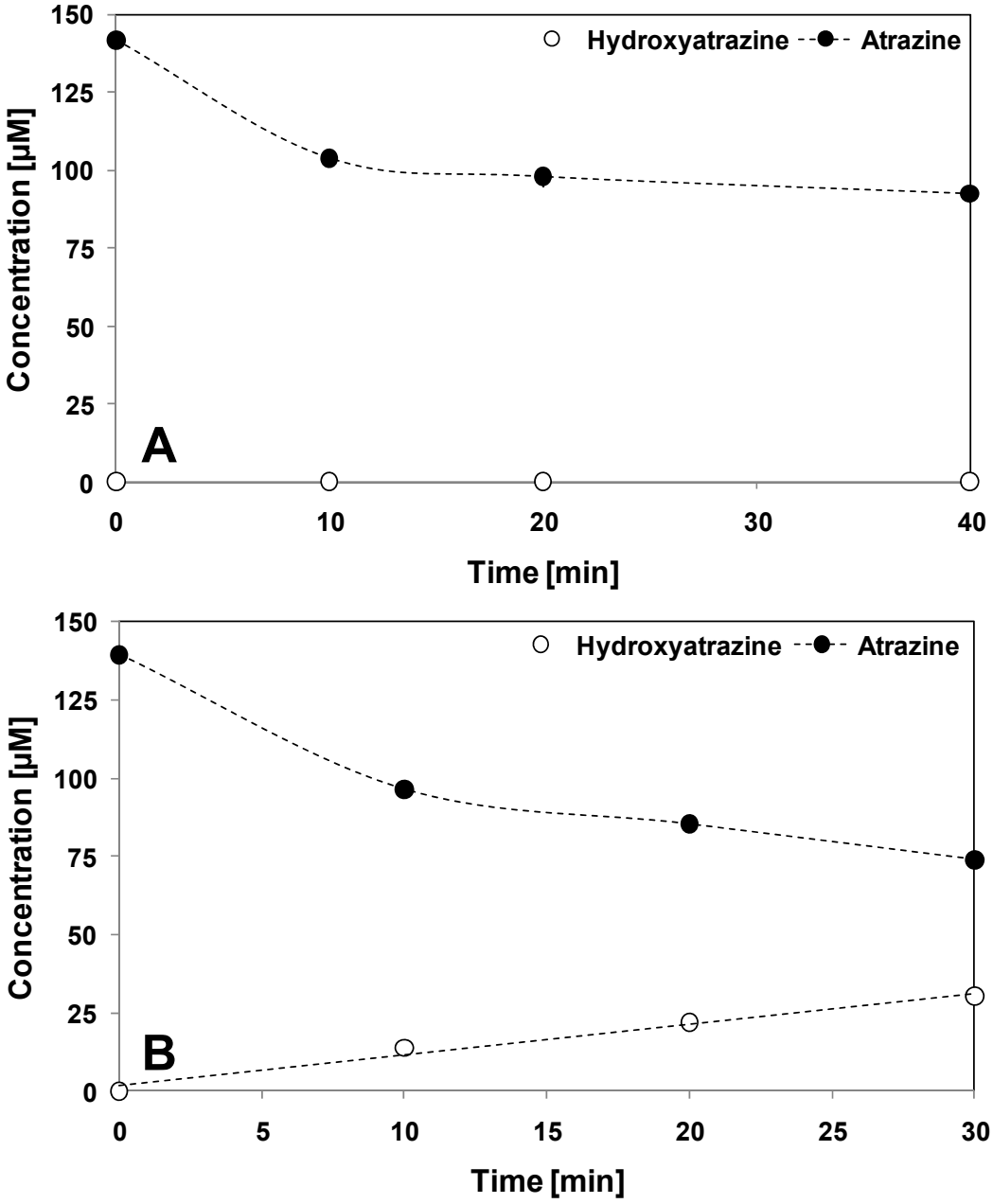

Figure 4.5 changes in atrazine and hydroxyatrazine concentration in solution: (A) adsorption of atrazine, (B) adsorption and biodegradation of atrazine (n = 3). The error bars are smaller than the symbols.

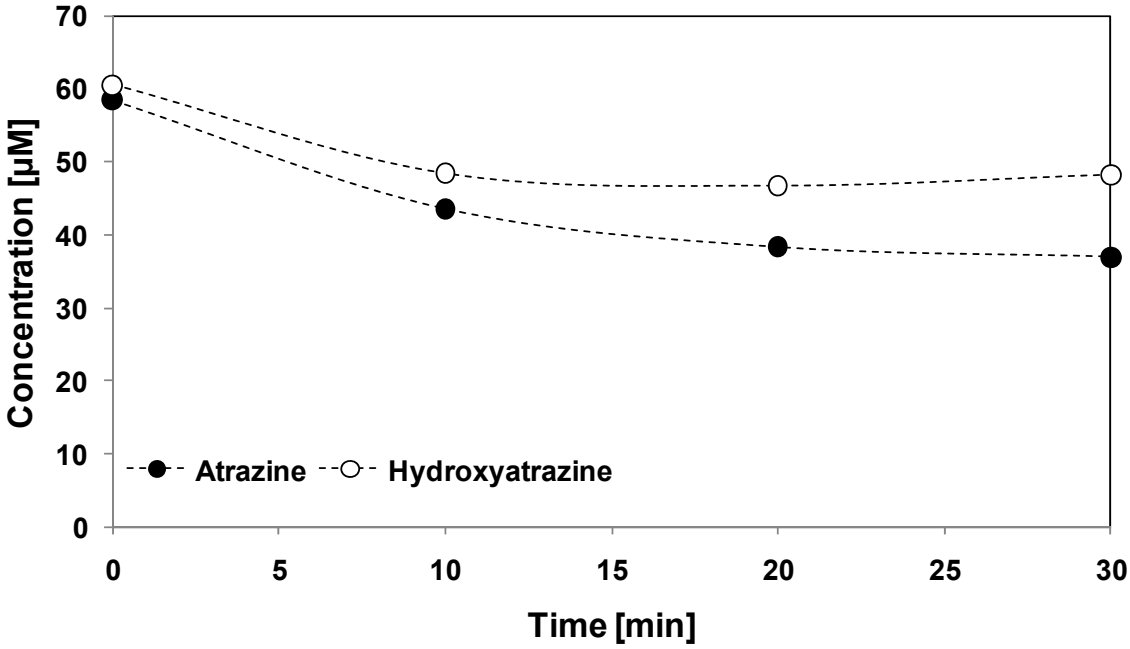

Figure 4.6 Adsorption of atrazine and hydroxyatrazine in cell-free microbeads.

For activity measurements at room temperature, at 10 days of encapsulation (~ 7 days for free cells), there was an increase in the specific activity, which was attributed to an increase in the permeability of the membranes since the viability of the encapsulated cells (N5, 24 h at 45°C) becomes even more negligible (Fig. 4.2). This is further supported by parallel experiments with acetone as a permeabilizing agent, where cells showed higher activities when compared to free and encapsulated cells (Fig. 4.8). However, for activity measurements at 4°C, the improvement was only significant for cells in acetone; which indicated that the activity of the enzyme not only depended on the permeability of the membrane but also on the temperature at which the assays were carried out.

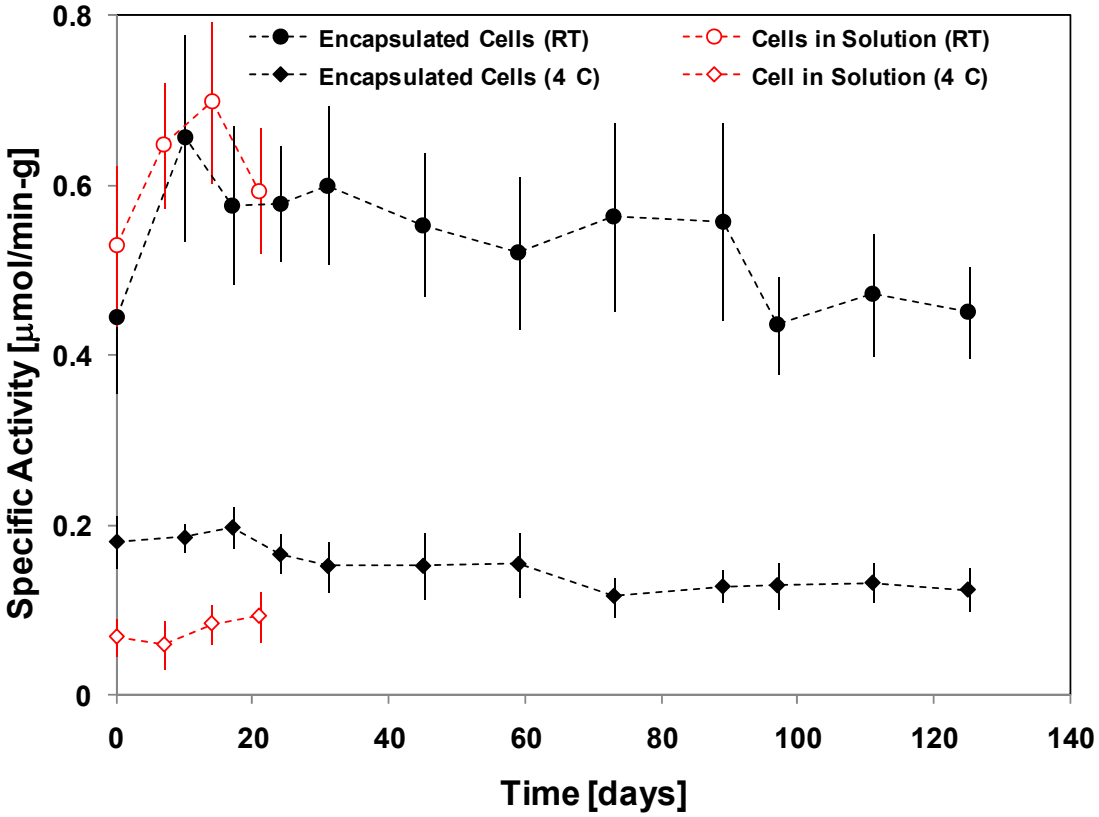

Figure 4.7 Specific activity of non-viable *E. coli* expressing AtzA in N5* microbeads at different temperatures.

4.4) Discussion

Activated carbon is widely used for removing contaminants in public drinking systems. However, activated carbon particles do not have selective adsorption for chemical compounds and also adsorb naturally occurring organic compounds [280]. Studies show that the presence of natural organic matter in the water reduces the adsorption kinetics of activated carbon and its capacity of atrazine adsorption [280, 281]. Therefore, there has been a search for alternative technologies that have high adsorption potential and selectivity. So far, the use of organoclays [282], chemically modified carbon [283], dialysis [284], UV light photodegradation [285], nanofiltration [286], non-

ionic polymeric resins [287], covalent sequestration [280], and ozone and OH radicals [288] have been examined. While these technologies have sometimes proven to be effective at the laboratory scale, their wide-spread implementation may be limited by efficiency and cost in comparison to activated carbon. In this study, an economical hybrid biomaterial was developed that possesses the adsorptive capability of activated carbon but in addition, selectively degrades atrazine. Moreover, the combination maintains atrazine removal capabilities for extended periods without saturation, thus eliminating the need for recharging.

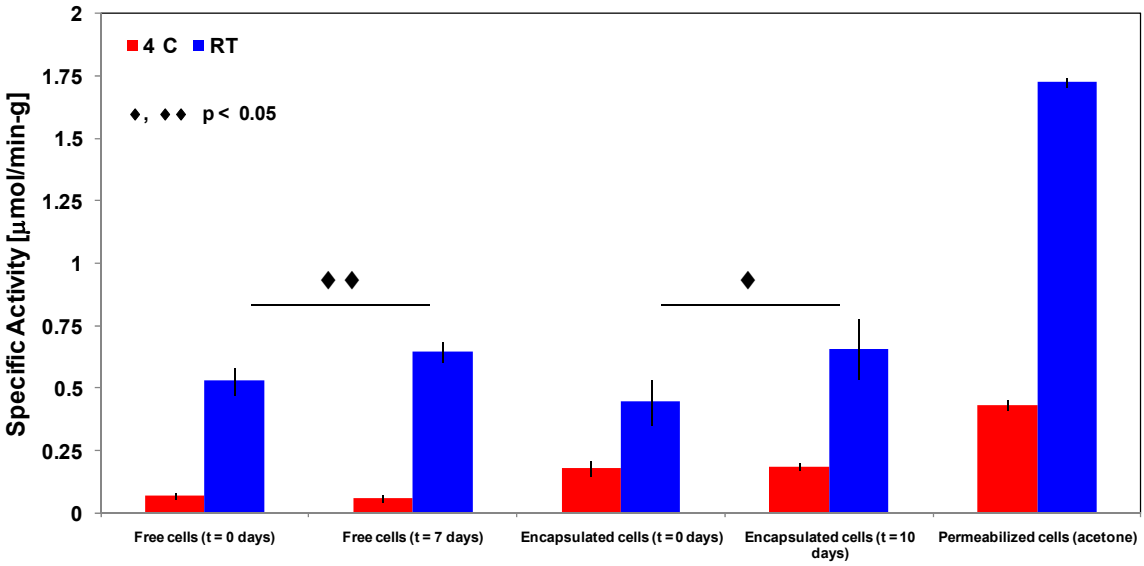

Fig. 4.8 Comparison of specific activity of E. coli expressing AtzA at different conditions (n = 3). Statistical analysis was performed using ANOVA test.

4.4.1) Viability of the encapsulated cells

Many bacteria have been immobilized in silica-based porous gels with the aim of developing biosensors, bioreactors, or bioremediation applications that require metabolically-driven reactions [4, 289]. All of these applications require long term cell viability after the encapsulation process. This requirement has directed most research

towards improvement of the survivability of the cells in the silica gels by using more mild encapsulation methods [22], or by the addition of osmoprotectants [8, 85]. On the other hand reactions that do not require metabolic activity, such as the hydrolytic removal of chlorine from atrazine, do not necessitate such considerations. It has been shown that recombinant *E. coli* cells expressing AtzA can still be highly active enzymatically without being viable [277]. In fact, for a drinking water application, non-viable encapsulated bacteria are desirable to mitigate against human exposure to bacteria, despite the known safety of the bacterial species used in our studies.

E. coli cells survived the process of encapsulation in the different gels tested when not cured at a high temperature (Fig. 4.2). Clusters of cells were distributed evenly through the gel. The porosity of the gel was in the nanometer range, which restricted the cells from migrating, growing and undergoing cellular division. The gels were permeable to water and to water soluble solutes (including atrazine and hydroxyatrazine) and gases. The viability of encapsulated cells changed depending on the composition of the gels. Within 3 weeks, there was a 93.4 % reduction in viable cells encapsulated in N1. It has been shown that surface silanol groups of the silica gels have a detrimental effect on the integrity of the cellular membranes of the encapsulated cells. This is thought to be one of the main reasons for the decrease in viability and survival of the encapsulated cells along with the lack of space for cellular division [8, 290].

The formulations N1 and N5 had the greatest decrease in viable cells after 3 weeks, 93.4 % and 92.2 %, respectively. In contrary, N3 gels had the highest viability after 3 weeks of encapsulation (49.3 %). This result was consistent with reported values

of viability of encapsulated *E. coli* TG1/pPBG11 cells using alkoxides and PEG as precursors of the porous gel [22]. However, 6.6 % or 7.8 % viability of encapsulated cells after 3 weeks was still too high for using bacteria in the purification of water.

The number of viable cells after encapsulation was negligible when the encapsulated cells were incubated in a convection oven for 24 h at 45°C. This treatment resulted in a viability decrease of almost 100% based on CFU counts. We suggest that this drop in viability is the result of a loss of cell membrane integrity. This hypothesis is supported by the structural changes observed via FTIR analysis in the lipid membranes of encapsulated cells due to thermal treatment. After encapsulation, there was a drop in the ν-CH_2 peak position, which indicated an increase in the packing of the membrane lipids. This could be due to specific bonding between the silica surface silanol groups and the lipid headgroups and/or dehydration due to extensive hydrogen bonding of the silica gel, and shrinkage. However, the initial decrease in the lipid headgroup spacing did not have a significant effect on the viability of the encapsulated cells since cells extracted from the gels after a short period of time could continue to grow and form colonies. On the other hand, when the encapsulated cells were thermally treated, ν-CH_2 peak position further shifted from ~ 2844 cm^{-1} to ~ 2847 cm^{-1} in an irreversible fashion, which indicated a permanent disruption of the lipid membrane. Comparisons of electron microscopy images of cells in solution and extracted cells from gels with and without thermal treatment showed the significant difference in the texture of the lipid cell membranes.

4.4.2) Atrazine biodegradation

Pseudomonas sp. strain ADP and purified AtzA have previously been encapsulated in silica gels for the purpose of biodegradation of atrazine [272, 278]. When a combination of alkoxide precursors is used for the synthesis of the silica gel, the encapsulated AtzA remained active for up to 3 weeks while maintaining 40 % of the activity of the free AtzA [272]. In contrast, it was reported that the encapsulated *Pseudomonas* sp. strain ADP required viability to biodegrade up to 60 % of the atrazine present in solution. Otherwise only 8 % atrazine biodegradation occurred [278]. In addition to the low performance detailed above, the further disadvantages of these two approaches are that AtzA requires an extensive process of purification, cells need to be alive and supplemented with nutrients, and the encapsulation process must not yield to detrimental by-products such as methanol that can seriously reduce the activity of the enzyme or the viability of the cells. The encapsulation of recombinant *E. coli* cells expressing AtzA in silica or SPEG gels overcame all the previous limitations, since the encapsulated cells did not require to be kept alive to maintain the activity of the overexpressed AtzA. The hybrid biomaterial we have developed not only mimics the adsorptive capabilities of activated carbon, but also provides an avenue for in situ herbicide degradation.

The adsorption of atrazine by silica was evident when gels that did not contain cells were incubated in the presence of 140 μM atrazine (30.2 ppm); there was a drop in the concentration of atrazine with two characteristic slope regions (Fig. 4.5A). We suggest that the initial steeper slope indicated atrazine adsorption on the surface area

within the silica matrix. As the available surface area decreased, atrazine adsorption slowed as indicated by the second slope. When cells were present in the porous gel, the slopes observed were steeper (i.e., more rapid depletion of atrazine) which was an indicative of the atrazine adsorption and biodegradation working in tandem. This combined mechanism of action was corroborated by the generation of hydroxyatrazine in the solutions exposed to gels with encapsulated cells (Fig. 4.5B).

All specific activity calculations were based on the rate of appearance of hydroxyatrazine to avoid overestimation of the values of atrazine biodegradation. Moreover, the adsorption of hydroxyatrazine in the porous gel was lower than what is seen with atrazine since no changes in their slope were observed. The specific activity of the enzyme after encapsulation of the cells depended on the precursors used for the gel synthesis and on the geometry of the gel (e.g., cylinder block or microbeads). In cylinder blocks, the activity ranged from 15 % to 22 % of the cells in solution. The low surface area per volume ratio limited the diffusion of atrazine and hydroxyatrazine through the cylinder block gel and was responsible for the low specific activity. It is known that the rates of diffusion in silica gels are slow [291]. One possible solution to this problem would be to increase the porosity of the silica or SPEG gels, but this was not done to ensure that the encapsulated cells remained entrapped in the gel and not accidentally released. Instead, microbeads with a diameter of ~ 1 mm with significantly higher specific surface area, but similar porosity as cylinder blocks were manufactured.

The activity of the encapsulated cells in microbeads ranged between 0.44 ± 0.06 μmol/g-min to 0.66 ± 0.12 μmol/g-min. This activity was comparable to free cells (Fig.

4.7). However, free cells lysed after 21 days, and were not suitable for further activity assays. In contrast, encapsulated cells in microbeads had stable activity for up 4 months. We suggest that although encapsulated cells are not viable and have disrupted lipid membranes after thermal treatment (Table 4.2 and Fig. 4.4C), most of the AtzA enzyme was still active and distributed in what remained of the encapsulated cells or adsorbed in the porous gel.

In measurements of the activity at 4°C, the results showed that there was a drop in the measured specific activity of both encapsulated and free cells. It is known that structural changes of enzymes in solution and in crowded environments (e.g., cytoplasm of a cell) are temperature dependent [292, 293]. Moreover, the lipid membrane of the free cells transitioned to a more ordered state at 4°C (lower ν-CH_2 peak position). This was not the case for the membranes of encapsulated cells with thermal treatment (Fig. 4.4C). We believe that in free cells at 4°C, the membrane becomes a strong barrier to the diffusion of atrazine into the interior of the cells due to its more ordered, crystalline structure. In heat-treated encapsulated cells at 4°C, the cell membrane is perturbed and therefore unable to transition into the ordered state seen in the normal membrane; it is less of a barrier to atrazine diffusion and therefore we observe a higher specific activity for encapsulated cells at 4°C.

4.5) Conclusions

This study presents an effective approach for the bioremediation of atrazine in water. The method consisted of the encapsulation of recombinant *E. coli* expressing AtzA

in porous silica gels. The synergistic interaction between the porous silica and the cells allowed the adsorption and biodegradation of the atrazine for over 4 months. The rates of conversion of atrazine by the encapsulated cells depended on the precursors used for the synthesis of the porous gels and on their final geometries (e.g., films or microbeads). When microbeads were used the rates of biodegradation of atrazine were close to the values obtained with free cells.

Chapter 5: Encapsulation of Mammalian Cells in Silica Nanoporous Gels: Interactions at the Biointerface[4]

5.1) Introduction

Encapsulation of cells in biomaterials using the silica sol-gel route has long been explored for the development of novel bio-functional materials [32, 86, 294]. Specifically, encapsulation of cells in silica matrices has shown great potential for the development of biotechnology applications such as biosensing [83, 295], biocatalysis [4, 92], bioremediation [296, 297], and energy conversion [91, 92], as well as in biomedical engineering for cellular therapies [39, 92].

Cells are encapsulated in silica matrices by the hydrolysis and condensation reactions of the acidic silicate sols, which yield to a polymeric oxo-bridged SiO_2 network [4]. The entire encapsulation process occurs at mild conditions of pH and temperature with the sol-gel transition completing within minutes [4, 289]. The silica matrix provides mechanical support and confers chemical and thermal stability, and is resistant to microbial attacks [6, 32]. However, lower long-term viability and function of the mammalian cells after encapsulation remains as one of the principal setbacks for this technology [86, 294]. In fact, so far only a limited number of applications involving functional cells encapsulated in silica nanoporous matrices have reached the market [294].

[4] This chapter is part of a manuscript in preparation that will be submitted to *Acta Biomaterialia*.

Nanoporous silica matrices allow for the exchange of oxygen, nutrients, electrolytes, metabolites, and other bioactive compounds [32]. However, proliferative division of the encapsulated prokaryotic or eukaryotic cells is prohibited due to the mechanical stiffness of the silica gel. This constitutes one of the major fundamental differences between polymeric and silica encapsulation [99-101, 103, 298]. It has been shown that prokaryotic cells can maintain their metabolic activity (MA) when encapsulated in silica gels. When encapsulated, the metabolism of the prokaryotic cells can be regulated by minimizing the concentration of the nutrients [8], inducing production of intracellular sugars prior to encapsulation [70], or inducing quorum sensing in the encapsulated cells by the addition of molecules such as acylated homoserine lactones [68]. Model eukaryotic cells (e.g., *Saccharomyces cerevisiae*) have also shown to maintain MA in silica encapsulation, when they are encapsulated at stationary-growth phase [75].

On the other hand, silica gel encapsulation of eukaryotic cells is a challenging task since all the previous strategies reported in the literature have failed in maintaining the membrane integrity and MA of the encapsulated eukaryotic cells for long periods of time [5, 6]. We propose that for successful mammalian cell encapsulation, all of the issues associated with sol-gel processing and encapsulation need to be addressed in a systematic manner. The main issues to be addressed are: the specific surface interactions between the matrix and the encapsulated cells at the biointerface, cytotoxicity induced by by-products generated during the hydrolysis and condensation reactions, the mechanical

compressive stresses formed during gelation and aging of the gel. Another source of mechanical stress buildup is proliferation-induced cell division.

The effects of silica gelation by-products (e.g., methanol, ethanol) on the membrane integrity and MA of mammalian cells have been reported [5, 6]. On the other hand, the effects of silica gel aging has not been fully explored [294]. The gel aging phase is most likely the stage when the surface interactions form and mature at the biointerface. Aditionally, compressive stresses also arise due to silica matrix syneresis, negatively effecting the membrane integrity and MA of the encapsulated mammalian cells [294].

In this study, we have investigated the membrane integrity and MA of encapsulated mammalian cells (e.g., human foreskin fibroblast, HFF; irradiated human foreskin fibroblasts, HFFIR, mouse embryonic fibroblasts, MEF; and irradiated mouse embryonic fibroblast, MEFIR) during aging of the silica matrix they are encapsulated in. Silica gels made from water soluble alkoxides, tetrakis (2-hydroxyethyl) orthosilicate (THEOS) and tetramethyl orthosilicate (TMOS) were used. The nanoporous silica matrix was synthesized in the presence of culture media. The by-product of THEOS hydrolysis, ethylene glycol (EG), had no effect on the membrane integrity and MA of the mammalian cells. On the other hand, methanol, the cytotoxic by-product of TMOS hydrolysis, was removed by evaporation prior to cell encapsulation.

Our results showed that encapsulated cells experience significant conformational changes in their lipid membranes during the gelation and aging of the nanoporous silica matrix. Measurements of the MA and viability of the encapsulated cells show that

majority of the cells tolerate the initial change in their lipid organization immediately after encapsulation. However, aging of the silica matrix beyond 6 h induce additional changes, causing a significant drop in MA and also leakage of intracellular lactate dehydrogenase (LDH) from the encapsulated cells. These are the signs that death of the encapsulated cells is accelerated during aging of the silica matrix.

We hypothesized that reducing the interactions at the biointerface during silica gel aging would be beneficial for the enhancement of the MA and viability of the encapsulated cells. The biointerface interactions were reduced by incorporating polyethylene glycol (PEG) at different molecular weights into the matrix. It is known that the hydrophilic part of PEG forms hydrogen bonds with silica surfaces and therefore prevents surface interactions [299, 300]. The immediate effect of PEG was the reduction of the time dependent decrease in MA of the encapsulated cells and the reduced LDH leakage. PEG stopped the specific chemical reactions at the biointerface, but as expected did not protect against the buildup of mechanical compressive stresses (due to matrix shrinkage and cellular division). We therefore further envisioned that arresting the cellular division of HFF and MEF cells by irradiation would be beneficial in decreasing the decay of MA in encapsulated cells.

5.2) Materials and methods

Tetrakis (2-hydroxyethyl) orthosilicate (THEOS) was purchased from Gelest (Morrisville, PA), Tetramethyl orthosilicate (TMOS) was obtained from Sigma. Colloidal silica nanoparticles (SNPs) were obtained from NYACOL Nano Technologies Inc. (Ashland, MA). SNPs were purified using dialysis through 3.5 kDa Spectra/Pore

membranes purchased from Spectrum Laboratories Inc. (Rancho Dominguez, CA). Linear PEG (at molecular weights (M_w) of 0.4, and 0.6 kDa) was purchased from Sigma. 4-arm PEG (M_w = 2 kDa) was purchased from Creative PEGWorks (Winston Salem, NC). PEG was used to increase the porosity of the silica gels as well as to modify its surface. All chemicals were used without further purification.

5.2.1) Cell culture

Human foreskin fibroblasts (HFF), and mouse embryonic fibroblasts (MEF) were obtained from the American Type Cell Collection (Manasas, VA). HFF and MEF cells were cultured in DMEM basal media supplemented with 15% fetal bovine serum (FBS), and 1 % penicillin/streptomycin. Cells were incubated in a 5% CO_2 atmosphere at 37°C until they reached 80 - 90 % confluence. Cells were then washed with phosphate buffer saline (PBS) and trypsinized with 0.25 % Trypsin-EDTA for 5 min at 37^{o}C. For cytotoxicity measurements and encapsulation experiments, cells were centrifuged at 800 rpm for 5 min. The supernatant was removed and the pelleted cells were suspended in their own growth media at a concentration of ~ 500,000 cells/ml.

5.2.2) Cell irradiation

HFF and MEF cells were irradiated for 15 min with an X-ray machine at a dose of 6,000, and 10,000 rads for HFF and MEF cells, respectively. Irradiated HFF (HFFIR) and irradiated MEF (MEFIR) cells stopped replicating after irradiation [301]. Encapsulation

of the irradiated cells was conducted in a similar fashion to that used for non-irradiated cells, as described previously.

5.2.3) Silica gel synthesis and characterization

Silica gels were synthesized by direct hydrolysis of 10 % (v/v) THEOS in cell culture media without using any acid catalyst. The culture media was prepared with 0.01 M of 85 nm diameter SNPs. Note that SNPs were used as nucleation seeds for the development of the silica network. The mixture was stirred vigorously for 60 s. During that time a change in the pH of the mixture (~ pH 5) was observed showing that THEOS was hydrolysed. The reaction then continued on as a condensation polymerization forming the nanoporous network. The neutral pH (~ 7) was recovered naturally after the sol-gel transition of the hydrolysed alkoxide was complete. Silica gels made out of the alkoxide TMOS were prepared in a similar fashion.

Some of the silica gels were produced using PEG (these gels are termed SPEG). Gels produced with linear PEG (M_w = 0.4, 0.6 kDa) were termed SPEG-l and gels produced with 4arm PEG (M_w = 2 kDa) were termed SPEG-4arm. In a typical preparation, PEG was dissolved in cell culture media and the resultant solution was mixed with hydrolysed THEOS solution. The final volume ratio of PEG in the mixture was 2.3, 4.5, or 10 % (v/v). PEG interacted with the silica matrix in two different ways: (a) by hydrogen bonding with the silanol groups that formed after the hydrolysis of the alkoxide (with the ether oxygen of PEG); and (b) by covalently linking to the silica

surface through transesterification reactions between the hydroxyl groups of PEG and the hydrolysed alkoxide [299, 300].

The prepared gels were characterized using FTIR spectroscopy, UV-vis spectroscopy and scanning electron microscopy (SEM). FTIR analysis of pure silica and SPEG gels was conducted to determine the changes in the chemical structures of the gels with incorporation of PEG. UV-vis spectroscopy was performed on aged samples prepared in 96-well plates to determine whether phase separation occurred in the gel. Scanning electron microscopy (SEM) analysis was performed with a Hitachi S-900 FESEM (Hitachi Co., Lawrenceville, GA) electron microscope. For SME analysis, silica gels were dehydrated in ethanol and transferred to a CO_2 critical point drier (Samdri-780A, Tousimis, Rockville, MD). Prior to imaging, dried samples were sputtered with Tungsten at a rate of 1 A°/min for 15 min. SEM images of the gels were analyzed in order to determine their porosity (the percentage void space using the ImageJ software [302]), and to explore their ultrastructure.

5.2.4) Cell encapsulation

For encapsulation in silica gels, 20 μL of 0.01 M SNPs suspended in culture media was mixed with 4 μL of THEOS. The mixture was vigorously vortexed for 1 min and was placed on ice to avoid condensation. After the pH recovered to 7, 20 μL of cell solution (500,000 cell/ml) was added, mixed by pipeting and transferred to a 96-well plate. In parallel experiments, cells were encapsulated in silica gels prepared with TMOS. In these gels the alkoxide was hydrolyzed in water catalyzed with 0.01 M HCl at 1/1/0.01

(v/v/v). After hydrolysis, the mixture was heated up to 65°C to remove the alcohol by-product [6]. Later, 20 μL of 0.01 M SNPs in culture media was mixed with 4 μL of hydrolyzed TMOS. This step neutralized the solution. Cells suspended in media (500,000 cell/ml) were added to this solution. Gelation of the silica gels was completed within 5 min, and 90 μL of media was added on top of the gels to avoid drying. The encapsulated cells were incubated at 5% CO_2 atmosphere and 37°C for up to 60 h.

For encapsulation in SPEG gels, linear or 4-arm PEG was added at a concentration of 2.3 %, 4.5 %, 10 % (v/v) to 20 μL of 0.01 M SNPs in culture media. The rest of the procedure was identical to that followed for making the gels that did not contain PEG.

5.2.5) Fluorescence microscopy

Membrane integrity of the encapsulated cells in silica and SPEG gels was measured using a live-dead fluorescence assay containing Hoechst (H) and Propidium Iodide (PI) fluorescent dyes. A Nikon Eclipse T200 microscope (Nikon Instruments Inc., Melville, NY) equipped with 10X, and 20X objectives were used to collect the bright field and fluorescent images.

5.2.6) Membrane analysis of the encapsulated cells

Conformation of the cell membrane lipids was determined using FTIR spectroscopy. Sample preparation and data collection were described elsewhere [303]. Spectral analysis was performed using Omnic software provided by the manufacturer.

The change in the lipid conformation was monitored by measuring the peak location of the ν-CH_2 (symmetric stretching) band located at 2850 cm^{-1} for cells in solution (and at 2843 cm^{-1} for the encapsulated cells). Due to overlapping of the PEG and ethylene glycol CH_2 bands in the 2900 - 2700 cm^{-1} region, FTIR analysis of encapsulated cells was only carried out in silica gels prepared without PEG.

5.2.7) Metabolic activity and lactate dehydrogenase leakage measurements

MA of the encapsulated cells was measured with alamar blue (AB) fluorescence [304]. For fluorescence measurements a SpectraMAX Gemini microplate reader (Molecular Devices Inc, Sunnyvale, CA) was used. The samples were excited at 540 nm and their emission was measured at 590 nm. LDH assay was performed 24 h after encapsulation of the cells. The assay was performed using a commercially available kit (Roche Applied Science, Indianapolis, IN). The levels of extracellular LDH concentration were determined using a UV-vis SpectraMAX microplate reader (Molecular Devices, Sunnyvale, CA) by absorbance at 492 nm. The readings were calibrated using blank wells, wells that only contain media, cells in media, and gels that do not contain any cells.

5.3) Results

5.3.1) Characterization of the silica and SPEG gels

In pure silica gels, when THEOS or hydrolyzed TMOS were mixed with the solution containing the cells, phase separation was not detected. The gelation time (T_g) of

the pure silica gels decreased with an increase in the alkoxide concentration. Fig. 5.1 shows that the there is a logarithmic correlation between T_g and volume ratio of THEOS. Gels prepared with TMOS had the same trend (data not shown). The presence of the cells did not affect the gelation time for the different concentrations of the alkoxides.

For SPEG-4-arm gels prepared with 2.3 % or 4.5 % PEG, the onset of the gelation was concurrent with phase separation, as indicated in Fig. 5.1. Therefore, it was not possible to determine the onset of gelation. In SPEG-4-arm gels prepared with concentrations of PEG higher than 4.5 % PEG, phase separation was drastically reduced. A logarithmic correlation between T_g and 4-arm PEG concentration was observed (Fig. 5.1).

Phase separation causes increased adsorption of light and therefore UV-vis spectroscopy can be used to detect phase separation (Fig. 5.2A). Interestingly, in some gels it was observed that even though phase separation was present, a gel structure was formed (Insert Fig. 5.2A). In SPEG-4-arm gels prepared with 10% PEG, phase separation was drastically reduced as indicated by high optical transmittance. The transmittance values of SPEG-l gels did not show significant phase separation at low or high concentrations of PEG (Fig. 5.2B). A drop in transmittance was observed in all gels at around 560 nm. This corresponded to absorbance by the cell culture media that was used as a solvent in all gels (Fig. 5.2C).

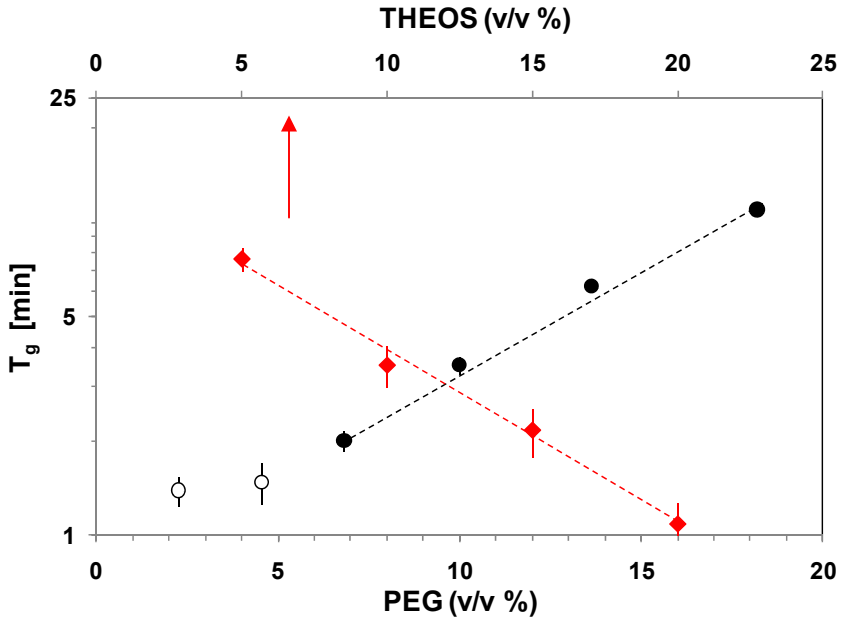

Figure 5.1 Gelation times (T_g) for gels made with THEOS and PEG. In these experiments, a constant concentration of 10 % (v/v) THEOS was used.

Fig. 5.3 shows the SEM micrographs of (A) pure silica gel, (B) SPEG-l gel (0.4 kDa), (C) SPEG-l (0.6 kDa), and (D) SPEG-4-arm. All gels were formed by the aggregation of SNPs in the form of a three dimensional network. Pure silica gels exhibited a more compact agglomeration of SNPs with less void space (or volume fraction) when compared to the SPEG gels, showing the role of PEG as a porogen. Increasing PEG size (by increasing the M_w) increased the void space fraction in the gels such that 13.77 % ± 2 %, 18. 45 % ± 1.3 %, 21.42 % ± 1.9 %, and 29.1 % ± 1.1 % of void space was obtained in pure silica, SPEG-l (0.4 kDa), SPEG-l (0.6 kDa), and SPEG-4-arm gels, respectively (Fig. 5.4).

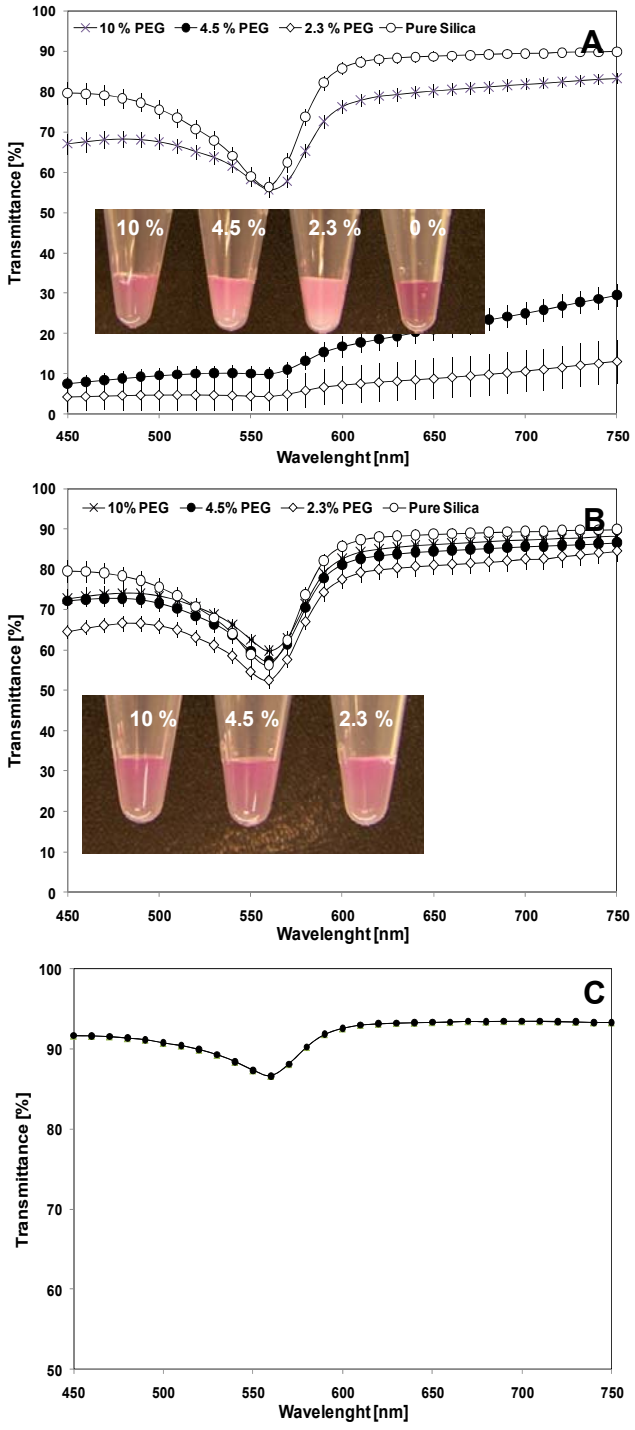

Fig 5.2 Optical properties of silica and SPEG gels prepared with 10 % (v/v) THEOS, different M_w and concentrations of PEG. Transmittance of (A) SPEG-4arm, (B) SPEG-l (M_w = 0.6 kDa), cell culture media. The drop in the transmittance at 560 nm is due to absorbance by albumin at that wavelength.

PEG was added to the gels to modify the silica surface. The interaction of the silica surface with PEG was confirmed by FTIR analysis in the region 3900 - 2500 cm^{-1} (Fig. 5.5). In silica gels, at 3737 cm^{-1} the IR spectrum showed a sharp peak (point O in Fig. 5.5), which corresponded to the stretching vibrations of the unbound silanol groups located on the silica surface (-SiOH) [156]. Moreover, at 3662 cm^{-1} a shoulder in the IR spectrum was observed (point P in Fig. 5.5). This shoulder originated from the stretching vibrations of the vicinal silanol groups [156]. In the IR spectra of the SPEG gels, the stretching vibrations of the surface silanols disappeared showing that PEG interacted with the silica surface binding with the silanol (-SiOH) groups. A similar interaction mechanism of organic polymers and sugars with silica through silanol groups was previously reported in colloidal silica [303, 305]. In SPEG gels, the asymmetric stretching vibrations of PEG ($-CH_2$) are located in the region 2900 cm^{-1} to 2750 cm^{-1} (point Q in Fig. 5.5).

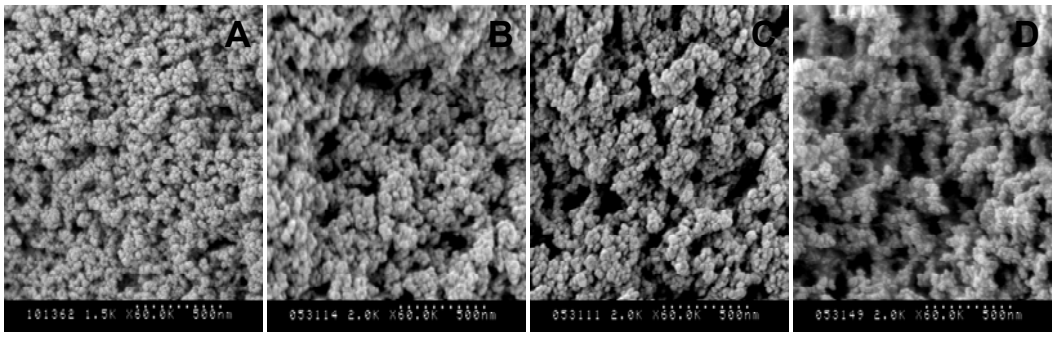

Figure 5.3 Electron microscopy micrographs of the nanostructure of the SPEG gels with 10 % (v/v) THEOS: (A) Pure silica gel, (B) 10 % SPEG-l (0.4 kDa), (C) 10 % SPEG-l (0.6 kDa), (D) 10 % SPEG-4arm (2 kDa).

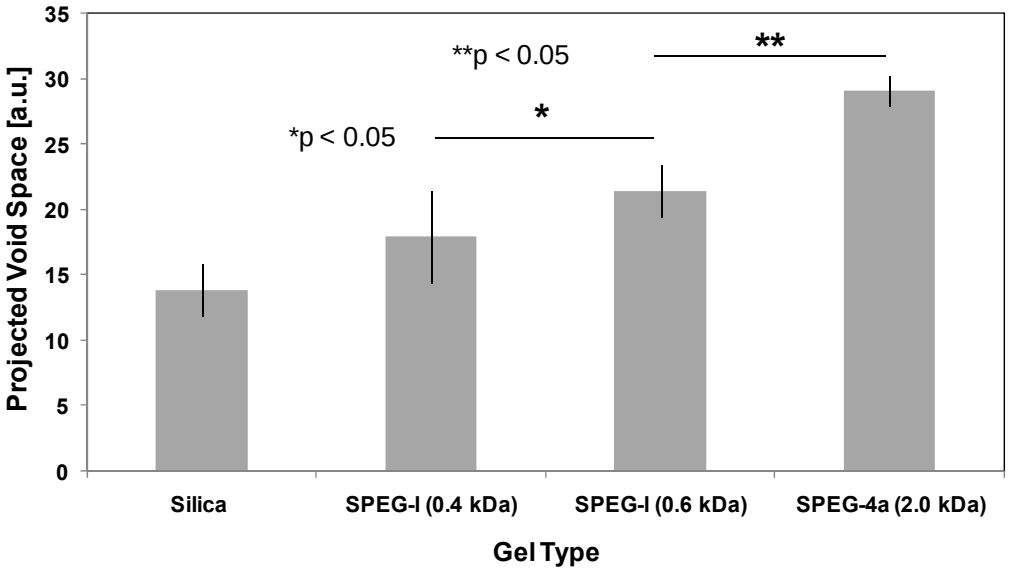

Figure 5.4 Comparison of the projected void space (a measure of porosity) obtained in different gels (n = 5). Statistical analysis was conducted using ANOVA.

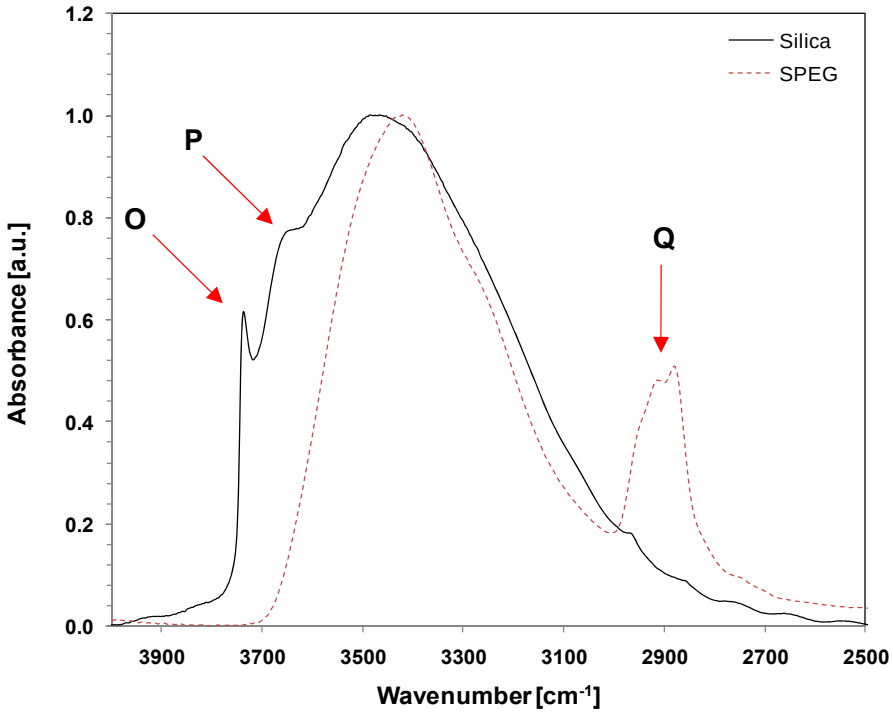

Figure 5.5 IR spectra of pure silica gel and 10% SPEG-4-arm (M_w = 2 kDa) gels showing the differences in their surface chemistry.

5.3.2) Cytotoxicity of the gel components

During the encapsulation process, mammalian cells are exposed to individual and aggregated SNPs in the surrounding solutions as gelation proceeds. It is known that SNPs can be mildly cytotoxic [306]. The toxicity of the encapsulation process was analyzed by incubating mammalian cells in 0.01 and 0.03 M SNP solutions (the concentrations used in our gels). After 24 h of incubation in the presence of SNPs, the cell membrane integrity and MA was measured. The results showed that exposure to SNPs did not cause membrane damage in HFFs and MEFs. Moreover, cells exposed to SNPs had comparable MA to control cells (Fig. 5.6).

Another factor for cytotoxicity is the formation of cytotoxic by-products such as EG during the hydrolysis reaction [38]. HFF and MEF cells were incubated with 0.19 and 0.38 M EG to test for cytotoxicity. The concentrations of EG used in these experiments were based on the stoichiometric reaction of 10 % (v/v) THEOS assuming a complete reaction. Incubation of HFF and MEF cells in EG for 48 h did not cause any cell membrane damage nor had any effects on the MA of the cells (Fig. 5.6).

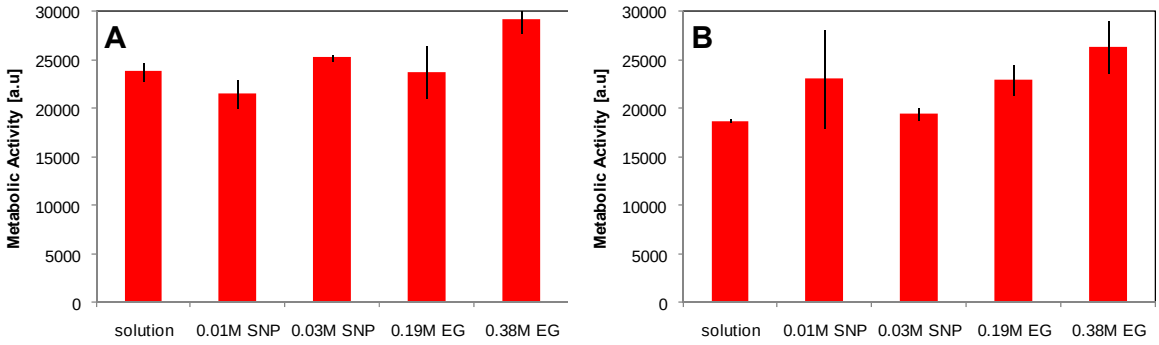

Figure 5.6 Cytotoxicity of SNPs and EG on: (A) HFF, (B) MEF. Cells were incubated in SNPs and by-products for 24 h.

5.3.3) Encapsulation of mammalian cells in pure THEOS silica gels

Immediately after encapsulation in pure THEOS gels, the MA of encapsulated HFF and MEF cells decreased to 5.3 % and 70 % of their values measured in media, respectively (Fig. 5.7). The decrease in the MA of the encapsulated cells was statistically significant when compared to the cells in solution (ANOVA, $p < 0.05$). After 12 h of encapsulation, HFFs exhibited only 46.3 % of the solution MA. After 24 h of encapsulation, MA of MEF and HFF cells had dropped to practically zero value. The drastic drop in MA of MEFs after encapsulation showed adverse interactions at the biointerface. Cells encapsulated in TMOS gels followed almost the identical trend (results not shown).

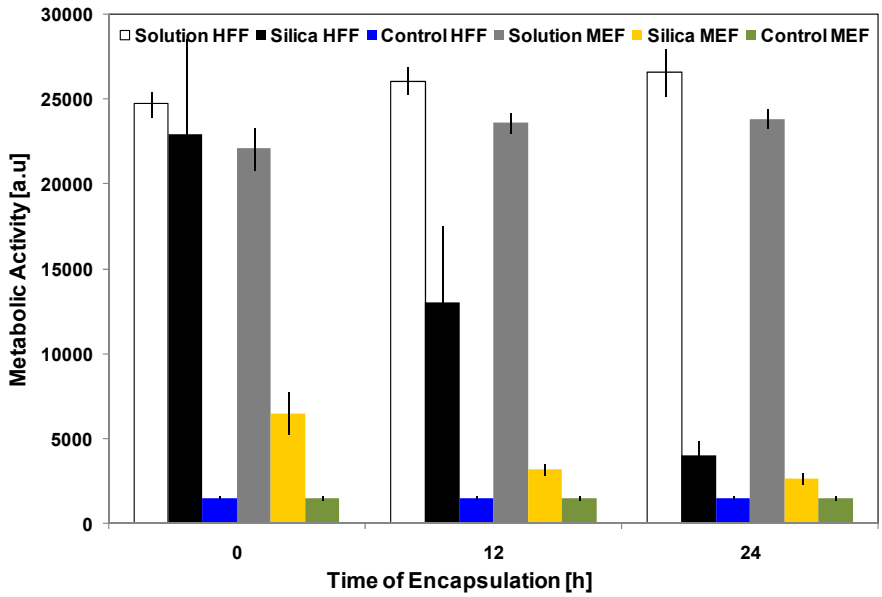

Figure 5.7 Metabolic activity of encapsulated HFF and MEF cells. Negative Controls (blue and green) were prepared by encapsulating dead HFF and MEF cells. Dead cells were prepared by incubation in 70% ethanol for 10 min. Compromised membrane integrity of the dead cells were verified before encapsulation.

The changes in the cell membrane lipid conformation of the encapsulated cells was quantified by monitoring the change in the peak location of the lipid acyl chain stretching peak (ν-CH_2) at ~ 2850 cm^{-1}. Immediately before the onset of the gel transition, the ν-CH_2 peak wavenumbers of the cells suspended in the silica sol and in growth media were almost identical. When the experiments were repeated 30 min after gelation, it was observed that the encapsulated cells had significantly lower ν-CH_2 values than the cells in media (Table 5.1). The decrease in the ν-CH_2 wavenumber upon encapsulation shows increased packing of the membrane lipids, potentially due to stiffening of the gel, interactions at the biointerface, buildup of compressive stresses, and partial dehydration of the cells. The change in the cell membrane fluidity with encapsulation was evidenced by the small change in the ν-CH_2 peak values observed with changing temperature (Table 5.1). $\Delta\nu$-CH_2 between 23°C and 0°C was 0.7 cm^{-1} and 0.8 cm^{-1} for HFF and MEF cells, respectively, when they were in solution. When encapsulated $\Delta\nu$-CH_2 decreased by 0.5 cm^{-1} for the same change in temperature.

Table 5.1 Structural changes in the cellular membranes with encapsulation.

Cell Type	ν-CH_2 Peak Location [cm^{-1}]				
	0°C		23°C		
	In media	Encapsulated for 1 h	In media	Encapsulated for 1 h	Encapsulated for 6 h
HFF	2851.8 ± 0.01	2843.8 ± 0.02	2852.3 ± 0.05	2844.5 ± 0.14	2845.6 ± 0.3
MEF	2851.5 ± 0.12	2843.1 ± 0.17	2852.3 ± 0.06	2843.6 ± 0.06	2844.9 ± 0.5
LNCaP	2851.8 ± 0.01	2843.4 ± 0.00	2852.3 ± 0.05	2843.9 ± 0.17	-
MCF-7	2852.0 ± 0.17	2843.1 ± 0.24	2852.6 ± 0.02	2843.7 ± 0.23	-

Increased packing of the cellular membranes with gelation did not have significant short-term effects on membrane integrity. Membrane integrity of encapsulated cells immediately after encapsulation was measured as 98.3 ± 4.2 % and 97.2 ± 3.5 % for

HFFs, and MEFs, respectively. Even though the membrane integrity assay using fluorescence microscopy indicated no membrane damage immediately after encapsulation, significant amounts of cytoplasmic material has leaked from the encapsulated cells. This was observed by LDH released from the encapsulated HFF and MEF cells (Fig. 5.8). After 24 h of encapsulation, there was 78 % ± 1.3 % and 80.1 % ± 1.3 % LDH release from encapsulated HFFs and MEFs with respect to their lysed controls. Moreover, FTIR analysis of the encapsulated cells conducted after 6 h showed that the ν-CH_2 peak positions shifted towards higher wavenumbers (Table 5.1), which was an indication of loosening in membrane packing and therefore membrane damage.

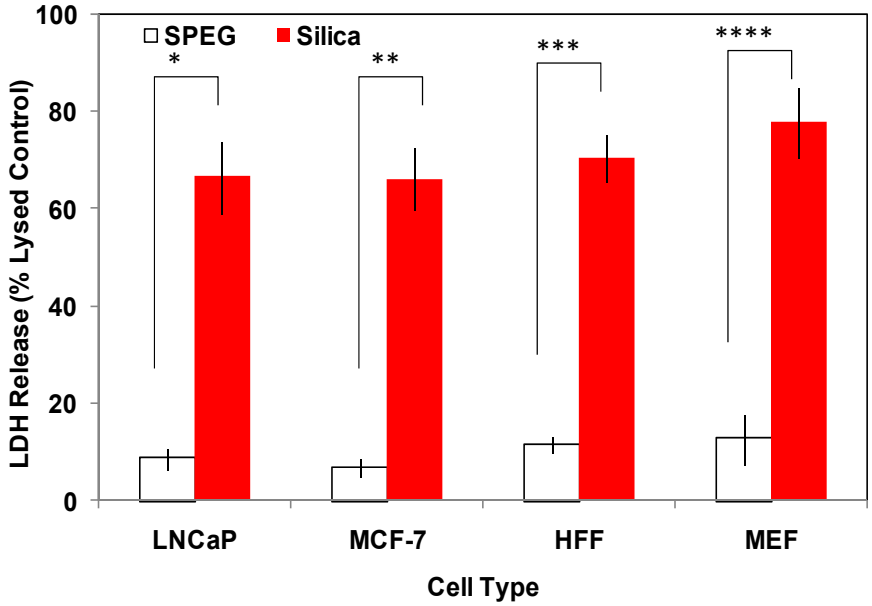

Figure 5.8 LDH release from encapsulated cells after 24 h of encapsulation. Statistical analysis was conducted using ANOVA. *, **, *, ***** $p < 0.05$ (n = 3). In these experiments, SPEG-4arm (10 %, Mw = 2 kDa) was used. Two additional cell lines, LNCaP and MCF-7 cells, were used for comparison.**

5.3.4) Encapsulation of mammalian cells in SPEG gels

The effect of the incorporation of PEG in the silica matrix (SPEG) was evaluated by monitoring the MA of the encapsulated cells after 24 h of encapsulation. MA of the encapsulated cells depended on the size and concentration of the PEG used in the gel synthesis (Fig. 5.9A-B). Cells encapsulated in 2.3, 4.5, and 10 % SPEG-l gels (0.4 kDa) had the largest drop in MA within 24 h, with reductions of 56.43 % and 67.83 % for HFF and MEF, respectively. The effectiveness of 0.6 kDa PEG and the 2 kDa PEG in preserving MA of the encapsulated cells depended on their concentration (Fig. 5.9). However, the drop in MA was always greater in the linear PEGs. This result suggested that PEG was effective in preventing the detrimental interactions of the silanol groups on the lipid membranes. Note that one reason for decreased MA in SPEG-4arm gel with concentration could be attributed to increased phase separation in the gels. Therefore, in the rest of the experiments 10 % SPEG-4arm gels were used.

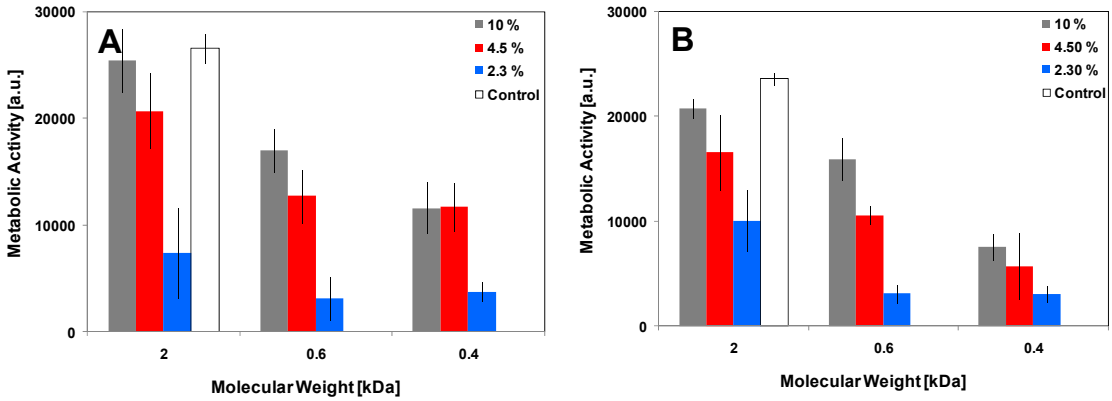

Figure 5.9 Effect of PEG concentration and size on the metabolic activity of encapsulated cells: (A) HFF, (B) MEF. Cells were incubated at 37°C and 5 % CO_2. Cells incubated were used as the control in media.

The effect of long time encapsulation on MA was detrimental (Fig. 5.10A-B) even in SPEG gels. However, incorporation of PEG into the silica matrix had a positive effect on the MA of the encapsulated cells. This result confirmed that one mechanism of damage to encapsulated cells is the specific interactions between the silica surface (-SiOH) and the cellular membranes, which could be minimized by incorporating PEG into the gels. The hydrophilic part of PEG forms hydrogen bonds with surface silanol groups [300]. With PEG the time dependent decrease in MA over time slows down, but does not completely stop. This shows that there are other factors such as the increase in compressive stress due to cell growth that are also involved in the decrease of MA.

LDH release from the SPEG-4-arm encapsulated cells after 24 h (Fig. 5.8) was measured. The amount of LDH released into the extracellular medium is proportional to the number of cells damaged or lysed [307]. Contrary to the results obtained in pure silica gels, encapsulated HFFs and MEFs in SPEG-4-arm gels only had extracellular LDH contents of 11.2 % and 13.5 %, respectively. Extracellular LDH measurements confirmed the detrimental effects of the bare silica surfaces on the encapsulated cells could be inhibited by functionalizing the silica surface with PEG.

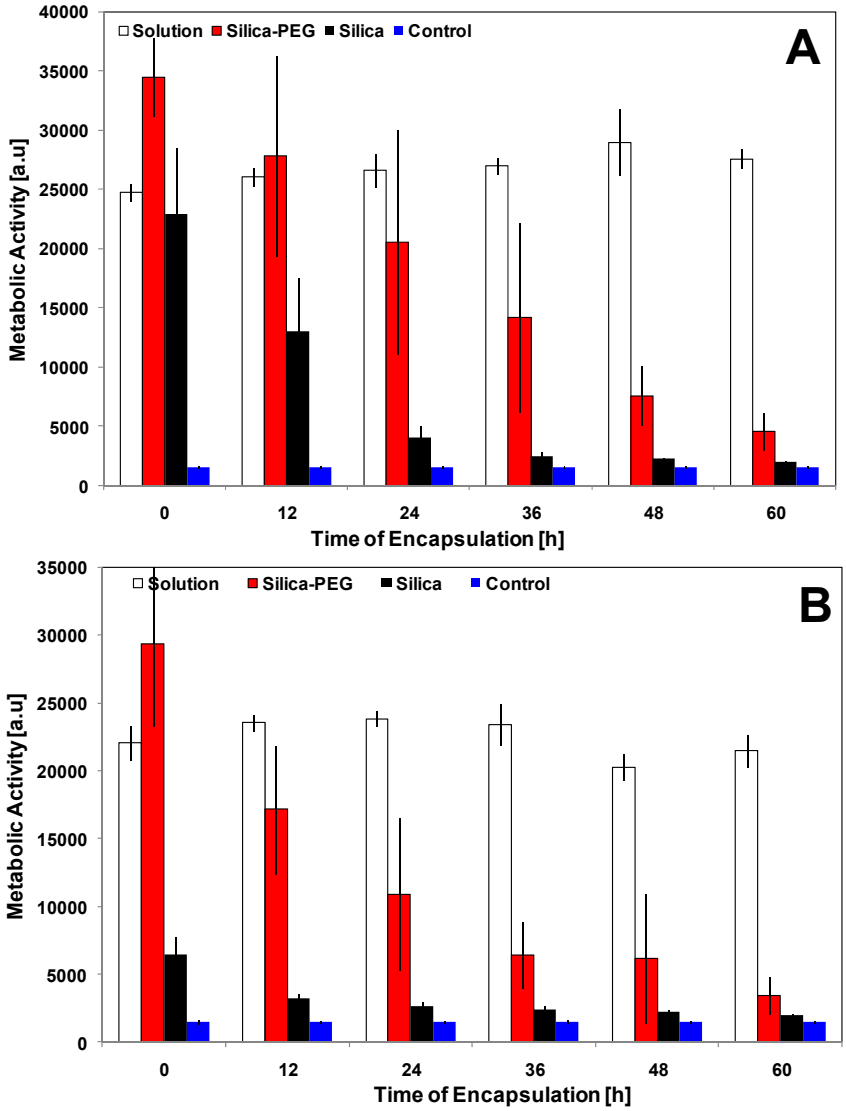

Figure 5.10 Metabolic activity of encapsulated: (A) HFF and (B) MEF. Negative controls (blue) were prepared by encapsulating dead HFF and MEF cells. Dead cells were prepared by exposure to in 70% ethanol for 10 min. Compromised membrane integrity of the "dead" cells were verified before encapsulation. Cells incubated at 37°C and 5 % CO_2 were used as the positive control.

We also explored the effects of arrested cellular division in the MA of the SPEG encapsulated cells. Similar to what was observed with the unirradiated HFFs and MEFs encapsulated in SPEG gels, the encapsulated HFFIR and MEFIR cells were also

metabolically more active when encapsulated (than in solution) as shown in Fig. 5.11A-B. When HFFIR cells were encapsulated in SPEG gels there was no decrease in the MA during the first 12 h of encapsulation, and MA decreased by only 11.1 % within the first 24 h ($p < 0.05$). 48 h after encapsulation MA of HFFIR was 65 %. However, the MA started to drop drastically after 48 h of encapsulation. Similarly, MEFIR cells encapsulated in SPEG gels maintained their MA for 24 h in encapsulation. MA started to drop after 36 h of encapsulation, to 70.9 % and 32.4 %, after 48 h and 60 h of encapsulation, respectively. The irradiated cells (HFFIR, and MEFIR) lost over 97 % of their MA after 84 h of encapsulation (data not shown).

5.4) Discussion

Even though THEOS is compatible with organic polymers forming hydrogels [308-310], SPEG gels exhibited phase separation at certain PEG sizes and concentrations (Fig. 5.2). The phase separation tendency is determined mainly by the PEG/silica ratio [311]. For SPEG-4arm gels synthesized with of 2.3 % and 4.5 % PEG, widespread macroscopic phase separation occurred. It is suggested that phase separation takes place by the adsorption of PEG on silica through hydrogen bonding of the ether oxygens in PEG and the surface silanols such that the surface of the gelling phase becomes hydrophobic and less soluble in the solvent [312].

In contrast, an increase in concentration above 4.5 % in PEG led to a delayed onset of the sol-gel transition, albeit without noticeable phase separation (Fig. 5.2A) and as a result, a uniform ultra structure was obtained. Moreover, in SPEG-l gels (M_w = 0.6 kDa or 0.4 kDa) no phase separation was observed (Fig. 5.2B). It is suggested that

bridging flocculation between the organic (PEG) and the inorganic silica (SiO_2), which causes phase separation, depends on the molecular weight and the concentration of the organic polymer [27]. Therefore, at concentrations above 4.5 % for SPEG-4-arm and at all the concentrations of SPEG-l, it is possible that bridging flocculation does not take place since the amount of PEG is enough to sterically stabilize the silica and cover its entire surface. This is supported by the studies conducted using X-ray scattering, where extremum concentrations of PEG (in silica PEG systems) produced stable reactions with no phase separation. However, at intermediate PEG concentrations, the organic polymer absorbed on the silica surface causing bridging flocculation [313].

THEOS gels were synthesized using cell culture media as the solvent. SEM characterization showed that the gels were formed by three dimensional aggregation of nanometer size particles with a random distribution of porosity (Fig. 5.3A). These results suggested that the soluble organic components present in the media acted as a catalyst for gelation and served as a template for silica condensation. It was previously shown that albumin, gelatin and casein could form a variety of hybrid nanostructures (e.g., fibrillar, spherical) when combined with THEOS at different pH values [314]. Interestingly, THEOS gels prepared with a cationic agent was also formed by the aggregation of particles of about 10 - 20 nm in diameter [315]. When PEG was incorporated, we observed an increase in the porosity of the gel. The pores however, remained randomly distributed.

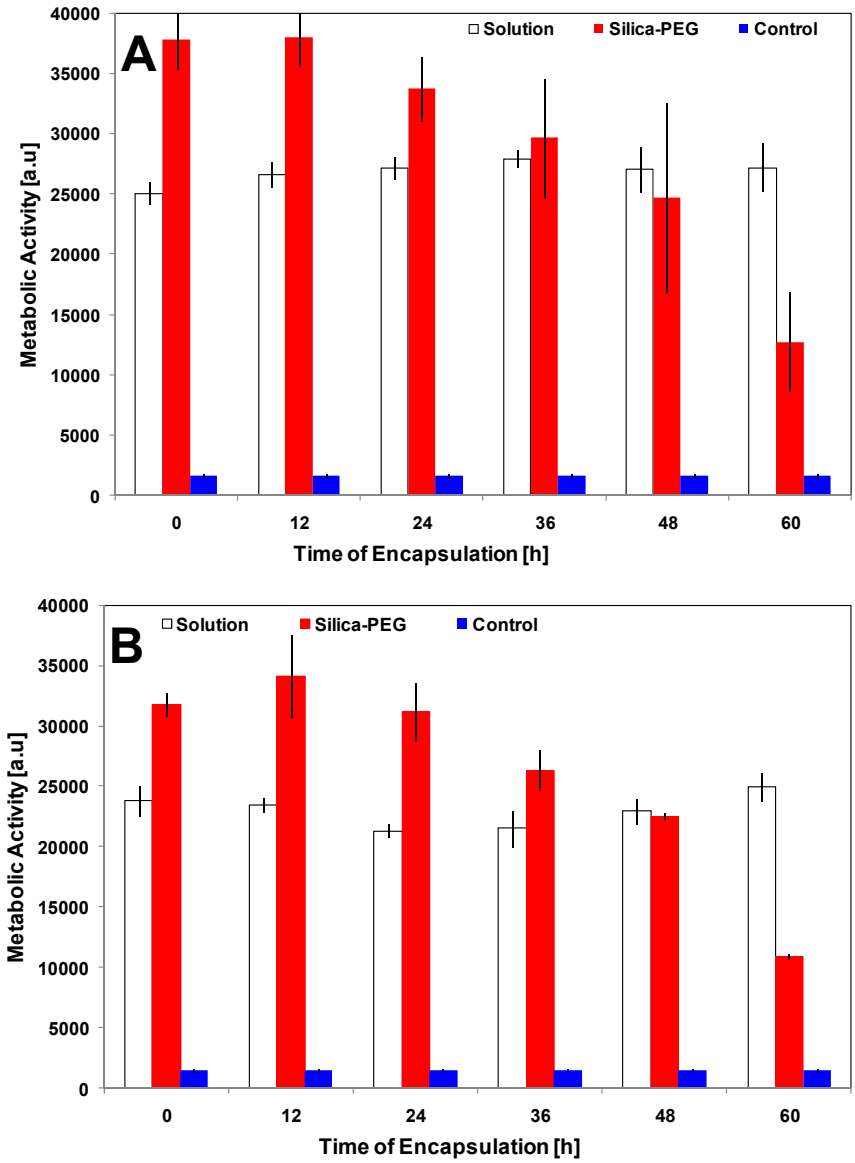

Figure 5.11 Metabolic activity of encapsulated irradiated cells: (A) HFF and (B) MEF. Negative controls (blue) were prepared by encapsulating dead HFF and MEF cells, dead cells were prepared by incubation in 70% ethanol for 10 min, and then their membrane integrity was verified with fluorescence microscopy. Cells seeded and incubated at 37°C and 5 % CO_2 were used as the positive control (Solution).

In our studies with cells, we focused on compositions that did not cause phase separation. FTIR analysis of the 3740 cm^{-1} region of pure silica and SPEG gels indicated strong interactions of silanol groups of the silica surface with PEG though hydrogen

bonding between the ether oxygens of PEG and the silica surface. [27]. This reduced the interactions at the biointerface between the encapsulated cells and the silica gel surface that is shown to be detrimental (Fig. 5.7) [22, 316, 317]. Moreover, transesterification reactions between hydrolyzed alkoxides and PEG may also occur during gelation [300], therefore, covalent bonding between PEG and silica can also be expected. NMR spectroscopy and Differential Scanning Calorimetry (DSC) based studies showed these interactions [300]. However, we did not obtain direct evidence of covalent bonding between the silica and PEG through FTIR analysis.

5.4.1) Encapsulation of mammalian cells in pure silica gels

It is known that the morphology and surface of silica nanoparticles can affect cell membrane integrity by oxidative stress, cell membrane damage and by inducing possible cell apoptosis/necrosis [106, 110, 318]. It is possible that after the silica gel forms, encapsulated cells are exposed to a combination of these detrimental stresses and their MA decreased. Long-term viability of mammalian cells encapsulated in silica gels has not been extensively explored; most of the published studies have focused on measuring the viability of the encapsulated cells immediately after encapsulation [5, 6].

Using IR spectroscopy we determined the structural changes in cellular membranes after encapsulation by analyzing the peak position of the ν-CH_2 band (~ 2850 cm^{-1}). For cells in solution, the cellular membranes are in the liquid-crystalline phase, characterized by increased lipid head group spacing, increasing disorder in acyl chains and a decreased bilayer thickness [319]. When the silica precursors gel, there is an abrupt change in viscosity. This is reflected on the ν-CH_2 peak position as it shifts towards

lower wavenumbers (~ 2844 cm^{-1}). The decrease in the ν-CH_2 wavenumber reflects an increased packing of the membrane lipids, indicating a transition of the encapsulated cell membranes into a gel phase. The gel phase of the lipid membrane is characterized by a decrease in lipid head group spacing and decreased membrane permeability [320]. In the short term, increased packing of the encapsulated cell membranes did not have a significant effect on membrane integrity as indicated by fluorescent measurements (Fig. 5.12).

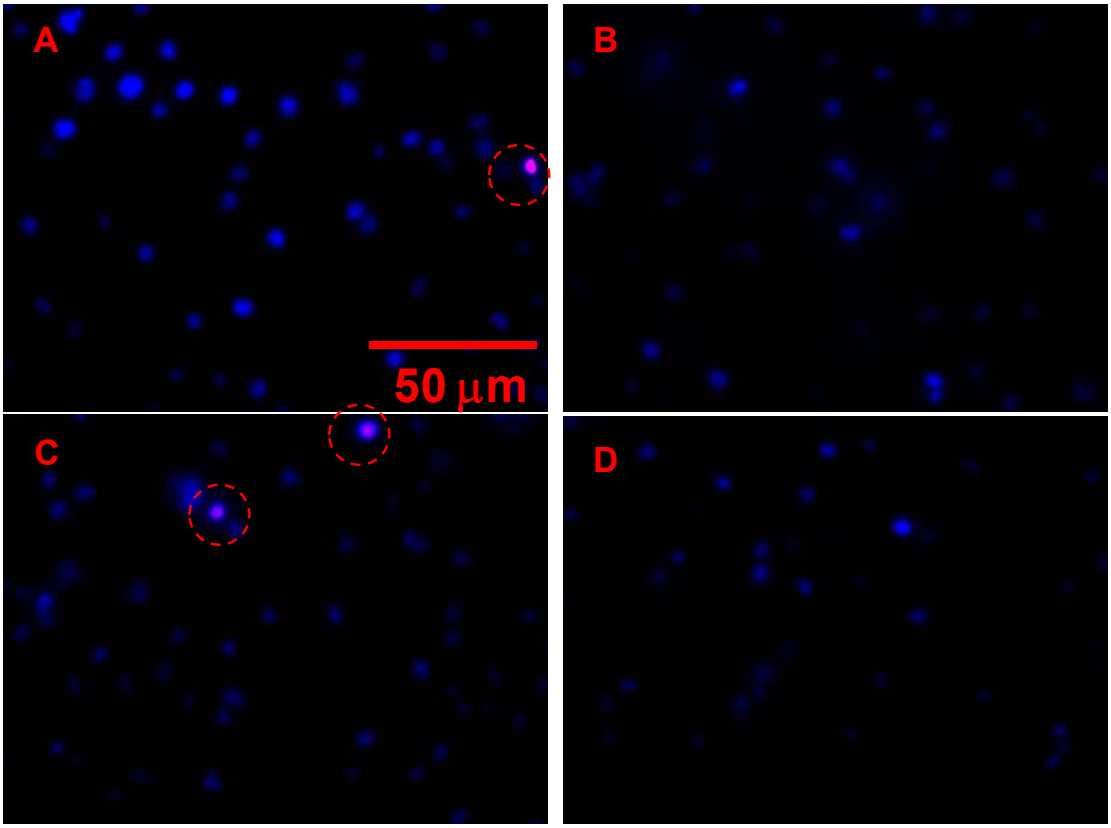

Figure 5.12 Fluorescence microscopy micrographs of encapsulated cells. Images were collected after encapsulation. Gels were prepared with 10 % (v/v) THEOS. (A) and (C) HFF and MEF cells in pure silica gel, respectively. (B) and (D) HFF and MEF cells in 10 % SPEG-4-arm gel, respectively.

The stress of encapsulation in silica gels can result in change in membrane permeability. This effect has been investigated for encapsulated bacteria [67]. For mammalian cells, we found that even though there was a change in the fluidity of the cellular membranes (i.e., drop of ν-CH_2 peak position), cells stayed metabolically active after encapsulation (Fig. 5.7). Therefore, it is possible that encapsulation induced further changes in the already altered cellular membranes. It has been hypothesized that hydrogen bonding interactions between silanol surface sites (-SiOH) and the negatively charged lipid head groups (e.g., $-PO_4^-$) or the negatively charged membrane proteins result in conformational changes in the lipid membranes, leading to their disruption [321]. There were two important findings in our results that supported this hypothesis: (1) there was a shift in ν-CH_2 peak position by 1.1 and 1.3 cm^{-1} for encapsulated HFF and MEF cells, respectively after encapsulation, and (2) LDH released into the surrounding media indicates excessive increase in permeability of the membranes.

Rigidity of the silica matrix mechanically constrains the encapsulated cells, and as a result, cellular division and growth are inhibited [322]. It has been shown that only certain types of bacterial and plant cells are able to perform cellular division after silica encapsulation [77, 92]. Our observations of encapsulated cells overtime showed that cells wanted to increase their size towards the rigid matrix in their intention to complete cellular division. Thus, a damaged cellular membrane of the encapsulated cells was not only caused by the silica surface interactions but also by the intrinsic cellular behavior. We further corroborated this hypothesis in our experiments with encapsulated cells where cellular division was arrested by irradiation. Within the first 12 h the irradiated cells

showed increased MA when compared to the normal cells (Fig. 5.7). These results show the presence of multiple factors that affect long term viability for encapsulated cells.

5.4.2) Encapsulation of mammalian cells in SPEG gels

There is a significant improvement in viability and MA of encapsulated prokaryotic and eukaryotic cells when a biocompatible-polymer interface between the cells and the silica surface is constructed [4, 8, 21, 22]. Recently, encapsulation of mammalian cells in SNP's surface functionalized with lysine groups at their surfaces has been reported [5]. Moreover, the encapsulation of clusters of cells in hydrolyzed alkoxides has been shown [6]. However, these studies did not measure the viability and MA of the encapsulated cells over time. In this study, the non-specific interactions between the cellular membranes and the silica surface were mediated by the incorporation of PEG (SPEG gels), and the effect in the membrane structure and MA of encapsulated cells were monitored.

5.5) Conclusion

We report the use of tetrakis (2-hydroxyethyl) orthosilicate (THEOS), a water soluble alkoxide, for the encapsulation of mammalian cells. This precursor allowed polymerization of silica at pH 7.4 using the cell culture media as a solvent. We were able to obtain silica monoliths for alkoxide concentrations as low as 10 % (v/v). The cytotoxicity of EG was tested using membrane integrity and MA assays, which indicated that the majority of the cells survive the encapsulation process. Cells were also

encapsulated in silica gels synthesized from TMOS to show that the detrimental effects in the viability and MA were independent of the silica precursor used.

We have explored different factors that affect the long time survival of the cells encapsulated in silica gels made up of THEOS and TMOS precursors. Silica nanoparticles were used as nucleation seeds during condensation of the alkoxides.

We showed that interactions at the biointerface, specifically between the membrane lipid head groups and the surface silanols are detrimental to the encapsulated cells. We have introduced a biopolymer (PEG) at different conformations (e.g., linear chain, non-linear chain), concentrations and observed that PEG interacts with the surface silanols and protect the encapsulated cells. Moreover, PEG could also be used to adjust the porosity of the gel, such that porosity increased with increasing PEG concentration in the silica gel even though it did not have a special effect on the structure of the gel. The gel ultrastructure was an agglomeration of SNPs. However, PEG should be used in the gel with care since at certain concentrations, it phase separates forming a heterogeneous gel.

We have also explored the effect of compressive stresses on the encapsulated cells. One source of mechanical stress is identified as the aging of the gel, which also causes dehydration of the encapsulated cells. Presence of PEG in the gel eliminates aging-related problems. The other source of compressive mechanical stress formation is the proliferation-driven cell division. The silica matrix imparts very limited mobility to the encapsulated cells since it is very stiff. Therefore, we hypothesized that removing the drive for cellular division would decrease the compressive stress buildup and would

therefore serve to increase the survival of encapsulated cells. When irradiated and encapsulated mammalian cells indeed survived for a long period of time. What we have not considered, in this experiment, however is the other potential biological effects of irradiation that may cause the cells survive adverse conditions.

Chapter 6: Development of Thixotropic Silica Gels for Reversible Encapsulation of Cancer Cells[5]

6.1) Summary

In the previous chapters, silica precursors (e.g., silica alkoxides, silica nanoparticles), organic macromolecules and polymers were described for the production of a porous gel. We considered these porous gels irreversible since after gelation, they formed a stiff and sturdy monolith structure encapsulating cells or macromolecules. One of the objectives of this chapter was to investigate induction of thixotropic behavior in silica gels. Thixotropy is the property of certain gels that are viscous under normal conditions, but become less viscous over time when shaken, agitated, or stressed [323]. Therefore, it was possible to achieve a thixotropic behavior of silica gels by modifying certain steps of gel synthesis and by using different organic polymer components.

A thixotropic gel (reversible gel) structurally consisted of micrometer size particles rich in hydrogen bonding sites thanks to silanol and hydroxyl groups on their surface (Fig. 6.1). The advantage of the thixotropic silica gels was that, they allowed the recovery of the encapsulated cells on demand. Therefore, our experiments demonstrated that novel applications for three dimensional cell culture, reversible cell encapsulation, drug delivery systems, and preservation of cells could be developed.

In this chapter, the encapsulation of cancer cells and normal cell lines in SPEG-4-arm and reversible silica gels was investigated. Our results showed a differential response

[5] This chapter is part of a publication that is currently under preparation.

in the metabolic activity (MA) of encapsulated cancer and normal cell lines. While normal cells maintained MA for up to 3 days, cancer cell lines were able to maintain MA for up to 1 week. This surprising result had drawn the investigation of using SPEG-4arm and reversible gels for the development of a screening cancer cell tool from tumors.

6.2) Materials and methods

Tetraethyl orthosilicate (TEOS), sodium silicate (27 weight % SiO_2, 10 weight % NaOH), and silica nanoparticles in powder (Cab-O-Sil, grade M5) were purchased from Sigma (St. Louis, MO). Nanoparticles were used to increase hydrogen bonding between the microparticles of the gel. Different precursors were used to form hybrid composites with tunable characteristics: Multi-arm PEG (M_w = 2 kDa), linear PEG (M_w = 10 or 20 kDa), dextran (M_w = 40 or 100 kDa), and trehalose (Mw = 378.33 Da).

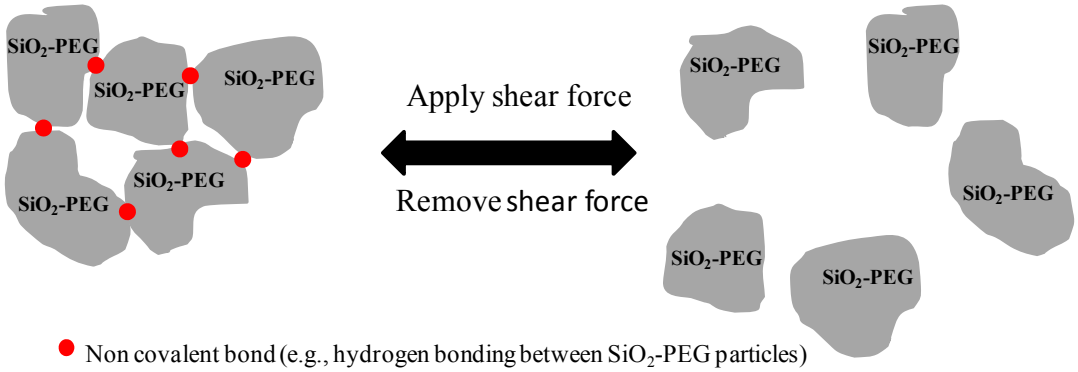

Figure 6.1 Schematic representation of a thixotropic transition. PEG can be replaced with any polymer capable of forming hydrogen bonds with SiO_2.

6.2.1) Thixotropic gel synthesis

The biomaterial synthesis was based on a modified version of the protocol developed for Pek et al. [105]. To make thixotropic gels, the alkoxide precursor (e.g., TEOS) was hydrolyzed at a volume ratio of 1:9, 1:7, and 1:4.5 alkoxide:water in the presence of an acid (e.g., acetic acid) as a catalyst for the alkoxide hydrolysis. Separately, 4-arm PEG (M_w = 2 kDa) was mixed with silica nanoparticles (e.g., 0, 5, 10 15 % w/w). Later, the pre-hydrolyzed alkoxide and the PEG solutions were mixed by vortexing for 5 min. The volume ratios of alkoxide:PEG should be kept at 1 or below to avoid precipitation or phase separation of the material. The final pH of the solution was adjusted to 7. The material was left to gel for 48 h at ambient temperature until a solid monolith was formed. Water was then added on the monolith and the material was gently grinded with pipeting to form micrometer size particles. The particle suspension was then centrifuged at 1500 RPM for about 5 min in order to remove the excess water added during the grinding step. The precipitate present was aggregates of micrometer size that form the thixotropic gel. In other formulations, trehalose was used instead of PEG (Table 6.1).

When sodium silicate was used as the silica precursor, 1.2 g of dextran (M_w = 40 or 100 kDa) was first mixed with 3.7 ml of 2 M acetic acid and 3.7 ml of water. Later, 500 mg of silica nanoparticles were added to the solution. The solution was stirred for 30 min. A solution of sodium silicate (e.g., 1.5, 2, 2.5, 3, or 3.5 M) was added dropwise while stirring. The mixture was then transferred into a convection oven at 37°C for 24 h. The resultant material did not need grinding since it did not form a monolith but a slurry

opaque solution was formed. The resultant mixture was centrifuged at 1500 RPM for 5 min to remove the excess water. In certain formulations, dextran was replaced with PEG (M_w = 10 or 20 kDa) (Table 6.2).

6.2.2) Characterization of the thixotropic gels

A large variety of thixotropic materials were generated in this research.. However, we have limited characterization to selected samples based on applications for cell encapsulation. Selected gels shown in Tables 6.1 and 6.2 were characterized using Scanning Electron Microscopy (SEM) and rheometry. Sample preparation for SEM analysis was described in the previous chapters. Sweep strain tests were conducted to determine the linear viscoelastic regime of the gels. Also, sweep stress tests were conducted to determine the apparent yield point stress (transition from the gel to the liquid state). Moreover, the values of the storage modulus were used for comparison of the stiffness of the different reversible gels produced. The measurements were done with an Ares AG2 Rheometer from TA Instruments (North Castle, DE). The tests were performed using a conical plate of 40 mm of diameter 2° steel cone at a truncation gap distance of 49 μm, as indicated in Fig. 6.2. All the measurements were conducted at 25°C.

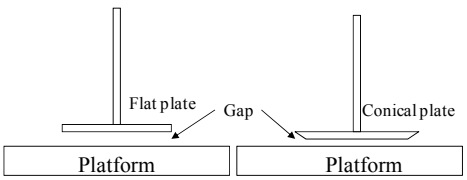

Figure 6.2 Schematic representation of the rheometer set up for different type of measurements.

6.2.3) Cell culture and encapsulation

Cell culture protocols used for human (HFF) and mouse embryonic fibroblasts (MEF) were described in the previous chapters. Human umbilical vein endothelial cells (HUVEC), were obtained from ATCC. HUVEC were cultured in F-12K growth medium containing 10 % FBS and supplemented with 0.1 g/ml of heparin and 0.05 mg/ml of endothelial cell growth supplement (ECGS).

The cancer cell lines were cultured as follows: Ovarian cancer cells (OVAR-5) were obtained from Dr. Amy Skubitz from the Laboratory Medicine and Pathology Department at the University of Minnesota. OVCAR-5 cells were cultured in RPMI-1640 growth medium supplemented with 10 % fetal bovine serum (FBS). Breast adenocarcinoma cells (MCF-7) were obtained from ATCC (Manasas, VA). MCF-7 cells were cultured in minimum Eagle's medium (MEM) supplemented with 10 % FBS, and 0.01 g/ml bovine insulin. The cell culture protocol for LNCaP cells was described in Chapter 2. All growth medium for the different cell lines were supplemented with 5 % Penicillin/Streptomycin.

For reversible cell encapsulation, HFFs or MEFs were suspended in their own growth media at a concentration of 4500 cells/μl. The thixotropic gel was vortexed to transition into a liquid state, and then the cell suspension was added (for gel compositions used see Table 6.1). In a typical experiment 200 μl of the gel was liquefied ("sol") by vortexing for 60 s. To the liquid "sol" 40 μl of the cell suspension was added. The cells were gently distributed in the reforming gel by pipeting in the sol. Gelation (or regelation) was complete within minutes. After gelation, culture media was added on the

gel. To extract the cells from the gel, excess volume of culture media was added to the gel (the volume ratio was 1:5 gel:media). Immediately, the suspension of the cells and the particles was filtered through a cell strainer. Most of the cells were captured in a petri-dish with cell culture media, while the particles remained in the cell strainer. Viability of the cells was measured after extraction from the gel using standard live/dead fluorescence dyes, as described in the previous chapters. The different cancer cell lines were encapsulated in the SPEG gels (encapsulation procedure described in Chapter 5), and in the reversible gels (see Table 6.3).

Table 6.1 Reversible gels produced using 4-arm, 2 kDa PEG and trehalose

Gel Name	Hydrolysis Ratio (v:v)	Alkoxide:PEG Ratio (v:v)	% SNP (w/w)
A1	1:9	0.60	0
A2	1:9	0.60	5
A3	1:9	0.60	10
A4	1:9	0.60	15
A5	1:7	0.60	0
A6	1:7	0.60	5
A7	1:7	0.60	10
A8	1:7	0.60	15
A9	1:4.5	0.60	0
A10	1:4.5	0.60	5
A11	1:4.5	0.60	10
A12	1:4.5	0.60	15

Gel Name	Hydrolysis Ratio (v:v)	Alkoxide:Trehalose (v:v)	% SNP (w/w)
B1	1:9	0.60	2.5
B2	1:10	0.60	3
B3	1:11	0.60	5

The catalyst was 0.15 M acetic acid

Table 6.2 Reversible gels produced using linear organic polymers

	Organic Precursor					Inorganic Precursor				Additive	
	Polymer	Size [kDa]	% Weight	Volume [ml]	Concentration [M	Precursor	Volume [ml]	Concentration [M]	Solvent [ml]	Type	% Weight
D1	Dextran	35-45	7.7	3.7	2	Sodium silicate	1.85	1.5	8.85	SNP	3.1
D2	Dextran	35-45	7.7	3.7	2	Sodium silicate	1.85	2	8.85	SNP	3.1
D3	Dextran	35-45	7.7	3.7	2	Sodium silicate	1.85	2.5	8.85	SNP	3.1
D4	Dextran	35-45	7.7	3.7	2	Sodium silicate	1.85	3	8.85	SNP	3.1
D5	Dextran	35-45	7.7	3.7	2	Sodium silicate	1.85	3.5	8.85	SNP	3.1
D6	Dextran	35-45	7.7	3.7	2	Sodium silicate	1.85	4.5	8.85	SNP	3.1
D7	Dextran	100	7.7	3.7	2	Sodium silicate	1.85	1.5	8.85	SNP	3.1
D8	Dextran	100	7.7	3.7	2	Sodium silicate	1.85	2	8.85	SNP	3.1
D9	Dextran	100	7.7	3.7	2	Sodium silicate	1.85	2.5	8.85	SNP	3.1
D10	Dextran	100	7.7	3.7	2	Sodium silicate	1.85	3	8.85	SNP	3.1
D11	Dextran	100	7.7	3.7	2	Sodium silicate	1.85	3.5	8.85	SNP	3.1
D12	Dextran	100	7.7	3.7	2	Sodium silicate	1.85	4.5	8.85	SNP	3.1
P1	PEG	20	7.7	3.7	2	Sodium silicate	1.85	5.73	8.85	SNP	2.5
P2	PEG	20	7.7	3.7	2	Sodium silicate	1.85	5.73	8.85	SNP	4.9
P3	PEG	10	5.1	2.5	0.01	TMOS	1.25	-	-	SNP	0.0
P4	PEG	10	5.1	2.5	0.01	TMOS	1.25	-	-	SNP	0.5
P5	PEG	10	5.1	2.5	0.01	TMOS	1.25	-	-	SNP	1.5
P6	PEG	10	5.1	2.5	0.01	TMOS	1.25	-	-	SNP	2.5

6.3) Results and discussion

Thixotropic biomaterials are “smart hydrogels” due to their responsiveness to external stimuli and they are very good candidates to be used for novel biomedical applications [324]. In this study we have developed thixotropic biomaterials for the encapsulation of cells. The thixotropic gel mainly consisted of a silica precursor and an organic polymer. The gelation process was due to the aggregation of micrometer sized particles, or spheres by inter-particle hydrogen bonding (Fig 6.1). When sodium silicate was used as a silica precursor along with linear PEG (M_w = 10 or 20 kDa), the particulate material that formed consisted of aggregation of sphere-like clusters of particles as indicated in Fig. 6.3A. This gel required minimal grinding. On the other hand, when an alkoxide precursor such as TEOS along with 4-arm PEG or sodium silicate with dextran was used, a one piece monolith was obtained. The monolith required extensive grinding to form small particles. Fig. 6.3B shows the heterogeneous sizes and shapes of the particles produced from these gels. All the gels formed from sphere-like aggregates

exhibited limited thixotropicity when compared to the gels formed with heterogeneous aggregates.

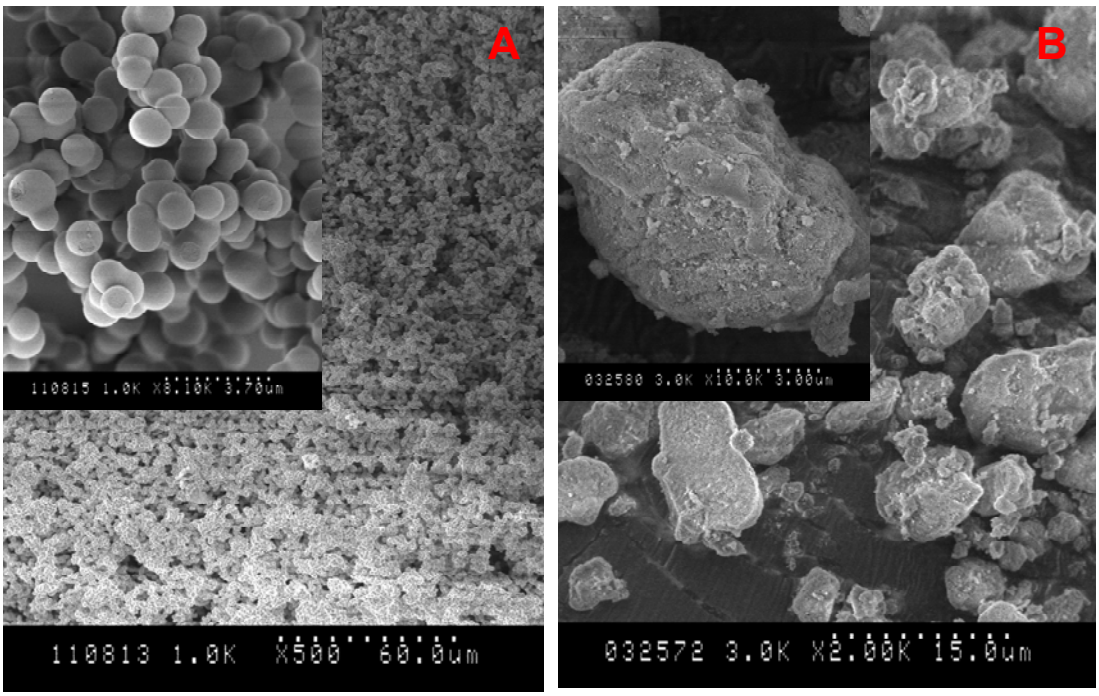

Figure 6.3 SEM images of gels: (A) Formed of sphere-like particle aggregates (A1), (B) Formed by heterogeneous particles (D1).

6.3.1) Rheology of the thixotropic gels

Viscoelastic characteristics of the thixotropic gel depended strongly on the type and concentration of the precursors in the final mixture [325]. Fig 6.4 shows the typical response of a thixotropic silica-dextran gel when an oscillatory shear stress is applied.

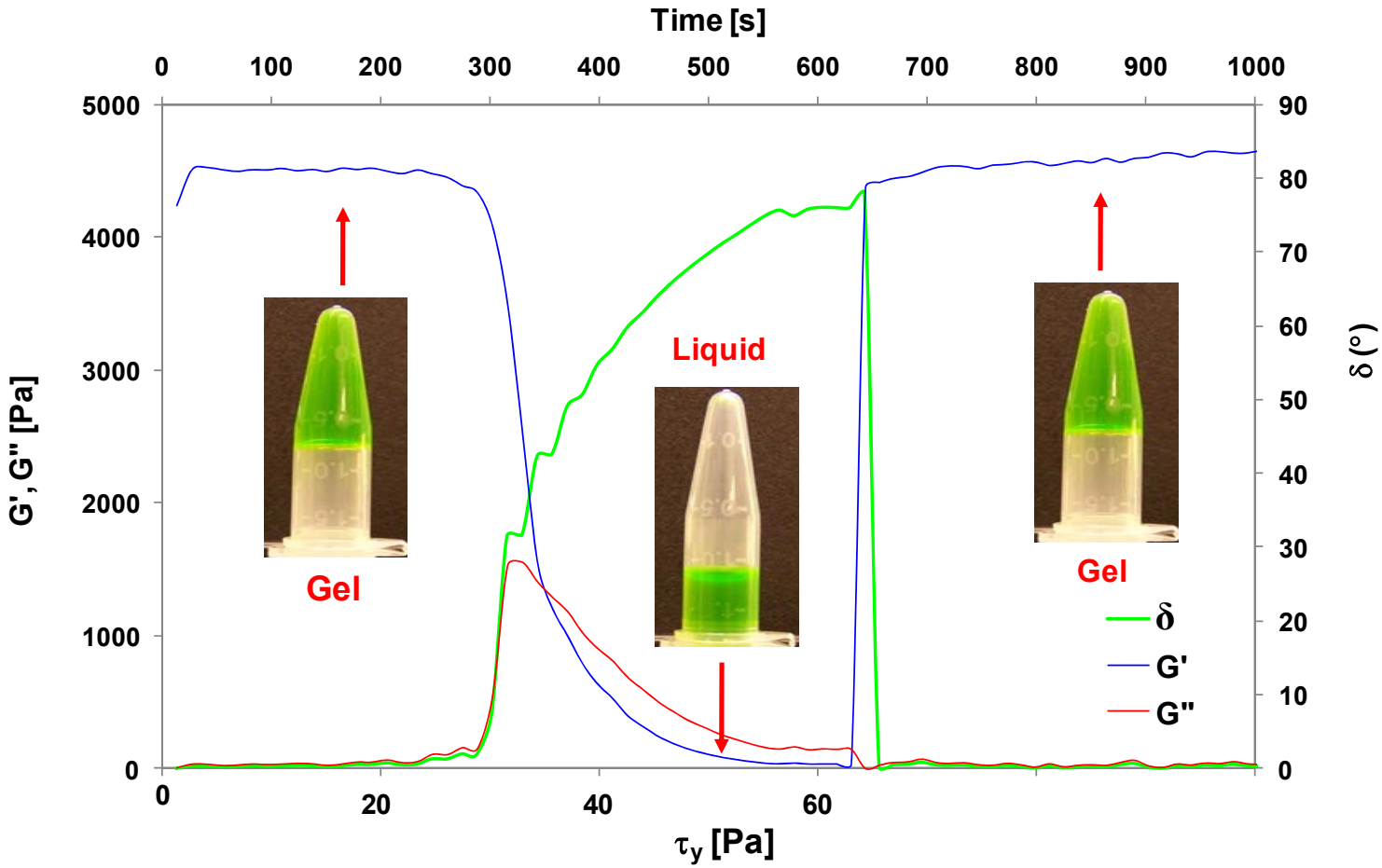

Fig 6.4 Typical response of a thixotropic silica gel. The gel shown here is D2 from Table 6.2.

Fig. 6.4 shows the transition of the storage modulus G' (elastic component), the loss modulus G" (viscous component) and δ (phase angle between G' and G") [326, 327]. An increase in G' is an indicator that a three dimensional network is formed by the aggregation of the colloidal particles and their hydrogen bonding [328]. The reduction in G' reflects a decrease in the hydrogen bonding interactions between particles that form the gel network structure [329]. Fig. 6.3 also shows the time evolution of G', G", and δ when a shear stress was applied. The apparent yield point stress was obtained by stress sweep experiments. In the gel state, G' was larger than G" and δ was lower than 45°. The gel starts to be liquefied when G'= G". In the liquid state, G' is less than G" while δ is larger than 45°. The stress value at which the gel transitions into a liquid is known as the yield point stress [330, 331].

The incorporation of cells into the reversible gels reduced their strength. Some gels were weakened to such an extent that they were not able to maintain their integrity after the addition of cell culture media. Therefore, Cab-O-Sil, a thickening and thixotropic agent, was added to the formula. Incorporation of different weight ratios of Cab-O-Sil increased the plateau value of the G' and shifted the apparent yield point stress to higher values (Fig. 6.5). For gels that contained dextran or PEG (M_w = 10 or 20 kDa) changing Cab-O-Sil concentrations produced precipitation of the sodium silicate. Therefore, a maximum amount of 800 mg of Cab-O-sil was used. In these gels, the concentration of the silica precursor was varied to change the plateau value of G' (Fig. 6.6). In general thixotropic gels made with dextran gels were stiffer than the gels made with 4-arm PEG. Dextran gels allowed the incorporation of up to 50 % of water respect to gel volume,

while 4-arm PEG only allowed up to 20 %. However, stiffness of the gels was not the only consideration. Even though the dextran gels were stiffer, they were not used for the encapsulation of mammalian cells since presence of excess Na^+ induced osmotic stress on the cells damaging and killing them.

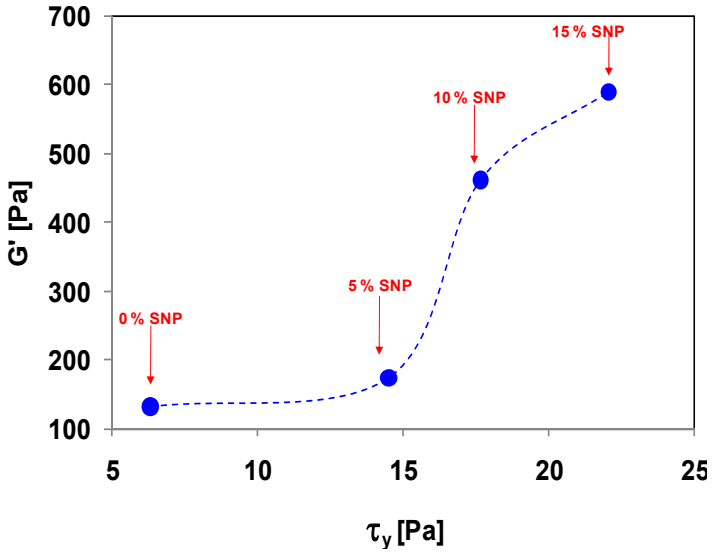

Figure 6.5 Effect of Cab-O-Sil concentration on the plateau value of G'. Gels A1 to A4 from Table 6.1 were used.

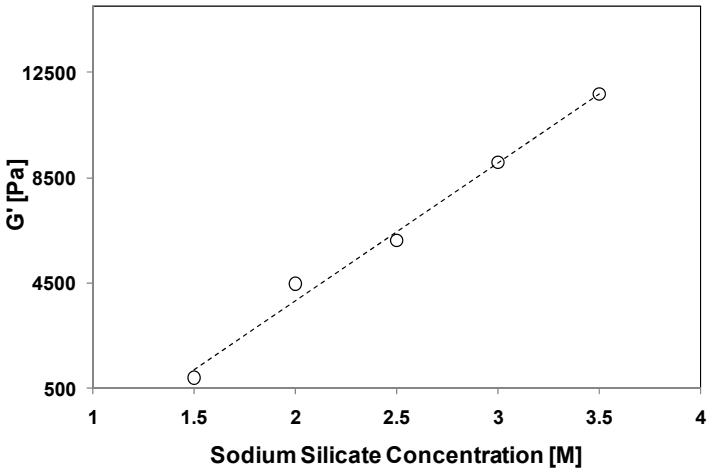

Figure 6.6 Effect of sodium silicate concentration on the plateau value of G'. Gels D1 to D5 from Table 6.2 were used.

6.3.2) Reversible encapsulation of mammalian cells

HFF cells were encapsulated in an A3 gel following the procedures described in the previous section. After gelation, 150 μl of media was added on top of the encapsulated cells (Fig. 6.7A). The thickness of the gel in the test tube was approximately 10 mm. The gels were stable in cell culture media. Encapsulated cells were incubated at 37°C and 5 % CO_2. The cells were extracted at different time points following the procedure described in the previous section. The gel was gently pipeted to disassemble the gel and to release the cells. A cell strainer was used to filter the cells out of the solution that contained the gel particles. The strained cells were collected in a petri dish in the presence of excess media (Fig. 6.7B). Post extraction membrane integrity of the cells was assayed with fluorescence microscopy (see Chapter 5 for details). The results indicated that during the first 90 min the membrane integrity remained within 93 ± 2 % of the control value measured with cells in suspension (Fig. 6.7C). However, within 210 - 270 min of encapsulation the membrane integrity dropped to approximately 60 ± 3.5 %.

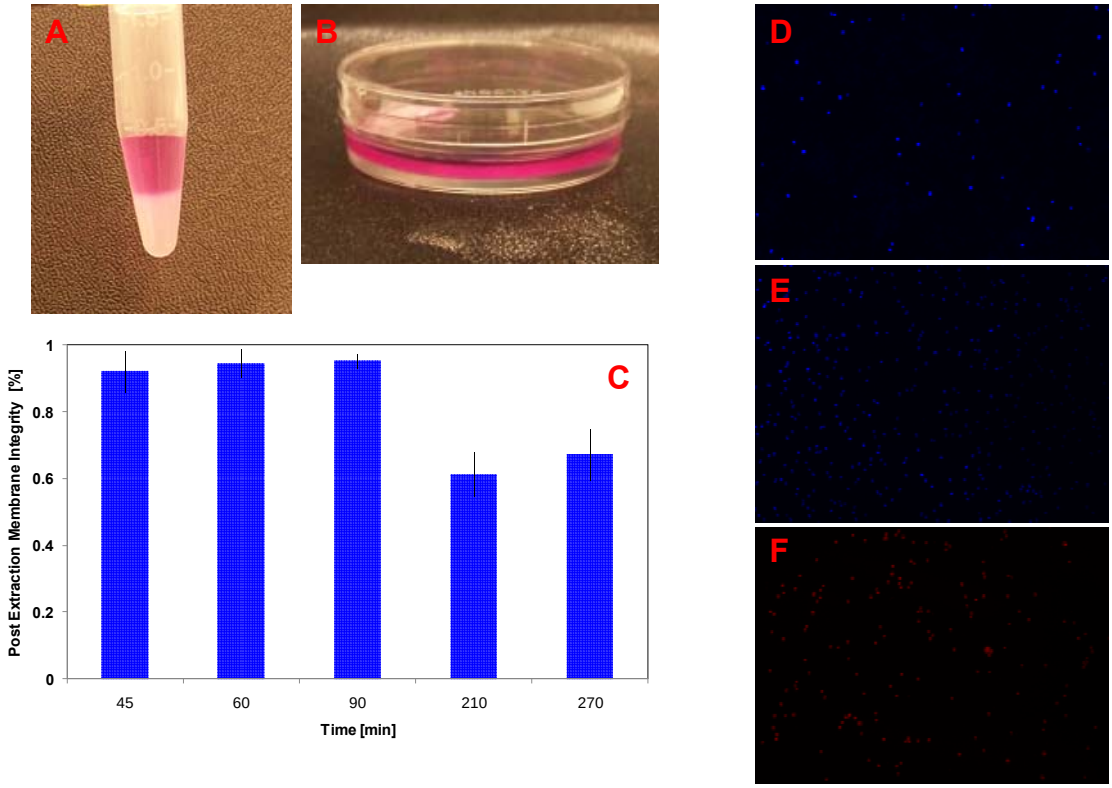

Figure 6.7 Reversible encapsulation of HFFs. (A) encapsulated cells in gel with culture media on top, (B) cells released from gel, (C) membrane integrity of the extracted cells at different time points as measured by fluorescence microscopy, (D) fluorescence image of extracted cells at 45 min, (E) fluorescence image of control cells (intact membrane), (F) fluorescence image of negative control cells (damaged membrane). All samples were stained with Hoescht and PI.

6.3.3) Encapsulation of cancer cells in silica-PEG (SPEG) gels

Different types of cancer cell lines were encapsulated in SPEG-4arm gels (M_w = 2k Da). We discovered that there was a differential response in the metabolic activity (MA) of cancer cells with respect to normal cells when they were encapsulated in these gels. Therefore, these results indicated that it would be possible to utilize mechanical inhibition of proliferation to selectively enhance the survival of cancer cells in a tissue-like environment.

Our results shown that anchorage-dependent cancer cell lines adapted better to the conditions imposed by encapsulation, where cellular division was inhibited. LNCaP cells, MCF-7 cells, and OVCAR-5 cells stayed metabolically active for up to 2 weeks after encapsulation. Fig. 6.8A-C shows the MA of different encapsulated cancer cell lines. For encapsulated LNCaP cells, there was not a significant change in MA over a week. Encapsulated MCF-7 showed a drop of 12 % in MA with respect to first day of encapsulation. On the other hand, encapsulated OVCAR-5 maintained their MA for over 3 days, experiencing a significant drop at the 4 day. Normal cell lines (HFFs, HUVEC, and MEFs) remained metabolically active for no more than 3 days (Fig. 6.9A-C). The difference in MA of the encapsulated cancer and normal cell lines was never reported before. Sustained activity in confinement was observed with bacteria before and was attributed to factors such as "quorum sensing" senescence, and inherent mechanisms of adaptation to the conditions of encapsulation [68, 87].

Further controls were also imposed on the experiments. For example, cells were killed after six days of encapsulation using a 70 % ethanol solution and their MA was compared to live encapsulated cells, and the results indicated a significant difference in MA measured in the live encapsulated and dead encapsulated cells proving the measurement/experimental technique ($p < 0.05$) as shown in Fig. 6.10.

6.3.4) Development of a cancer cell isolation platform

Tumors are considered as abnormal tissues composed of multiple cell types and an extracellular matrix [332]. In tumors, not only there are cancer cells of different phenotypes, but there are also normal cells (e.g., fibroblasts, myoblasts, endothelial cells,

epithetelial cells, and stromal cells). This makes isolating cancer cells from tumor specimens and biopsies an extremely time-consuming process since all cell types usually grow together in the culture environment. Therefore, researchers who work with isolated cancer cell lines need special isolation processes [333]. However, these processes are very intricate and time-consuming, requiring repetitive processing of the cells over time.

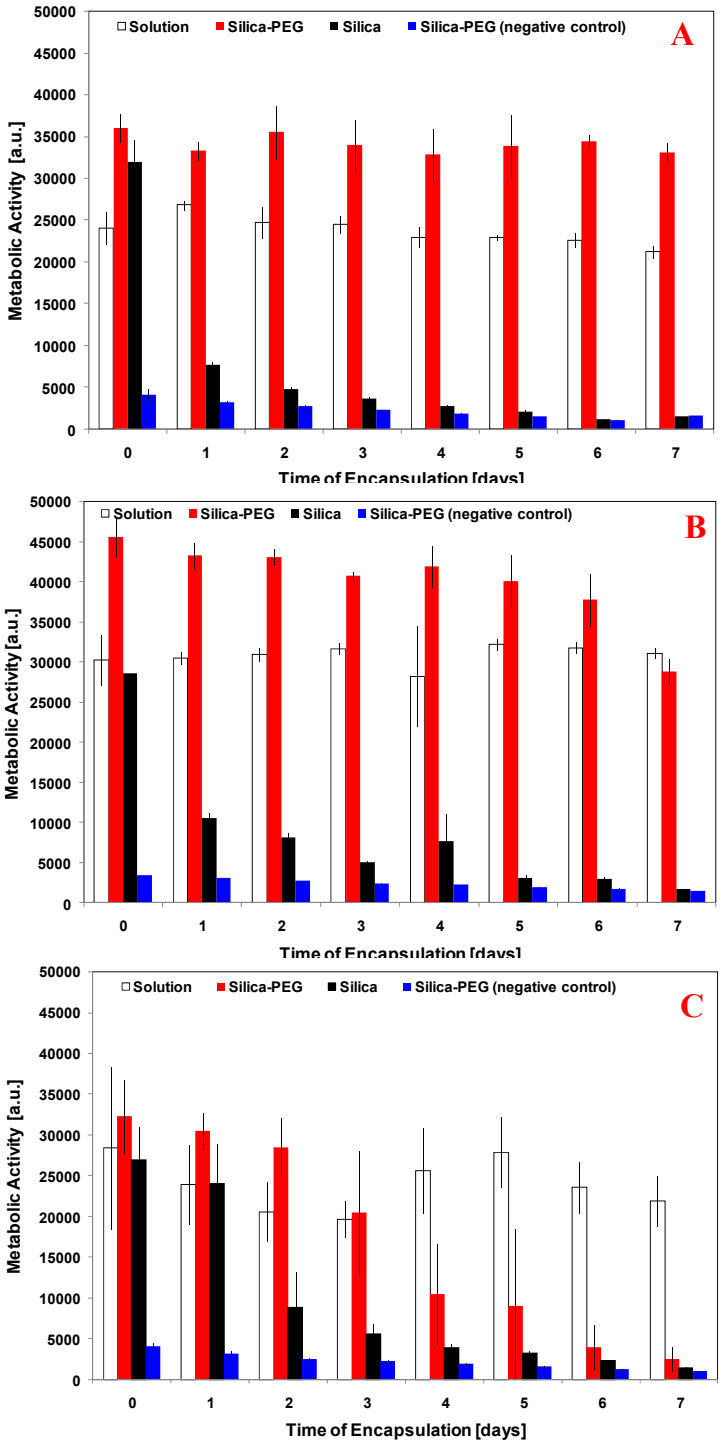

Figure 6.8 Cancer cell lines encapsulated in SPEG-4arm (M_w = 2kDa) gels. (A) LNCaP, (B) MCF-7, (C) OVCAR-5. Solution indicates cells incubated in culture media, and the negative control is encapsulated dead cells. These cells were exposed to 70 % ethanol prior to encapsulation (n = 3).

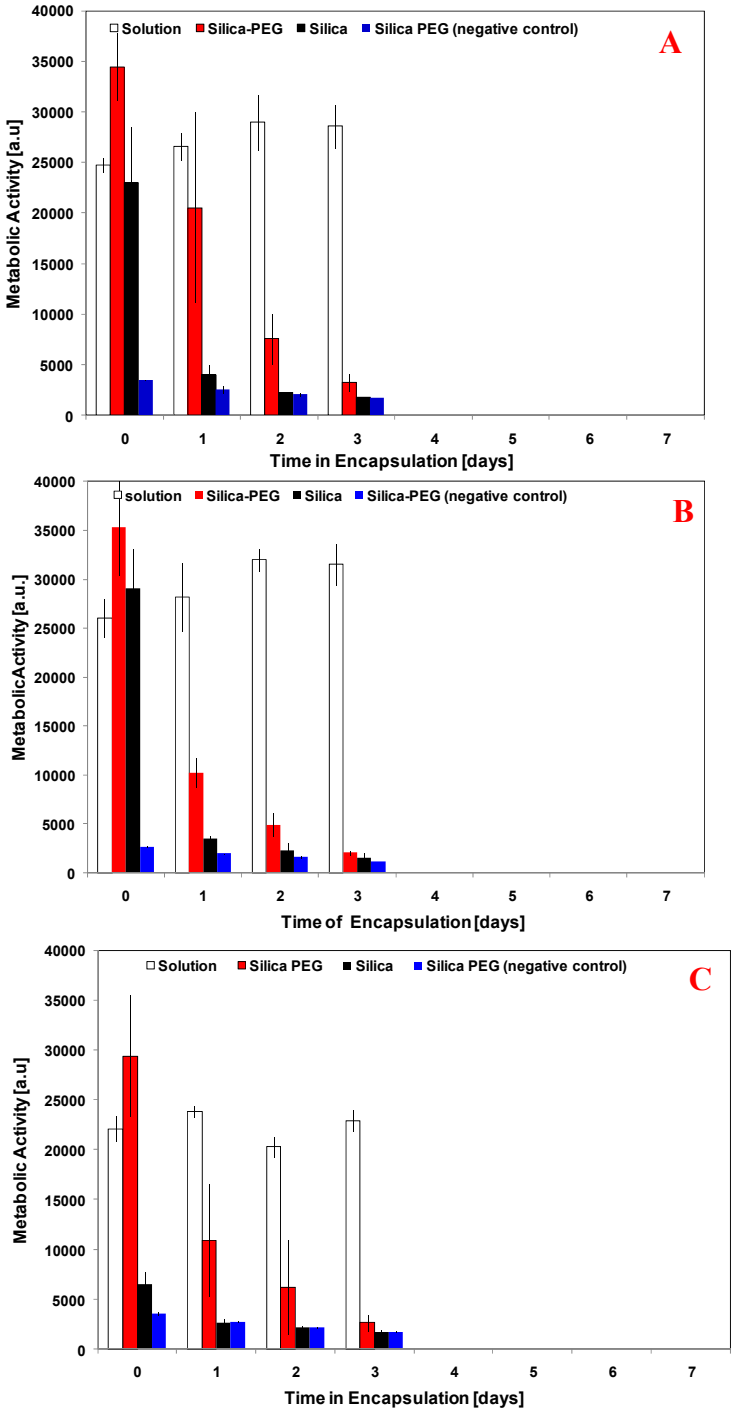

Figure 6.9 Normal cell lines encapsulated in SPEG-4arm (M_w = 2kDa) gel. (A) HFF, (B) HUVEC, (C) MEF. Solution indicates cells in culture media, and the negative control is encapsulated dead cells. These cells were exposed to 70 % ethanol prior to encapsulation (n =3).

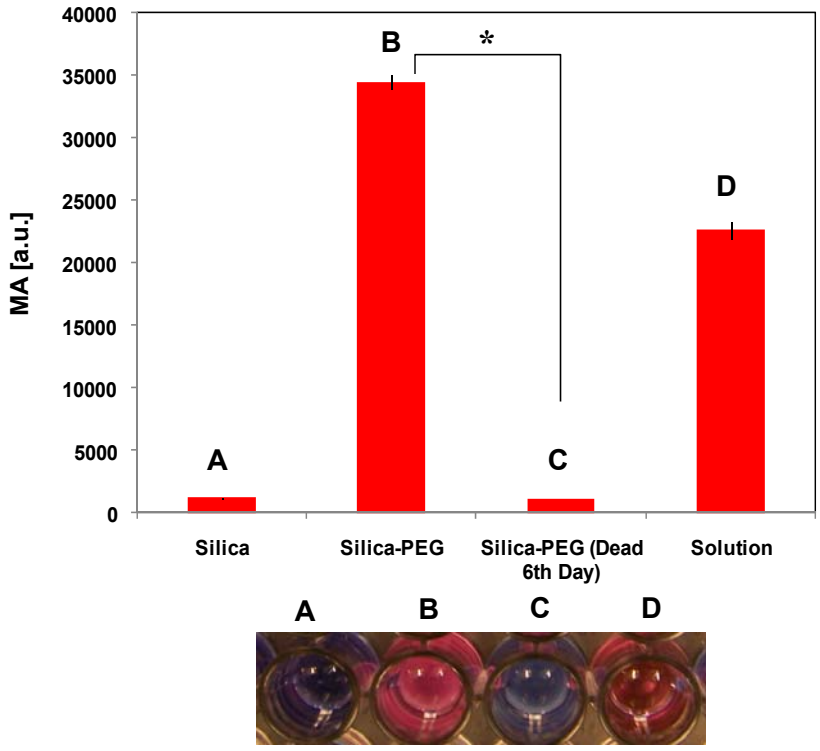

Figure 6.10 MA of encapsulated LNCaP cells after six days of encapsulation. The test well was prepared with the addition of 40 µl of ethanol and incubated for 12 h prior to the addition of alamar blue (n = 3).

Viable cancer cells from tumors are needed for functional and cytotoxicity studies with new cancer drugs. Moreover pure population of cancer cells are needed for genomic, proteomic, and metabolomics studies. There is also a need in the research community for new cell lines to be established from isolated cancer cells. This is a high priority especially for the types of cancers for which only a handful of cell lines are currently available (e.g., prostate cancer). Therefore, we explored the possibility of encapsulating a combination of cancer cells and normal cells in order to determine the potential of using SPEG gels as a screening tool for cancer cells in tumors.

Table 6.3 Encapsulation of mixed cell populations. (i) Extraction from SPEG gel, (p) extraction from reversible gels. Time refers to extraction time after encapsulation.

Cell mixed population	Encapsulated cell densities in millions [cells/ml]	Gel type	Time [h]
HFF (F) and OVCAR-5 (O)	18.3 (F):15.23 (O)	SPEG (i), (p)	24, 48
	2.3 (F):2.4 (O)		
HFF (F) and LNCaP (L)	22.8 (F):45.8 (L)	SPEG (i), (p)	24, 48
	4.4 (F):4.8 (L)		

Different cell densities of cancer and normal cells were mixed at 1/1 (v/v) ratio (Table 6.3). The mixed cell population was then encapsulated in the SPEG-4-arm gels described in the previous chapter. Cells were extracted from the gels 24 and 48 h after encapsulation. The extracted cells were incubated in 6-well plates at 37°C and 5 % CO_2 for different periods of time to measure proliferation activity. In order to verify that the gels could be used to select for the cancer cells, a specific cancer cell antibody (EPCAM/TROP1 antibody) than binds the epithelial cell adhesion molecule (EpCAM or CD326) present in the surface of the cells was used. EpCAM is a transmembrane glycoprotein that is identified as a marker for carcinoma, attributed to its high expression on rapidly proliferating tumors of epithelial origin [334]. Normal epithelia express EpCAM at a variable but generally lower level than carcinomas [334]. Cells recovered from the gels were stained with EPCAM/TROP1 antibody as a primary antibody. For detecting, a secondary antibody (Immunoglobulin G, IgG) conjugated with a fluorescence reporter was used for fluorescence microscopy visualization (see appendix section for immunohistochemistry protocol).

From HFF:OVCAR-5 and HFF:LNCaP mixed cell populations, only OVCAR-5 and LNCaP cells were recovered after encapsulation since the incubated cells stained positive for EpCAM as indicated in Fig. 6.11 and Fig. 6.12. However, very few fibroblasts were observed in some mixed populations extracted at 24 h, which was in agreement with our results on HFF encapsulation in SPEG-4-arm gels. Fig. 6.11A-C and Fig. 6.11B-D show OVCAR-5 cells stained after 26 and 22 days after extraction, respectively. Moreover, Fig. 6.12A-C and Fig6.16B-C show LNCaP cells stained after 7 and 6 days after extraction, respectively. It was observed that the rate of attachment and growth for the recovered cells was slower than the non-encapsulated OVCAR-5 or LNCaP cells. However the morphology of the cells was very similar under the optical microscope.

Even though the majority of the SPEG-gel particles were removed during the cell extraction process (e.g., filtering with a cell strainer), small particles remained within the cell surface as can be observed from the fluorescence micrographs as very bright red dots (yellow arrow in Fig. 6.11 and Fig. 6.12). It is possible that these particles might have interfered with the cell growth rate. Our results clearly show the selectivity of the SPEG or reversible gels for screening of cancer cells.

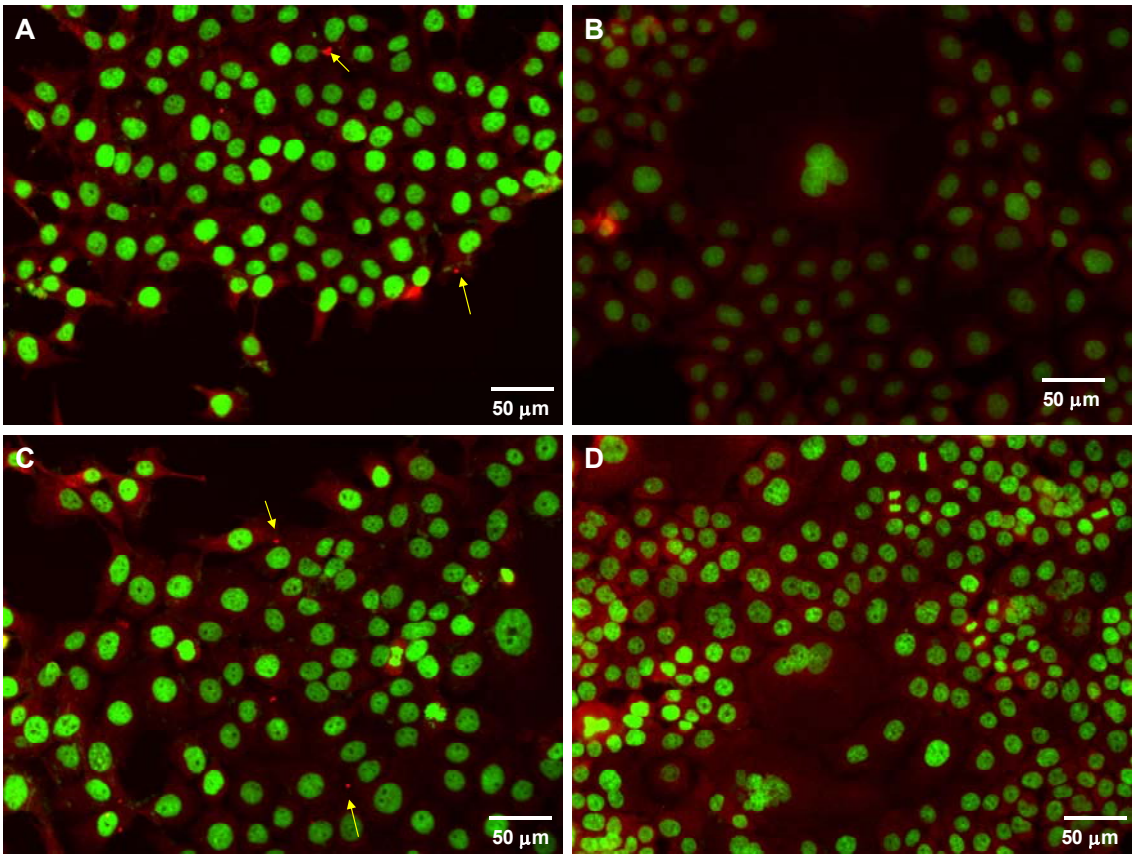

Figure 6.11 Recovered OVCAR-5 cells after encapsulation of HFF:OVCAR-5 mixed cell population. No Fibroblasts were not detected after 48 h post extraction. (A) Cells extracted from SPEG-4-arm gel after 24 h of encapsulation, (B) cells extracted from SPEG-4-arm gel after 48 h of encapsulation, (C) cells extracted from reversible gel after 24 h of encapsulation, and (D) cells extracted from reversible gel after 48 h of encapsulation.

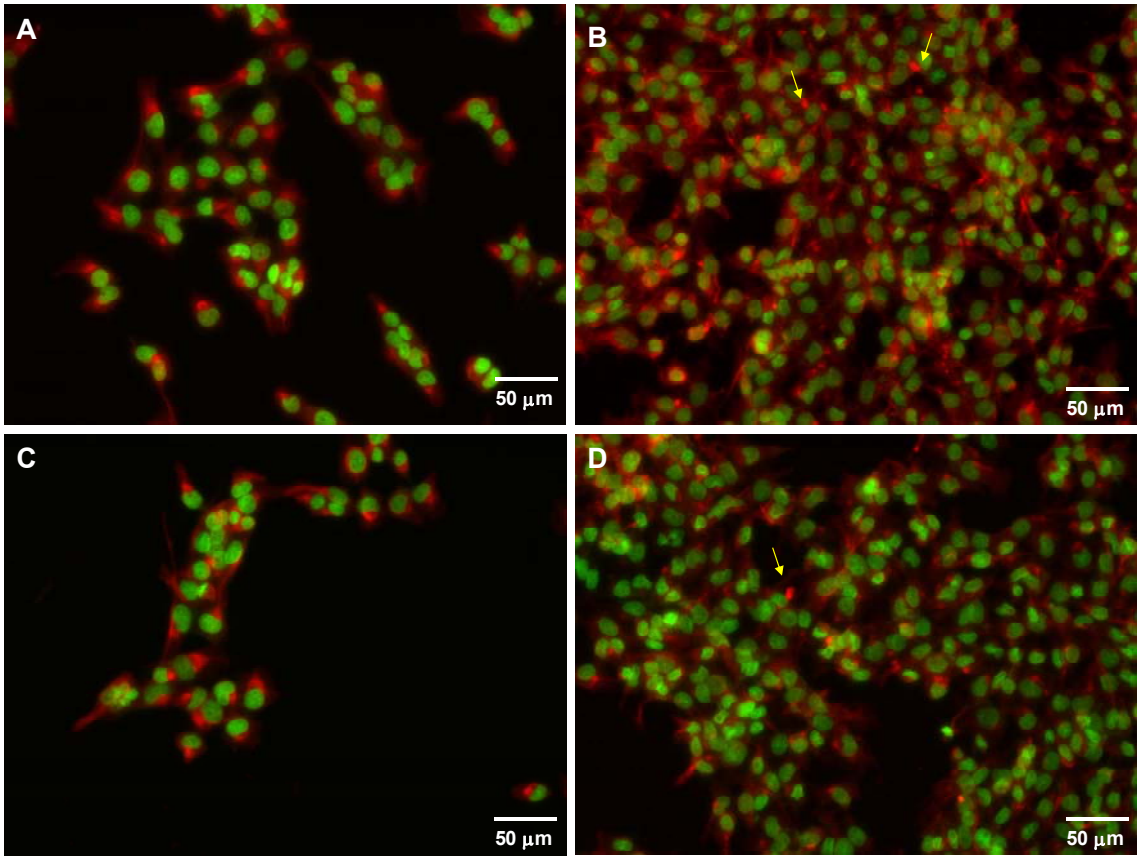

Figure 6.12 Recovered LNCaP cells after encapsulation a HFF:LNCaP mixed cell population. Fibroblasts were not detected at 48 h. (A) Cells extracted from SPEG-4arm gel after 24 h of encapsulation, (B) cells extracted from SPEG-4arm gel after 48 h of encapsulation, (C) cells extracted from SPEG-4arm particulated gel after 24 h of encapsulation, and (D) cells extracted from SPEG-4arm particulated gel after 48 h of encapsulation.

6.5) Conclusions

In this chapter we have shown the versatility of the silica gels to develop a wide range of applications. First we described a facile methodology for the formation of thixotropic silica gels or hybrid gels since an organic polymer was used as an additive, the resultant gel was formed by the aggregation of micrometer size particles that interacted to each other by hydrogen bonding. This unique characteristic of the gel allowed the formation of "reversible" biomaterials. Encapsulation of cells for cell culture,

and even a novel methodology for preservation of cells were described with the new materials developed.

In the second part of this chapter, we described the benefits of encapsulated cancer cells in the SPEG-4arm gels for the development of a screening biomaterial from tumor cells. The selectivity of the biomaterial was demonstrated by the analysis of the recovered cells.

Chapter 7: Research Summary

In this dissertation, studies were undertaken to investigate the changes in the structure of water and proteins under confinement in silica gel nanoporous materials. Moreover, the encapsulation of cells in silica gels was explored in order to understand the interactions at the silica-lipid membrane interface. Finally, the potential of the silica gel technology is described as different biotechnology and biomedical applications by using encapsulated cells. The important results and conclusions drawn from these studies are summarized as follows:

Confinement of water in silica gel induced structural changes in its hydrogen bonding configuration (Chapter 2)

Molecular motions and properties of water and biomacromolecules change when confined in nanoporous matrices. Freezing and melting points of water are depressed, and generally, the activity of enzymes and stability of proteins are increased. We performed temperature ramp FTIR analyses of silica matrix confined water to identify the kinetic and thermodynamic transitions of water at cryogenic temperatures, and to understand the changes in hydrogen bonding of confined water. In our studies, confined water did not freeze at temperatures as low as -180^{o}C, but underwent liquid-liquid, and liquid-glass transitions during cooling. During warming from cryogenic temperatures, the formations of cubic and hexagonal ice were detected. Evidence was obtained for the universal behavior of water in close proximity to surfaces.

Confined water dictates the structure of proteins (Chapter 3)

Confinement of the proteins in silica matrices allowed us to explore the role of water hydrogen bonding on the structures of the proteins in a broad range of temperatures (-120°C to 95°C). The changes in the secondary structures of proteins correlated to the changes in the H-bonding characteristics of the confined water. Our results showed that the kinetic and thermodynamic transitions of water dictate the structural transitions of encapsulated proteins. At low temperatures confinement suppressed freezing of water, which remained in the liquid state. We obtained direct evidence that the changes in the hydrogen bonding of water induced changes in the structure of confined proteins. At high temperatures, a reduction of hydrogen bonding of water facilitated protein-silica interactions and the confined proteins underwent denaturation. However, the incorporation of the osmolyte, trehalose, reduced protein-silica interactions, and altered the hydrogen bonding of water. As a result, the high temperature thermal stability of the confined proteins was greatly improved.

Silica gel encapsulation for bacteria: Contaminated water treatment (Chapter 4)

A biotechnology application based on the silica gel encapsulation of recombinant bacteria expressing a biocatalysis for a water treatment application was investigated. *E. coli* cells expressing the atrazine dechlorinating enzyme AtzA in a silica/polymer porous gel were used. This novel recombinant enzyme-based method utilizes both adsorption and degradation to remove atrazine from water. A combination of silica nanoparticles (Ludox TM40), alkoxides, and an organic polymer were used for the synthesis of the porous gel. Gel curing temperatures of 23°C or 45°C were used to either maintain cell

viability or to render the cells non-viable, respectively. The enzymatic activity of the encapsulated viable and non-viable cells was high and extremely stable over the time period analyzed. At room temperature, the encapsulated non-viable cells maintained a specific activity between (0.44 ± 0.06) μmol/g-min and (0.66 ± 0.12) μmol/g-min for up to 4 months, comparing well with free, viable cells specific activities (0.61 ± 0.04 μmol/g-min). Gels cured at 45°C had excellent structural rigidity and contained non-viable cells, making these gels potentially compatible with water treatment facility applications. When encapsulated, non-viable cells were assayed at 4°C, activity increased three fold over free cells, potentially due to differences in lipid membranes as shown by FTIR spectroscopy and electron microscopy.

Silica gel encapsulation for the immobilization of mammalian cells under non-growth conditions (Chapter 5)

Cells encapsulated in silica gels experienced significant conformational change in their lipid membranes during the gelation and aging of the nanoporous silica matrix. After encapsulation, the drastic change in the lipid configuration of the encapsulated cells was not reflected in their membrane integrity or metabolic activity (MA). Additional rearrangements of the lipid membranes due to aging of the silica matrix induced significant reduction of the viability and MA of the encapsulated cells.

Incorporation of a biocompatible polymer (PEG) at different M_w and sizes during the material synthesis (SPEG gels) reduced the non-specific surface interactions and allowed the encapsulated cells to maintain their MA. However, cellular division of the encapsulated cells was restricted under these conditions of encapsulation, and the cells

eventually lost their MA. Arresting cellular division of the encapsulated cells was explored by irradiating the cells prior to encapsulation and it was reflected as an improvement of the MA over time. Limiting surface interactions and changing the metabolism of the cells facilitated the adaptation of the cells to encapsulation under restrictive growing conditions.

Development of thixotropic silica gels for reversible encapsulation of cancer cells (Chapter 6)

A thixotropic silica gel was developed for the reversible encapsulation of cells; the material consisted on microparticles that assemble based on their ability to form hydrogen bonds. The gel transitioned into a liquid when a shear stress was applied, and the gel reformed when the shear load was removed. The thixotropic material was used for the reversible encapsulation of cells, in which the membrane integrity of the recovered cells was 93 % of their control after 90 min of encapsulation. SPEG-4-arm and reversible gels allowed the encapsulation of cancer cells with a notorious improvement in the MA when compared to normal cells (e.g., Fibroblasts, endothelial cells). Therefore it allowed the development of a novel screening tool for cancer cell biology when cancer and normal cells were encapsulated together.

Suggested Future Directions

Future work should be towards:

- Development of additional biotechnology applications using the sol-gel processing for the encapsulation of bacteria. Sequestration of CO_2 from encapsulated algae, production of H_2 from encapsulated cyanobacteria, and bioremediation of water and soils are very suitable and promising directions.

- The investigation of additional biocompatible polymers as potential additives to the silica matrix. Special attention should be for biopolymers present in the extracellular matrix of carcinogenic tumors in the case of cancer applications. In that regard, the ability of the material to tune their surface chemistry and mechanical properties can be used as a testing tool for mimicking different kinds of tumor environments in order to investigate cancer cell senescence, tumorogenesis and metastasis.
- Control of the surface interactions by the incorporation of adequate extracellular matrix motifs such as the tripeptide motif arginine-glycine-aspartate (RGD) in the gel surface (for mammalian cell encapsulation).

Chapter 8: References

1. Bathia, S.R., *Polyelectrolytes for cell encapsulation.* Current Opinion in Colloid and Interface Science, 2005. **10**: p. 45-51.
2. Nedovic, V. and R. Willaert, *Applications of Cell Immobilization Biotechnology*. Focus on Biotechnology. Vol. 8B. 2005: Springer.
3. Guisan, J.M., *Immobilization of Enzymes and Cells* Methods in Biotechnology, ed. J.M. Walker. 2006, Totowa, New Jersey: Humana Press.
4. Avnir, D., et al., *Recent bio-applications of sol-gel materials.* Journal of Materials Chemistry, 2006. **16**: p. 1013-1030.
5. Snyder, M.A., et al., *Benign, 3D encapsulation of sensitive mammalian cells in porous silica gels formed by Lys-Sil nanoparticles assembly.* Microporous and Mesoporous Materials, 2009. **118**: p. 387-395.
6. Nieto, A., et al., *Cell viability in a wet silica gel.* Acta Biomaterialia, 2009. **5**: p. 3478-3487.
7. Rooke, J.C., A. Léonard, and B.-L. Su, *Targeting photobioreactors: Immobilization of cyanobacteria within porous silica gel using biocompatible methods.* Journal of Materials Chemistry, 2008. **18**: p. 1333-1341.
8. Nassif, N., et al., *Living bacteria in silica gels.* Nature Materials, 2002. **1**: p. 42-44.
9. Ruiz-Hitzky, E., K. Ariga, and Y. Lvov, *Bio-inorganic Hybrid Nanomaterials*. 2008, Weiheim: whiley-VCH.
10. Brinker, C.J. and G.W. Scherer, *Sol-Gel Science: The Physics and Chemistry of Sol-Gel Processing*. 1990: Academic Press. 912.
11. Sinko, K., *Influence of chemical conditions on the nanoporous structure of silicate aerogels.* Materials, 2010. **3**: p. 704 - 740.
12. Kandimalia, V.B., V.S. Tripathi, and H. Ju, *Immobilization of Biomolecules in Sol-Gels: Biological and Analytical Applications.* Critical Reviews in Analitycal Chemistry, 2006. **36**: p. 73-106.
13. Wright, J.D. and N.A.J.M. Sommerdijk, *Silica Sol-Gels: Reaction mechanisms* in *Sol-Gel Materials: Chemistry and Applications* 2001, Taylor & Francis Books Ltd: London. p. 15-31.
14. Meunier, C.F., et al., *Living hybrid materials capable of energy conversion and CO_2 assimilation.* Chem. Commun., 2010. **46**: p. 3843 - 3859.
15. Stöber, W., A. Fink, and E. Bohn, *Controlled Growth of Monodisperse Silica Spheres in the Micron Size Range.* Journal of Colloid and Interface Science, 1967. **26**: p. 62-69.
16. Yokoi, T., et al., *Periodic Arrangement of Silica Nanoshperes Assisted by Amino Acids.* JACS Communication, 2006. **128**(42): p. 13664-13665.
17. Cao, X.J., H.Z. Cummins, and J.F. Morris, *Structural and rheological evolution of silica nanoparticle gels.* Soft Matter, 2010. **6**(5425 - 5433).
18. Hench, L.L. and J.K. West, *The Sol-gel Process.* Chemical Reviews, 1990. **90**: p. 33 - 72.

19. Bergna, H.E. and W.O. Roberts, *Colloidal Silica Fundamentals and Applications*. Surfactant Science Series. 2006: CRC Press.
20. Vega, A.J. and G.W. Scherer, *Study of structural evolution of silica gel using 1H and 29Si NMR.* Journal of Non-Crystalline Solids, 1989. **111**: p. 153-166.
21. Baca, H.K., et al., *Cell-Directed Assembly of Bio/Nano Interfaces-A New Scheme for Cell Immobilization.* Acc. Chem. Res., 2007. **40**: p. 836-845.
22. Ferrer, M.L., et al., *Biocompatible Sol-Gel Route for Encapsulation of Living Bacteria in Organically Modified Silica Matrices.* Chemistry of Materials, 2003. **15**: p. 3614-3618.
23. Ferrer, M.L., et al., *Bacteria Viability in Sol-gel Materials Revisited: Cryo-SEM as a Suitable Tool to Study the Structural Integrity of Encapsulated Bacteria* Chem. Mat., 2006. **18**: p. 1458-1463.
24. Sinko, K., *Influence of Chemical conditions on the Nanopore Structure of Silicate Aerogels.* Materials, 2010. **3**: p. 704 - 740.
25. Chambers, R.C., et al., *Influence of steric effects on the kinetics of ethyltrimethoxysilane hydrolysis in a fast sol-gel system.* Chem. Mater., 1993. **5**: p. 1481 - 1486.
26. Brinker, C.J., et al., *Sol-gel transition in simple silicates.* J. Non-Cryst. Solids, 1982. **48**: p. 47 - 64.
27. Iler, R.K., *The Chemistry of Silica: solubility, polymerization, colloid and surface properties, and biochemistry*. 1979, New York: John Wiley & Sons.
28. Rao, A.V. and N.N. Parvathy, *Effect of gel parameters on monolithicity and density of silica aerogel.* J. Mater. Sci. , 1993. **28**: p. 3021 - 3026.
29. Meador, M.A.B., et al., *Structure-property relationships in porous 3D nanostructures as a fuction of preparation conditions: isocyanate cross-linked silica aerogels.* Chem. Mater., 2007. **19**: p. 2247 - 2260.
30. Sanchez, C., et al., *Applications of advanced hybrid organic-inorganic nanomaterials: from laboratory to market.* Chemical Society Reviews. **40**(2): p. 696-753.
31. Kickelbick, G., *Hybrid Materials: synthesis, Characterization, and Applications*, ed. G. Kickelbick. 2007: Wiley.
32. Meunier, C.F., P. Dandoy, and B.-L. Su, *Encapsulation of cells within silica matrices: Towards a new advance in the conception of living hybrid materials.* Journal of Colloid and Interface Science, 2009. **342**: p. 211 - 224.
33. Sanchez, C., et al., *"Chimie douce": A land of opportunities for the designed construction of functional inorganic and hybrid organic-inorganic nanomaterials*
C. R. Chimie, 2010. **13**: p. 3 - 39.
34. Hench, L.L., *Sol-gel Silica. Properties, Processing and Technology Transfer*. 1998: Noyes Publications.
35. Gill, I., *Bio-doped nanocomposite polymers sol-gel bioencapsulations.* Chem. Mat., 2001. **13**: p. 3404 -3421.
36. Gill, I. and A. Ballesteros, *Bioencapsulation within Synthetic Polymers (Part 1): Sol-gel Encapsulated Biologicals.* Trends in Biotechnology, 2000. **18**: p. 282-296.

37. Leonard, A., et al., *Cyanobacteria immobilaized in porous silica gels: exploring biocompatible synthesis routes for the development of photobioreactors.* Energy and Environmental Science, 2010. **3**: p. 370 - 377.
38. Schipunov, Y.A., et al., *Gelling of otherwise nongelable polysaccharides.* Journal of Colloidal and Interface Science, 2005. **287**: p. 373-378.
39. Desimone, M., et al., *Production of monoclonal antibodies from hybridoma cells immobilized in 3D sol-gel matrices.* Journal of Materials Chemistry, 2011. **21**: p. 13865 - 13872.
40. Gill, I. and A. Ballesteros, *Encapsulation of biologicals within silicate, siloxanes and hybrid sol-gel polymers: An efficient and generic approach.* Journal of the American Chemical Society, 1998. **120**: p. 8587 - 8598.
41. Livage, J., et al. *Enzyme and cells confined in silica nanopores*. in *Mat. Res. Soc. Symp. Proc.* 2001.
42. Wu, X.J. and M.M.F. Choi, *An optical glucose biosensor based on entrapped-glucose oxidase in silicate xerogel hybridised with hydroxyethyl carboxymethyl cellulose.* Analytica Chimica Acta, 2004. **514**: p. 219 - 226.
43. Pandey, P.C., et al., *Studies on the electrochemical performance of glucose biosensor based on ferrocene encapsulated ormosil and glucose oxidase modified graphite paste electrode.* Biosensors and Bioelectronics, 2003. **18**: p. 1257 - 1268.
44. Li, Y.X., et al., *A chemiluminiscence optical fiber glucose biosensor based on co-immobilizing glucose oxidase and horseradish peroxidase in a sol-gel film.* Chemical Research in Chinese Universities, 2002. **18**: p. 12 - 15.
45. Ramanathan, K., B.R. Jonsson, and B. Danielsson, *sol-gel based thermal biosensor for glucose.* Analytica Chimica Acta, 2001. **427**: p. 1 - 10.
46. Diaz, A.N., M.C.R. Peinado, and M.C.T. Minguez, *Sol-gel horseradish peroxidase biosensor for the chemiluminiscent flow determination of hydrogen peroxide.* Analytica Chimica Acta, 1998. **363**: p. 221 - 227.
47. Kim, M.A. and W.Y. Lee, *Amperometric phenol biosensor based on sol-gel silicate/Nafion composite film.* Analytica Chimica Acta, 2003. **479**: p. 143 - 150.
48. Lee, W.Y., et al., *Microfabricated conductometric urea biosensor based on sol-gel immobilized urease.* Analytica Chimica Acta, 2000. **404**: p. 195 - 203.
49. Li, C.I., et al., *Sol-gel encapsulation of lactate dehydrogenase for optical sensing of L-lactate* Biosensors and Bioelectronics, 2002. **17**: p. 323 - 330.
50. Sanchez, F.G., A.N. Diaz, and M.C.R. Peinado, *Free and sol-gel immobilized alkaline phosphatase-based biosensor for the determination of pesticides and inorganic compounds.* Analytica Chimica Acta, 2003. **484**: p. 45 - 51.
51. Kumar, A., et al., *Co-immobilization of cholesterol oxidase and horseradish peroxidase in a sol-gel film* Analytica Chimica Acta, 2000. **414**: p. 43 - 50
52. Li, B., Z. Zhang, and L. Zhao, *Chemiluminiscent flow-through sensor for hydrogen peroxide based on sol-gel immobialized hemoglobin as catalyst.* Analytica Chimica Acta, 2001. **445**: p. 161 - 167.
53. Brennan, J., *Biofriendly Sol-Gel Processing for the Entrapment of Soluble and Membrane-Bound Proteins: Towards Novel Solid-Phase Assays for High-Throughput Screening.* Acc. Chem. Res., 2007. **40**: p. 827-835.

54. Reátegui, E. and A. Aksan, *Structural Changes in Confined Lysozyme.* Journal of Biomechanical Engineering ASME, 2009. **131**: p. 074520.
55. Reátegui, E. and A. Aksan, *Effects of the Low Temperature Transitions of Confined Water on the Structure of Isolated and Cytoplasmic Proteins.* J. Phys. Chem. B., 2009. **113**(39): p. 13048-13060.
56. Rathore, N., T.A.K. IV, and J.J.d. Pablo, *Confinement Effects on the Thermodynamics of Protein Folding: Monte Carlo Simulations.* Biophysical Journal, 2006. **90**: p. 1767-1773.
57. Gregory, R.B., *Protein-Solvent Interactions*. 1995, New York: Marcell Deker Inc. 555.
58. Khan, I., et al., *Sol-Gel Trapping of Functional Intermediates of Hemoglobin: Geminate and Biomolecular Recombination Studies.* Biochemistry, 2000. **39**: p. 16099-16109.
59. Liu, D.-M. and I.-W. Chen, *Encapsulation of protein molecules in transparent porous silica matrices via an aqueous colloidal sol-gel process.* Acta Materialia, 1999. **47**(18): p. 4535-4544.
60. Eggers, D.K. and J.S. Valentine, *Molecular Confinement Influences Protein Structure and Enhances Thermal Protein Stability.* Protein Science, 2001. **10**: p. 250-261.
61. Shibayama, N. and S. Saigo, *Fixation of the Quaternary Structure of Human Adult Hemoglobin by Encapsulation in Transparent Porous Silica Gels.* Journal of Molecular Biology, 1995. **251**: p. 203-209.
62. Benigno, A.J., E. Ahmed, and M. Berg, *The influence of solvent dynamics on the lifetime of solute–solvent hydrogen bonds.* Journal of Chemical Physics, 1996. **104**(19): p. 7382-7394.
63. Franks, F., *Water: A Comprehensive Treatise*. **1979**, New York: Plenum Press.
64. Massari, A.M., I.J. Finkelstein, and M.D. Fayer, *Dynamics of Proteins Encapsulated in Silica Sol-Gel Glasses Studied with IR Vibrational Echo Spectroscopy.* Journal of the American Chemical Society, 2006. **128**: p. 3990-3997.
65. Eggers, D.K. and J.S. Valentine, *Crowding and Hydration Effects on Protein Conformation: A Study with Sol-Gel Encapsulated Proteins.* Journal of Molecular Biology, 2001. **314**: p. 911-922.
66. Rooke, J.C., et al., *Photosynthesis within porous silica gel: viability and activity of encapsulated cyanobacteria.* Journal of Materials Chemistry, 2008. **18**(2833-2841).
67. Nassif, N., et al., *Viability of Bacteria in Hybrid Aqueous Silica Gels.* Journal of Sol-Gel Science and Technology, 2003. **26**: p. 1141-1144.
68. Nassif, N., et al., *Bacteria quorum sensing in silica matrix.* Journal of Materials Chemistry, 2004. **14**: p. 2264-2268.
69. Perullini, M., et al., *Optimizing Silica Encapsulation of Living Cells: In Situ Evaluation of Cellular Stress.* Chem. Mat., 2008. **20**(9): p. 3015-3021.

70. Alvarez, G.S., M.F. Desimone, and L.E. Diaz, *Immobilization of Bacteria in Silica Matrices Using Citric Acid in the Sol-Gel Process.* Applied Microbiology and Biotechnology, 2007. **73**: p. 1059-1064.
71. Alvarez, G.S., et al., *Effect of various parameters on viability and growth of bacteria immobilized in sol-gel derived silica matrices.* Biothecnological Products and Process Engineering, 2009. **82**: p. 639-646.
72. Lesot, P., et al., *Structural-dynamical relationship in silica PEG hybrid gels.* Journal of Materials Chemistry, 1998. **8**(1): p. 147-151.
73. Inama, L., et al., *Entrapment of viable microorganisms by SiO_2 sol-gel layers on glass surfaces: trapping, catalyic performance and immobilization durability of saccharomyces cerevisiae.* Journal of Biotechnology, 1993. **30**: p. 197 - 210.
74. Baca, H.K., et al., *Cell-Directed Assembly of Lipid-Silica Nanostructures Providing Extended Cell Viability*, in *Science*. 2006. p. 337-341.
75. Harper, J.C., et al., *Encapsulation of S. cerevisiae in poly(glycerol) silicate derived matrices: Effect of matrix additives and cell metabolic phase on long-term viability and rate of gene expression* Chemistry of Materials, 2011. **23**: p. 2555 - 2564.
76. kunkova, G., et al., *Monitoring of the viability of cells immobialized by sol-gel process.* Journal of Sol-Gel Science and Technology, 2004. **31**: p. 335 - 342.
77. Finnie, K.S., J.R. Bartlett, and J.L. Woolfrey, *Encapsulation of sulfate-reducing bacteria in a silica host.* Journal of Materials Chemistry, 2000. **10**: p. 1099 - 1101.
78. Yu, D., et al., *Aqueous sol-gel encapsulation of geneticaaly engineered moraxella spp. cells for the detection of organophospathes.* Biosensors and Bioelectronics, 2005. **20**: p. 1433 - 1437.
79. Nguyen-Ngoc, H. and C. Tran-Minh, *Sol-gel process for vegetal cell encapsulation.* Materials Science and Engineering C, 2007. **27**: p. 607 - 611.
80. Chen, J., et al., *Efficient immobilization of whole cells of Methylomonas sp. strain GYJ3 by sol-gel entrapment.* Journal of Molecular Catalysis B: Enzymatic, 2004. **30**: p. 167 - 172.
81. Coiffier, A., et al., *Sol-gel encapsulation of bacteria: a comparison between alkoxide and aqueous routes.* Journal of Materials Chemistry, 2001. **11**: p. 2039-2044.
82. Fennouh, S., et al., *Sol-Gel Entrapment of Escherichia Coli.* Journal of Sol-Gel Science and Technology, 2000. **19**: p. 647-649.
83. Premkumar, J.R., et al., *Sol-gel luminiscence biosensor: Encapsulation of recombiant E. coli reporters in thick silicate films.* Analytica Chimica Acta, 2002. **462**: p. 11 - 23.
84. Desimone, M.F., et al., *Efficient Preservation in a Silicon Oxide Matrix of Escherichia coli, Producer of Recombinant Proteins.* Applied Microbiology and Biotechnology, 2005. **68**: p. 747-752.
85. Perullini, M., et al., *Improving silica matrices for encapsulation of Escherichia coli using osmoprotectors.* Journal of Materials Chemistry, 2011. **21**: p. 4546 - 4552.

86. Perullini, M., et al., *Improving bacteria viability in metal oxide hosts via an alginate-based hybrid approach.* Journal of Materials Chemistry, 2011. **21**: p. 8026 - 8031.
87. Carnes, E.C., et al., *Confinement-induced quorum sensing of individual Staphylococcus aureous bacteria.* Nature Chemical Biology, 2009.
88. Fiedler, D., et al., *Algae biocers: Astaxanthin formation in sol-gel immobilized living microalgae.* Journal of Materials Chemistry, 2006. **17**: p. 261 - 266.
89. Gautier, C., et al., *Sol-gel dissolution extend diatom viability and reveals their silica dissolution capability.* Chem. Commun., 2006: p. 4611 - 4613.
90. Meunier, C.F., et al., *Investigation of different silica precursors:Design of biocompatible silica gels with long term bio-activity of entrapped thylakoids towards the artificial leaf.* Journal of Materials Chemistry, 2009. **19**: p. 4131 - 4137.
91. Dickson, D.J., C.J. Page, and R.L. Ely, *Photobiological hydrogen production from Synechocystis sp. PCC6803 encapsualted in silica sol-gel* International Journal of Hydrogen Energy, 2009. **34**: p. 204 - 215.
92. Rooke, J.C., et al., *Novel photosyntheic CO_2 bioconvertor based on green algae entrapped in low-sodium silcia gels.* Journal of Materials Chemistry, 2011. **21**: p. 951 - 959.
93. Rooke, J.C., et al., *Hybrid photosynthetic materials derived from microalgae Cyanidium caldarium encapsulated within silica gel.* Journal of Colloid and Interface Science. **344**(2): p. 348-352.
94. Pope, E.J.A., K. Braun, and C.M. Peterson, *Bioartificial Organs I: Silica Gel Encapsulated Pancreatic Islets for the Diabetes Mellitus.* Journal of Sol-Gel Science and Technology, 1997. **8**: p. 635-639.
95. Boninsegna, S., et al., *Encapsulationof individual pancreatic islets bysol-gel SiO_2: A novel procedure for perspective cellular grafts.* Journal of Biotechnology, 2003. **100**: p. 277 - 286.
96. Atchison, N., et al., *silica-nanoparticle coatings by adsorption from lysine-silica-nanoparticle sols on inorganic and biological surfaces.* Angewandte Chemie, 2011. **50**: p. 1 - 6.
97. Muraka, M., et al., *SiO2 Entrapment of Animal Cells: Liver-specific Metabolic Activities in Silica-Overlaid Hepatocytes.* Artificial Organs, 2002. **26**(8): p. 664 - 669.
98. Boninsegna, S., et al., *Alginate microspheres loaded with animal cells and coated by a siliceous layer.* Journal of Sol-Gel Science and Technology, 2003. **26**: p. 1151 - 1157.
99. Sakai, S., et al., *MIN6 cells-enclosing aminopropyl-silicate membrane templated by alginate gels differences in guluronic acid content.* International Journalof Pharmaceutics, 2004. **270**: p. 65 - 73.
100. Sakai, S., et al., *Proliferation and Insulin Secretion Functional of Mouse Insulinoma Cells Encapsulated in Alginate/Sol-Gel Synthesis Aminopropyl-Silicate/Alginate Microcapsule.* Journal of Sol-Gel Science and Technology, 2003.

101. Kataoka, K., et al., *An organic-inorganic hybrid scaffold for the culture of HepG2 cells in biorecator.* Biomaterials, 2005. **26**: p. 2509 - 2516.
102. Desimone, M.F., et al., *Fibroblast encapsulation in hybrid silica-collagen hydrogels.* Journal of Materials Chemistry, 2010. **20**: p. 666 - 668.
103. Mahony, O., et al., *Silica-gelatin hybrids with tailorable degradation and mechanical properties for tissue regeneration.* Advanced Functional Materials, 2010. **20**: p. 3835 - 3845.
104. Ren, L., et al., *Novel approach to fabricate porous gelatin-siloxane hybrids for bone tissue engineering.* Biomaterials 2002. **23**: p. 4765 - 4773.
105. Pek, Y.S., et al., *A thixotropic nanocomposite gel for three-dimensional cell culture.* Nature Nanotechnology, 2008. **3**: p. 671-675.
106. Wang, F., et al., *Oxidative stress contributes to silica nanoparticle cytotoxicity in human embrionic kidney cells.* Toxicology in Vitro, 2009. **23**: p. 808-815.
107. Silvio, L.D., *Cellular response to biomaterials*, ed. C. Press. 2009, New York.
108. Lord, M.S., et al., *The effect of silica nanoparticle coatings on serum protein adsorption and cellular response.* Biomaterials 2006. **27**: p. 4856-4862.
109. Cousins, B.G., P.J. Doherty, and R.L. Williams, *The effect of silica nanoparticles coatings on cellular response.* Journal of Material Science: Materials and Medicine 2004. **15**: p. 355-359.
110. Lipski, A.M., et al., *The effect of silica nanoparticle-modified surfaces on cell morphology, cytoskeketal organization and function.* Biomaterials, 2008.
111. Puleo, D.A. and R. Bizios, *Biological Interactions on Material Surfaces: Understanding and Controlling Protein, Cell, and Tissue Responses*. 2009: Springer.
112. Koolman, J. and K.-H. Rohm, *Taschenatlas der Biochemie*. 1998.
113. Blitz, J.P. and V.M. Gun'ko, *Surface Chemistry in Biomedical and Environmental Science*. 2006, Amsterdam.
114. Flickinger, M.C., et al., *Painting and Printing Living Bacteria: Engineering Nanoporous Biocatalytic Coatings to Preserve Microbial Viability and Intensify Reactivity.* Biotechnology Progress, 2007. **23**(1): p. 2-17.
115. Pierre, A.C., *The Sol-Gel Encapsulation of Enzymes.* Biocatalysis and Biotransformation, 2004. **22**(3): p. 145-170.
116. Lei, C., et al., *Characterization of Functionalized Nanoporous Supports for Protein Confinement.* Nanotechnology, 2006. **17**: p. 5531-5538.
117. Ping, G., et al., *Effects of Confinement on Protein Folding and Protein Stability.* Journal of Chemical Physics, 2003. **118**(17): p. 8042-8048.
118. Branyik, T. and G. Kuncova, *Encapsulation of Microbial Cells into Silica Gel.* Journal of Sol-Gel Science and Technology, 1998. **13**: p. 283-287.
119. Campostrini, R., et al., *Immobilization of Plant Cells in Hybrid Sol-Gel Materials.* Journal of Sol-Gel Science and Technology, 1996. **7**: p. 87-97.
120. Bjerketorp, J., et al., *Advances in Preservation Methods: Keeping Biosensor Microorganisms Alive and Active.* Current Opinion in Biotechnology, 2006. **17**: p. 43-49.

121. Peterson, E.S., et al., *Folding Myoglobin within a Sol-Gel Glass: Protein Folding Constrained to a Small Volume.* Biophysical Journal, 2008. **95**: p. 322-332.
122. Frauenfelder, H., et al., *Protein Folding is Slaved to Solvent Motions.* Proceedings of the National Academy of Sciences of the United States of America, 2006. **103**(42): p. 15469-15472.
123. Frauenfelder, H., P.W. Fenimore, and B.H. McMahon, *Hydration, Slaving and Protein Function.* Biophysical Chemistry, 2002. **98**: p. 35-48.
124. Caliskan, G., et al., *Protein and Solvent Dynamics: How Strongly are they Coupled?* Journal of Chemical Physics, 2004. **121**(4): p. 1978-1983.
125. Chen, S.-H., et al., *Observation of fragile-to-strong dynamic crossover in protein hydration water.* Proceddings of the National Academy of Sciences of the United States of America, 2006. **103**(24): p. 9012-9016.
126. Oleinikova, A. and I. Brovchenko, *Percolation transition of hydration water in biosystems.* Molecular Physics, 2006. **104**(22): p. 3841-3855.
127. Moilanen, D.E., et al., *confinement or the Nature of the Interface? Dynamics of nanoscopic Water.* Journal of the American Chemistry Society, 2007. **129**(46): p. 14311-14318.
128. Cupri, V., et al., *Structure and dynamics of water confined in a nanoporous sol-gel silica glass: a neutron scattering study.* Molecular Physics, 2003. **101**(22): p. 3323-3333.
129. Roche, C.J., F. Guo, and J.M. Friedman, *Molecular Level Probing of Preferential Hydration and its Modulation by Osmolites through the USe of Pyranine Complexed to Hemoglobin.* The Journal of Biological Chemistry, 2006. **281**(50): p. 38757-38768.
130. Clegg, J.S., *Intracellular Water and the Cytomatrix: Some Methods of Study and Current Views.* Journal of Cell Biology, 1984. **99**(1): p. 167S-171S.
131. Clegg, J.S., *Properties and Metabolism of the Aqueous Cytoplasm and its Boundaries.* American Journal of Physiology, 1984. **246**: p. R133-R151.
132. Zimmerman, S.B. and S.O. Trach, *Estimation of Macromolecule Concentrations and Excluded Volume Effects for the Cytoplasm of Escherichia Coli.* Journal of Molecular Biology, 1991. **222**: p. 599-620.
133. Scalettar, B.A., J.R. Abney, and C.R. Hackenbrock, *Dynamics, Structure and Function are Coupled in the Mitochondrial Matrix.* Proceedings of the National Academy of Sciences of the United States of America, 1991. **88**: p. 8057-8061.
134. Ellis, R.J. and A.P. Minton, *Cell Biology: Join the Crowd.* Nature, 2003. **425**: p. 27-28.
135. Minton, A.P., *The Influence of Macromolecular Crowding and Macromolecular Confinement on Biochemical Reactions in Physiological Media.* Journal of Biological Chemistry, 2001. **276**(14): p. 10577-10580.
136. Pelton, J.T. and L.R. McLean, *Spectroscopy Methods for Analysis of Protein Secondary Structure.* Analytical Biochemistry, 2000. **277**: p. 167-176.
137. Holzbaur, I.E., A.M. English, and A.A. Ismail, *FTIR Study of the Thermal Denaturation of Horseradish and Cytochrome c Peroxidases in D_20.* Biochemistry, 1996. **35**: p. 5488-5494.

138. Dong, A., P. Huang, and W.S. Caughey, *Protein Secondary Structures in Water from Second-Derivative Amide I Infrared Spectra.* Biochemistry, 1990. **29**: p. 3303-3308.
139. Dong, A., et al., *Infrared Spectroscopy Studies of Lyophilization and Temperature Induced Protein Aggregation.* Journal of Pharmaceutical Sciences, 1995. **84**: p. 415-424.
140. Lee, D.C., et al., *Second-Derivative Infrared Spectroscopy Studies of the Secondary Structures of Bacteriorhodopsin and Ca^{2+} - ATPase.* Biochemistry, 1985. **24**: p. 4364-4373.
141. Susi, H. and M. Byler, *Protein Structure by Fourier Transform Infrared Spectroscopy: Second Derivative Spectra.* Biochemical and Biophysical Research Comunnications, 1983. **115**(1): p. 391-397.
142. Zhang, J. and Y.-B. Yan, *Probing Conformational Changes of Proteins by Quantitative Second-Derivative Infrared Spectroscopy.* Analytical Biochemistry, 2005. **340**: p. 89-98.
143. Kauppinen, J.K., et al., *Fourier transforms in the computation of self-deconvoluted and first-order derivative spectra of overlapped band contours.* Anal. Chem., 1981. **53**(9): p. 1454-1457.
144. Dzwolak, W., et al., *FTIR Study on Heat-Induced and Pressure-Assisted Cold-Induced Changes in Structure of Bovine α-Lactalbumin: Stabilizing Role of Calcium Ion.* Biopolymers (Biospectroscopy) 2001. **62**: p. 29-39.
145. Sokolowski, F. and D. Naumann, *FTIR study on thermal denaturation and aggregation of recombinant hamster prion $SHaPrP^{90-232}$.* Vibrational Spectroscopy, 2005. **38**: p. 39-44.
146. Kong, J. and Y.U. Shaoning, *Fourier Transform Infrared Spectroscopic Analysis of Protein Secondary Structures.* Acta Biochimica et Biophysica Sinica, 2007. **38**(8): p. 549-559.
147. Pechkova, E., et al., *Thermal Stability of Lysozyme Langmuir-Schaefer Films by FTIR Spectroscopy.* Langmuir, 2007. **23**: p. 1147-1151.
148. van Stokkum, I.H.M., et al., *Temperature-Induced Changes in Protein Structures Studied by Fourier Transform Infrared Spectroscopy and Global Analysis.* Biochemistry, 1995. **34**: p. 10508-10518.
149. Luo, S., et al., *A Study of Protein Secondary Structure by Fourier Transform Infrared/Photoacoustic Spectroscopy and Its Application for Recombinant Proteins.* Analytical Biochemistry, 1994. **216**: p. 67-76.
150. Wolkers, W.F., et al., *Effects of freezing on membranes and proteins in LNCaP prostate tumor cells* Biochimica et Biophysica Acta, 2007. **1768**(3): p. 728-736.
151. Brubach, J.-B., et al., *Signatures of the hydrogen bonding in the infrared bands of water.* The Journal of Chemical Physics, 2005. **122**: p. 184509 1- 7.
152. Freda, M., et al., *Transmittance Fourier Transform Infrared Spectra of Liquid Water in the Whole Mid-Infrared Region: Temperature Dependence and Structural Analysis.* Applied Spectroscopy, 2005. **59**(9): p. 1155-1159.

153. Schmidt, J.R., S.A. Corcelli, and J.L. Skinner, *Pronounced non-COndon effects in the ultrafast infraed spectroscopy of water.* The Journal of Chemical Physics, 2005. **123**(044513): p. 1-13.
154. Mallamace, F., et al., *Evidence of the Existence of the Low-Density Liquid Phase in Supercooled, Confined Water.* Procedings of the National Academy of Sciences of the United States of America, 2007. **104**(2): p. 424-428.
155. Mallamace, F., et al., *Role of the Solvent in the Dynamical Transitions of Proteins: The Case of the Lysozyme-Water System.* J. chem. Phys. , 2007. **127**: p. 045104.
156. Davis, K.M. and M. Tomozawa, *An Infrared spectroscopy study of water-related species in silica glasses.* Journal of Non-Crystalline Solids, 1996. **201**: p. 177-198.
157. Glinka, Y.D., *Two- photon-excited luminescence and defect formation in SiO_2 nanoparticles induced by 6.4-eV ArF laser light.* Physical Review B, 2001. **62**(7): p. 4733-4742.
158. Asay, D.B. and S.H. Kim, *Evolution of the Absorbed Water Layer Structure on Silicon Oxide at Room Temperature.* J. Phys. Chem. B, 2005. **109**: p. 16760-16763.
159. Cupri, V., D. Majolino, and V. Venuti, *Diffusional and Vibrational dynamics of water in Na zeolites by neutron and Fourier transform infrared spectroscopy.* J. Phys.: Condens. Matter, 2004. **16**: p. S5297-S5316.
160. Devlin, J.P., J. Sadlej, and V. Buch, *Infrared Spectra of Large H_20 Clusters: New Understanding of the Elusive Bending Mode of Ice.* J. Phys. Chem. A, 2001. **105**: p. 974-983.
161. Mishima, O. and H.E. Stanley, *The Relationship Between Liquid, Supercooled and Glassy Water.* Nature, 1998. **396**: p. 329-335.
162. Hansen, E.W., M. Stocker, and R. Schmidt, *Low-Temperature Phase Transition of Water Confined in Mesopores Probed by NMR. Influcence on Pore Size Distribution.* Journal of Physical Chemistry, 1996. **100**(6): p. 2195-2200.
163. Schreiber, A., I. Ketelsen, and G.H. Findenegg, *Melting and Freezing of Water in Ordered Mesoporous Silica Materials.* Physical Chemistry and Chemical Physics, 2001. **3**: p. 1185-1195.
164. Alcoutlabi, M. and G.B. McKenna, *Effects of Confinement on Material Behavior at the Nanometer Size Scale.* Journal of Physics: Condensed Matter, 2005. **17**: p. R461-R524.
165. Faraone, A., et al., *Fragile-to-strong liquid transition in deeply supercooled confined water.* Journal of Chemical Physics, 2004. **121**(22): p. 10843-10846.
166. Murphy, D.M. and T. Koop, *Review of the Vapor Pressures of Ice and Supercooled Water for Atmospheric Applications.* Quarterly journal of the Royal Meteorological Society, 2005. **131**: p. 1539-1565.
167. Mishima, O. and H.E. Stanley, *The Relationship between liquid, supercooled and glassy water*, in *Nature*. 1998. p. 329-335.
168. Oguni, M., et al., *Glass Transitions of Ordinary and Heavy Water within Silica-Gel Nanopores.* Chem. Asian J., 2007. **2**: p. 514-520.

169. Swenson, J., H. Jansson, and R. Bergman, *Relaxation Process in Supercooled Confined Water and Implications for Protein Dynamics.* Physical Review Letters, 2006. **96**: p. 247802.
170. Trofymluk, O., A.A. Levchenko, and A. Navrotsky, *Interfacial Effects on Vitrification of Confined Glass-Forming Liquids.* Journal of Chemical Physics, 2005. **123**: p. 194509.
171. Johari, G.P., *Water's Size-dependent Freezing to Cubic Ice.* Journal of Chemical Physics, 2005. **122**: p. 194504.
172. Chonde, M., M. Brindza, and V. Sadtchenko, *Glass transition in pure and doped amorphous solid water: An ultrafast microcalimetry study.* The Journal of Chemical Physics, 2006. **125**: p. 0945011-09450110.
173. Kittaka, S., et al., *Enthalpy and Interfacial free energy changes of water capillary condensed in mesoporous silica, MCM-41 and SBA-15.* Physical Chemistry Chemical Physics, 2006. **8**: p. 3223-3231.
174. Johari, G.P., *Thermodynamics of water-cubic ice and other liquid-solid coexistance in nanometer-size particles.* Journal of Chemical Physics, 1998. **109**(3): p. 1070-1073.
175. Christenson, H.K., *Confinement effects on freezing and melting.* J. Phys. Condes. Matter, 2001. **13**: p. R95-R133.
176. Kanakubo, M., et al., *Melting point depression of ionic liquids confined in nanospaces.* Chem. Commun., 2006: p. 1828-1830.
177. Alphonse, N.K., et al., *Direct Raman Evidence for a Weak Continuous Phase Transition in Liquid Water.* Journal of Physical Chemistry A, 110. **110**: p. 7577-7580.
178. Chen, S.-H., et al., *Observation of fragile-to-strong dynamic crossover in protein hydration water.* PNAS, 2006. **103**(24): p. 9012-9016.
179. Tournier, A.L., J. Xu, and J.C. Smith, *Translational hydration water dynamics drives the protein glass transition.* Biophysical Journal, 2003. **85**: p. 1871-1875.
180. Morozov, V.N. and S.G. Gevorkian, *Low-Temperature Glass Transition in Proteins.* Biopolymers, 1985. **24**: p. 1785-1799.
181. Frauenfelder, H., G. Petsko, and D. Tsernoglou, *Temperature-dependent X-ray-difraction as a probe of protein structural dynamics.* Nature, 1979. **280**: p. 558-563.
182. Bhatnagar, B.S., R.H. Bogner, and M.J. Pikal, *Protein Stability During Freezing: Separation of Stresses and Mechanisms of Protein Stabilization.* Pharmaceutical Development and Technology, 2007. **12**(5): p. 505-523.
183. Strambini, G.B. and E. Gabellieri, *Proteins in frozen solutions: Evidence of ice-induced partial unfolding.* Biophysical Journal, 1996. **70**(2): p. 971-976.
184. Tang, X. and M.J. Pikal, *The Effect of Stabilizers and Denaturants on the Cold Denaturation Temperatures of Proteins and Implications for Freeze-Drying.* Pharmaceutical Research, 2005. **22**(7): p. 1167-1175.
185. Tang, X.C. and M.J. Pikal, *Measurement of the Kinetics of Protein Unfolding in Viscous Systems and Implications for Protein Stability in Freeze-Drying.* Pharmaceutical Research, 2005. **22**(7): p. 1176-1185.

186. Vitkup, D., et al., *Solvent Mobility and the Protein 'Glass' Transition.* Nature Structural Biology, 2000. **7**(1): p. 34-38.
187. Frauenfelder, H., S.G. Sligar, and P.G. Wolynes, *The Energy Landscapes and Motions of Proteins.* Science, 1991. **254**: p. 1598-1603.
188. Pastor, I., et al., *Structure and dynamics of lysozyme encapsulated in a silica sol-gel matrix.* J. Phys. Chem. B, 2007. **111**: p. 11603-11610.
189. Bagchi, B., *Water dynamics in the hydration layer around proteins and micelles.* Chemical Reviews, 2003. **105**(9): p. 3197-3219.
190. Perez, C. and K. Griebenow, *Fourier-transform infrared spectroscopic investigation of the thermal denaturation of hen egg-white lysozyme dissolved in aqueous buffer and glycerol* Bitechnology Letters, 2000. **22**: p. 1899-1905.
191. Samuni, U., et al., *Conformational Dependence of Hemoglobin Reactivity under High Viscosity Conditions: The Role of Solvent Slaved Dynamics.* Journal of the American Chemical Society, 2007. **129**: p. 12756-12764.
192. Viappiani, C., et al., *New insights into allosteric mechanisms from trapping unstable protein conformations in silica gels.* Proceddings of the National Academy of Sciences of the United states of America, 2004. **100**(40): p. 14414-14419.
193. Morishige, K. and k. Kawano, *Freezing and melting of water in a single cylindrical pore: The pore-size dependence of freezing and melting behavior.* Journal of Chemical Physics, 1999. **110**(10): p. 4867-4872.
194. Shereiber, A., I. Ketelsen, and G.H. Findenegg, *Melting and freezing of water in ordered mesoporous silica materials* Physical Chemistry Chemical Physics, 2001. **3**: p. 1185-1195.
195. Cammarata, M., et al., *Structure and dynamics of water confined in silica hydrogels: X-ray scattering and dielectric spectroscopy studies.* Eur. Phys. J. E, 2003. **12**: p. S63-S66.
196. Kumar, P., et al., *Effect of water-wall interaction potential on the properties of nanoconfined water.* Physical Review E, 2007. **11**: p. 0112021-8.
197. Tombari, E., G. Salvetti, and C. Ferrari, *Thermodynamic functions of water and ice confined to 2 nm radius pores.* The Journal of Chemical Physics, 2005. **122**: p. 1047121-9.
198. Liu, L., et al., *Quasielastic and Inelastic neutron Scattering investigation of fragile-to-strong crossover in deeply supercooled water confined in nanoporous silica matrices.* Journal of Physics: Condensed Matter, 2006. **18**: p. S2261-S2284.
199. Kumar, P., *Breakdown of the Stokes- Einstein relation in supercooled water.* PNAS, 2006. **103**(53): p. 12955-12956.
200. Mallamace, F., et al., *Dynamical properties of confined supercooled water and NMR study.* Journal of Physics: Condensed Matter, 2006. **18**: p. S2285-S2297.
201. Mallamace, F., et al., *Evidence of the existence of the low-density liquid phase in supercooled, confined water.* Proceedings of the National Academy of Science of the United States of America 2006. **104**(2): p. 424-428.

202. Mallamace, F., et al., *Role of the Solvent in the Dynamical Transitions of Proteins: The Case of the Lysozyme-Water System.* The Journal of Chemical Physics, 2007. **127**: p. 045104.
203. Mallamace, F., et al., *The anomalous behavior of the density of water in the range 30 K < T < 373 K.* Procedings of the National Academy of Sciences of the United states of America, 2007. **104**(47): p. 18387-18391.
204. Mallamace, F., et al., *The fragile-to strong dynamic crossover transition in confined liquid water: nuclear magnetic resonance results.* The Journal of Chemical Physics, 2006. **124**(16): p. 161102-1 - 161102-4.
205. Rault, J., R. Neffati, and P. Judeinstein, *Melting of Ice in Porous Glass: Why Water and Solvents Confined in Small Pores do not crystallize?* European Physical Journal B, 2003. **36**: p. 627-637.
206. Rennie, G.K. and J. Clifford, *Melting of Ice in porous solids.* J. Chem. Soc. Faraday Trans. 1, 1977. **73**(680-689).
207. Faivre, C., D. Bellet, and G. Dolino, *Phase transitions of fluids confined in porous silicon: A differential calorimetry investigation.* Eur. Phys. J. B, 1999. **7**: p. 19-36.
208. Gregory, R.B., *Protein Hydration and Glass Transition Behavior*, in *Protein-Solvent Interactions*. 1995, Marcel Dekker, Inc.: New York. p. 191-264.
209. Ping, G., et al., *Studies of effects of macromolecular crowding and confinement on protein folding and protein stability.* Journal of Molecular Recognition, 2004. **17**: p. 433-440.
210. Tian, M., et al., *Structural Stability Effects on Adsorption of Bacteriophage T4 Lysozyme to Colloidal Silica.* Journal of Colloid and Interface Science, 1998. **200**: p. 146-154.
211. Czeslik, C. and R. Winter, *Effects of temperature on the conformation of lysozyme adsorbed to silica particles.* Phys. Chem. Chem. Phys. , 2001. **3**: p. 235-239.
212. Menaa, B., et al., *Protein Adsorption onto Organically Modified Silica Glass Leads to a Different Sructure than Sol-Gel Encapsulation.* Biophysical Letters, 2008. **95**(8): p. L51-L53.
213. Tarasevich, Y.I., *Interaction of Globular Albumins with the Silica Surface.* Theoretical and Experimental Chemistry, 2001. **37**(2): p. 98-102.
214. Kumar, P., et al., *Glass Transition in Biomolecules and the Liquid-Liquid Critical Point of Water.* Physical Review Letters, 2006. **97**: p. 177802.
215. Bandyopadhyay, S., S. Chakrabotry, and B. Baghci, *Secondary Structure Sensitivity of Hydrogen Bond Lifetime Dynamics in the Protein Hydration Layer.* Journal of the American Chemical Society, 2005. **127**: p. 16660-16667.
216. Chaplin, M. *www.lsbu.ac.uk/water/index.html*. [cited.
217. Kocherbitov, V. and T. Arnebrant, *Hydration of Thermally Denatured Lysozyme Studied by Sorption Calorimetry and Differential Scanning Calorimetry.* Journal of Physical Chemistry B, 2006. **110**: p. 10144-10150.
218. Peyrard, M., *Glass Transition in protein Hydration Water.* Physics Review E, 2001. **64**: p. 011109-1-5.

219. Réat, V., et al., *Solvent dependence of dynamic transitions in protein solutions.* Proceedings of the National Academy of Sciences of USA, 2000. **97**(18): p. 9961-9966.
220. Tarek, M. and D.J. Tobias, *Role of Protein-Water Hydrogen Bond Dynamics in the Protein Dynamical Transition.* Physical Review Letters, 2002. **88**(13): p. 138101-1-4.
221. Aksan, A. and M. Toner, *Roles of Thermodynamic State and Molecular Mobility in Biopreservation*, in *The Biomedical Engineering Handbook*, J.D. Bronzino, Editor. **2006**, Taylor & Francis: Boca Raton.
222. Debenedetti, P.G., *Supercooled and glassy water.* Journal of Physics: Condensed Matter, 2003. **15**: p. R1669-R1726.
223. Brennan, J.D., et al., *Using Sugar and Amino Acid Additives to Stabilize Enzymes within Sol-Gel Derived Silica.* Chem. Mater. , 2003. **15**: p. 737-745.
224. Kumar, A., et al., *Diagnostics applications of enzyme-doped sol-gel derived glasses* Advances in Biosensors, 2003. **5 (Prospectives in Biosensors)**: p. 101-130.
225. Bronshtein, A., et al., *Sol-gel matrices doped with atrazine antibodie: Atrazine biding properties* Chem. Mat., 1997. **9**(11): p. 2632-2639.
226. Aholo, M., et al., *Silica xerogel carrier material for controlled release of toremifene citrate* Int. J. Pharm., 2000. **195**: p. 219-227.
227. Reetz, M.T., et al., *Second generation sol-gel encapsulated lipases: Robust heterogeneous biocatalyst* Adv. Synth. Catal., 2003. **345**(6-7): p. 717-728.
228. Hall, D., *On the Role of the Macromolecular Phase Transitions in Biology in Response to Change in Solution Volume or Macromolecular Composition: Action as an Entropy Buffer.* Biophysical Chemistry, 2002. **98**: p. 233-248.
229. Fenimore, P.W., et al., *Bulk-solvent and hydration-shell fluctuations, similar to α- and β-fluctuations in glasses, control protein motions and functions.* Proceedings of the National Academy of Sciences of USA, 2004. **101**(40): p. 14408-14413.
230. Sulkowska, A., *Interaction of drugs with bovine and human serum albumin.* Journal of Molecular Structure, 2002. **614**(1): p. 227-232(6).
231. Berman, H.M., et al., *The Protein Data Bank.* Nucleic Acids Research, 2000. **28**: p. 234-242.
232. Ragoonanan, V. and A. Aksan, *Heterogeneity in Dessicated Solutions: Implications for Biostabilization.* Biophysical Journal, 2008. **94**: p. 2212-2227.
233. Barth, A. and C. Zscherp, *What vibrations tell us about proteins.* Quarterly Reviews of Biophysics, 2002. **35**(4): p. 369-430.
234. Fornés, V. and J. Chaussidon, *An Interpretation of the Evolution with Temperature of the $\nu_2+\nu_3$ Combination Band in Water.* Journal of Chemical Physics, 1978. **68**(10): p. 4667-4671.
235. Saitow, K.-i., K. Kobayashi, and K. Nishikawa, *How are Hydrogen Bonds Perturbed in Aqueous $NaClO_4$ Solutions Depending on the Concentration?: A Near Infrared Study.* Journal of Solution Chemistry, 2004. **33**(6-7): p. 689-698.

236. Czarnik-Matusewicz, B. and S. Pilorz, *Study of the temperature-dependent near-infrared spectra of water by two dimensional correlation spectroscopy and principal components analysis.* Vibrational Spectroscopy, 2006. **40**: p. 235-245.
237. Malsam, J. and A. Aksan, *Hydrogen Bonding and Kinetics/Thermodynamic Transitions of Aqueous Trehalose Solutions at Cryogenic Temperatures.* J of Phys Chem B, 2009.
238. Knubovets, T., et al., *Structure, thermostability, and conformational flexibility of hen egg-white lysozyme disolved in glycerol.* Proceddings of the National Academy of Sciences of the United states of America, 1999. **96**: p. 1262-1267.
239. Carter, D.C. and J.H. Ho, *Structure of Serum Albumin.* Adv. Protein Chem., 1994. **45**: p. 153-203.
240. Huang, H. and M. Zhao, *Changes of trypsin in activity and secondary structure induced by complex with trypsin inhibitors and tea polyphenol.* Eur Food Res Technol, 2008. **227**: p. 361-365.
241. Kabsch, W. and C. Sander, *Dictionary of Protein Secondary Structure: Pattern Recognition of Hydrogen Bonded and Geometrical Features* Biopolymers, 2004. **22**: p. 2577-2637.
242. Ahmad, S., et al., *ASAView: Solvent Accesibility Graphics for Proteins.* BMC Bioinformatics, 2004. **5**: p. 51.
243. Lakowicz, J.R., *Introduction to Fluorescence*, in *Principles of Fluorescence Spectroscopy*. 2006, Springer Science+Business Media, LLC. p. 1-25.
244. Mallamace, F., et al., *The fragile-to strong dynamic crossover transition in confined liquid water: nuclear magnetic resonance results.* J. chem. Phys., 2006. **124**(16): p. 161102-1 - 161102-4.
245. Mantsch, H.H. and D. Chapman, *Infrared Spectroscopy of Biomolecules*. 1996, New York: Wily-Liss, INC. 359.
246. Privalov, P.L., *Stability of Proteins: Proteins Which Do not Present a Single Cooperative System.* Advances in Protein Chemistry, 1982. **35**: p. 1-104.
247. Kurzynski, M., *The Thermodynamic Machinery of Life*. 2006, New York: Springer.
248. Magazu, S., F. Migliardo, and A.J. Ramirez-Cuesta, *Concentration dependence of vibrational properties of bioprotectant/water mixtures by inelastic neutron scattering.* Journal of the Royal Society Interface, 2007. **4**: p. 167-173.
249. Magazu, S., et al., *Correlation Between Bioprotective Effectiveness and Dynamic Properties of Trehalose-Water, Maltose-Water and Sucrose-Water Mixtures.* Carbohydrate Research, 2005. **340**: p. 2796-2801.
250. Fuller, B.J., A.N. Lane, and E.E. Benson, *Life in the Frozen State*. 2004, Boca Raton: CRC Press.
251. Miller, D.P., J.J. de Pablo, and H. Corti, *Thermophysical properties of trehalose and its concentrated aqueous solutions.* Pharmaceutical Research, 1997. **14**(5): p. 578-590.
252. Fenimore, P.W., et al., *Slaving: Solvent fluctuations dominate protein dynamics and functions.* Proceedings of the National Academy of Sciences of USA, 2002. **99**(25): p. 16047-16051.

253. Brovchenco, I. and A. Oleinikova, *Role of interfacial water in biological function*, in *Interfacial and confined Water*. 2008, Elseiver: Germany. p. 305.
254. Ricci, M.A., et al., *Water in confined geometries: experiments and simulations.* Journal of Physics-Condensed Matter, 2000. **12**: p. A345-A350.
255. Crupi, V., et al., *Confinement influence in liquid water studied by Raman and neutron scattering.* Journal of Physics-Condensed Matter, 2000. **12**(15): p. 3625-3630.
256. www.sigmaaldrich.com, 2010.
257. Lundqvist, M., I. Sethson, and B.-H. Jonsson, *Protein adsorption onto silica nanoparticles: conformational changes depend on the particle's curvature and the protein stability.* Langmuir, 2004. **20**(24): p. 10639-10647.
258. Vergetel, A.A., R.W. Siegel, and J.S. Dordick, *Silica nanoparticle size influences the estructure and enzymatic activity of adsorbed lysozyme.* Langmuir, 2004. **20**(16): p. 6800-6807.
259. Chen, S.-H., et al., *Experimental evidence of fragile-to-strong dynamic crossover in DNA hydration water.* The Journal of Chemical Physics, 2006. **125**(171103): p. 1-4
260. He, Y., et al., *Protein Dynamical Transition Does not Require Protein Structure.* Physical Review Letters, 2008. **101**(178103): p. 1-4.
261. Kobayashi, T., J.A. DiVerdi, and G.E. Maciel, *Silica Gel Surface: Molecular Dynamics of Surface Silanols.* J. Phys. Chem. C, 2008. **112**: p. 4315-4326.
262. Koynokova, R., J. Brankov, and B. Tenchov, *Modulation of Lipid Phase Behavior by Kosmotropic and Chaotropic Solutes.* European Biophysics Journal, 1997. **25**: p. 261-274.
263. Chuang, I.-S. and G.E. Maciel, *Probing Hydrogen and the Local Environment of Silanols on Silica Surfaces via Nuclear Spin Cross Polarization.* Journal of the American Chemical Society, 1996. **118**: p. 401-406.
264. Chuang, I.-S. and G.E. Maciel, *A Detailed Model of Local Structure and Silanol Hydrogen Bonding of Silica Gel Surfaces.* J. Phys. Chem. B, 1997. **101**: p. 3052-3064.
265. McDonald, R.S., *Study of the Interaction between Hydroxyl Groups of Aerosil Silica and Adsorbed Non-polar Molecules by Infrared Spectrometry.* Journal of the American Chemical Society, 1956. **79**: p. 850-854.
266. Zhang, J., et al., *In situ loading of basic fibroblast growth factor within porous silica nanoparicles for a prolonged release.* Nanoscale Res. Lett., 2009.
267. Cordone, L., et al., *Harmonic Behavior of Trehalose-Coated Carbon-Monoxy-Myoglobin at High Temperature.* Biophysical Journal, 1999. **76**: p. 1043-1047.
268. Cordone, L., et al., *Internal dynamics and protein-matrix coupling in trehalose-coated proteins.* Biochimica Et Biophysica Acta-Proteins and Proteomics, 2005. **1749**(2): p. 252-281.
269. Hédoux, A., et al., *Evidence of a two-stage thermal denaturation process in lysozyme: A raman scattering and differential scanning calorimetry investigation.* J. Chem. Phys. , 2006. **124**: p. 014703-1-7.

270. Radosevich, M., et al., *Degradation and mineralization of atrazine by a soil bacterial isolate.* Applied and Environmental Microbiology, 1995. **61**(1): p. 297 - 302.
271. Macias-Flores, A., et al., *Atrazine biodegradation by a bacterial community immobilized in two types of packed-bed biofilm reactors.* World Journal Microbiology and Biotechnology, 2009. **25**(2): p. 1995 - 2204.
272. Kauffmann, C. and R.T. Mandelbaum, *Entrapment of atrazine chlorohydrolase in sol-gel glass matrix.* Journal of Biotechnology, 1998. **62**: p. 168 -176.
273. Mandelbaum, R.T., L.P. Wackett, and D.L. Allan, *Rapid Hydrolysis of Atrazine to Hydroxyatrazine by Soil Bacteria.* Environmental Science and Technology, 1993. **27**: p. 1943 - 1946.
274. Sousa, M.L.d., et al., *Cloning, characterization and expression of a gene region from Pseudomonas sp. strain ADP involved in the dechlorination of atrazine.* Applied and Environmental Microbiology, 1995. **61**: p. 3373-3378.
275. Martinez, B., et al., *Complete nucleotide sequence and organization of the atrazine catabolic plasmid pADP-1 from Pseudomonas sp. strain ADP* Journal of Bacteriology, 2001. **183**(19): p. 5684 - 5697.
276. Goswami, K. and R.E. Green, *Microbial degradation of the herbicide atrazine and its 2-hydroxyanalog in submerged soils.* Environmental Science and Technology, 1971. **5**: p. 426 - 429.
277. Strong, L.C., et al., *Field-scale remediation of atrazine-contaminated soil using recombinant Escherichia coli expressing atrazine chlorohydrolase.* Environmental Microbiology, 2000. **2**(1): p. 91 - 98.
278. Rietti-Shati, M., D. Ronen, and R.T. Mandelbaum, *Atrazine degradation by Pseudomonas strain ADP entrapped in sol-sel glass.* Journal of Sol-Gel Science and Technology, 1996. **7**: p. 77 - 79.
279. Reátegui, E. and A. Aksan, *Effects of the low temperature transitions of confined water on the structure of isolated and cytoplasmic proteins.* Journal of Physical Chemistry B, 2009. **113**(39): p. 13048-13060.
280. Acosta, E.J., et al., *Removal of water using covalent sequestration.* Journal of Agricultural and Food Chemistry, 2004. **52**: p. 545 - 549.
281. Pelekani, C. and V.L. Snoeyink, *Competitive adsorption between atrazine and methylene blue on activated carbon: the importance of pore size distribution.* Carbon, 2000. **38**: p. 1423 - 1436.
282. Bottero, J.Y., et al., *Adsorption of atrazine onto zeolites and organoclays, in the presence of background organics.* Water Research, 1994. **28**: p. 483 - 490.
283. Yue, Z., et al., *Chemical activated carbon on a fiberglass substrate for removal of trace atrazine from water.* Journal of Materials Chemistry, 2006. **16**: p. 3375 - 3380.
284. Devitt, E. and M.R. Wiesner, *Dialysis investigations of atrazine-organic matter interactions and the role of a divalent metal.* Environmental Science and Technology, 1998. **32**(1): p. 232 - 237.
285. Parra, S., et al., *Photocatalytic degradation of atrazine using suspended and supported TiO_2.* Applied Catalyis B: Environmental, 2004. **51**(2): p. 107 - 116.

286. Majewska-Nowak, K., et al., *The influence of organic carbon concentration on atrazine removal by UF membranes.* Desalination, 2002. **147**(1 - 3): p. 177 - 122.
287. Doulia, D., et al., *Removal of atrazine from water by use of nonionic polymeric resins.* Journal of Environmental Science and Health, Part A: Environmental Science and Engineering, 1997. **32**(9): p. 2635 - 2656.
288. Acero, J.L., K. Stemmler, and U.v. Gunten, *Degradation kinetics of atrazine and its degradation products with ozone and OH radicals: a predictive tool for drinking water treatment* Environmental Science and Technology, 2000. **34**: p. 591 - 597.
289. Livage, J., T. Coradin, and C. Roux, *Encapsulation of biomolecules in silica gels.* Journal of Physics: Condensed Matter, 2001. **13**: p. R673-R691.
290. Depagne, C., C. Roux, and T. Coradin, *How to design cell-based biosensors using the sol-gel process.* Analitycal and Bioanalyical Chemistry, 2011. **400**: p. 965 - 976.
291. Hosticka, B., et al., *Gas flow through aerogels.* Journal of Non-Crystalline Solids, 1998. **225**: p. 293 - 297.
292. Eisenthal, R., et al., *The thermal behavior of enzyme activity: implications for biotechnology.* Trends in Biotechnology, 2006. **24**(7): p. 289 - 292.
293. Reátegui, E. and A. Aksan, *Effects of water on the structure and low/high temperature stability of confined proteins.* Physical Chemistry Chemical Physics, 2010. **12**: p. 10161-10172.
294. Depagne, C., C. Roux, and T. Coradin, *How to design cell-based biosensors using the sol-gel process.* Analytical Bioanalytical Chemistry, 2011. **400**: p. 965 - 976.
295. Premkumar, J.R., et al., *Fluorescent Bacteria Encapsulated in Sol-Gel Derived Silicate Films.* Chem. Mater., 2002. **14**: p. 2676 - 2686.
296. Soltman, U., et al., *Algae-silica hybrid materials for biosorption of heavy metals.* J. Water Resource and Protection, 2010. **2**: p. 115 - 122.
297. Kaur, I., A.K. Bhatnagar, and Singh Ved Pal and Stapleton Raymond D, Jr., *Algae-dependent bioremediation of hazardous wastes*, in *Progress in Industrial Microbiology*. 2002, Elsevier. p. 457-516.
298. Nedovic, V. and R. Willaert, *Fundamentals of Cell Immobilization Biotechnology*. Focus on Biotechnology, ed. M. Hofman and J. Anne. 2004, Dordrecht: Klumer Academic Publishers.
299. Stefanescu, M., M. Stoia, and O. Stefasnecu, *Thermal and FTIR study of the hybrid ethylene glycol silica matrix.* J. Sol-Gel Sci. Technol., 2007. **41**: p. 71 - 78.
300. Lesot, P., et al., *Structural-dynamical relationships in silica PEG hybrid gels.* Journal of Materials Chemistry, 1998. **8**(1): p. 147 - 151.
301. www.atcc.org. 2011.
302. Abramoff, M.D., P.J. Magalhaes, and S.J. Ram, *Image Processing with ImageJ.* Biophotonics International, 2004. **11**(7): p. 36 - 42.
303. Reátegui, E. and A. Aksan, *Effects of Water on the Structure and Low/High Temperature Stability of Confined Proteins.* Physical Chemistry and Chemical Physics, 2010. **12**: p. 10161-10172.

304. Fields, R.D. and M.V. Lancaster, *Dual-attribute continuous monitoring of cell proliferation/cytotoxicity.* Am. Biotechnol. Lab, 1993. **11**(4): p. 48-50.
305. Rubio, J. and J.A. Kitchener, *The Mechanism of Adsorption of Poly(Ethylene Oxide) Flocculant on Silica.* Journal of Colloid and Interface Science, 1976. **57**: p. 132 - 142.
306. Chang, J.-S., et al., *In vitro citotoxicity of silica nanoparticles at high concentrations strongly depends on the metabolic activity type of the cell line.* Environmental Science and Technology, 2009. **41**(6): p. 2064-2068.
307. Khattak, S.F., S.R. Bathia, and S.C. Roberts, *Pluronic F127 as a Cell Encapsulation Material: Utilization of Membrane Stabilizing Agents.* Tissue Engineering, 2005. **11**(5 - 6): p. 974 - 983.
308. Shchipunov, Y.A., *Sol-gel derived biomaterials of silica and carrageenans.* Journal of Colloid and Interface Science, 2003. **268**: p. 68 - 76.
309. Shchipunov, Y.A. and T.Y. Karpenko, *Hybrid polysaccharide-silica nanocomposite prepared by the sol-gel technique.* Langmuir, 2004. **20**(10): p. 3882 - 3887.
310. Shchipunov, Y.A., et al., *Gelling otherwise nongelable polysaccharides.* Journal of Colloid and Interface Science, 2005. **287**: p. 373 - 378.
311. Nunez, O., K. Nakanishi, and N. Tanaka, *Preparation o monolithic silica columns for high performance liquid chromatography.* Journal of Chromatography, 2008. **1191**: p. 231 - 252.
312. Nakanishi, K., *Pore structure control of silica gels based on phase separation.* Journal of Porous Materials, 1997. **4**: p. 67 - 112.
313. Agren, P., J. Counter, and P. Laggner, *A light and X-ray scattering study of the acid catalyzed silica synthesis in the presence of polyethylene glycol.* Journal of Non-Cristalline Solids, 2000. **261**: p. 195 - 203.
314. Shchipunov, Y. and N. Shipunova, *Regulation of silica morphology by proteins serving a s a template for mineralization.* Colloids and Surfaces B: Biointerfaces, 2008. **63**: p. 7 - 11.
315. Meyer, M., A. Fisher, and H. Hoffmann, *Novel Ringing Silica Gels That Do not Shrink.* J. Phys. Chem. B, 2002. **106**: p. 1528 - 1533.
316. Shalev, M. and A. Miriam, *Sol-gel entrapped levonorgestrel antibodies: activity and structural changes as a function of different polymer formats.* Materials, 2011. **4**: p. 469 - 486.
317. Conroy, J.F.T., et al., *Cells in sol-gel I: a cytocompatible route for the production of macroporous silica gels.* Journal of Sol-Gel Science and Technology, 2000. **18**: p. 269 - 283.
318. Chang, J.-S., et al., *In Vitro Cytotoxicity of Silica Nanoparticles at high Concentrations Strongly Depends on the Metabolic Activity Type of Cells.* Environmental Science and Technology, 2007. **41**(6): p. 2064-2068.
319. Nagle, J.F., *Theory of the Main Lipid Bilayer Phase Transition* Annual Review of Physical Chemistry, 1980. **31**: p. 157 - 196.
320. Cevc, G., *Isothermal Lipid Phase Transitions.* Chemistry and Physics of Lipids, 1991. **57**: p. 293 - 307.

321. Sahai, N., *Biomembrane Phospholipid-Oxide Surface Interactions: Crystal Chemical and Thermodynamic Basis.* Journal of Colloidal and Interface Science, 2002. **252**: p. 309-319.
322. Branyik, T., et al., *Encapsulation of Microbial Cells into Silica Gels.* Journal of Sol-Gel Science and Technology, 1998. **13**: p. 283 - 287.
323. Tadros, T.F., *Rheology of dispersions: Principles and applications*, ed. W.-V.V. GmbH. 2010, Weinheim.
324. Tsitsilianis, C., *Responsive reversible hydrogels from associative "smart" macromolecules.* Soft Matter, 2010. **6**: p. 2372 - 2388.
325. Tomme, S.R.V., et al., *Self-gelling hydrogels based on oppositely charged dextran microspheres.* Biomaterials, 2005. **26**: p. 2129 - 2135.
326. Mezger, T.G., *The rheology handbook: For users of rotational and oscillatory rheometry*. 2002: Vencentz Verlog.
327. Larson, R.G., *The structure and rheology of complex fluids*. 1999: Oxford University Press.
328. Shchipunov, Y.A., *Entrapment of biopolymers into sol-gel -derived silica nanocomposites*, in *Bio-inorganic Hybrid Nanomaterials*. 2008.
329. Park, J., et al., *Rheological characterization and optimization of gelled electrolyte for sealed lead-acid batteries by small amplitude dynamic oscillation measurement.* Journal of Non-Crystalline Solids, 2005. **351**: p. 2352 - 2357.
330. Semancik, J.R., *Yield stress measurements using controlled stress rheometry*, P. RH-058, Editor, TA Instruments
331. Barnes, H.A., J.F. Hutton, and K. Walters, *An introduction to rheology*. 1991, New York: Elseiver.
332. Egeblad, M., E.S. Nakasone, and Z. Werb, *Tumors as organs: Complex tissues that interface with the entire organism.* Cell, 2010. **18**.
333. Shepherd, T.G., et al., *Primary culture of ovarian surface ephitelial cells and ascites-derived ovarian cancer cells from patients.* Nature Protocols, 2006. **1**(6): p. 2643 - 2649.
334. Trzpis, M., et al., *Epithelial cell adhesion molecule: More than a carcinoma marker and adhesion molecule.* The American Journal of Patology, 2007. **171**(2): p. 386 - 395.
335. Kielberg, V., *Cryopreservation of mammalian cells* in *Thermo Scientific*. 2010. p. 1 - 2.
336. Rowley, S.D. and G.L. Anderson, *Effect of DMSO exposure without cryopreservation on hematopoietic progenitor cells.* Bone Marrow Transplant, 1993. **11**(5): p. 389 - 393.
337. Meryman, H.T., *Cryopreservation of living cells: principles and practice.* Transfussion, 2007. **47**: p. 935 - 945.

Appendix A: Sample preparation for SEM (Hitachi S-900)

A) For Cells attached to a substrate or encapsulated cells in silica gels

All steps are performed at room temperature.

1) Cells are attached to a cover slip or a glass slide. This is done by using cover slips or glass slides coated with poly-l-lysine solutions.

2) Samples are soaked in 2% (v/v) glutaraldehyde and 0.1 M sodium cacodylate solution for 10 to 18 hr. (18 hr for cells in gel).

3) Samples are rinsed with 0.1 M sodium cacodylate solution, three times to wash out excess of glutaraldehyde.

4) Samples are soaked in 1% (v/v) osmium tetraoxide and 0.1 M sodium cacodylate for 2 to 4 hr. (4 hr for cells in gel)

5) Samples are rinsed with 0.1 M sodium cacodylate solution, three times to wash out excess of osmium tetraoxide.

6) Samples are soaked in ethanol dilutions of 50, 70, 80, 95, and a 100 % for 30 min. each one.

7) Samples are transferred to a critical point drying machine for drying at the critical point of CO_2.

8) Samples are metal coated, depended on the resolution required, a thin or thick layer of metal can be chosen. Usually for high resolution imaging thinner coatings are required.

9) Transfer samples to the microscope for imaging.

10) Some samples may require cryo-fracture. In that case, at 95 % ethanol dehydration (step 6) transfer the sample to a holder with liquid nitrogen and using a surgery blade

gently cut the sample in pieces. Then, soaked the samples back in 95 % ethanol and continue with the regular procedure.

B) For silica gels

The fixation steps with the buffers above mentioned are not necessary since there is no need to preserve any organic material. Therefore, for this particular case the procedure start at step 6.

Appendix B: Macroporous silica materials

A) Macroporous Materials

Macroporous materials were synthesized following the route developed by Nakanishi.[6]

A.1) Materials

- Polyethylene glycol M_w = 10 kDa (400 mg, 450 mg, or 500 mg)

- Acetic acid 0.01 M (5 ml)

- TMOS (2.5 ml)

A.2) Procedure

- Prepare container at 0^0C for mixing the materials.

- Pour PEG and AA in the container and maintain stirring until uniform mixture is achieved; set up the stirred at 1200 RPM between 5 to 10 minutes will be enough.

- Add TMOS in a drop wise manner, and keep stirring for additional 30 minutes.

- Stop stirring, remove stirrer.

- Remove samples and pipette into appropriate containers.

- Let the samples gel and age at 40^0C for at least 48 hrs. The aging process can be done in the presence of water or not.

- Remove samples from 40°C.

It was observed that the porosity of the macroporous gels decreased when the concentration of PEG was increased as indicated in Fig. A.

---

[6] Nakanishi K. 1997 Pore structure control of silica gels based on phase separation, Journal of Porous Materials 4, 67 – 112

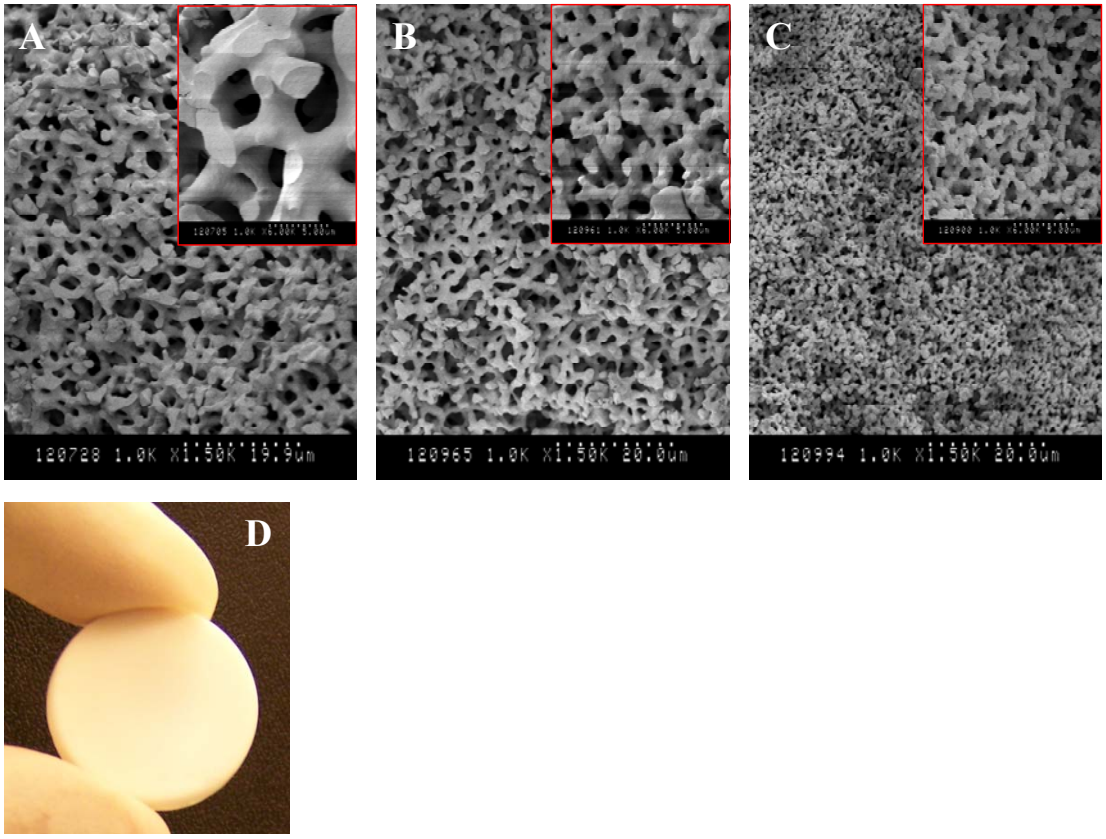

Figure S1 Changes in the macroporosity of silica gels by the incorporation of different concentrations of PEG. (A) 400 mg, (B) 450 mg, (C) 500 mg. (D) Material was casted as a disc, material was white opaque.

B) Macroporous Materials with *E.coli*

B.1) Materials

- Polyethylene glycol 10 kDa (400 mg)

- Acetic acid 0.0125 M (4 ml)

- TMOS (2.5 ml)

- Bacteria Solution in water (1 ml)

B.2) Procedure

- Prepare container at 0^0C for mixing the materials.

- Pour PEG and AA in the container and maintain stirring until uniform mixture is achieved; set up the stirred at 1200 RPM between 5 to 10 minutes will be enough.

- Add TMOS in a drop wise manner, and keep stirring for additional 30 minutes.

- Stop stirring, remove stirrer, and then add 1 ml of bacterial solution.

- Remove samples and pipette into appropriate containers.

- Let the samples gel and age at 40^0C for at least 48 hrs. The aging process can be done in the presence of water or not.

- Remove samples from 40°C.

Fig. S2 shows the macroporous structure in the presence of bacteria. The presence of the bacteria did not affect the interconnectivity of the macroporous matrix.

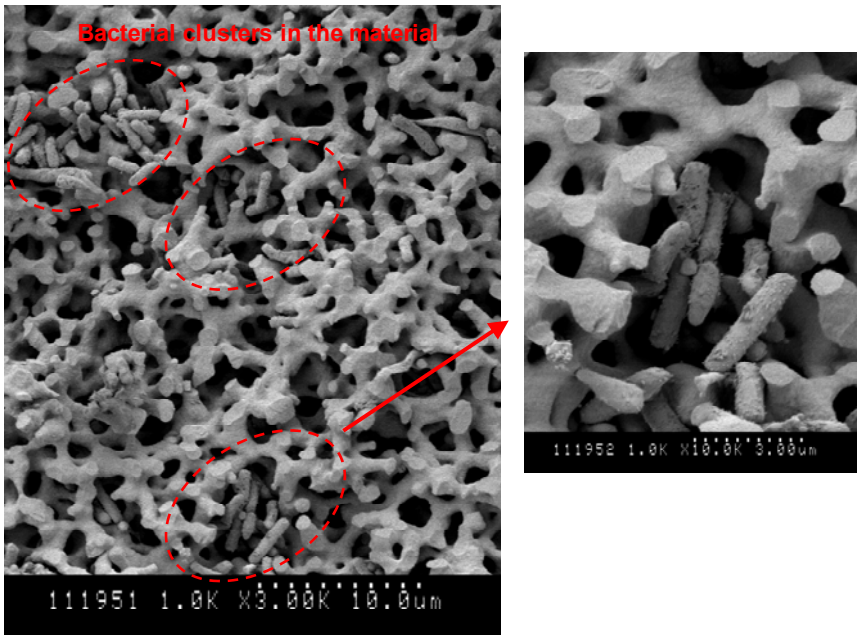

Figure S2 Development of a macroporous silica matrix with the incorporation of *E. coli*.

Appendix C: Culture media for microalgae *Neochloris oleoabundans*

In 1 l of distilled water add:

1) 250 mg of sodium nitrate.

2) 250 mg of potassium phosphate dibasic.

3) 75 mg of magnesium sulfate heptahydrate.

4) 25 mg of calcium chloride dihydrate.

5) 25 mg of sodium chloride.

6) 15 mg of ferric ammonium citrate

7) 100 mg of dirt.

After adding all the compounds (1) to (7) mixed completely by shaking the bottle, and then autoclaved for sterilization.

Appendix D: Algae encapsulation in reversible silica gels

Cultures of the microalgae *Neochloris oleoabundans* were obtained from Dr. Brett Barry at the Department of Bioproducts and Biosystems Engineering of the University of Minnesota. The cells were growth in specific growth medium (see appendix 6), and incubated at 25°C under continuous illumination (150 μ mol m^{-2} s^{-1}) using cool white commercial fluorescent lamps. Continuous orbital shaking was provided. The concentration of the algae in suspension was measured by optical density (OD). Cells were used in the experiments when they read an OD value of 0.65. Cells were encapsulated at a volume ratio of 2/1 or 4/1 (gel:algae solution). In these experiments, reversible gels synthesized with sodium silicate, dextran and PEG (see Table 6.2) were used since they exhibited higher stiffness values when compared to the reversible gels made of 4arm PEG (M_w = 2 kDa) shown in Table 6.1. The encapsulation procedure was similar to that described for mammalian cells.

Neochloris oleoabundans were encapsulated in the D1 reversible gel (Table 6.2 in Chapter 6). After encapsulation cells were stored at room temperature exposed to light (150 μ mol m^{-2} s^{-1}) and at 4°C for up to a month. Cells were released by adding excess algae media (Fig. S1) on the gel and gently vortexing or pipeting. The released cells were transferred into a culture flask with 150 ml of algae growth medium and an increase in cell growth was observed with time.

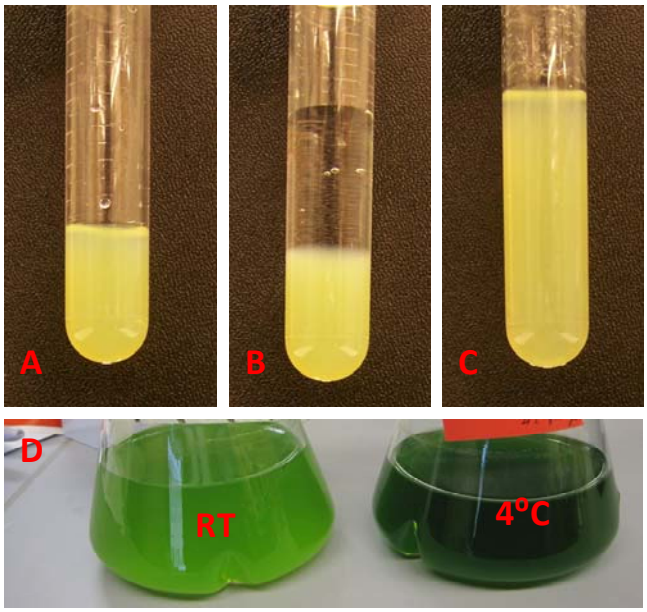

Figure S3 Encapsulated algae in reversible gel (D1). (A) Encapsulated cells, (B) encapsulated cells with buffer prior to release, (C) released cells, (D) growing cells.

Appendix E: Freeze-thaw of cells encapsulated in reversible gels

Freeze-thaw was performed as follows: (1) Cells were frozen using a controlled rate freezer (Planer Co. UK), following a standard freezing protocol established for mammalian cells [335]. (2) Cells were rapidly thawed by immersing in a water bath kept at 37°C. encapsulated microalgae were flash frozen by immersing in liquid nitrogen and rapidly thawed by immersion in a water bath kept at 37°C.

The preferred method for long-term storage of cells is cryopreservation using cryoprotectants such as dimethyl sulfoxide (DMSO) [336, 337]. However, the residual amounts of DMSO left in the solution after the cells have been thawed has toxic effects on the cells [337]. We explored the possibility of using the reversible encapsulation technology for cryopreservation of cells in a way that would not require DMSO. Cells were encapsulated in different reversible gels (A3, A7, and A11) at concentrations of 4500 cells/μl. Only up to 15 % of the gel volume was added in terms of cell solution, in order to maintain the stiffness of the gel. The negative control was cells in solution, and the positive control was cells in 10 % DMSO. Samples were frozen following a standard freezing protocol used for mammalian cells [335], and then stored in liquid nitrogen vapor at -80°C for a week. Samples were then rapidly thawed at 37°C and the membrane integrity of the cells was assayed. The results showed that the cells encapsulated in reversible gels were comparable to the cells frozen in DMSO (in terms of membrane integrity) values of membrane integrity when compared with DMSO. Fig. S4 shows the possibility of using reversible encapsulation as an alternative to cryopreservation using cryoprotectants.

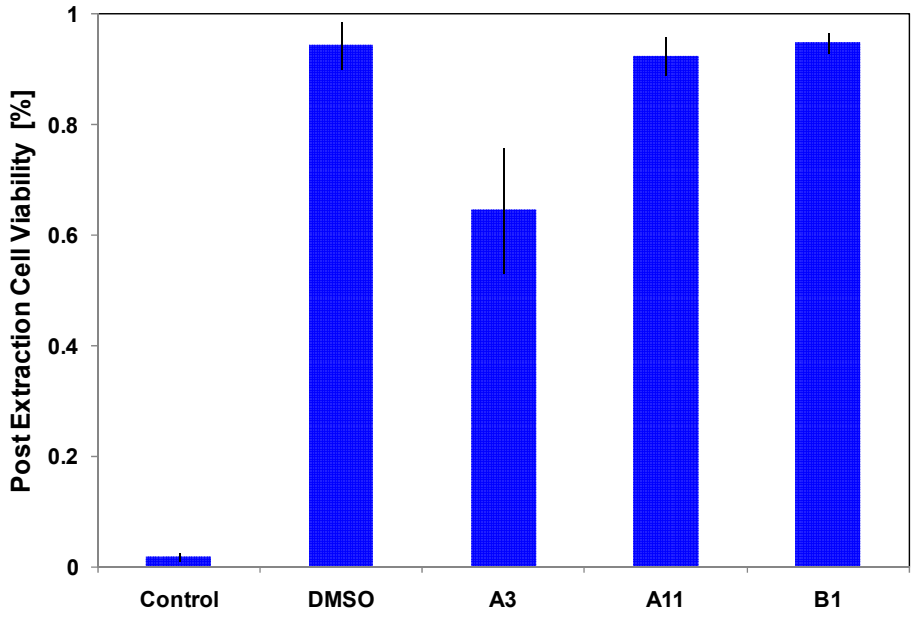

Figure S4 Post-extraction membrane integrity of cells encapsulated in different thixotropic gels after freeze-thaw (refer to Table 6.1 for compositions).

Freeze-thaw of microalgae also showed promising results (Fig. S5). The encapsulated algae were flash freezing in liquid nitrogen, and storage for a week in liquid nitrogen vapor at – 80°C as indicated in Fig. S3. Encapsulated cells were thawed at 37°C for 5 min. Algae was released from the gel as described before, and then the cells were cultured for 3 weeks (Fig. S5).

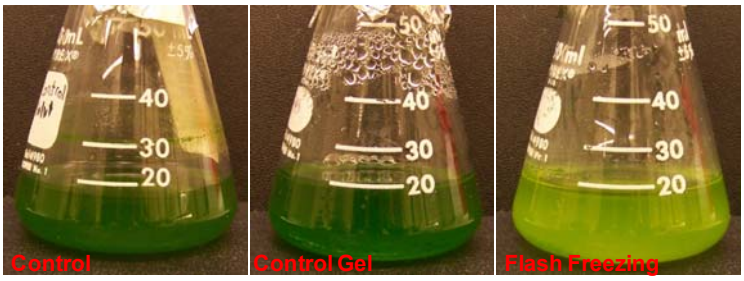

Figure S5 Freeze-thawed algae. Cells were cultured for 3 weeks after freeze-thaw.

Appendix F: Immunohistochemistry[7]

This protocol is used for staining cells with specific antibodies in order to determine the phenotype of the labeled cells.

1) First, cells were seeded or incubated on a cover slip or 6-well plate until the desired cell density was obtained.

2) Remove all the media form the culture cells and wash twice with PBS.

3) Add 300 – 400 µl of 2 – 4 % of formaldehyde fixative solution to each well, and incubate for 20 min.

4) Wash the cells twice with PBS and cover with 400 µl of wash buffer. The samples can be storage at 2 – 8°C for up to 3 months or they may be stained immediately. Wash buffer is prepared with 0.1 % BSA in 1X PBS.

5) Wash the cells twice with 400 µl of wash buffer

6) Block non-specific staining by adding 400 µl of blocking buffer and incubate for 45 min at room temperature.

7) Remove blocking buffer.

8) Dilute the primary antibody (EpCAM/TROP1) in 1X PBS at a concentration of 25 µg/ml.

9) Add 1 ml of the diluted antibody to the cells and incubate at room temperature for 1 h. It is possible to incubate overnight at 2 – 8°C.

10) Wash two times in 400 µl of wash buffer.

---

[7] Part this protocol was obtained from R&D Systems

11) Dilute the secondary antibody in 1X PBS at a volume ratio of 1/200.

12) Add 400 µl of the secondary antibody to the cells and incubate for 1 h at room temperature in the dark.

13) Rinse two times in 400 µl of wash buffer.

14) Add 300 µl of diluted DAPI solution to each sample, and incubated 2 – 5 min at room temperature. DAPI is a nuclear dye that stains all the cells.

15) Rinse once with PBS and once with water.

16) Visualize using a fluorescence microscope with the appropriate filters.